

# Analysis of the viscoelastic deformation behaviour of continuous fibre-reinforced polymers subjected to the automotive painting process



Y. L. M. van Dijk

*This thesis has been written in fulfilment of the degree of  
Master of Science*



## Written agreement on imposing a non-disclosure notice

This agreement applies to the master thesis of

Mr.	Yannick van Dijk
with the title	Analysis of the viscoelastic deformation behaviour of continuous fibre-reinforced polymers subjected to the automotive painting process.

for which the supervision by BMW AG has been carried out by

Mr.	Thomas Grätzl
from department	MK-520


The following notice applies to the entire thesis, starting from the first page after the cover page, until the provided ending date:

### Non-disclosure notice

This thesis contains sensitive information that is subjected to confidentiality. It is therefore prohibited to duplicate, publish, or release this thesis without receiving written approval of BMW AG in advance. This right of veto ends at 31/10/2022.

The ending date of this agreement is 31/10/2022 and in mutual agreement with the non-disclosure notice shown above.

Yannick van Dijk



*Signature*

*Landshut 06.11.2017*

*Date and place*

Thomas Grätzl



*Signature*

*Landshut, 6.11.17*

*Date and place*





# **Analysis of the viscoelastic deformation behaviour of continuous fibre-reinforced polymers subjected to the automotive painting process**



**Y.L.M. van Dijk**

This thesis has been written in fulfilment of the degree of

*Master of Science*



Delft University of Technology  
Faculty of Aerospace Engineering  
Department of Aerospace Structures and Materials

Graduation Committee

---

Dated 24-11-2017

---

Dr. S.R. Turteltaub  
*Chair holder*

---

Dr. I. Fernandez-Villegas  
*External department committee member*

---

Dr. M. Abouhamzeh  
*Supervisor Delft University of Technology*

---

T. Grätzl MSc  
*Supervisor BMW Group*





# Abstract

The automotive industry has developed an interest in manufacturing structural parts from continuous fibre-reinforced polymers because legislation is becoming more strict on the permissible CO<sub>2</sub> emission of newly produced vehicles. Additional requirements on the level of recyclability has raised the question if composite materials with a thermoplastic matrix in particular can be utilised in the body structure. From the perspective of cost sensitivity, the conventional automotive manufacturing chain has to remain as it is and requires the body structure to pass through the automotive paint shop and subjects all structural elements to significant hygrothermal loading. The objective of this research is to analyse the deformation behaviour of continuous fibre-reinforced thermoplastics subjected to hygrothermal loading characteristic for the automotive painting process.

Studying the theory behind viscoelastic problems revealed that numerical solutions to the integral form of the linear viscoelastic constitutive equations often pose a problem regarding computational memory usage because of the importance of strain history. Utilising a recursive formulation of the constitutive equations eliminated this problem and identified the required material parameters for the numerical model. Thermal expansion, hygroscopic shrinkage, polymer-chemical effects, and stress relaxation were the four phenomena that governed the deformation. Measurements with a dilatometer, a micrometer, and an analytical scale yielded quantitative results about hygrothermal expansion. Thermogravimetric analysis provided information on the moisture diffusion and dynamic mechanical analysis quantified the stress relaxation behaviour. Quasi-static tensile tests confirmed the linearity of the viscoelasticity and digital image correlation supplied the major Poisson's ratio.

A finite element model has been developed that implements hygrothermal expansion and takes into account orthotropic linear viscoelastic behaviour by means of a material user subroutine. Adopting a sequential uncoupled simulation approach allowed the prediction of heat transfer, moisture diffusion, and stress distribution. A semi-numerical simulation approach enabled the calculation of the expansion of symmetric balanced laminates through classical laminate theory whilst taking into account the time- and temperature-dependency of the mechanical properties computed with a micromechanical model created for special orthotropic laminae. Sensitivity studies justified the usage of one-dimensional heat transfer- and moisture diffusion simulations. Moreover, mesh- and time step convergence studies revealed the sensitivity of the simulation to these parameters.

Dilatometer experiments with dry- and moisture saturated multi-directional specimens confirmed the correct calculation of hygrothermal expansion. Increasing in complexity, measuring the out-of-plane deformation of a clamped unidirectional tensile specimen subjected to a temperature profile that resembles the most severe thermal loading found in the automotive painting process confirmed a satisfactory agreement between the numerical results and the experimental data. Geometric compensation for the thermal expansion of the fixture and choosing graphite as construction material kept the thermal expansion of the fixture to a minimum. Components with the geometry of the roof bow that is currently in series production for the BMW 7 Series were manufactured by a thermoforming method to allow validation of the simulation with complex geometry. A proper agreement between the predicted deformation behaviour by the semi-numerical simulation and the optical measurements of the dry- and moisture saturated roof bows with various multi-directional lay-ups validated the functioning of the developed simulation.



# Contents

List of Figures . . . . .	i
List of Tables . . . . .	vii
Nomenclature. . . . .	xi
Preface . . . . .	xiii
1 Introduction . . . . .	1
1.1 Motivation . . . . .	1
1.2 Problem statement . . . . .	3
1.3 Conceptual design of the research . . . . .	4
1.4 Structure of the thesis . . . . .	5
2 State of the art . . . . .	7
2.1 The automotive paint shop. . . . .	8
2.2 Hygrothermal response of thermoplastics . . . . .	9
2.3 Numerical modelling of viscoelasticity . . . . .	11
3 Viscoelastic theories. . . . .	17
3.1 Introduction to viscoelasticity . . . . .	17
3.2 Integral formulations . . . . .	19
3.3 Differential formulations . . . . .	21
3.4 Thermal- and hygroscopic effects. . . . .	30
3.5 Anisotropy and viscoelastic correspondence . . . . .	34
3.6 Constitutive equations . . . . .	37

4	Material characterisation . . . . .	49
4.1	Overview of experimental characterisation . . . . .	49
4.2	Thermogravimetric analysis . . . . .	52
4.3	Dilatometer experiments . . . . .	55
4.4	Micrometer measurements . . . . .	60
4.5	Quasi-static tensile tests . . . . .	62
4.6	Digital image correlation . . . . .	65
4.7	Relaxation experiments . . . . .	66
4.8	Dynamic mechanical analysis . . . . .	68
4.9	Micromechanical model . . . . .	75
5	Finite element modelling . . . . .	83
5.1	Model framework . . . . .	83
5.2	User subroutine development . . . . .	88
5.3	Verification of user subroutine . . . . .	90
5.4	Convergence- and simplification verification studies . . . . .	96
6	Experimental validation . . . . .	101
6.1	Validation strategies . . . . .	101
6.2	Dilatometer validation . . . . .	102
6.3	Coupon level validation . . . . .	110
6.4	Component level validation . . . . .	116
7	Improvement of the simulation . . . . .	121
7.1	Analytical hygrothermal expansion of multi-directional laminates . . . . .	121
7.2	Results of improved simulation . . . . .	124
7.3	Sensitivity to physical effects and fibre orientation . . . . .	128
8	Conclusion . . . . .	135
9	Recommendations . . . . .	139
	References . . . . .	145
A	UMAT user subroutine . . . . .	147
B	Technical drawings . . . . .	149







# List of Figures

2.1	Typical Fickian moisture diffusion showing a two-stage process of moisture uptake. . . . .	10
3.1	The phenomena creep and relaxation, respectively left and right, represented arbitrarily. . . . .	18
3.2	Isochrones of glass-fibre reinforced polyamide-6 as reference for non-linear viscoelastic behaviour. Data was obtained from CAMPUSplastics [50]. . . . .	19
3.3	Schematic representation of the linear elastic spring and the linear viscous dashpot left and right, respectively. . . . .	22
3.4	Schematic representation of the Kelvin-Voigt model. . . . .	24
3.5	Schematic representation of the Maxwell model. . . . .	26
3.6	Schematic representation of the generalised Maxwell model. . . . .	29
3.7	The principle of time-temperature superposition to obtain a mastercurve from multiple viscoelastic functions measured at different temperature conditions. . . . .	32
3.8	Sign convention for the stress tensor as defined for three dimensions. . . . .	35
3.9	Influence of the time step size on the accuracy of the constitutive equations. . . . .	47
4.1	Diffusion coefficients obtained for the composite material. . . . .	54
4.2	Arrhenius curve describing the development of the diffusion coefficient as a function of temperature. . . . .	55
4.3	Temperature profile and resulting strain values for the dry- and moist specimens in transverse direction in the dilatometer experiment. . . . .	57
4.4	Calculated tangential coefficients of thermal expansion of the dry composite material in transverse direction for two heat cycles. . . . .	58
4.5	Comparison between the tangential coefficients of thermal expansion between the dry- and moisture saturated composite material in transverse direction for the first heat cycle. . . . .	59
4.6	Temperature profile and resulting strain values for the dry- and moist specimens in longitudinal direction in the dilatometer experiment. . . . .	59

4.7	Calculated tangential coefficients of thermal expansion of the dry composite material in longitudinal direction for two heat cycles. . . . .	60
4.8	Micrometer measurements for the determination of the coefficients of moisture expansion. . .	61
4.9	Stress-strain curves of the dry composite material in longitudinal direction at 23 °C and 180 °C, shown in the upper and lower part, respectively. . . . .	63
4.10	Stress-strain curves of the dry composite material in transverse direction at 23 °C and 180 °C, shown in the upper and lower part, respectively. . . . .	64
4.11	Normalised relaxation curves of the dry composite material in transverse direction at 23 °C. .	67
4.12	Normalised relaxation curves of the dry composite material in transverse direction at 180 °C. .	67
4.13	Reconstructed relaxation curve at 23 °C demonstrating the Boltzmann superposition principle of the dry composite material in transverse direction. The absolute difference between the two curves has been indicated with the dashed line. . . . .	68
4.14	Reconstructed relaxation curve at 180 °C demonstrating the Boltzmann superposition principle of the dry composite material in transverse direction. The absolute difference between the two curves has been indicated with the dashed line. . . . .	68
4.15	Mastercurve of the storage modulus in transverse direction of the composite material with 20 °C taken as reference temperature. . . . .	70
4.16	Mastercurve of the storage modulus in transverse direction of the composite material with 20 °C taken as reference temperature superposed by means of one shift factor to the mastercurve constructed with 70 °C as reference temperature. . . . .	70
4.17	Cole-cole diagram of the DMA measurements carried out in transverse direction to the fibre-orientation. . . . .	71
4.18	Fitted Prony series with 32 terms for the mastercurve of the storage modulus of the dry composite material in transverse direction. . . . .	73
4.19	Relaxation modulus of the dry composite material in transverse direction obtained through the fitted Prony series of the storage modulus. . . . .	73
4.20	Fit of the Williams-Landel-Ferry equation of the experimentally determined shift factors. . . .	74
4.21	Instantaneous transverse stiffness moduli obtained by DMA and comparable values from quasi-static tensile tests. . . . .	74
4.22	Orthotropic stiffness coefficients of the unidirectional laminate as a function of time. . . . .	79
4.23	A schematic overview of the order of calculations carried out in the micromechanical model. .	80
5.1	The boundary conditions for the stress simulation of the validation coupon. . . . .	85



5.2	The boundary conditions for the stress simulation of the validation component. . . . .	85
5.3	Flowchart of the numerical modelling workflow for a moisture saturated specimen. . . . .	87
5.4	Applied boundary conditions for the verification tests in order from 1 to 5 from left to right. .	91
5.5	Verification results of the uniaxial isothermal step strain input. . . . .	92
5.6	Verification results of the bi-axial isothermal step strain input. . . . .	93
5.7	Verification results of pressurised linear viscoelastic rocket fuel under isothermal conditions. .	94
5.8	Verification results and thermal boundary conditions of the non-isothermal uniaxial step strain input. . . . .	95
5.9	Verification results of the non-isothermal uniaxial single square-wave pulse strain input. . . . .	96
5.10	Sensitivity analysis to limiting the heat transfer simulation to one dimension. . . . .	97
5.11	Sensitivity analysis to limiting the mass diffusion simulation to one dimension. . . . .	97
5.12	Results of the mesh convergence study of the stress simulation for the component validation experiment. . . . .	98
5.13	Results of the time step size convergence study of the stress simulation for the component validation experiment. . . . .	98
6.1	The temperature envelope used for the validation dilatometer experiments. . . . .	103
6.2	Experimental data and simulation of validation dilatometer experiment with a dry specimen with a $[90_{16}^{\circ}]$ lay-up. . . . .	103
6.3	Experimental data and simulation of validation dilatometer experiment with a dry specimen with a $[+30_4^{\circ} / -30_4^{\circ}]_s$ lay-up. . . . .	104
6.4	Experimental data and simulation of validation dilatometer experiment with a dry specimen with a $[+60_4^{\circ} / -60_4^{\circ}]_s$ lay-up. . . . .	104
6.5	Experimental data and simulation of validation dilatometer experiment with a dry specimen with a $[0_4^{\circ} / 90_4^{\circ}]_s$ lay-up. . . . .	105
6.6	Experimental data and simulation of validation dilatometer experiment with a dry specimen with a $[+45^{\circ} / -45^{\circ} / 0_5]_s$ lay-up. . . . .	106
6.7	Experimental data and simulation of validation dilatometer experiment with a specimen conditioned to full moisture saturation with a $[90_{16}^{\circ}]$ lay-up. . . . .	106
6.8	Experimental data and simulation of validation dilatometer experiment with a specimen conditioned to full moisture saturation with a $[+30_4^{\circ} / -30_4^{\circ}]_s$ lay-up. . . . .	107

6.9	Experimental data and simulation of validation dilatometer experiment with a specimen conditioned to full moisture saturation with a $[+60_4^\circ / - 60_4^\circ]_s$ lay-up. . . . .	108
6.10	Experimental data and simulation of validation dilatometer experiment with a specimen conditioned to full moisture saturation with a $[0_4^\circ / 90_4^\circ]_s$ lay-up. . . . .	108
6.11	Experimental data and simulation of validation dilatometer experiment with a specimen conditioned to full moisture saturation with a $[+45^\circ / - 45^\circ / 0_5]_s$ lay-up. . . . .	109
6.12	Geometrical concept to incorporate geometric compensation for the thermal expansion of the fixture. . . . .	111
6.13	Coefficients of thermal expansion of the two types of graphite material that were used for the fixture of the coupon level validation experiments. . . . .	112
6.14	The fixture for clamping the tensile test specimen during the coupon level validation experiments.	113
6.15	Simulated surface temperature by means of convection in comparison to the measured air- and measured surface temperature of the suspended specimen. . . . .	114
6.16	The utilised experimental setup to measure the deflection of the coupons and components. . .	114
6.17	Experimental data and simulation of the center out-of-plane deformation of a dry- and moisture saturated tensile test specimen with $[90_{16}^\circ]_s$ lay-up subjected to the cathodic dip painting temperature profile. . . . .	115
6.18	The fixture for clamping the component during the component level validation experiments. .	116
6.19	Experimental data and results of the initial simulation approach of the center out-of-plane deformation of a dry reference component with $[90_{16}^\circ]_s$ lay-up subjected to the cathodic dip painting temperature profile. . . . .	116
6.20	Experimental data and results of the initial simulation approach of the center out-of-plane deformation of a dry reference component with $[0 / + 45^\circ / - 45^\circ / 0_4]_s$ lay-up subjected to the cathodic dip painting temperature profile. . . . .	117
6.21	Experimental data and results of the initial simulation approach of the center out-of-plane deformation of a dry reference component with $[(+60^\circ / - 60^\circ)_3 / 0^\circ]_s$ lay-up subjected to the cathodic dip painting temperature profile. . . . .	119
7.1	Numerical results of the improved simulation approach of the center out-of-plane deformation of a dry reference component with $[90_{16}^\circ]_s$ lay-up subjected to the cathodic dip painting temperature profile. . . . .	125
7.2	Numerical results of the improved simulation approach of the center out-of-plane deformation of a dry reference component with $[0 / + 45^\circ / - 45^\circ / 0_4]_s$ lay-up subjected to the cathodic dip painting temperature profile. . . . .	126

7.3	Numerical results of the improved simulation approach of the center out-of-plane deformation of a dry reference component with $[(+60^\circ / -60^\circ)_3 / 0^\circ]_s$ lay-up subjected to the cathodic dip painting temperature profile. . . . .	127
7.4	Results of the sensitivity study for the component with a $[90^\circ_{16}]$ lay-up to the influence of time-temperature superposition, hygroscopic shrinkage, and polymer-chemical effects. . . . .	128
7.5	Results of the sensitivity study for the component with a $[0 / +45^\circ / -45^\circ / 0_4]_s$ lay-up to the influence of time-temperature superposition, hygroscopic shrinkage, and polymer-chemical effects. . . . .	129
7.6	Results of the sensitivity study for the component with a $[(+60^\circ / -60^\circ)_3 / 0^\circ]_s$ lay-up to the influence of time-temperature superposition, hygroscopic shrinkage, and polymer-chemical effects. . . . .	130
7.7	Results of the sensitivity study for the component with a $[0 / +45^\circ / -45^\circ / 0_4]_s$ lay-up to the influence of imperfections in fibre orientation. . . . .	131
7.8	Results of the sensitivity study for the component with a $[(+60^\circ / -60^\circ)_3 / 0^\circ]_s$ lay-up to the influence of imperfections in fibre orientation. . . . .	133
B.1	Technical drawing of the main part of the fixture for the coupon level validation experiments. . . . .	149
B.2	Technical drawing of the parts used for clamping the coupon in the fixture for the coupon level validation experiments. . . . .	150
B.3	Technical drawings of the fixture for the component level validation experiments. . . . .	151





# List of Tables

2.1	Chemical- and thermal loads imposed on structural members during the automotive painting process [4, 6, 7]. . . . .	9
4.1	Overview of the conducted experiments for the material characterisation of the unidirectional composite material. . . . .	52
4.2	Material parameters that have been taken from the datasheet. . . . .	52
4.3	Diffusion coefficients at different temperatures. . . . .	55
4.4	Arrhenius fit parameters. . . . .	55
4.5	Lamina coefficients of hygroscopic expansion. . . . .	61
4.6	Instantaneous moduli of CF60-PA6 at room temperature. . . . .	63
4.7	Major Poisson's ratio at room temperature of unidirectional CF60-PA6. . . . .	65
4.8	Convergence table for number of Prony terms for fit of storage modulus mastercurve. . . . .	72
4.9	Values of the relaxation times and determined Prony coefficients for the independent stiffness components of a unidirectional layer of CF60-PA6. . . . .	81
5.1	Simulation parameters in ABAQUS. . . . .	86
5.2	Material parameters that have been used for the user subroutine verification. . . . .	91
6.1	Lay-up selection for dilatometer validation experiments. . . . .	102
6.2	Discrepancies between simulation and experimental data for the dilatometer validation experiments. . . . .	109
7.1	Discrepancy between improved simulation result and experimental measurement at maximum deflection. . . . .	127
7.2	Simulated lay-ups to assess the influence of fibre orientation on the out-of-plane deformation behaviour. . . . .	132



# Nomenclature

## Roman Symbols

$A_s$	Surface area for convection . . . . .	$[m^2]$
$a_T$	Horizontal temperature shift factor . . . . .	$[-]$
$a_W$	Horizontal moisture content shift factor . . . . .	$[-]$
$C(t)$	Creep compliance function . . . . .	$[n.a.]$
$C_1$	First coefficient in Williams-Landel-Ferry equation . . . . .	$[-]$
$C_2$	Second coefficient in Williams-Landel-Ferry equation . . . . .	$[^{\circ}C]$
$C_p$	Specific heat . . . . .	$[J/(kg^{\circ})]$
$C_{ijkl}$	Anisotropic stiffness tensor . . . . .	$[Pa]$
$C_{ij}$	Orthotropic stiffness tensor . . . . .	$[Pa]$
$D$	Diffusion coefficient . . . . .	$[m^2/s]$
$D_0$	Frequency factor . . . . .	$[m^2/s]$
$D_1$	First coefficient in time-moisture superposition equation . . . . .	$[-]$
$D_2$	Second coefficient in time-moisture superposition equation . . . . .	$[-]$
$E$	Loss modulus . . . . .	$[Pa]$
$E'$	Storage modulus . . . . .	$[Pa]$
$E(t)$	Relaxation modulus . . . . .	$[Pa]$
$E^*$	Complex modulus . . . . .	$[Pa]$
$E_{\infty}$	Long term modulus . . . . .	$[Pa]$
$E_A$	Activation energy . . . . .	$[J/mol]$
$E_i$	Stiffness of linear elastic spring . . . . .	$[Pa]$
$FV$	Field variable . . . . .	$[-]$
$G$	Shear modulus . . . . .	$[Pa]$
$G_{\varepsilon}$	Reduced time derivative of strain . . . . .	$[s]$
$h$	Convection coefficient . . . . .	$[-]$

$H(t)$	Heaviside function . . . . .	[ <i>n.a.</i> ]
$K$	Sollubility . . . . .	[ $-$ ]
$K_m$	Polymer bulk modulus . . . . .	[ <i>Pa</i> ]
$L$	Length . . . . .	[ <i>m</i> ]
$l$	Diffusion distance . . . . .	[ <i>m</i> ]
$M$	Moisture content . . . . .	[ $-$ ]
$P$	Rheological stress operator . . . . .	[ <i>n.a.</i> ]
$Q$	Rheological strain operator . . . . .	[ <i>n.a.</i> ]
$q_{conv}$	Convective heat flow . . . . .	[ <i>W</i> ]
$R$	Gas constant . . . . .	[ <i>J/(mol K)</i> ]
$R(\xi)$	Recursive stress contribution due to strain history . . . . .	[ <i>Pa</i> ]
$T$	Temperature . . . . .	[ $^{\circ}C$ ]
$t$	Time . . . . .	[ <i>s</i> ]
$T_{air}$	Air temperature . . . . .	[ $^{\circ}C$ ]
$T_{end}$	End temperature of the verification test . . . . .	[ $^{\circ}C$ ]
$T_{ref}$	Reference temperature for time-temperature superposition . . . . .	[ $^{\circ}C$ ]
$T_{start}$	Start temperature of the verification test . . . . .	[ $^{\circ}C$ ]
$T_{sur}$	Surface temperature . . . . .	[ $^{\circ}C$ ]
$v_f$	Fibre volume fraction . . . . .	[ $-$ ]
$v_m$	Matrix volume fraction . . . . .	[ $-$ ]
$W$	Mass of specimen . . . . .	[ <i>kg</i> ]
$W_{ref}$	Reference moisture content for time-moisture superposition . . . . .	[ $-$ ]

### Greek Symbols

$\alpha_T$	Tangential coefficient of thermal expansion . . . . .	[ $1/^{\circ}C$ ]
$\alpha_{kl}$	Anisotropic tangential coefficient of thermal expansion . . . . .	[ $/^{\circ}C$ ]
$\bar{\alpha}_T$	Secant coefficient of thermal expansion . . . . .	[ $1/^{\circ}C$ ]
$\beta_M$	Tangential coefficient of moisture expansion . . . . .	[ $-$ ]
$\beta_{kl}$	Anisotropic tangential coefficient of moisture expansion . . . . .	[ $-$ ]
$\dot{\epsilon}$	Strain rate . . . . .	[ $1/s$ ]
$\eta$	Viscosity . . . . .	[ <i>Pa s</i> ]

$\gamma$	Shear strain . . . . .	$[-]$
$\lambda$	Thermal conductivity . . . . .	$[W/(m\text{ }^{\circ}C)]$
$\nu$	Poisson's ratio . . . . .	$[-]$
$\omega$	Frequency . . . . .	$[Hz]$
$\phi$	Creep function . . . . .	$[n.a.]$
$\psi$	Relaxation function . . . . .	$[n.a.]$
$\rho$	Density . . . . .	$[kg/m^3]$
$\sigma$	Stress . . . . .	$[Pa]$
$\tau$	Relaxation time . . . . .	$[s]$
$\varepsilon$	Strain . . . . .	$[-]$
$\xi$	Reduced time obtained by time-temperature superposition . . . . .	$[s]$

### Acronyms / Abbreviations

BIW	Body-in-white
BMW AG	Bayerische Motoren Werke Aktiengesellschaft
CDP	Cathodic dip painting
CFRP	Carbon fibre-reinforced polymers
CFRTP	Carbon fibre-reinforced thermoplastics
CME	Coefficient of moisture expansion
CTE	Coefficient of thermal expansion
DIC	Digital image correlation
DMA	Dynamic mechanical analysis
GLARE	Glass reinforced aluminium
RSS	Residual sum of squares
TGA	Thermogravimetric analysis



# Preface

Conducting the present thesis research has allowed me to grow in scientific perspective, it has provided me with valuable insights on career paths, and it led to personal development on a multitude of areas. For this I am thankful and my gratitude goes to Thomas Gräetzel for being my daily supervisor at the BMW Group and supporting me where possible with full dedication. I am confident that our cooperation has been fruitful and I am glad that I was given the opportunity to apply my theoretical knowledge in practice.

I have equally appreciative thoughts about my supervisors Morteza Abouhamzeh and Sonell Shroff at Delft University of Technology. Planning meetings was never troublesome and the encouraging willingness to provide feedback or advice was present at all times. The level of supervision and critical reflection always felt excellent and resulted in the motivation that made me wear a smile and have a positive mindset every day, all day long.

*Y.L.M. van Dijk*  
*Landsbut, November 2017*





# 1

## Introduction

This thesis presents the research project that has been carried out at the BMW Group Landshut in fulfilment of a master degree at Delft University of Technology. The objective of the thesis is to develop a numerical model that simulates the viscoelastic deformation behaviour of continuous fibre-reinforced thermoplastics. The loading conditions that cause the viscoelastic deformation behaviour are chosen to be in correspondence with the automotive painting process. This chapter outlines the context of the thesis and provides the limitations on the scope of the research. Moreover, it informs on the significance of the research by presenting the problem that must be solved and its impact. The last section of the introduction shows the structure of the thesis.

### 1.1 Motivation

Characteristic for the automotive industry are the high volume production and the consequential cost-sensitivity. To illustrate the manufacturing numbers, BMW produced 165,377 units of the BMW X5 model in 2016. The total number of BMW X models that were produced that year is 411,171. In combination with the high degree of automation in the manufacturing process, adaptations to the manufacturing chain are to be avoided whenever possible in order to ensure a profitable production. The high-end manufacturers in the automotive industry are encouraged to innovate at all possible technical disciplines to maintain their position in the market. Nevertheless, changes to production vehicles are implemented at a regular interval and are only accepted if they pose a minimum risk towards raising unexpected costs.

BMW has shown successful utilisation of composite materials in series production through the BMW i3 and BMW i8 models. Both models feature passenger cells that are fully produced with carbon-fibre reinforced plastics, or CFRP. It is important to note that the production chain for these models has been newly established to suit the CFRP design. Both projects served as a platform to promote the development of CFRP manufacturing techniques and to display the possibilities of CFRP-dominated designs. Despite achieving the production of a full CFRP passenger cell, replacing currently existing metal structural parts of series produced models with composite structural members poses a challenge to be carried out in an economically attractive manner.

In the last decade, the attention for global warming has grown significantly. Because of the large share of harmful vehicle emissions in this environmental issue, many governmental institutions restrict the allowed average CO<sub>2</sub> emissions of manufacturers' fleets. The European Parliament released a regulation in 2009 that stipulates average allowed CO<sub>2</sub> emissions for a new car fleet of 130g/km [1]. The same regulation sets the target of an average emission level of 95g/km CO<sub>2</sub> for new car fleets from 2020 onwards. A further decrease in maximum allowed average CO<sub>2</sub> emissions is expected as a target range has been set by the Environment Committee of the European Parliament for 2025 of 68 – 78g/km [2].

These regulations effectively force car manufacturers to improve their vehicles to lower the emissions of their car models to guarantee their existence in the future. Successful reduction in emissions are shown especially through technological advances in the fields of propulsion, aerodynamics, and structural design. For instance, lowering the reliance on the internal combustion engine by implementation of an electric engine, either in hybrid- or fully electric configuration, contributes to the reduction in average fleet emissions. However, the distance range of state-of-the-art fully electric cars remains limited and the considerably higher purchase price even of hybrid vehicles is a reason for many consumers to keep driving cars that fully rely on fossil fuels.

The emissions of cars that only have an internal combustion engine can potentially be improved through adaptations in aerodynamic design. The gradually increasing computational power of processors allows for more detailed and comprehensive computational fluid dynamics calculations that may lead to a reduction in aerodynamic drag. The design space for aerodynamicists is, however, limited by the practical use that a vehicle must display. Consumer cars are most often purchased for their practical use and these models are subjected to the requirement of providing ample occupant space and -comfort.

The last discipline where significant reductions in car emissions can be realised is structural design. Conventional automotive vehicle design initially started with the application of steel for structural members. Aluminium has replaced steel in many parts of the structural design due to its more lightweight character. Specific areas that require a high energy absorption capability for crash safety reasons and are subjected to limited available space for structural members still contain steel. The reduction in a car's structural weight will have secondary effects in the sense that it requires less power for equivalent driving performance. A reduction in propulsion performance will result in an even more lightweight design when iterated appropriately.

Following the aerospace industry, employing composite materials in vehicle structural design has proven to allow further reductions in weight. Nevertheless, there are many more aspects that must be considered in vehicle design than only the vehicle weight. Crash safety, manufacturing cycle times, quality assurance, and costs are a few examples. The reduction in fleet emissions is a vital mission for a car manufacturer's existence, but equally important is selling vehicles. Thus, the implementation of composite materials in structural design of vehicles that are sold to price-aware consumers must be performed in a manner that restrains the increase in cost. Furthermore, the driving performance and safety of the car must not be affected in a negative way.

The gradual increase in the application of composite materials in the vehicle structure of series produced vehicles is apparent in the design of the BMW 7 Series. The body structure features a 'Carbon Core' and is comprised of parts that have been manufactured from CFRP, aluminium, and high-strength steel. Selective material choice results in a lightweight structure that is stiff, strong, and has high specific energy absorption capabilities for safety. In contrast to the production of the BMW i3 and BMW i8 models, the manufacturing process of the BMW 7 Series has not been altered due to the original BMW 7 Series only including metal body structure parts. It is important to note that every structural composite part features thermoset matrix material at the moment.

Although thermoset matrix material generally enables the production of composite structures at a lower raw material cost, recent coming into force of legislative changes on recyclability favours the use of thermoplastic matrix material. Analogous to restrictions on vehicle emissions, the European Parliament imposes requirements to the recyclability of end-of-life vehicles. A directive that aims to steer vehicle manufacturers towards accounting for dismantling, reuse, and recovery of their products was released in 2000 [3]. The directive imposes that new vehicles produced in 2015 and onwards must have a minimum of 95% weight percentage that is either reusable or recoverable. Structures made of CFRP with a thermoset matrix material are most often only recycled in the form of filler material and do not serve a structural purpose.

On the contrary, thermoplastic matrix materials offer recycling possibilities through thermoforming or even complete separation of fibre- and matrix material by a melting procedure. Thermoplastic composites also have advantages over thermoset counterparts in terms of fast processing, chemical resistance, fire-, smoke-, and toxicity properties, and their almost indefinite shelf life. What can be of particular interest for the automotive industry is the unique fast processing capability of thermoplastics. This type of matrix material does not require a curing step in the manufacturing process. Instead, composites with thermoplastic matrix material only require consolidation to have taken place at the end of the part shaping process. A thermoplastic matrix material also offers cost-effective joining methods to be applied.

## 1.2 Problem statement

The mentioned advantages of thermoplastics in the previous section have lead to an interest of the automotive industry. Application of thermoplastic matrix material for structural part helps in achieving the recyclability requirements. The BMW Group investigates the possibility of replacing the currently existing thermoset matrix system for structural body parts with a thermoplastic matrix system; exemplary to the present thesis work is the BMW 7 Series. One crucial aspect of replacing the material type of structural components is to make sure that it has no degradation in structural performance as consequence. From a cost perspective, it is given that the conventional automotive process chain should not be subjected to adaptations. Hence, all parts that will be manufactured with a thermoplastic matrix system experience the same processing steps as their thermoset counterpart. The conventional automotive process chain can be coarsely divided in the following four categories: press shop, body shop, paint shop, and final assembly.

The paint shop, of which Section 2.1 provides a detailed description, poses the largest challenge in substituting the thermoset matrix material to a thermoplastic replacement. Although structural parts do not get painted, the automotive process chain inherently requires structural parts to undergo various steps in the painting process. In short, the complete body-in-white, or BIW, is subjected to a cathodic dip painting process, or CDP process, to obtain a durable surface of the exterior. Ovens dry the BIW after the CDP process at a maximum temperature of 190°C [4]. The material that has been investigated during the thesis research is continuous carbon-fibre reinforced polyamide-6 that was supplied by Celanese. Laminates manufactured with unidirectional tape that has the trading name Celstran CF60-PA6 have been utilised for the material characterisation- and validation experiments.

It is clear that passing the thermoplastic structural parts through the ovens subjects them to temperatures well above the glass transition temperature. Connection of thermoplastic parts to the rest of the BIW constrains the possibility to expand freely and introduces thermal stresses and causes deformation. The problem at hand is to assess this deformation behaviour by means of numerical simulation. A validated numerical simulation aids in designing thermoplastic structural parts that meet specific requirements on allowable deformation during the drying process. A viscoelastic material model is needed for this simulation that takes into account both thermal- and hygroscopic effects.

### 1.3 Conceptual design of the research

It is important for a valuable outcome of the thesis research to understand how suggested solutions or methods can be utilised in the development process of vehicles. The significance of this research lies within the recommendations that can be provided based on the research' outcomes. Recommendations to the strategy for numerical modelling of the viscoelastic deformation behaviour of thermoplastics have advantages in twofold. Firstly, they can enhance the quantitative quality of future analyses by providing information on which strategies can be proven to be effective and accurate for the problem at hand. Secondly, the produced knowledge concerning modelling strategy will save time at other departments that are tasked with carrying out simulations.

This section discusses the conceptual design of the research in which the research objective and research questions are outlined. Research questions have been posed as guidance for research activities and answering these research questions has lead to the conclusion of this thesis. The aim and scope of the research have been defined prior to conducting the literature review to allow a selection of relevant sources. It is noted that the context of the thesis is practice-oriented as the conclusions of the thesis are aimed to provide information for changing a current situation into a more desirable one.

The outcome of the research provides information on how to analyse the viscoelastic deformation of thermoplastic fibre-reinforced components subjected to the automotive painting process. The product of the conducted research is a validated numerical model that accurately simulates the mentioned deformation behaviour. It is noted that the numerical analysis of viscoelastic deformation behaviour itself is not a novelty and literary works on this topic are readily available. However, the focus of this research lies on thermoplastic materials and the numerical model takes into account hygrothermal loading representative for the automotive paint shop and polymer chemical effects that occur as a result of the hygrothermal loading. The following research objective has been formulated.

*The research objective is to provide the possibility to predict the structural performance of thermoplastic composite parts that pass through the ovens in the automotive painting process by developing a validated simulation of the viscoelastic deformation behaviour of fibre-reinforced thermoplastics subjected to transient hygrothermal loading.*

A set of research questions has been deducted from the research objective. The knowledge that was necessary to answer the research questions was identified through the method of corroborative knowledge. Knowledge that was critical to carrying out the research objective was obtained by answering the research questions. The most important and first main research question concerns prescriptive knowledge and answering this question allows making recommendations to fellow engineers on analysing viscoelastic deformation behaviour of structures within the scope set in the thesis; which is exactly the research objective. The set of research questions is listed next.

- What is the most suitable viscoelastic theory to be applied for the numerical model?
  - What are the hygrothermal loading conditions imposed by the automotive painting process?
  - Is there an interaction between the hygrothermal- and mechanical loading?
  - Given the automotive painting process, will the thermoplastic matrix material act linear-viscoelastic or non-linear-viscoelastic?
  - What is the required level of accuracy of the analysis?
  - Can a user-subroutine provide significant value to the viscoelastic analysis?

- Which methods exist to reduce the computational cost of viscoelastic analyses?
  - What is the benefit in terms of run-time to apply such a method?
  - To what extent do methods to reduce computational cost reduce the accuracy of the analysis?
- What are the possible combinations of building blocks in finite element software for viscoelastic analyses?
- What meshing strategy will be applied for the through-thickness representation of the laminate?
- How will the numerical model be experimentally validated?
  - On what scale will the experimental validation take place?
  - Which variable or variables are suitable for the experimental validation?
  - What are the requirements for the experimental setup?
- Which mechanical properties are required as input for the numerical model?
  - What are the associated standard test methods for these mechanical properties?
  - How many tests shall be conducted in order to generate a statistically robust dataset?

This thesis research was made possible by the availability of carrying out a large variety of material characterisation tests to analyse the deformation behaviour of the thermoplastic composite material. Obtaining test specimens to carry out the material characterisation tests was facilitated through the budget that was available for the overarching PhD assignment.

## 1.4 Structure of the thesis

The main research conducted to provide answers to the research questions can be divided into three main parts: the material characterisation, the development of the numerical model, and the experimental validation. A literature review is provided in Chapter 2 that has been performed to get acquainted with the technological state of the art in the automotive paint shop, the hygrothermal behaviour of thermoplastics, and the numerical modelling of viscoelastic material behaviour. The theoretical knowledge that was required to carry out the thesis activities is reported in Chapter 3.

The constitutive equations described in Chapter 3 for the numerical model led to the identification of the required material parameters for the simulation. The material characterisation carried out to obtain these material parameters is documented in Chapter 4. The development of the numerical model is discussed in Chapter 5 and follows the material characterisation in a chronological order. The developed numerical model has been validated against several different levels of complexity. The methods, results, and conclusions of the validation are presented in Chapter 6. An improvement to the numerical model is described in Chapter 7 as the original approach led to unsatisfactory results. The conclusion of the thesis research is documented in Chapter 8 and recommendations are provided in Chapter 9.



# 2

## State of the art

Numerical simulation of viscoelastic materials by application of the finite element method has been reported on from 1965 and onwards. It can be concluded that the numerical analysis of viscoelastic deformation behaviour is no novel field of research. Nevertheless, the field of application for these simulations keeps changing as technological developments in manufacturing techniques take place. The mentioned increase in mandatory recyclability level of automotive products has raised the interest of applying thermoplastic matrix material in structural components. The automotive process chain dictates that these parts travel through drying ovens and this subjects the parts to severe temperatures.

Publications on numerical simulations carried out for manufactured structural parts including thermal conditions up to these temperatures are rare. A validated simulation model that assesses the structural performance of fibre-reinforced thermoplastic automotive parts during and after the cathodic dip painting process is a leading-edge contribution to the engineering capabilities of the automotive industry. In preparation of developing the simulation model, studying literature on the influences of environmental conditions on the mechanical behaviour of fibre-reinforced polymers and findings on various viscoelastic analysis techniques provides insight to create a modelling strategy.

A literature study also allows the reader to place the present work in a reference framework. The novelty of the thesis can be assessed as well as its value in closing scientific gaps that exist. The literature study has been divided into different parts that are discussed in three subsequent sections; the automotive paint shop, hygrothermal effects on the mechanical behaviour of fibre-reinforced thermoplastics, and numerical modelling of viscoelasticity. It is recognised that a numerical model alone is not sufficient in switching the matrix material system for structural parts. Economical-, environmental-, and regulatory influences, amongst others, must be taken into account as well [5]. Nevertheless, the literature review focuses purely on mechanical viewpoints.

## 2.1 The automotive paint shop

The processing steps that are generally carried out in the automotive paint shop are discussed in this section to provide an overview of the various hygroscopic- and thermal loads subjected to the structural elements of the car. Seven major processes comprise the automotive paint shop. Initially, a pre-treatment is applied that includes degreasing, rinsing, activation, phosphation and passivation [4] to clean the BIW from processing agents. Degreasing solutions are a mixture of a builder and surfactants, which typically are alkaline salts and organic compounds, respectively [4, 6]. The builder should remove inorganic- and pigment pollutants. Oils, lubricants or soaps, contrarily organic contaminants, should be eliminated by the surfactants.

The function of rinsing is to wash away the solution with tap- or demineralised water to prevent contamination of the next processes. The activation, phosphation and passivation steps ensure a good adherence basis for the coating layers to come and provide corrosion protection. Aqueous alkaline dispersions of titanium orthophosphate increase the number of crystallisation nuclei on metal surfaces during activation and accelerates the phosphation process [4]. The main purpose of phosphating is the formation of a thin, insoluble and corrosion resistant conversion layer. Lastly, passivation completes the pre-treatment by enhancing corrosion resistance through zirconium-based solutions.

The BIW is subjected to cathodic dip painting after the pre-treatment and this constitutes the largest hygro-thermal load. This processing step provides the BIW with a uniform coating thickness and an insoluble, high adherence layer that protects against corrosion. Furthermore, the cathodic dip painting increases chip resistance and ensures a smooth surface for establishing an adhesion base for succeeding coatings. To coat the entire BIW, it is dipped into a submersion tank with epoxy based solutions and a voltage in the range of 300V to 450V is applied. The BIW becomes a cathode for the positively charged coating particles that are attracted to the BIW as a consequence. The newly formed layer is dried in the cathodic dip painting oven at temperatures up to 170°C to 190°C [4, 7].

The welding seams and flanges of the BIW are sealed with polyvinyl chloride once the BIW has passed through the cathodic dip painting oven. The sealing is required to prevent diffusion of moisture between metal sheets that may cause corrosion and is often combined with the application of damping material for noise- and vibration reasons. Examples of damping material are solid bituminous pads or spray-on applications. The temperature in the sealing dryer can reach up to 165°C if the sealing is combined with spray-on damping [7].

Integrated processes are becoming the norm for modern paint shops of which a primerless integrated paint process is the state of the art. The two base coats that are applied consecutively provide UV protection and chip protection, and produce colouring and aesthetic effects, respectively [4]. The clear coat is also sprayed on and is usually a two-component system consisting of acrylate resins and special isocyanate hardeners. This coating provides chemical resistance and protection from scratches. It also improves the appearance and increases weathering resistance. A film of wax is applied to preserve cavities in the BIW from corroding.

Parts made from continuous fibre-reinforced thermoplastics are primarily intended for structural body applications and do not have to be painted because they cannot be seen and do not corrode. As such, the polyvinyl chloride, base- and clear coat are only sprayed on designated parts and the thermoplastic parts do not interact with these layers. Consequently, the only chemical load occurs throughout the pre-treatment and CDP processes as the entire BIW is immersed. On the other hand, thermal loads affect the composite parts during all processes. Table 2.1 summarises the chemical- and thermal loads subjected to the continuous fibre-reinforced thermoplastic parts and their respective duration throughout the automotive paint shop.



Table 2.1 *Chemical- and thermal loads imposed on structural members during the automotive painting process [4, 6, 7].*

Process	Thermal load	Chemical load
Pre-treatment	50 °C - 60 °C	Alkaline- and acid solutions
Cathodic dip painting process	30 °C	Epoxy based solutions
Cathodic dip painting oven	170 °C - 190 °C	<i>n.a.</i>
Polyvinyl chloride sealing	<i>n.a.</i>	<i>n.a.</i>
Polyvinyl chloride oven	165 °C	<i>n.a.</i>
Primerless integrated painting process	150 °C	<i>n.a.</i>

It is noted that the scope of the thesis is limited to the effect of the cathodic dip painting oven and the influence of chemical effects of the alkaline-, acid-, and epoxy based solutions on the mechanical properties of the composite material is not accounted for in the simulation. However, the moisture content of the composite material is assumed to be fully saturated after the pre-treatment and the cathodic dip painting process. Hence, the hygroscopic shrinkage that occurs due to moisture egress out of the composite material during the drying process in the cathodic dip painting oven is implemented in the simulation.

## 2.2 Hygrothermal response of thermoplastics

Prior to starting the development of a simulation, it is valuable to identify all significant external factors that have an influence on the mechanical behaviour of fibre-reinforced thermoplastics. This section provides an overview of documented research towards the influence of temperature and moisture content on the mechanical properties of fibre-reinforced thermoplastics. The aim of this section is to identify all processes that must be captured in the simulation to accurately predict deformation behaviour.

The inherent structure of fibre-reinforced thermoplastics results in the mechanical behaviour being completely described by the fibre, matrix, and the interphase between the fibre and matrix. Interface failure is governed by matrix failure between two adjacent plies and does not constitute mechanical behaviour on its own. Temperature- and moisture influences are most apparent for matrix properties, but the interphase characteristics are also influenced [8]. The mechanical properties of the matrix are lowered as a result of swelling and plasticisation [9].

Considering the simulation problem at hand, it is necessary to understand how moisture is transported in- and out of the material and how this influences the mechanical properties. Polymeric materials absorb moisture through three different processes. Direct diffusion of water molecules into the matrix- or sometimes fibre material is the most common mechanism of water absorption [10]. The two other processes are moisture transport along the interphase by a capillary effect and storing moisture in voids and microcracks that are present in the polymer.

Despite multiple moisture absorption processes, a single law has been developed in 1855 that is shown to accurately capture moisture absorption for many thermoplastic polymers [11]. Equation 2.1 is known as Fick's law and describes moisture transport through the diffusivity of the moisture in the polymer, denoted with the symbol  $D$ . Moisture diffusion into a composite is stated to also depend on the viscosity of the matrix material and the fibre volume fraction [12].

$$\frac{\delta M}{\delta t} = D \left( \frac{\delta^2 M}{\delta x^2} + \frac{\delta^2 M}{\delta y^2} + \frac{\delta^2 M}{\delta z^2} \right) \quad 2.1$$

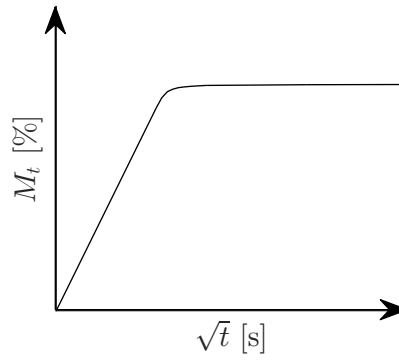


Figure 2.1 *Typical Fickian moisture diffusion showing a two-stage process of moisture uptake.*

Diffusivity of moisture into, or out of, the polymer is dependent on the activation energy,  $E_a$ , the gas constant,  $R$ , and the absolute temperature,  $T$ , and can be calculated with Eq. 2.2. The symbol  $W$  in Eq. 2.1 represents the moisture concentration and is defined as the weight of the moisture as a fraction of the weight of the dry composite material. From Eq. 2.2, the accelerating influence of the temperature on the diffusion constant is directly visible. However, generally speaking, the moisture concentration of the environment decreases with increasing temperature. It is to be expected that the moisture content of a fibre-reinforced thermoplastic specimen drops when subjected to elevated temperatures in air.

$$D = D_0 e^{-\frac{E_a}{RT}} \quad 2.2$$

Water transport into a polymeric material can be considered to be a two-stage process. Initially, the diffusion of water molecules takes place at a relatively high, constant rate. As the moisture content inside the polymer approaches saturation, the diffusion rate decreases until an equilibrium is reached with the environment. A curve that represents a typical Fickian moisture diffusion is shown in Figure 2.1.

It has often been concluded in literature that an increase in moisture content lowers the glass transition temperature of thermoplastic polymers [13, 14]. Diffusion of water molecules results in a larger separation between the macromolecules of the polymer. The polymeric material swells and chain- and side group mobility increases. A larger separation between the chains also decreases the secondary intermolecular bonding forces and this explains why the polymer is softer and displays a more ductile nature at equal temperature, translating to a lower glass transition temperature [15].

Papanicolaou states that cyclic thermal loading can cause initiation of microcracks that leads to a higher saturation moisture content [16]. Although the cited work concerns thermoset matrix material, the analogue to thermoplastic matrix material seems plausible. The simulation in this thesis does not model the initiation of damage, but knowledge about possible initiation of microcracks during thermal loading may provide an insight during the evaluation of the validation experiments.

In 2013, Batista [14] investigated how the mechanical- and thermal performance of carbon fibre-reinforced polyetherimide, or PEI, is affected by environmental influences. Dynamic mechanical analysis, interlaminar shear strength tests, and non-destructive inspections were applied before and after submitting the laminates to hygrothermal weathering. The results show reduced glass transition temperature values and storage moduli due to plasticisation. However, it must be noted that the weathering was carried out at a temperature of 80 °C, whereas the glass transition temperature of PEI lies roughly between 216 °C and 220 °C.

The effect of moisture absorption on the thermal- and mechanical properties of injection-moulded short glass-fibre-reinforced polyamide-6,6 composites was investigated by Hassan in 2012 [13]. Short-fibre laminates were prepared with fibre volume fractions of 4%, 8%, and 12%. The article documents a decrease of enthalpy as a result of adding glass-fibre reinforcements to the polyamide-6,6. The reduction of enthalpy displays a lower degree of crystallinity. In agreement with the work of Batista [14], the glass transition temperatures reduce with increased moisture content. Furthermore, including the glass-fibre reinforcement is stated not to change the glass transition temperature to a significant extent. However, it must be kept in mind that the largest fibre volume content is only 12%.

An experimental study was carried out by Eftekhari in 2016 [17] to analyse how the tensile behaviour of thermoplastic composites is affected by temperature, moisture, and hygrothermal ageing. The specimens of interest of this study have been manufactured with polyamide-6,6. The article reports that the water absorption of the short-glass-fibre-reinforced polyamide-6,6 specimens displayed Fickian behaviour. Ageing the specimens in water and drying them afterwards yielded increased stiffness and strength. Hygrothermal ageing at 85 °C damaged the interface of the specimens. The results of tensile tests carried out at elevated temperatures show an increase in ultimate strain and a decrease in strength and stiffness, as expected.

The degree of crystallinity for a semi-crystalline polymer affects many mechanical properties. Subjecting a semi-crystalline polymer to elevated temperatures above the glass transition temperature leads to the growth of crystalline areas and the degree of crystallinity increases. A higher degree of crystallinity results in increased density, elastic modulus, tensile strength, hardness, and heat conductivity [18]. Contrarily, the mechanical damping, impact toughness, ultimate strain, compressibility, and thermal expansion decrease. The temperature that corresponds to a maximum rate of growth of the crystals in polyamide 6 is reported to be 145 °C [19]. In addition to an overall higher degree of crystallinity, Dencheva [20] reports that providing oriented cable of semi-crystalline polyamide 6 with an annealing treatment promotes a phase transition of the crystal structure from  $\gamma$ -form to  $\alpha$ -form. Both the Young's modulus and the yield stress of the polyamide 6 were observed to have increased drastically.

## 2.3 Numerical modelling of viscoelasticity

The analytical solution of viscoelastic governing equations is possible only for limited geometries and under specific assumptions. Components that are to be designed for series production involve complex geometry and analytical solutions do not provide the information to analyse such structures to the required level of accuracy. The increasing availability of computational power led to an increased use in the field of engineering to address this problem. The finite element method, or FEM, was developed as a result of this. This method enables the analysis of structures considering their exact geometry and relevant material properties.

The most widely used version of FEM discretises a geometrical domain that must be analysed in a finite number of elements. In FEM, the displacement field of every element is determined through interpolation of the displacement values of the individual nodes of that element. A stress field is calculated through application of the constitutive equations and utilising the displacement information of the nodes [21]. The solution of the analysis is obtained by applying the principle of virtual work to the equilibrium equations. The system of simultaneous equations that is obtained are solved by making use of numerical computational power.

The application of FEM refers only to discretising the geometrical domain and solving the underlying equilibrium equations. It is noted that the usage of a computer is not inherently required for analysing a structure through FEM. Nevertheless, the analysis of complex structures can only be reasonably solved with a computer due to the sheer size of the system of equations that is obtained because of the high number of elements. Numerical analyses can differ in their underlying constitutive equations and how these equations are written in finite element formulation. Specific formulation of the constitutive equations can yield an increase in computational efficiency. This section provides an overview of the various strategies that have been adopted to numerically analyse viscoelasticity.

Before the introduction of composite materials, the focus of viscoelastic analysis has been on isotropic materials. The integral formulation of the governing equations to include a viscoelastic behaviour can not be solved directly in a numerical manner. This problem was solved by Hopkins and Hamming [22] and Lee and Rogers [23] by applying the method that is known as finite difference, or FD. Hopkins and Hamming developed a method to construct the creep function from a measured relaxation function. This method involves the numerical solution of the integral equation that connects the two mentioned functions. The numerical method involves the trapezoid rule for integration, which is shown in Eq. 2.3.

$$f(t_{n+1}) = f(t_n) + \frac{1}{2} [\psi(t_{n+1}) + \psi(t_n)] [t_{n+1} - t_n] \quad \text{where} \quad f(t) = \int_0^t \psi(\tau) d\tau \quad 2.3$$

The symbol  $\psi$  in Eq. 2.3 denotes the relaxation function. The creep function is introduced through the general expression that is presented in Eq. 2.4 which was originally shown in the work by Gross [24]. The symbol  $\phi$  is used in Eq. 2.4 to represent the creep function.

$$\int_0^t \phi(t - \tau) \psi(\tau) d\tau = t \quad 2.4$$

The symbol  $\tau$  in Eq. 2.4 represents the moment in time of load application. A finite difference approximation is made for the integral formulation shown in Eq. 2.4 and the final equation obtained through mathematical manipulation to calculate the creep function from the measured relaxation function is displayed in Eq. 2.5.

$$\phi(t_{n+\frac{1}{2}}) = \frac{t_{n+1} - \sum_{i=0}^{n-1} \phi(t_{i+\frac{1}{2}}) [f(t_{n+1} - t_i) - f(t_{n+1} - t_{i+1})]}{f(t_{n+1} - t_n)} \quad 2.5$$

Lee and Rogers follow the same approach as has been demonstrated by Hopkins and Hamming. Their results confirm the excellent agreement between the numerical method to reconstruct the creep function from relaxation data and the analytical solution that is obtained for Maxwell behaviour. This approach requires that the results from all previous time steps need to be stored in order to be able to progress the solution through time. This has the inconvenient consequence that rather simple problems lead to inefficient calculations and large data volumes.

Elimination of the need to store all previous time steps was proposed by Zak in 1968 [25]. The developed numerical method was intended to analyse the stress and deformation in solid propellant materials. The equations that have been applied are the integral form of linear viscoelastic equations that include the effect of thermal expansion on the strain. Because the viscoelastic behaviour was modelled through Dirichlet-Prony series, a recursion relation could be established. The advantage of the recursive notation is that it allows to progress the solution through time without the need to store all previous information of solutions that would else be necessary.

It is noted that the mentioned works do not include any FEM efforts. An early implementation of viscoelastic behaviour adopting FEM is reported by King [26] in 1965. A finite element code was developed to analyse viscoelastic problems that concern plane stress and -strain. The underlying equations were based on the integral form of the constitutive equations regarding creep compliance. The method that was applied is based on the assumption that an elastic part and a creep part comprises the creep compliance. An additional assumption was made that the strain remains constant across a time step.

Taylor and Chang [27] published an article about the development of a thermoviscoelastic finite element code one year later than King. The code was applicable to materials that are considered to be thermorheologically simple, a classification that is explained in detail in Section 3.4. In a later work that was published in 1970, Taylor et al. [28] stress the disadvantage of the step-forward finite difference integration method as it requires all past solutions to be kept in storage. Instead, an algorithm is suggested that has a recursive nature and describes the material behaviour through the use of Maxwell elements.

The advantage over previously developed finite element code that make use of the step-forward finite difference method is how the computational effort is affected by the analysis' accuracy. In finite difference methods, the computational effort is proportional to the number of previous time steps. It follows that a longer analysis inherently grows in computational effort in comparison to the results. For the approach that includes the recursive formulation, the computational effort is determined by the amount of Maxwell elements that are used to describe the viscoelastic behaviour of the material. Hence, the computational effort does not grow relative to the results if the simulation spans a longer time frame.

Zienkiewicz and Watson [29] included both thermal- and ageing effects in their finite element code that was written for a two-dimensional isotropic material. Analogous to King [26], the creep compliance was separated into an elastic- and creep part, meaning that the first part is time-independent and the latter is time-dependent. Modelling of the time-dependent part is achieved by expression in the form of a Kelvin model. A solution was obtained through an incremental manner during which the stresses are assumed to remain constant, this is contrary to King's model in which the strains are assumed to be invariable.

More documentation on the development of finite element formulations for the deformation behaviour of isotropic viscoelastic materials are provided by Lynch [30], White [31], and Rashid and Rockenhauser [32]. Lynch developed a finite element code that utilises a finite difference method to put the single integral form of the constitutive equation into a numerical form. A finite element procedure is applied to the constitutive equations to obtain a set of algebraic equations for the global set of elements that can be solved through Gauss-Seidel iteration. White had included the recursive relations of Zak [25] in his model and Rashid and Rockenhauser made use of the method that was first applied by Lee and Rogers [23].

An interesting observation is made when investigating the starting point of all the methods that have been applied to develop the previously mentioned finite element codes. Every method has the integral form of the constitutive equation as basis for the finite element notation. In 1968, Zienkiewicz et al. [33] published an article on a numerical method to evaluate viscoelastic stresses of which the constitutive equations are represented in derivative formulation. The viscoelastic behaviour of the material is represented by multiple Kelvin models connected in series.

It is noted that because of the Kelvin model representation, the rate of total creep can be stored separately for each model and no problem is encountered for storing data that is encountered for an integral formulation. The finite difference approximation that was applied for the incrementation of time was based on an initial strain approach. Greenbaum and Rubinstein [34] developed a similar finite element code in 1968 that implements the initial strain method to progress through time. In this initial strain method, the creep strains for an increment in time are regarded as initial strain to update the stress field for the next time step. The end of the simulation was either governed by a final time, or when a steady-state condition was reached.

A different approach than either the integral- or derivative form in the time domain was taken by Webber [35] in 1969; the correspondence principle was applied. The correspondence principle entails applying the Laplace transform to the convolution integrals of the constitutive equations which converts the integrals to algebraic equations. The viscoelastic equations in the time domain are transformed to elastic-like equations in the transform variable domain. Hence, the name elastic-viscoelastic correspondence principle is given to this method.

Referring back to the works discussed, Taylor [27] and Zienkiewicz [33] made use of Maxwell or Kelvin models respectively to represent the viscoelastic material behaviour of the considered materials. This representation is only accurate when the viscoelastic behaviour of the material is linear. The construction of more complex rheological models is namely based on the linear superposition of simple models. Reference is made here to the construction of the generalised Maxwell or -Kelvin model, amongst others. Finite element codes that simulate non-linear viscoelastic behaviour have been developed by Bazant [36], Carpenter [37], and Schapery [38].

It is noted that the mentioned written works to this point only concern isotropic materials. The development of finite element codes taking into account the anisotropy of a material has been documented by various authors as well. The selection of literature on the numerical modelling of anisotropic viscoelastic materials has been limited to orthotropic materials with the research objective of the thesis in mind. An early development of a finite element code to simulate the deformation behaviour of orthotropic viscoelastic materials is reported by Lin and Hwang [39]. It must be noted that a plane stress assumption was applied as classical laminate theory had been used to obtain the relaxation moduli of the laminate.

A similar approach was taken by Hilton and Yi [40] in 1993. The constitutive relations that were implemented in the model were equal to the equations that had been used by Lin and Hwang [39] and the finite element formulation that had to be solved was similar too. However, the strategy in solving the finite element formulation is what distinguishes the two works. A Laplace transform was used by Hilton and Yi, whereas a reduced time approach was applied by Lin and Hwang. Further research conducted by Yi [41] was focused on expanding the developed finite element code to support the prediction of the onset of delamination and to analyse a free edge response.

A finite element code that supported a three-dimensional representation of orthotropic viscoelastic material behaviour was written by Kennedy and Wang [42]. This finite element code was developed for constitutive equations that were written in integral form utilising the non-linear representation of viscoelasticity that was documented by Lou and Schapery [43]. The work of Kennedy and Wang was based on constitutive equations that were written by creep compliances. Another three-dimensional finite element code was developed by Zocher [44] that was analogous to the work of Kennedy and Wang. However, the work of Zocher is constructed around relaxation moduli as opposed to creep compliances.

Additionally, Zocher implemented a recursive formulation of the constitutive equations by which the need to store the complete strain history of the simulation could be avoided. The recursive formulation of Zocher has been used frequently in the simulation of viscoelastic deformation behaviour and is still found in recent literature. Ding et al. [45] have developed a more general formulation of the constitutive equations to model the residual stresses during the curing of thermo-rheologically complex materials. The variation in thermal expansion, chemical shrinkage, and stress relaxation are accounted for in the model.

The recursive formulation of the constitutive equations has also been used by Abouhamzeh et al. [46] in an analysis approach of the deformation behaviour of viscoelastic composites with a thermal dependency. A set of self-consistent equations have been used at micromechanical level to obtain the orthotropic viscoelastic material behaviour of linear nature. Abouhamzeh et al. [47] calculated the residual stresses in strips made of glass reinforced aluminium, or GLARE, by means of a UserMat that was written to implement the recursive formulation in ANSYS. The validation of the model was carried out by comparison of the predicted values and digital image correlation, or DIC, measurements of the curvature of narrow non-symmetric strips of GLARE. The authors report an improved accuracy of the viscoelastic model with temperature dependency over both an elastic model with- and an elastic model without temperature dependence.





# 3

## Viscoelastic theories

The development of a simulation to analyse the deformation behaviour of a viscoelastic material requires knowledge about the relation between forces and displacements. This relation is often expressed in terms of how a specific stress leads to a specific strain, or vice versa. The reason for defining stress and strain as opposed to force and displacement is because this allows straightforward comparison between geometries with different cross-sectional area and lengths. The purpose of this chapter is to present the theoretical knowledge that is required to develop the numerical model that aids in achieving the research objective outlined in Section 1.3.

An introduction to viscoelasticity is provided in Section 3.1 and the phenomena creep and relaxation are explained. The deformation behaviour of viscoelastic materials can be described by means of either integral- or differential formulations of the constitutive equations. These two types of formulations are discussed in Section 3.2 and Section 3.3, respectively. The influence of moisture content and temperature is treated subsequently in Section 3.4 because of the hygrothermal loading that is present due to the processing steps mentioned in Section 2.1. The additional physical relations that must be taken into account due to the composite nature of the material are presented in Section 3.5. The constitutive equations that have been utilised for the numerical model are derived in Section 3.6, the concluding section of this chapter.

### 3.1 Introduction to viscoelasticity

The mechanical response of both elastic solids and viscous fluids are relatively well understood and can often be simulated for engineering purposes to high accuracy. However, most polymers show characteristics of both materials. They can neither be classified as an elastic solid or as a viscous fluid. Instantaneous tensile load application to a polymer results in an instantaneous elastic response in the expected form of strain. If the magnitude of the load is kept constant for the remainder of time, the strain gradually increases. This phenomenon is called creep and is characteristic for materials that show a viscoelastic behaviour.

An other phenomenon that is displayed by viscoelastic materials is relaxation. This is essentially the inverse of creep and is directly related to it. Relaxation is visible when a constant elongation is applied to a viscoelastic specimen. The force that is required to achieve the displacement is initially equal to what can be expected from the instantaneous elastic response obtained from the creep behaviour. As time passes, the required force decreases and the specimen is said to relax. The two phenomena creep and relaxation are shown graphically in Figure 3.1, left and right, respectively.

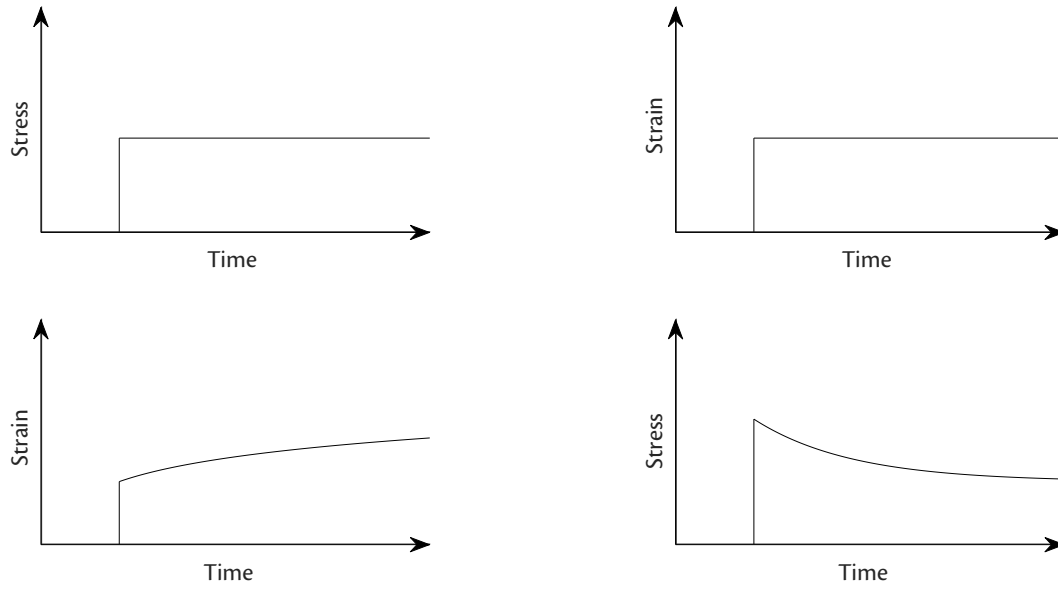


Figure 3.1 *The phenomena creep and relaxation, respectively left and right, represented arbitrarily.*

One distinction must be made prior to modelling the deformation behaviour of viscoelastic structures. Viscoelasticity can be categorised as either linear or non-linear. A material that is said to be linearly viscoelastic conforms to Boltzmann's superposition principle. Boltzmann's superposition principle states that the deformation response of a linear viscoelastic material to a combined load is a linear superposition of the deformation responses to the individual loads [48]. In other words, the deformation response as a result of applying an incremental load to a specimen is independent of the load history [49].

Prior to determining an approach to model the deformation behaviour of viscoelastic materials, it is essential to know whether a material is linearly- or non-linearly viscoelastic. Such knowledge can be obtained by experimentally testing whether or not the Boltzmann principle holds for the given material. As part of preliminary research to defining a modelling approach for the given problem, this experiment was carried out. Section 4.7 provides a description of the experiment that has been carried out to determine the linearity of the viscoelastic material.

It is noted that the linearity of viscoelastic deformation behaviour can also be analysed by means of isochrones obtained from relaxation or creep experiments. Isochrones of relaxation experiments are constructed by evaluating the stress value for multiple relaxation experiments that have been carried out at different strain levels at one particular time. Isochrones can also be constructed for creep experiments, for which a plot is made of the strain values at one particular time for experiments that have been carried out with different stress magnitudes. Linear viscoelastic behaviour results in linear isochrones. An example of isochrones is displayed in Figure 3.2; the data has been taken from creep experiments of glass-fibre reinforced polyamide-6 that has the name Akulon Ultraflow K-FHG0 [50].

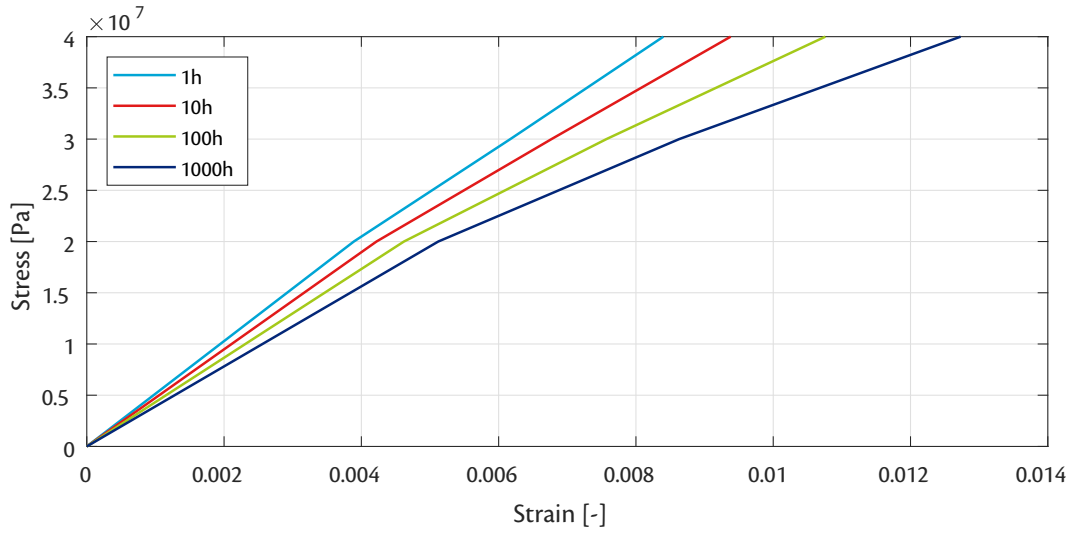


Figure 3.2 *Isochrones of glass-fibre reinforced polyamide-6 as reference for non-linear viscoelastic behaviour. Data was obtained from CAMPUSplastics [50].*

The main point of attention demonstrated through the previous two phenomena is the time dependency that is introduced for the mechanical behaviour of viscoelastic materials. As opposed to elastic engineering materials prior to the onset of damage, the loading history of the structure becomes significant in the determination of the deformation behaviour. The importance of the loading history has consequences for the numerical analysis of such structures. The next section provides examples of analytical methods to model viscoelastic material behaviour.

### 3.2 Integral formulations

In the examples that describe creep- and relaxation behaviour, either the applied displacement or subjected force serves as external stimulus, whilst the other is measured as mechanical response. The relationships that connect stress and strain are called constitutive equations and can sometimes be derived analytically. For linear viscoelastic materials, the constitutive equations can be written in integral formulation or by linear ordinary differential equations [49]. This section presents the derivation of the integral form and presents possible alternative forms that may be convenient depending on the problem at hand.

It is important to note that the equations presented in this section are only valid under isothermal conditions. The influence of thermal- and hygroscopic effects is discussed in Section 3.4. Furthermore, the presented equations do not consider ageing of the material. Contrary to thermal- and hygroscopic effects, ageing is not treated in this thesis as the duration of the simulation is assumed to be small enough to neglect ageing effects.

It is by definition possible to calculate a stiffness value at each moment in time for the relaxation phenomenon displayed in Figure 3.1. The resulting stiffness value inherently decreases as time progresses and is accordingly called the relaxation modulus, denoted with  $E(t)$ . The relaxation modulus describes the stress response for a one-dimensional bar, that is subjected to a step strain input at time  $t_1$ , as shown in Eq. 3.1.

$$\sigma(t) = E(t - t_1)\varepsilon \quad \text{for } t \geq t_1 \quad 3.1$$

This relationship can be extended to analyse the stress response to a combination of arbitrary loads. A continuous strain input function may be discretised as a series of step functions. An incremental step in strain input, which is defined as  $\Delta\varepsilon_k$ , results in the incremental stress response through the relaxation modulus as presented in Eq. 3.2.

$$\Delta\sigma_k(t) = E(t - t_k)\Delta\varepsilon_k \quad \text{for } t \geq t_k \quad 3.2$$

The calculation of the general stress response due to the combined arbitrary strain input is equal to the summation of the individual strain responses to the individual step strain inputs. This is only valid for linear viscoelastic materials and is known as Boltzmann's superposition principle that was mentioned earlier in the previous section. The mathematical expression of Boltzmann's superposition principle is displayed in Eq. 3.3.

$$\sigma(t) \approx \sum_{k=1}^N \Delta\sigma_k(t) = \sum_{k=1}^N E(t - t_k)\Delta\varepsilon_k \quad \text{for } t \geq t_k \quad 3.3$$

It is noted that the stress response that is calculated from Eq. 3.3 is still an approximation because of the finite summation that introduces discretisation errors. The strength of analytical solutions is often to provide an exact description of the problem. Hence, the summation will now be converted to an integral. The right hand side of Eq. 3.3 is multiplied and divided by the time interval that was used to discretise the strain input. This mathematical restructuring is shown in Eq. 3.4 for clarity.

$$\sigma(t) \approx \sum_{k=1}^N E(t - t_k) \frac{\Delta\varepsilon_k}{\Delta t_k} \Delta t_k \quad \text{for } t \geq t_k \quad 3.4$$

If the limit of the sum,  $N$ , shown in Eq. 3.4 is increased to infinity and the time interval,  $t_k$ , is decreased to zero, Eq. 3.4 is written as Eq. 3.5 as the sum becomes an integral. The time interval, which is denoted with  $t_k$ , has been replaced with the symbol  $\tau$  as the time is in the continuous spectrum due to the change of the discrete sum into a continuous integral.

$$\sigma(t) = \int_{0^+}^t E(t - \tau) \frac{d}{d\tau} \varepsilon(\tau) d\tau \quad 3.5$$

The lower limit of the integral in Eq. 3.5 is set to  $0^+$  as the derivative of the strain with respect to  $\tau$  is undefined at the initial time. To allow a step discontinuity from the initial time to the time  $0^+$ , Eq. 3.5 is expanded to Eq. 3.6.

$$\sigma(t) = E(t)\varepsilon(0^+) + \int_{0^+}^t E(t - \tau) \frac{d}{d\tau} \varepsilon(\tau) d\tau \quad 3.6$$

The left hand side of Eq. 3.6 can be taken into the integral as the relationship that is shown in Eq. 3.7 holds.

$$\int_0^{0+} E(t - \tau) \frac{d}{d\tau} \varepsilon(\tau) d\tau = E(t) \int_0^{0+} \frac{d}{d\tau} \varepsilon(\tau) d\tau \equiv E(t) \varepsilon(0^+) \quad 3.7$$

Thus, the lower limit of the integral in Eq. 3.6 may be extended to 0. The resulting expression is shown in Eq. 3.8 and forms the constitutive equation for an isotropic material in integral form.

$$\sigma(t) = \int_0^t E(t - \tau) \frac{d}{d\tau} \varepsilon(\tau) d\tau \quad 3.8$$

The result that is depicted in Eq. 3.8 is known as the Boltzmann integral. The complete procedure that is started at Eq. 3.1 can also be carried out for a strain response to a stress input. Doing so yields a similar expression with a term that is called the creep compliance. The creep compliance can be seen as the inverse of the relaxation modulus and the two are interrelated through the expressions shown in Eq. 3.9 [49].

$$\begin{aligned} \int_0^t E(t - \tau) \frac{d}{d\tau} C(\tau) d\tau &= H(t) \\ \int_0^t C(t - \tau) \frac{d}{d\tau} E(\tau) d\tau &= H(t) \end{aligned} \quad 3.9$$

The symbols  $C$  and  $H$  in Eq. 3.9 denote the creep compliance and Heaviside function, respectively. It is worth noting that the integrals displayed in Eq. 3.9 are convolution integrals. These integrals are mathematically equivalent and the function of the relaxation modulus can be obtained once the function of the creep compliance is known. Experimental data of creep tests can hence be used to provide information about the relaxation behaviour.

### 3.3 Differential formulations

The combination of both elastic- and viscous properties is what defines a viscoelastic material. Pure elastic- and viscous materials can be mechanically represented by springs and dashpots, respectively. It follows that linear viscoelastic material can be described by a linear combination of springs and dashpots. The governing equations for the linear combination are derived through the governing equations for a single spring and -dashpot. This section presents the governing equations for springs and dashpots, and describes the linear combination of these elements to describe viscoelastic behaviour; a characterisation method known as rheology.

The two fundamental rheological elements required for the construction of viscoelastic models are the linear elastic spring and linear viscous dashpot. The constitutive equation for the linear elastic spring includes force and displacement. On the other hand, force and displacement rate govern the constitutive equation for the linear viscous dashpot. In terms of structural engineering, it is more logical to replace force with stress and to substitute displacement with strain. The linear elastic spring and linear viscous dashpot are shown schematically in Figure 3.3. Their constitutive equations in stress-strain form are displayed in Eq. 3.10.



Figure 3.3 Schematic representation of the linear elastic spring and the linear viscous dashpot left and right, respectively.

$$\begin{aligned} \sigma &= E \cdot \varepsilon && \text{Linear elastic spring} \\ \sigma(t) &= \eta \cdot \frac{d}{dt}\varepsilon(t) && \text{Linear viscous dashpot} \end{aligned} \quad 3.10$$

The constant denoted with  $\eta$  in Eq. 3.10 is the viscosity of the dashpot. From here on, the linear elastic spring and linear viscous dashpot are referred to as simply spring and dashpot. Since the research objective of this thesis is strain-governed, the mechanical behaviour of the rheological elements and -models are presented as stress responses to strain loading. The stress response of a spring element under strain loading is shown in Eq. 3.11. Note that the strain history is irrelevant and the stress response is instantaneous.

$$\begin{aligned} \sigma(t) &= E\varepsilon(t) \\ E(t) &= E \end{aligned} \quad 3.11$$

It is noted that the relaxation modulus is equal to the constant stiffness of the spring and independent of time, as expected. The response to strain loading of a dashpot is not as straightforward and is shown for an arbitrary strain history in Eq. 3.12. The function  $f(t)$  is used to allow for all possibilities of strain history.

$$\sigma(t) = \eta \frac{d}{dt}\varepsilon(t) \equiv \eta \frac{d}{dt} [f(t)H(t - t_1)] \quad 3.12$$

Carrying out the differentiation and applying the properties of the step- and delta function results in the stress response displayed in Eq. 3.13. Inspection of the stress response makes it clear that an instantaneous strain loading has an infinite stress as result because of the presence of the delta function. Afterwards, the stress drops to the size of the derivative of the strain function. The relaxation modulus of a dashpot is an impulse function, which is shown in Eq. 3.13.

$$\begin{aligned} \sigma(t) &= \eta \left[ H(t - t_1) \frac{d}{dt}f(t) + f(t_1)\delta(t - t_1) \right] \\ E(t) &= \eta\delta(t) \end{aligned} \quad 3.13$$

Viscoelastic material behaviour may be described by combining the mechanical responses of springs and dashpots. The term rheology is generally used for the flow of matter. Viscoelastic materials show such a flow of matter even though they are not liquid. As a result, rheological operators can be utilised to describe viscoelastic material behaviour. A rheological operator expresses the mathematical operation on a strain history that is carried out to obtain the stress response. This is particularly appropriate for the constitutive equations of the spring and dashpot. Referring back to these constitutive equations, as shown in Eq. 3.10, the two fundamental rheological operators used to describe viscoelasticity are shown in brackets in Eq. 3.14.

$$\begin{aligned}\sigma(t) &= [E] \varepsilon(t) \\ \sigma(t) &= \left[ \eta \frac{d}{dt} \right] \varepsilon(t)\end{aligned}\tag{3.14}$$

The argument to identify rheological operators is that rheological operators can be regarded as algebraic characters to which the rules of addition and multiplication, as well as the properties that are involved with differentiation, for real numbers apply. In words, rheological operators are linear, commutative, associative, and distributive [49]. The previous states that the four algebraic manipulations on rheological operators may be carried out in any order.

Before discussing the rheological expressions for simple combinations of springs and dashpots, a small overview is presented on the general formulation that applies to rheological operators. From the differential operator that is present in the rheological expression of a single dashpot, shown in the bottom expression of Eq. 3.14, it may be expected that higher-order derivatives can be the result of multiplication of two dashpots. Because every possible combination of springs and dashpots must be able to be constructed by algebraic operations, the general expression for any rheological model is always in the form as shown in Eq. 3.15.

$$p_0 \sigma + p_1 \frac{d^1}{dt^1} \sigma + \dots + p_m \frac{d^m}{dt^m} \sigma = q_0 \varepsilon + q_1 \frac{d^1}{dt^1} \varepsilon + \dots + q_n \frac{d^n}{dt^n} \varepsilon\tag{3.15}$$

The differential operators on the left hand side of Eq. 3.15 originate from the fact that the constitutive equations can also be written in strain-stress form. Moreover,  $q_0$  can not be equal to zero for solid material behaviour as the constitutive equation would then only contain derivatives of strain. The consequence of this would be that the stress state is depending only on the strain rate, which violates solid material behaviour.

The expression shown in Eq. 3.15 may be shortened to the relation displayed in Eq. 3.16. The stress- and strain operators that are present in the right hand side of Eq. 3.16, denoted with  $P$  and  $Q$ , respectively, make use of a linear differential operator notation. It is possible to obtain the desired stress-strain relation by using the operator that is obtained through the division of  $Q$  by  $P$ .

$$\sum_{k=0}^m \left[ p_k \frac{d^k}{dt^k} \right] \sigma(t) = \sum_{j=0}^n \left[ q_j \frac{d^j}{dt^j} \right] \varepsilon(t) \quad \text{or} \quad [P] \sigma = [Q] \varepsilon\tag{3.16}$$

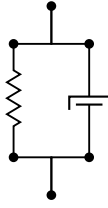


Figure 3.4 *Schematic representation of the Kelvin-Voigt model.*

What remains is to construct rheological expressions that correspond to combinations of springs and dashpots. This construction is carried out in three consecutive steps. The first step is to note the groups of rheological elements that are connected in parallel or in series with each other. The constitutive equations should be written accordingly for the individual components of every group. It is convenient to write the constitutive equations in stress-strain form for elements that are connected in parallel. Contrary, the constitutive equations for elements that are connected in series are written in strain-stress form.

The previous is argued by the stress- and strain resultants of the groups; for elements that are connected in parallel, the total stress is equal to the sum of the stress in the separate elements. Furthermore, all elements are subjected to the same strain which allows the addition of rheological operators. Hence, it makes sense to write the constitutive equations for elements that are connected in parallel in stress-strain form. An analogous reasoning applies to elements that are connected in series, albeit the other way around. Obeying to the outlined strategy, the constitutive equations for the groups are shown in Eq. 3.17.

$$\begin{aligned} \sigma &= \sum \frac{Q_i}{P_i} \varepsilon && \text{Elements in parallel} \\ \varepsilon &= \sum \frac{P_i}{Q_i} && \text{Elements in series} \end{aligned} \tag{3.17}$$

The second step in the construction of the rheological model is to convert all constitutive equations to either stress-strain form or strain-stress form. The decision on which form to choose is dependent on the overall assembly. If the groups of rheological elements are connected in parallel, all constitutive equations should be converted to stress-strain form. Naturally, the opposite applies to a rheological model in which the groups are connected in series. The final step is to sum the stress- or strain response after which the constitutive equation for the rheological model has been found.

The most simple rheological model that can be constructed without being trivial contains one spring and one dashpot. The spring and dashpot can either be placed in series or in parallel. These two models are called the Maxwell- and Kelvin-Voigt model, respectively. To illustrate the previously outlined method for obtaining the constitutive equations of a rheological model, the Kelvin-Voigt model is analysed next. A graphical representation of the Kelvin-Voigt model is depicted in Figure 3.4

By inspection of Figure 3.4, the constitutive equations for the spring and dashpot shall be written in stress-strain form as the rheological elements are connected in series. These constitutive equations have already been mentioned, but are shown in Eq. 3.18 for ease of reading. Since there is only one group of rheological elements present for this model, there is no need to rewrite constitutive equations from one form to the other. Furthermore, it is noted that the strain in each rheological element is equal because of the parallel construction.



$$\begin{aligned}\sigma_s &= E \cdot \varepsilon_s & \text{with} & \varepsilon_s = \varepsilon \\ \sigma_d &= \eta \partial_t \cdot \varepsilon_d & \text{with} & \varepsilon_d = \varepsilon\end{aligned}\tag{3.18}$$

Addition of the two expressions shown in Eq. 3.18 leads to the constitutive equation of the Kelvin-Voigt model, as presented in Eq. 3.19. Comparing the constitutive equation of the Kelvin-Voigt model with the general form for rheological models that is shown in Eq. 3.15, it is already possible to comment on the mechanical behaviour. As  $q_0$  is not equal to zero, the Kelvin-Voigt model behaves as a solid. Additionally, because  $m$  is smaller than  $n$ , the Kelvin-Voigt model also does not display an instantaneous response [49].

$$\sigma = (E + \eta \partial_t) \varepsilon \tag{3.19}$$

In the following, the stress response to strain loading of the Kelvin-Voigt model will be analysed, keeping in mind the research objective of the thesis. The controlled variable in this analysis is strain, for which an arbitrary input is chosen analogous to the input shown on the right hand side of Eq. 3.12. For completeness, the strain input is displayed in Eq. 3.20.

$$\varepsilon(t) = f(t)H(t - t_1) \tag{3.20}$$

Substitution of Eq. 3.20 into Eq. 3.19 produces the stress response of the Kelvin-Voigt model for an arbitrary strain load, as shown in Eq. 3.21.

$$\sigma = E \cdot f(t)H(t - t_1) + \eta \left[ H(t - t_1) \frac{d}{dt} f(t) + f(t_1) \delta(t - t_1) \right] \tag{3.21}$$

The relation that is shown in Eq. 3.21 can be utilised to obtain the relaxation modulus of the Kelvin-Voigt model. A constant strain input with unit magnitude is applied for the function  $f(t)$  in Eq. 3.21 to this extent. The resulting expression is presented in Eq. 3.22.

$$E(t - t_1) = E \cdot H(t - t_1) + \eta \delta(t - t_1) \tag{3.22}$$

In case the moment of applying the unit magnitude strain input is chosen to coincide with the origin of time measurement, meaning  $t_1 = 0$ , Eq. 3.22 can be simplified to Eq. 3.23.

$$E(t) = E \cdot H(t) + \eta \delta(t) \tag{3.23}$$

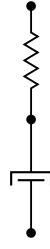


Figure 3.5 *Schematic representation of the Maxwell model.*

A stress recovery experiment is carried out by measuring the stress response to the application of a single repetition of a square wave strain input. In other words, a constant strain input of arbitrary magnitude is applied at a specific time,  $t_1$ . Then, the constant strain input is removed again at a specific point later in time,  $t_2$ . The mathematical expression for the strain input is given in Eq. 3.24.

$$\varepsilon(t) = \varepsilon_0 \cdot H(t - t_1) - \varepsilon_0 \cdot H(t - t_2) \quad 3.24$$

The other most simple, non-trivial, rheological model that can be constructed with two elements is the Maxwell model. Contrary to the Kelvin-Voigt model, the spring and dashpot are placed in series. The Maxwell model is shown schematically in Figure 3.5. Analogous to the analysis of the Kelvin-Voigt model, the constitutive rheological expression is derived first. Afterwards, the relaxation modulus is determined and the response to a stress recovery experiment is inspected.

The first step in deriving the constitutive rheological expression is to write down the constitutive equations for each element. It is noted that the individual elements are connected in series and therefore a strain-stress form is used. The individual constitutive equations are shown in Eq. 3.25.

$$\varepsilon_s = \frac{1}{E} \cdot \sigma_s \quad \text{with} \quad \sigma_s = \sigma \quad 3.25$$

$$\varepsilon_d = \frac{1}{\eta \partial_t} \cdot \sigma_d \quad \text{with} \quad \sigma_d = \sigma \quad 3.26$$

The expressions in Eq. 3.25 are summed to obtain the strain response of the Maxwell model. The resulting expression is provided in Eq. 3.27. For completeness, it is noted that the overall construction of the rheological model is in series and hence no conversion is necessary of the constitutive equations.

$$\varepsilon = \frac{1}{E} \cdot \sigma + \frac{1}{\eta \partial_t} \cdot \sigma = \frac{(E + \eta \partial_t)}{E \cdot \eta \partial_t} \sigma \quad 3.27$$

Rewriting Eq. 3.27 into the standardised formulation, as shown in Eq. 3.15, allows commenting on the material behaviour characteristics of the Maxwell model prior to evaluating a strain response. The standardised form for the Maxwell model is presented in Eq. 3.28; since  $m$  is equal to  $n$ , the Maxwell model displays an instantaneous response. The fact that  $q_0$  is equal to zero means that the Maxwell model describes a fluid.

$$(E + \eta \partial_t) \sigma = (E + \eta \partial_t) \varepsilon \quad 3.28$$

Contrary to the constitutive equation for the Kelvin-Voigt model, the stress response to a strain input of the Maxwell model is not calculated as easily due to the constitutive equation being an ordinary linear differential equation. To obtain a solution, the constitutive equation is rewritten to the form shown in Eq. 3.29.

$$\left(\frac{E}{\eta} + \partial_t\right) \sigma = (E \partial_t) \varepsilon \quad 3.29$$

A time parameter is introduced and the strain input is written for an arbitrary function,  $f(t)$ , resulting in the expression that is presented in Eq. 3.30.

$$\partial_t \sigma + \frac{1}{\tau} \sigma = E \partial_t f(t) \quad \text{with} \quad \tau \equiv \frac{\eta}{E} \quad 3.30$$

The expression in Eq. 3.30 is a first order linear ordinary differential equation (ODE) and adheres to the standard form as shown in Eq. 3.31. Finding a solution to this problem requires rewriting the problem in terms of differentials and introducing a continuous function to multiply with, denoted with  $u(t)$ .

$$\partial_t y(t) + p(t) \cdot y(t) = q(t) \quad 3.31$$

Multiplication of the ODE with the newly introduced function results in the expression shown in Eq. 3.32. It is noted that the left hand side of Eq. 3.32 is the exact differential for the resulting expression obtained for the multiplication of  $u(t)$  with  $y(t)$ .

$$u(t) \cdot dy(t) + u(t) \cdot p(t) \cdot y(t) \cdot dt = u(t) \cdot q(t) \cdot dt \quad 3.32$$

A multiplication function  $u(t)$  must be found that complies with the expression shown in Eq. 3.33.

$$d[u(t) \cdot y(t)] = u(t) \cdot q(t) \cdot dt \quad 3.33$$

In order for the multiplication function to comply with this requirement, the left hand side of Eq. 3.33 must be equal to the left hand side of Eq. 3.32. For ease of reading, this requirement is shown in Eq. 3.34.

$$d[u(t) \cdot y(t)] = u(t) \cdot dy(t) + u(t) \cdot p(t) \cdot y(t) \cdot dt \quad 3.34$$

The left hand side of Eq. 3.34 can be expanded and similar terms can be cancelled with the right hand side. Then, all terms that refer to the multiplication function  $u(t)$  are put on the left side. The resulting expression from these operations is shown in the left side of Eq. 3.35. The value for the multiplication function  $u(t)$  can be found by utilising the integral properties of the natural logarithm and the derived expression is shown on the right side of Eq. 3.35.

$$\frac{du(t)}{u(t)} = p(t) \cdot dt \quad \Rightarrow \quad u(t) = e^{\int p(t) \cdot dt} \quad 3.35$$

Referring back to the constitutive equation for the Maxwell model, the multiplication factor to find a solution of stress response for the Maxwell model is determined to be as shown in Eq. 3.36.

$$u(t) = e^{\frac{t}{\tau}} \quad \text{as} \quad p(t) = \frac{1}{\tau} \quad 3.36$$

The solution for the ODE that is shown in Eq. 3.30 is obtained by integrating the expression that is presented in Eq. 3.33. The result of the integration and the necessary dummy variable to clarify the result of the integration are shown in Eq. 3.37. The integration is carried out over a definite range as it is assumed that the strain history is zero for times smaller than a specific value.

$$u(t) \cdot y(t) - u(t_1) \cdot y(t_1) = \int_{t_1}^t u(s) \cdot (s) \, ds \quad 3.37$$

Application of the expression in Eq. 3.37 to the constitutive equation shown in Eq. 3.30, yields the relation that is presented in Eq. 3.38.

$$e^{\frac{t}{\tau}} \cdot \sigma(t) - e^{\frac{t_1}{\tau}} \cdot \sigma(t_1) = E \int_{t_1}^t e^{\frac{s}{\tau}} \cdot \dot{\epsilon} \, ds \quad 3.38$$

For evaluating the stress response under strain loading, it is assumed that there is zero stress in the material at the start of the experiment, denoted by  $t_1$ . Hence, the expression in Eq. 3.38 can be rewritten to be equal to Eq. 3.39.

$$\sigma(t) = E \int_{t_1}^t e^{-\frac{t-s}{\tau}} \cdot \dot{\epsilon} \, ds \quad 3.39$$

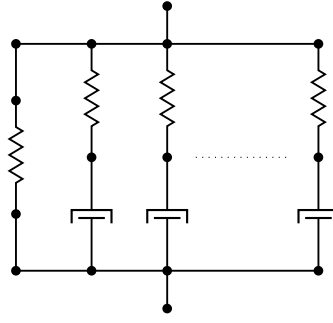


Figure 3.6 *Schematic representation of the generalised Maxwell model.*

Although the simplicity of both the Maxwell- and Kelvin-Voigt model is suitable to demonstrate the usefulness of rheological modelling, their applicability in engineering sense is limited to represent viscoelastic material behaviour. It is readily known that usage of the Maxwell- or Kelvin-Voigt model to represent the deformation behaviour of viscoelastic composites yields poor results. The proposed solution to accurately capture the correct behaviour of real materials is to build more complex rheological models by combining the Maxwell- and Kelvin-Voigt models.

The two most commonly applied examples of this principle are known as the generalised Maxwell model and the generalised Kelvin chain. The generalised Maxwell model is constructed of an arbitrary number of Maxwell models that are connected in parallel. An isolated spring is added in parallel to change the material behaviour from viscous to solid. The generalised Maxwell model is shown schematically in Figure 3.6 and the mathematical expressions for the stress contributions of every rheological submodel in the generalised Maxwell model are shown in Eq. 3.40.

$$\begin{aligned} \sigma_i &= \frac{E_i \cdot \eta_i \partial_t}{(E_i + \eta_i \partial_t)} \varepsilon_i && \text{For the Maxwell models} \\ \sigma_0 &= E_\infty \cdot \varepsilon_0 && \text{For the isolated spring} \end{aligned} \quad 3.40$$

It is noted that the terms  $\varepsilon_i$  and  $\varepsilon_0$  represent the individual strains for each rheological submodel. However, these individual strains must be equal due to the fact that the submodels are connected in parallel. Hence, the terms  $\varepsilon_i$  and  $\varepsilon_0$  can be replaced by the global strain term  $\varepsilon$  and the individual stress contributions can be summed to calculate the stress response of the entire generalised Maxwell model as displayed in Eq. 3.41.

$$\sigma = \left[ E_\infty + \sum_{i=1}^N \frac{E_i \cdot \eta_i \partial_t}{(E_i + \eta_i \partial_t)} \right] \varepsilon \quad 3.41$$

The relaxation behaviour of the every single Maxwell model in the generalised Maxwell model may be rewritten using the method that was described to rewrite Eq. 3.28 to Eq. 3.39. The isolated spring does not display any relaxation behaviour and because the single Maxwell models are connected in parallel their relaxation behaviour may be added in a linear manner. The resulting expression of the relaxation behaviour is shown in Eq. 3.42 and constitutes the key relation to which the the constitutive equations described in Section 3.6 are founded on.

$$E(t) = E_{\infty} + \sum_{i=1}^N E_i \cdot e^{-\frac{t}{\tau_i}} \quad 3.42$$

The expression on the right hand side of Eq. 3.42 is often referred to as a Prony series. Inspection of Eq. 3.42 leads to the conclusion that the generalised Maxwell model always shows an instantaneous response, regardless of the isolated spring. The generalised Maxwell model will always be used in combination with the isolated spring in the scope of this thesis due to the solid material behaviour of the composite material in the research objective.

### 3.4 Thermal- and hygroscopic effects

Elevated temperatures accelerate the relaxation behaviour of a thermoplastic matrix constituent and this has an influence on the deformation behaviour of the composite material as a whole. In addition to thermal effects, hygroscopic effects on the deformation behaviour of composite materials are present as an increase in moisture content lowers the instantaneous stiffness of the thermoplastic matrix constituent [14]. A variation in instantaneous stiffness also changes the magnitude of the relaxation behaviour and is thus regarded to be of significance as well for the simulation of viscoelastic deformation behaviour. This section presents methods that have been developed to model the thermal- and hygroscopic effects on viscoelasticity and introduces the concept of thermorheological complexity.

The deformation behaviour of viscoelastic polymers can be described by viscoelastic functions that define either the modulus or compliance of the material. These functions can be visualised by means of a double logarithmic representation of the modulus or compliance as a function of time or frequency. It is commonly known that the viscoelastic functions of polymers show a time- and temperature dependency. These dependencies originate from the molecular motion and -transitions that are present for the polymer.

The most significant thermoplastic molecular transition is known as the glass-transition and is often described in literature as the  $\alpha$ -transition. This transition is associated with the segmental motion of the main polymeric chain. It is noted that the main polymeric chains still exhibit mobility even below the glass-transition and that relaxation times can be defined in this region as well. Secondary transitions are denoted as  $\beta$ - or  $\gamma$ -transitions and are related to the motion of side- or end group or restricted motion of the main polymeric chains above the glass transition.

The contribution of every molecular transition can be described by an individual viscoelastic function. The overall relaxation behaviour of the polymer is then obtained by addition of the individual viscoelastic functions. A polymer that displays only one molecular transition has only one viscoelastic function to describe the overall relaxation behaviour. The shape of the viscoelastic function for a molecular transition is independent of temperature. However, a difference in temperature does result in a shift of the viscoelastic function along the time-axis. Because the shapes of the viscoelastic functions for two temperature conditions are equal, one function can be superposed with the other function by a shift along the time-axis[51].

This superposition is fundamental to the time-temperature superposition principle in which a time-temperature equivalence can be identified. However, this superposition principle is only valid if the viscoelastic functions display an identical shape. A superposition can not be achieved with only shifting along the time-axis if the shapes of the overall viscoelastic functions are unequal. Different molecular transitions have varying temperature dependencies as the molecular structures involved are dissimilar. This implies that the overall viscoelastic functions of a polymer with two active molecular transitions do not have the same shape and that the principle of time-temperature superposition does not hold.

Polymers with only one active molecular transition are said to be thermorheologically simple and the time-temperature superposition can be applied. On the contrary, the presence of multiple molecular transitions will cause a polymer to be thermorheologically complex and the time-temperature superposition principle fails [51]. Examples for which the application of time-temperature superposition is not valid have been documented by [52] and [53], for polymer mixtures and block copolymers, respectively. It is also reported that the time-temperature superposition principle does not hold when the relaxation curves span a temperature range that includes phase transitions or polymer degradation [54].

Inspection of a Cole-Cole diagram can be utilised to conclude whether or not a polymer is thermorheologically simple. In the context of viscoelastic material behaviour, a Cole-Cole diagram is a plot of the loss modulus as a function of the storage modulus [53]. A Cole-Cole diagram must display a continuous line for a polymer to be thermorheologically simple. The argumentation for this statement is derived from the requirement that all viscoelastic functions must have the same temperature dependence for a polymer to be thermorheologically simple [55]. A discontinuous Cole-Cole diagram indicates that the temperature-dependence of the loss modulus shows a discrepancy with the temperature dependence of the storage modulus and indicates thermorheological complex behaviour.

The shift factors for thermorheologically complex polymers become also a function of time. A method was proposed by Fesko and Tschögl [56] to calculate shift factors that are required to superpose a single point of a viscoelastic function with a corresponding point of another viscoelastic function measured at a different temperature. The method was developed for polymeric materials that include two phases; which is characteristic for block copolymers and polymer blends. However, knowledge about the viscoelastic functions of the constituent homopolymers and the temperature dependencies must be known in advance.

The linearity of the viscoelastic behaviour also governs whether or not the principle of time-temperature superposition will be successful. It has been stated that the successful application of time-temperature superposition is dependent on an equal influence of temperature on the viscoelastic functions. The deformation behaviour of non-linear viscoelastic materials depends, amongst other parameters, on the magnitude of the loading. Hence, the viscoelastic functions must inherently also be influenced by the magnitude of the loading [57]. Hence, the classical principle of time-temperature superposition can not be applied to non-linear viscoelastic materials.

Viscoelastic curves that have been obtained through relaxation tests under conditions of various temperatures show a discrepancy in relaxation modulus. A continuous curve may be constructed, if the material is thermorheologically simple, by plotting the individual relaxation curves on a logarithmic time scale and shifting them horizontally along the time axis. The resulting continuous curve is referred to as a mastercurve and the observation of this possibility has been reported by [58], [59], and [60], amongst others. The shifting of the curves is an act of superposing and provides an explanation for the name of this principle. Vertical shift factors may be added to account for thermal expansion effects, but these shift factors can be neglected for most polymers [61]. The principle of the time-temperature superposition is depicted schematically in Figure 3.7.

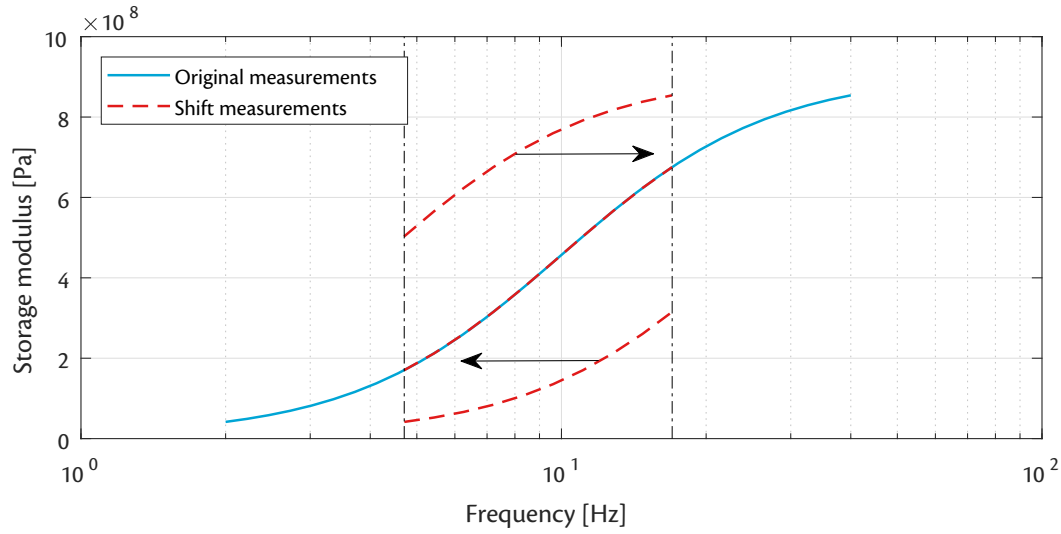


Figure 3.7 *The principle of time-temperature superposition to obtain a mastercurve from multiple viscoelastic functions measured at different temperature conditions.*

The amount of shifting on the logarithmic time scale is indicated with a shift factor. Continuous relaxation curves can be obtained for thermorheologically simple polymers by only applying horizontal shifting. Different shift factors are found for tests that have been conducted under different temperature conditions. The horizontal shift factors are denoted with  $a_T$  and the subscript is included to indicate the dependence on temperature. It is noted that the all viscoelastic functions, such as modulus and compliance, have equal shift factors for a homogeneous isotropic material that is thermorheologically simple [55]. The time-temperature superposition principle can therefore also be applied to the storage- and loss modulus in the frequency domain.

One experimental method to determine the shift factors as a function of temperature is to measure the zero-shear viscosity which implies measuring the viscosity of the polymer as the shear rate approaches zero. The shift factor  $a_T$  for temperature  $T$  may then be computed with respect to the reference temperature  $T_{ref}$  with Eq. 3.43 [54]. The symbol  $\eta_0$  denotes the zero-shear viscosity.

$$a_T \approx \frac{\eta_0(T)}{\eta_0(T_{ref})} \quad 3.43$$

Although this experimental procedure may provide an accurate method to obtain a mastercurve, measuring the zero-shear viscosity is often troublesome for polymers that have relatively high molecular weights. The essence in constructing a mastercurve is that a single continuous relaxation curve is obtained. Shifting of the individual curves may therefore also be conducted based on the experimental relaxation data alone. An algorithm is presented in the following that proposes a method aimed to yield more accurate results in comparison to visual inspection.

The initial mastercurve is initially only comprised of the measurements that have been conducted at the reference temperature. The initial mastercurve is fitted with an appropriate polynomial that properly describes the curvature of the mastercurve and which is believed to show the expected behaviour for extrapolation. Data obtained in the neighbourhood of the reference temperature is best fitted with a first order polynomial, whereas a third order polynomial is more suited for temperatures further away from the glass transition temperature.



The curve that represents the data of an adjacent temperature measurement is then shifted with the objective to minimise the mean squared error between the shifted values and the previously fitted polynomial evaluated at the time values, or frequency values for DMA measurements, that the curve has been shifted to. The mastercurve is expanded after the minimisation to include the values of the curve that was shifted. A suitable polynomial is then fitted to the updated mastercurve and the minimisation is carried out again for the curve that corresponds to the next adjacent temperature. This process is repeated until all curves have been shifted and the full mastercurve has been obtained.

It is noted that this method was developed during the thesis research and no literature research was conducted to this approach as the results proved to be satisfactory. Nevertheless, alternative algorithms were found in literature during the search for existing methods as comparison to the one which is previously described during the documentation phase of the thesis. These alternative methods involve minimising the mastercurve' arc length [62] and the Closed-Form-Shifting technique [57]. The latter technique is in the process of standardisation under part 6 of ISO 108. However, both mentioned algorithms from literature require overlap in the individual curves. The previously described algorithm does not.

A finite set of experimentally determined shift factors can be utilised to obtain an expression that allows the calculation of the shift factor for every desired temperature within the temperature range of the experiments. A mathematical expression was determined by Williams, Landel, and Ferry by making use of the viscosity model published by Doolittle [63]. This viscosity model was based on the assumption that the viscosity of a glassy material is inversely related to the ratio between the entire volume of the glassy material and the free space between the molecules. The details of this model are out of the scope of the thesis research and thus only the final expression known as the Williams-Landel-Ferry equation is displayed in Eq. 3.44 [64].

$$\log a_T = -\frac{C_1 (T - T_{ref})}{C_2 + T - T_{ref}} \quad 3.44$$

The Arrhenius equation is also a mathematical expression that can be employed to calculate the shift factors as a function of temperature. The Arrhenius equation that describes viscosity as a temperature-dependent variable is shown in Eq. 3.45. A similar form can be used to describe the rate of mass diffusion as shown in Eq. 2.2 in Section 2.2. The important constants in Eq. 3.45 are  $E_a$  and  $R$  which denote the activation energy and gas constant, respectively.

$$\eta(T) = A \cdot e^{-\frac{E_a}{RT}} \quad 3.45$$

The mathematical expression for a horizontal shift factor derived from Eq. 3.45 is shown in Eq. 3.46. It is noted that the temperatures denoted with  $T$  and  $T_{ref}$  in Eq. 3.46 must be formulated as absolute temperature since Eq. 3.45 governs reaction rates for which absolute temperatures must be provided. It is noted that the Celsius temperature scale can be used for the Williams-Landel-Ferry equation shown in Eq. 3.44.

$$\log a_T = \frac{E}{R} \left( \frac{1}{T} - \frac{1}{T_{ref}} \right) \quad 3.46$$

The Arrhenius equation is often used for a temperature range that is significantly higher than the glass transition temperature of the polymer. The Williams-Landel-Ferry is more commonly used for a wide range of temperatures [54]. Choosing between using the Arrhenius- or the Williams-Landel-Ferry equation can be numerically argued by plotting the shift factors as a function of the reciprocal of temperature. An ideal description by the Arrhenius model produces a straight line through the data if the relaxation behaviour agrees to the Arrhenius model. A similar technique can be applied for the suitability of the Williams-Landel-Ferry equation by plotting  $\Delta T / \log a_T$  as a function of  $\Delta T$ .

A similar approach exists to account for the influence of moisture content on the relaxation behaviour of composite materials analogous to the influence of temperature. Conducting relaxation experiments with specimens that only vary in moisture content at constant temperatures and -strain levels yields relaxation curves that are only influenced by the moisture content. Maksimov had observed that it was possible to calculate a shift factor in an analogous method to time-temperature superposition to obtain one continuous curve from the individual relaxation measurements [65]. The equation to calculate this shift factor resembles the Williams-Landel-Ferry equation and the computation depends on the moisture content that is denoted with  $W$ .

$$\log a_W = -\frac{D_1 (W - W_{ref})}{D_2 + W - W_{ref}} \quad 3.47$$

The term  $W_{ref}$  corresponds to the moisture content in the test specimen that is chosen as reference moisture content. Predictions made through applying calculated moisture content shift factors were in good agreement with control tests that had been carried out. It can thus be concluded that the influence of moisture content on the relaxation behaviour can be accounted for through the method of time-humidity superposition.

The combined effect of temperature- and moisture content on the relaxation behaviour of the composite material may be predicted by a linear superposition of the results that are obtained by separately carrying out time-temperature superposition and time-humidity superposition, provided that valid mastercurves are obtained for both principles. Two methods are described by Patankar [66] to determine a doubly-shifted mastercurve that accounts for hygrothermal effects.

The first approach involves constructing mastercurves at constant temperature conditions and with varying moisture contents, yielding hygroscopic shift factors depending on temperature  $a_W(T, W)$ . The second step in this approach involves shifting the constructed mastercurves for varying temperature conditions to obtain a single grand mastercurve and thermal shift factors,  $a_T(T, W)$ . The second approach applies the same principle but has the order of time-temperature superposition and time-humidity superposition reversed. The grand mastercurve can then be used to determine a shift factor for arbitrary temperature- and moisture content conditions.

### 3.5 Anisotropy and viscoelastic correspondence

Both the integral- and differential formulations that have been derived in Section 3.2 and Section 3.3, respectively, concern one-dimensional viscoelasticity. This section presents the implications of utilising these viscoelastic formulations for a three-dimensional problems. This section focuses on orthotropic materials as the objective component is comprised of a balanced and symmetric laminate. The viscoelastic correspondence principle is also discussed in this section as it provides a valuable tool in defining the constitutive equations from the mathematical expressions valid for one lamina.

The stress state in any point of the laminate in three dimensions is fully described by the second order stress tensor that is displayed in Eq. 3.48. The principal directions denoted with the indices 1, 2, and 3 follow the sign convention that is shown in Figure 3.8. The directions of the components of the three-dimensional stress tensor are also indicated in Figure 3.8.

$$\sigma_{ij}(t) = \begin{bmatrix} \sigma_{11}(t) & \sigma_{12}(t) & \sigma_{13}(t) \\ \sigma_{21}(t) & \sigma_{22}(t) & \sigma_{23}(t) \\ \sigma_{31}(t) & \sigma_{32}(t) & \sigma_{33}(t) \end{bmatrix} \quad 3.48$$

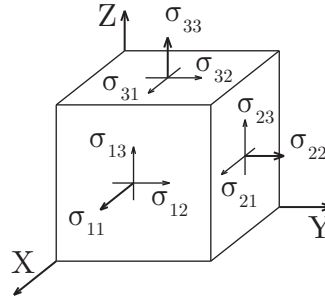


Figure 3.8 Sign convention for the stress tensor as defined for three dimensions.

The approach to generalising one-dimensional viscoelastic formulations to three dimensions is based on the principle of superposition. Every component of stress must have a linear relation with each component of the strain. The previous holds for any linear material [49]. The principle of superposition within this context can be written as shown in Eq. 3.49. The notation of  $\sigma_{ij}(t)|_{\varepsilon_{kl}}$  is used to indicate that the stress is induced by the strain and nothing else.

$$\sigma_{ij}(t) = \sum_{k=1}^3 \sum_{l=1}^3 \sigma_{ij}(t)|_{\varepsilon_{kl}} \quad \text{with } i, j = 1, 2, 3 \quad 3.49$$

It holds that every individual term in the linear summation is a one-dimensional viscoelastic constitutive equation. A fourth order tensor can be constructed that contains all scalars governing these individual constitutive relations. It is noted that this fourth order tensor can be constructed for both the stress-strain- and the strain-stress relationships. Only the stress-strain governing fourth order tensor is shown in Eq. 3.50 denoted with  $C_{ijkl}$ . It is noted that the expression shown in Eq. 3.50 is the three-dimensional equivalent to Eq. 3.8.

$$\sigma_{ij}(t) = \int_0^t C_{ijkl}(t - \tau) \frac{d}{d\tau} \varepsilon_{kl} d\tau \quad 3.50$$

The fourth order tensor  $C_{ijkl}$  contains 81 elements that describe the full relaxation behaviour in three dimensions. However, the number of elements reduces to a total of 36 because of the symmetry in the stress- and strain tensors applicable to engineering composite materials [49]. This symmetry is found in the first- and second pairs of indices, namely  $i, j$  and  $k, l$ . The notation that is shown in Eq. 3.50 can be rewritten by utilising the mentioned symmetry to the expression that is shown in Eq. 3.51.

$$\sigma_{ij} = \int_0^t C_{ij}(t - \tau) \frac{d}{d\tau} \varepsilon_{kl} d\tau \quad 3.51$$

The three-dimensional constitutive equation can be simplified to a further extend due to balanced and symmetric laminate of the objective component. Symmetry planes exist for this type of laminate in which the direct stresses are decoupled from the shear strain and in which the shear stresses are decoupled from the normal strain. The directions in which this decoupling is satisfied are known as the principal directions of the laminate. A balanced and symmetric laminate results in orthotropic material behaviour and exhibits three material symmetry planes.

The result of the three material symmetry planes is the decoupling of the three normal stresses from the three shear strains. A total reduction of 6 independent stiffness components is obtained. The number of independent stiffness components is further reduced by 9 as the shear stresses on a symmetry plane decouple from the shear strains on the other symmetry planes [49]. The remaining independent stiffness components are shown in Eq. 3.52 [67].

$$\begin{Bmatrix} \sigma_{11} \\ \sigma_{22} \\ \sigma_{33} \\ \sigma_{12} \\ \sigma_{13} \\ \sigma_{23} \end{Bmatrix} = \begin{bmatrix} C_{11} & C_{12} & C_{13} & 0 & 0 & 0 \\ C_{12} & C_{22} & C_{23} & 0 & 0 & 0 \\ C_{13} & C_{23} & C_{33} & 0 & 0 & 0 \\ 0 & 0 & 0 & C_{44} & 0 & 0 \\ 0 & 0 & 0 & 0 & C_{55} & 0 \\ 0 & 0 & 0 & 0 & 0 & C_{66} \end{bmatrix} \cdot \begin{Bmatrix} \varepsilon_{11} \\ \varepsilon_{22} \\ \varepsilon_{33} \\ \gamma_{12} \\ \gamma_{13} \\ \gamma_{23} \end{Bmatrix} \quad 3.52$$

Every independent relaxation component that is shown in Eq. 3.52 can be represented by means of a Prony series analogous to the expression that is shown in Eq. 3.42. However, experimental measurements are often conducted with unidirectional layers and the mechanical properties for a specific lay-up are constructed through a micromechanical model. It is therefore important to have knowledge on how to construct the laminate relaxation components from the lamina' properties. The remainder of this section discusses the viscoelastic correspondence principle that was used to define the relaxation components of the laminate.

Many micromechanical equations exist in elastic formulation to determine a laminate's engineering properties from respective constituent' properties. The elastic-viscoelastic correspondence principle allows these equations to be used to calculate the laminate's engineering properties for a viscoelastic formulation. The fundamental method of doing so is to substitute each material property and input variable in an elastic constitutive equation by its Carson- and Laplace transform, respectively [49]. The Laplace- and Carson transform are displayed for an arbitrary function in the upper and lower expression in Eq. 3.53, respectively.

$$\begin{aligned} L\{f(t)\} &\equiv \int_0^{\infty} e^{-st} f(t) dt \\ LC\{f(t)\} &\equiv \int_0^{\infty} e^{-st} f(t) dt \cdot s \end{aligned} \quad 3.53$$

### 3.6 Constitutive equations

The constitutive equations applicable to anisotropic linear viscoelasticity are derived in this section. The derivation that is presented was first introduced in combination with a recursive formulation by Zocher [44]. The derivation of the constitutive equations begins at the definition of the constitutive relationship between stress and strain. This relationship is expanded in an analogous fashion to the Boltzmann' superposition principle described by Gutierrez-Lemini [49] which yields the Boltzmann' integral. The Boltzmann' integral is extended to account for anisotropy and the time-temperature superposition is included in the formulation. The last two steps involve deriving the recursive formulation and transforming the equations to increment algebraic form for finite element implementation.

Starting from the constitutive equation for an isotropic material, Eq. 3.54 shows how the relaxation modulus relates an applied strain to stress. The term  $\varepsilon_0$  is provided with the subscript to indicate that the applied strain is the only strain present and that it has a constant magnitude.

$$\sigma(t) = E(t)\varepsilon_0 \quad 3.54$$

To allow an integral formulation of the governing stress-strain relationship as shown in Eq. 3.54, it is assumed that the material has not undergone any deformation before an initial point in time. This is shown mathematically in Eq. 3.55.

$$\begin{aligned} \sigma(t) &= 0 & \text{for } t < 0 \\ \sigma(t) &= E(t)\varepsilon_0 & \text{for } t \geq 0 \end{aligned} \quad 3.55$$

Because of the conditions shown in Eq. 3.55, Eq. 3.54 may be written to include the Heaviside function with the step located at the initial time, which is taken zero.

$$\sigma(t) = E(t) \cdot H(t)\varepsilon_0 \quad 3.56$$

Since the model is required to be able to also capture the application of strains that do not coincide with the initial time, Eq. 3.56 is written to represent the application of the strain at an arbitrary time  $t_1$ , as shown in Eq. 3.57.

$$\sigma(t) = E(t - t_1) \cdot H(t - t_1)\varepsilon_0 \quad 3.57$$

In addition, the structure will not only be subjected to a single strain input. Hence, it is necessary to extend the stress response to allow multiple instances of strain input. Assuming a linear viscoelastic behaviour, Boltzmann's superposition principle can be employed to do so. According to the Boltzmann superposition principle, the overall stress response to the overall strain input is identical to the linear addition of the individual stress responses to the individual strain inputs. Equation 3.58 displays the Boltzmann superposition principle. Please note that this introduces a discretisation of the time into time intervals that are denoted with  $t_k$ .

$$\sigma(t) \approx \sum_{k=1}^N E(t - t_k) \Delta \varepsilon_k \quad \text{for } t \geq t_k \quad 3.58$$

Since the material of the problem at hand is a composite material, the constitutive equation, Eq. 3.8, must be rewritten to represent an anisotropic material. It is noted that the anisotropic relaxation moduli, denoted with  $C_{ijkl}$ , are dependent on the temperature. The fourth order tensor can be reduced to a matrix with 6 rows and 6 columns due to the orthotropic material behaviour of the material of interest and is denoted with  $C_{ij}$ .

In addition, the strain that actually leads to internal stresses is defined as the total strain of the material minus the free hygrothermal strains. This portion of the strain is defined as the effective strain in the present work. The effective strain, total strain, and free hygrothermal strain are denoted with the symbols,  $\bar{\varepsilon}_{kl}$ ,  $\varepsilon_{kl}$ , and  $\varepsilon_{kl}^*$ , respectively. The constitutive equation can then be written as shown in Eq. 3.59.

$$\sigma_{ij}(t) = \int_0^t C_{ij}(T, t - \tau) \frac{\delta \bar{\varepsilon}_{kl}}{\delta \tau} d\tau \quad 3.59$$

The stress tensor that is shown in Eq. 3.59 contains 3 direct stresses and 3 shear stresses. The order in which the stresses appear in the stress tensor has been chosen to be in agreement with the order that is followed by ABAQUS [68] and the Voigt notation that is applied is displayed in Eq. 3.60.

$$\sigma_{ij} = \begin{bmatrix} \sigma_{11} \\ \sigma_{22} \\ \sigma_{33} \\ \sigma_{12} \\ \sigma_{13} \\ \sigma_{23} \end{bmatrix} \quad 3.60$$

The concept of effective strain is shown mathematically in Eq. 3.61. Equation 3.61 also displays the definition of the free hygrothermal strain,  $\varepsilon_{kl}^*$ .

$$\bar{\varepsilon}_{kl} = \varepsilon_{kl} - \varepsilon_{kl}^* \quad \text{where} \quad \varepsilon_{kl}^*(x_k, t) = \alpha_{kl} \Delta T + \beta_{kl} \Delta C \quad 3.61$$

To eliminate the temperature dependency in the anisotropic relaxation moduli, a time-temperature superposition principle is applied. Without losing generality, the shift factor,  $a_{T,C}$ , is also said to be dependent on moisture content. Equation 3.62 shows how real time, denoted with  $t$ , can be transformed into what is called reduced time, denoted with  $\xi$ , to simulate the effect of temperature and moisture content on the anisotropic relaxation moduli.

$$\xi(t) \equiv \int_0^t \frac{1}{a_{T,C}} d\tau \quad \xi'(\tau) \equiv \int_0^\tau \frac{1}{a_{T,C}} d\tau \quad 3.62$$

Assuming that the entire real time domain is shifted to reduced time to simulate the effect of the temperature- and moisture content envelope on the relaxation behaviour of the anisotropic material, a change of variables is introduced that is shown in Eq. 3.63.

$$\begin{aligned} t &\Rightarrow \xi \\ \tau &\Rightarrow \xi' \end{aligned} \quad 3.63$$

Equation 3.64 shows the constitutive equation in the reduced time domain. It is noted here that the anisotropic relaxation moduli are now dependent only on the reference temperature that has been chosen for the time-temperature superposition principle. The notation of this dependency is dropped from here on to save space and ensure easier reading.

$$\sigma_{ij}(\xi) = \int_0^\xi C_{ij}(T_0, \xi - \xi') \frac{\delta \bar{\epsilon}_{kl}(\xi')}{\delta \tau} d\tau \quad 3.64$$

Equation Eq. 3.64 is considered valid as shown, however, it cannot be implemented for a numerical analysis. An incremental formulation is required that allows progressing through reduced time and calculating the stress response of the material. Such an incremental notation is obtained by defining an incremental step in reduced time as shown in Eq. 3.65.

$$\xi_{n+1} = \xi_n + \Delta\xi \quad 3.65$$

Please note that  $\xi_{n+1}$  represents the reduced time of the incremented step. The current reduced time step is denoted with  $\xi_n$  and the increment in reduced time is represented by  $\Delta\xi$ . Following this notation, the stress state at the incremented time step can then be written as Eq. 3.66.

$$\sigma_{ij}(\xi_{n+1}) = \int_0^{\xi_{n+1}} C_{ij}(\xi_{n+1} - \xi') \frac{\delta \bar{\epsilon}_{kl}(\xi')}{\delta \xi'} d\xi' \quad 3.66$$

The objective of how the constitutive equations are set up is to obtain a recursive incremental notation. This means that part of the stress state is retrieved from a previously known stress state. Splitting the integral shown in Eq. 3.66 into two distinct periods allows a recursive notation. The split in reduced time domain is made at the moment of the previously known solution,  $\xi_n$ .

$$\sigma_{ij}(\xi_{n+1}) = \int_{\xi_n}^{\xi_{n+1}} C_{ij}(\xi_{n+1} - \xi') \frac{\delta \bar{\varepsilon}_{kl}(\xi')}{\delta \xi'} d\xi' + \int_0^{\xi_n} C_{ij}(\xi_{n+1} - \xi') \frac{\delta \bar{\varepsilon}_{kl}(\xi')}{\delta \xi'} d\xi' \quad 3.67$$

The change that is experienced by the anisotropic relaxation moduli as the reduced time is incremented, is defined as shown in Eq. 3.68.

$$\Delta C_{ij} = C_{ij}(\xi_{n+1} - \xi') - C_{ij}(\xi_n - \xi') \quad 3.68$$

Defining the change in anisotropic relaxation moduli is performed to be able to rewrite the right hand side of Eq. 3.66 to a more convenient form for when the Prony series is introduced. The difference in stress across the reduced time step is noted with the use of the difference in anisotropic relaxation moduli in Eq. 3.69.

$$\Delta \sigma_{ij} = \int_{\xi_n}^{\xi_{n+1}} C_{ij}(\xi_{n+1} - \xi') \frac{\delta \bar{\varepsilon}_{kl}(\xi')}{\delta \xi'} d\xi' + \int_0^{\xi_n} \Delta C_{ij} \frac{\delta \bar{\varepsilon}_{kl}(\xi')}{\delta \xi'} d\xi' \quad 3.69$$

Up until now, it has been assumed that the anisotropic relaxation moduli are known. Carrying out the integrals shown in Eq. 3.69 is only possible when the anisotropic relaxation moduli can be expressed explicitly. The anisotropic relaxation moduli are assumed to be approximated well by a Prony series expansion. This assumption allows to write the anisotropic relaxation moduli as displayed in Eq. 3.70. It is noted that there is a reduced time independent and -dependent part to the right hand side of Eq. 3.70. The term  $C_{ij\infty}$  is referred to as the long term modulus. Furthermore,  $C_{ijm}$  and  $\tau_{ijm}$  represent the elastic coefficients and relaxation times of the elements in a generalised Maxwell model, respectively.

$$C_{ij}(\xi_{n+1} - \xi') = C_{ij\infty} + \sum_{m=1}^{M_m} C_{ijm} e^{-(\xi_{n+1}-\xi')/\tau_{ijm}} \quad 3.70$$

An additional requirement of evaluating the integrals of Eq. 3.69 is that the reduced time derivative of the effective strain is known at the reduced time of interest. An approximation by linearisation is introduced here and it is assumed that the strain at reduced time  $\xi_n$  is known from the previous solution. Equation 3.71 shows how the strain at the incremented reduced time is approximated. In Eq. 3.71,  $G_\varepsilon$  is defined to be the derivative of the effective strain with respect to the reduced time.

$$\bar{\varepsilon}_{kl}(\xi') = \varepsilon_{kln} + G_\varepsilon \cdot (\xi' - \xi_n) \Rightarrow \frac{\delta \bar{\varepsilon}_{kl}(\xi')}{\delta \xi'} \approx G_\varepsilon \quad 3.71$$

The change in orthotropic relaxation moduli between the incremented reduced time step and the known solution can be written with implementation of the Prony series as shown in Eq. 3.72.



$$\Delta C_{ijm} = C_{ij\infty} + \sum_{m=1}^{M_m} C_{ijm} e^{-(\xi_{n+1}-\xi')/\tau_{ijm}} - C_{ij\infty} - \sum_{m=1}^{M_m} C_{ijm} e^{-(\xi_n-\xi')/\tau_{ijm}} \quad 3.72$$

Application of the definition of the incremental time step, as shown in Eq. 3.65, allows rewriting the exponential term of the second term on the right hand side of Eq. 3.72. The result of rewriting the exponential is straightforward, but it is shown in Eq. 3.73 for clarity and ease of reading.

$$\sum_{m=1}^{M_m} C_{ijm} e^{-(\xi_{n+1}-\xi')/\tau_{ijm}} = \sum_{m=1}^{M_m} C_{ijm} e^{-(\xi_n+\Delta\xi-\xi')/\tau_{ijm}} \quad 3.73$$

Expanding the addition of the exponent of the right hand side in Eq. 3.73 into the multiplication of two exponential functions, allows extending the convenient notation of the second term on the right hand side of Eq. 3.72 to the expression that is displayed in Eq. 3.74.

$$\sum_{m=1}^{M_m} C_{ijm} e^{-(\xi_{n+1}-\xi')/\tau_{ijm}} = \sum_{m=1}^{M_m} C_{ijm} \left( e^{-(\xi_n-\xi')/\tau_{ijm}} \cdot e^{-\Delta\xi/\tau_{ijm}} \right) \quad 3.74$$

Substitution of the convenient form that is obtained in Eq. 3.74 back into the definition of the change in anisotropic relaxation moduli in Eq. 3.72, results in the relation that is provided in Eq. 3.75.

$$\Delta C_{ijm} = - \sum_{m=1}^{M_m} C_{ijm} e^{-(\xi_n-\xi')/\tau_{ijm}} \left( 1 - e^{-\Delta\xi/\tau_{ijm}} \right) \quad 3.75$$

Applying the notation that is shown in Eq. 3.75, the expression for the change in stress over the reduced time step, displayed in Eq. 3.69, can be rewritten to Eq. 3.76. This expression clearly has one part that depends purely on the chosen reduced time step and one part that depends purely on the history; the recursive formulation is apparent.

$$\begin{aligned} \Delta\sigma_{ij} = & \int_{\xi_n}^{\xi_{n+1}} \left( C_{ij\infty} + \sum_{m=1}^{M_m} C_{ijm} e^{-(\xi_{n+1}-\xi')/\tau_{ijm}} \right) \frac{\delta\bar{\epsilon}_{kl}(\xi')}{\delta\xi'} d\xi' \\ & - \int_0^{\xi_n} \sum_{m=1}^{M_m} C_{ijm} e^{-(\xi_n-\xi')/\tau_{ijm}} \left( 1 - e^{-\Delta\xi/\tau_{ijm}} \right) \frac{\delta\bar{\epsilon}_{kl}(\xi')}{\delta\xi'} d\xi' \end{aligned} \quad 3.76$$

Applying also the linearisation approximation, as shown in Eq. 3.71, to Eq. 3.76, allows to take the differential out of the integral. Hence, the increment in stress can be written as displayed in Eq. 3.77.

$$\begin{aligned}
\Delta\sigma_{ij} = & G_\varepsilon \int_{\xi_n}^{\xi_{n+1}} \left( C_{ij\infty} + \sum_{m=1}^{M_m} C_{ijm} e^{-(\xi_{n+1}-\xi')/\tau_{ijm}} \right) d\xi' \\
& - G_\varepsilon \left( 1 - e^{-\Delta\xi/\tau_{ijm}} \right) \int_0^{\xi_n} \sum_{m=1}^{M_m} C_{ijm} e^{-(\xi_n-\xi')/\tau_{ijm}} d\xi'
\end{aligned} \tag{3.77}$$

Prior to carrying out the integrals, a definition is presented in Eq. 3.78 that relates the relaxation time to the damping- and elastic coefficients of the generalised Maxwell model. Please note that  $\eta_{ijm}$  represents the damping coefficients. Making use of the notation of the damping coefficients results in simpler equations after carrying out the integrals.

$$\eta_{ijm} = C_{ijm} \cdot \tau_{ijm} \tag{3.78}$$

To complete the recursive notation of the second integral in Eq. 3.77, again a time split is made. The first part contains the entire history up to the second previously known solution. In mathematical terms, this is the period from 0 to  $\xi_n - \Delta\xi$ . The second part is from  $\xi_n - \Delta\xi$  to  $\xi_n$ . Hence, the second integral of the right hand side of Eq. 3.77 is rewritten by splitting the integral to cover the two mentioned time periods. The result of the rewriting is shown in the upper part of Eq. 3.79, the result of the integration is displayed in the lower part.

$$\begin{aligned}
\int_0^{\xi_n} \sum_{m=1}^{M_m} C_{ijm} e^{-(\xi_n-\xi')/\tau_{ijm}} d\xi' &= \int_0^{\xi_n-\Delta\xi} \sum_{m=1}^{M_m} C_{ijm} e^{-(\xi_n-\xi')/\tau_{ijm}} d\xi' + \int_{\xi_n-\Delta\xi}^{\xi_n} \sum_{m=1}^{M_m} C_{ijm} e^{-(\xi_n-\xi')/\tau_{ijm}} d\xi' \\
&= \sum_{m=1}^{M_m} \eta_{ijm} \left( e^{-\Delta\xi/\tau_{ijm}} - e^{-\xi_n/\tau_{ijm}} \right) + \sum_{m=1}^{M_m} \eta_{ijm} \left( 1 - e^{-\Delta\xi/\tau_{ijm}} \right)
\end{aligned} \tag{3.79}$$

The following two integrals are defined that will allow the recursive statement on the second term in Eq. 3.77. It is noted that the integration limits shown in Eq. 3.81 span exactly the early reduced time part of the reduced time split. Please note that the definition of  $R(\xi_n)$  in Eq. 3.81 represents the left hand side of Eq. 3.79.

$$R(\xi_n) = \int_0^{\xi_n} \sum_{m=1}^{M_m} C_{ijm} e^{-(\xi_n-\xi')/\tau_{ijm}} d\xi' \tag{3.80}$$

$$R(\xi_{n-1}) = R(\xi_n - \Delta\xi) = \int_0^{\xi_n-\Delta\xi} \sum_{m=1}^{M_m} C_{ijm} e^{-(\xi_n-\Delta\xi-\xi')/\tau_{ijm}} d\xi' \tag{3.81}$$

Usage of previously known information is possible if that information can be written to be part of the mathematical formulation shown in the lower part of Eq. 3.79. Hence, the integral on the right hand side of Eq. 3.81 is carried out. The result of the integration is shown in Eq. 3.82.

$$\int_0^{\xi_n - \Delta\xi} \sum_{m=1}^{M_m} C_{ijm} e^{-(\xi_n - \Delta\xi - \xi')/\tau_{ijm}} d\xi' = \sum_{m=1}^{M_m} \eta_{ijm} \left(1 - e^{-(\xi_n - \Delta\xi)/\tau_{ijm}}\right) \quad 3.82$$

The left hand side of the lower part of Eq. 3.79 is now manipulated in such a way to include the result of the integration that is carried out in Eq. 3.82 in its formulation. The first step of the manipulation is shown in the upper part of Eq. 3.83, further rewriting is shown in the middle part, and the bottom part shows how the result of Eq. 3.82 fits into the rewritten expression.

$$\begin{aligned} \sum_{m=1}^{M_m} \eta_{ijm} \left(e^{-\Delta\xi/\tau_{ijm}} - e^{-\xi_n/\tau_{ijm}}\right) &= \sum_{m=1}^{M_m} \eta_{ijm} e^{-\Delta\xi/\tau_{ijm}} \left(1 - \frac{e^{-\xi_n/\tau_{ijm}}}{e^{\Delta\xi/\tau_{ijm}}}\right) \\ &= e^{-\Delta\xi/\tau_{ijm}} \sum_{m=1}^{M_m} \eta_{ijm} \left(1 - e^{-(\xi_n - \Delta\xi)/\tau_{ijm}}\right) \\ &= e^{-\Delta\xi/\tau_{ijm}} \cdot R(\xi_{n-1}) \end{aligned} \quad 3.83$$

Substitution of the result back into Eq. 3.79 and acknowledging the definition of  $R(\xi_n)$  to be the left hand side of Eq. 3.79, yields the key equation to the recursive notation. It is noted that Eq. 3.84 only depends on the second previous solution, corresponding to  $\xi_n - \Delta\xi$ .

$$R(\xi_n) = e^{-\Delta\xi/\tau_{ijm}} R(\xi_{n-1}) + G_\varepsilon^- \sum_{m=1}^{M_m} \eta_{ijm} \left(1 - e^{-\Delta\xi/\tau_{ijm}}\right) \quad 3.84$$

The incremental stress formulation is updated with the recursive notation. This is performed by substituting the right hand side of Eq. 3.84 for the second integral on the right hand side of Eq. 3.77. This is valid as  $R(\xi_n)$  was defined to be that exact integral; please see Eq. 3.79 and Eq. 3.80.

$$\begin{aligned} \Delta\sigma_{ij} = & G_\varepsilon^+ \left( \Delta\xi C_{ij\infty} + \sum_{m=1}^{M_m} \eta_{ijm} \left(1 - e^{-\Delta\xi/\tau_{ijm}}\right) \right) \\ & - \left(1 - e^{-\Delta\xi/\tau_{ijm}}\right) \left[ e^{-\Delta\xi/\tau_{ijm}} R(\xi_{n-1}) + G_\varepsilon^- \sum_{m=1}^{M_m} \eta_{ijm} \left(1 - e^{-\Delta\xi/\tau_{ijm}}\right) \right] \end{aligned} \quad 3.85$$

A distinction is made between  $G_\varepsilon^+$  and  $G_\varepsilon^-$  because their function is inherently different. For the recursive part of the constitutive equation, which is the lower part of Eq. 3.85, the partial derivative of the effective strain with respect to the reduced time is taken from the known solution for the period from  $\xi_n - \Delta\xi$  to  $\xi_n$ .

The non-recursive part, which is the upper part of Eq. 3.85, adds an incremental strain to the solution to remain in equilibrium with the recursive part and external loads, both thermally and mechanically. The corresponding time periods to the partial derivatives are shown in Eq. 3.86.

$$\begin{aligned} G_{\varepsilon}^{+} &= \frac{\Delta \bar{\varepsilon}_{kl}}{\Delta \xi'} && \text{from } \xi_n \text{ to } \xi_n + \Delta \xi \\ G_{\varepsilon}^{-} &= \frac{\Delta \bar{\varepsilon}_{kl}}{\Delta \xi'} && \text{from } \xi_n - \Delta \xi \text{ to } \xi_n \end{aligned} \quad 3.86$$

Taking the previous comments into account,  $G_{\varepsilon}^{-}$  is calculated from the previous known solution. The term  $G_{\varepsilon}^{+}$ , on the other hand, is substituted for its definition shown in the upper part of Eq. 3.86 to introduce the strain variable.

$$\begin{aligned} \Delta \sigma_{ij} = & \underbrace{\Delta \bar{\varepsilon}_{kl} \left( C_{ij\infty} + \frac{1}{\Delta \xi} \sum_{m=1}^{M_m} \eta_{ijm} \left( 1 - e^{-\Delta \xi / \tau_{ijm}} \right) \right)}_A \\ & - \underbrace{\left( 1 - e^{-\Delta \xi / \tau_{ijm}} \right) \left[ e^{-\Delta \xi / \tau_{ijm}} \cdot R(\xi_{n-1}) + G_{\varepsilon}^{-} \sum_{m=1}^{M_m} \eta_{ijm} \left( 1 - e^{-\Delta \xi / \tau_{ijm}} \right) \right]}_B \end{aligned} \quad 3.87$$

Remembering the definition of the effective strain enables splitting the effective strain into the total strain and the free hygrothermal strain. This is required to be able to write a finite element notation for which the mechanical strain dependent and -independent parts must be separated. The incremental stress is written for the mechanical- and free hygrothermal strain separately as shown in Eq. 3.88 using the notation of  $A$  and  $B$  for the incremental- and recursive parts displayed in Eq. 3.87. It is noted that the part denoted with  $A$  in Eq. 3.87 is the exact definition of the Jacobian and will be used for the finite element method.

$$\Delta \sigma_{ij} = \Delta \varepsilon_{kl} \cdot A - \Delta \varepsilon_{kl}^{*} \cdot A - B \quad 3.88$$

A virtual strain is defined in Eq. 3.89 with the symbol  $\mu_{ij}$  that is derived from the virtual displacement test functions denoted with  $v_i$  and  $v_j$ .

$$\mu_{ij} \equiv \frac{1}{2} \left( \frac{\delta v_i}{\delta v_j} + \frac{\delta v_j}{\delta v_i} \right) \quad 3.89$$

The equilibrium equation that is required to solve the initial boundary value problem can be written in the symmetric variational form shown in Eq. 3.90 by means of the method of weighted residuals [44].

$$\int_{\Omega} \sigma_{ji} \mu_{ij} dV = \int_{\Omega} \rho f_i v_i dV + \int_{\delta \Omega_2} T_i v_i dS \quad 3.90$$

The incrementalisation of the stress, the virtual strain, the actual displacement, and the virtual displacement are shown in Eq. 3.91 as these are required for the incrementalisation of Eq. 3.90.

$$\begin{aligned}
 \sigma_{ji}^{n+1} &= \sigma_{ji}^n + \Delta\sigma_{ji} \\
 \mu_{ij}^{n+1} &= \mu_{ij}^n + \Delta\mu_{ij} \\
 u_i^{n+1} &= u_i^n + \Delta u_i \\
 v_i^{n+1} &= v_i^n + \Delta v_i
 \end{aligned} \tag{3.91}$$

The incrementalisation of Eq. 3.90 is given by the expression that is displayed by Eq. 3.92. The superscript  $n+1$  denotes that the respective variable is evaluated for the incrementalised reduced time step.

$$\int_{\Omega} \sigma_{ji}^{n+1} \mu_{ij}^{n+1} dV = \int_{\Omega} \rho f_i^{n+1} v_i^{n+1} dV + \int_{\delta\Omega_2} T_i^{n+1} v_i^{n+1} dS \tag{3.92}$$

It is stated that the virtual displacements and -strains at reduced time  $\xi_n$  must be equal to zero for the correct solution of the actual displacements. Hence, substitution of the expressions shown in Eq. 3.91 for the variables in Eq. 3.92 and keeping only the incremental stress on the left hand side results in the relation depicted in Eq. 3.93.

$$\int_{\Omega} \Delta\sigma_{ji} \Delta\mu_{ij} dV = \int_{\Omega} \rho f_i^{n+1} \Delta V_i dV + \int_{\delta\Omega_2} T_i^{n+1} \Delta V_i dS - \int_{\Omega} \sigma_{ji} \Delta\mu_{ij} dV \tag{3.93}$$

The incremental stress shown in Eq. 3.93 is now substituted by the short notation that distinguishes between mechanical- and free hygrothermal strains as was defined in Eq. 3.88. The result of this substitution is shown in Eq. 3.94 for which it is noted that there are both mechanical- and free hygrothermal strains on the left hand side.

$$\int_{\Omega} [\Delta\varepsilon_{kl} \cdot A - \Delta\varepsilon_{kl}^* \cdot A - B] \Delta\mu_{ij} dV = \int_{\Omega} \rho f_i^{n+1} \Delta V_i dV + \int_{\delta\Omega_2} T_i^{n+1} \Delta V_i dS - \int_{\Omega} \sigma_{ji} \Delta\mu_{ij} dV \tag{3.94}$$

The solution of the finite element method must be found in the mechanical strains that are estimated by the solver. Hence, all mechanical stress independent parts are carried over to the right hand side. The result of this transformation is shown in Eq. 3.95.

$$\begin{aligned}
 \int_{\Omega} \Delta\varepsilon_{kl} \cdot A \cdot \Delta\mu_{ij} dV = & \int_{\Omega} \rho f_i^{n+1} \Delta V_i dV + \int_{\delta\Omega_2} T_i^{n+1} \Delta V_i dS + \int_{\Omega} \Delta\varepsilon_{kl}^* \cdot A \cdot \Delta\mu_{ij} dV \\
 & + \int_{\Omega} B \cdot \Delta\mu_{ij} dV - \int_{\Omega} \sigma_{ji} \Delta\mu_{ij} dV
 \end{aligned} \tag{3.95}$$

A strain-displacement relations operator is introduced in Eq. 3.96 which is normally computed by default by the finite element software.

$$\begin{aligned}\Delta \varepsilon_{kl} &= [\mathbf{D}] [\Delta u] \\ \Delta \mu_{ij} &= [\mathbf{D}] [\Delta v]\end{aligned}\tag{3.96}$$

This operator is applied to convert the virtual displacements to virtual strains which allows the solver to iteratively search for strain values that lead to convergence of the equilibrium equation. The equilibrium equation that only contains strain values is shown in Eq. 3.97.

$$\begin{aligned}\int_{\Omega} ([\mathbf{D}] [\Delta \mathbf{v}])^T A [\mathbf{D}] [\Delta \mathbf{u}] &= \int_{\Omega} [\Delta \mathbf{v}]^T \rho [\mathbf{f}^{\mathbf{n}+1}] dV + \int_{\delta\Omega_2} [\Delta \mathbf{v}]^T [\mathbf{T}^{\mathbf{n}+1}] dS \\ &+ \int_{\Omega} ([\mathbf{D}] [\Delta \mathbf{v}])^T \Delta \varepsilon_{kl}^* A dV + \int_{\Omega} ([\mathbf{D}] [\Delta \mathbf{v}])^T B dV \\ &- \int_{\Omega} ([\mathbf{D}] [\Delta \mathbf{v}])^T [\sigma_{ji}^{\mathbf{n}}] dV\end{aligned}\tag{3.97}$$

An approximate solution of the initial boundary value problem can then be posed by means of shapes functions, indicated with  $\psi$  and trial displacements, denoted with  $\Delta u_i^I$  and  $\Delta v_j^J$ . The finite element interpolants for an individual element can then be defined to be sum of the product of the trial displacement and the corresponding shape function, as displayed in Eq. 3.98.

$$\begin{aligned}\Delta u_{ih}^e(x, y, z, \xi) &= \sum_{I=1}^{N_e} \Delta u_i^I(x, y, z, \xi) \\ \Delta v_{jh}^e(x, y, z, \xi) &= \sum_{J=1}^{N_e} \Delta v_j^J(x, y, z, \xi)\end{aligned}\tag{3.98}$$

The final formulation of the finite element notation can then be written as shown in Eq. 3.99. It is noted that  $[\Delta v^e]$  is chosen arbitrarily and that the integral shown on the left hand side of Eq. 3.99 excluding the  $[\Delta v^e]$  term represents the element stiffness matrix. The integrals on the right hand side of Eq. 3.99 excluding the  $[\Delta v^e]$  term are defined as the contribution to the element load vector as a result of external forces, surface traction, hygrothermal expansion, recursive stresses, and existing internal stresses.

$$\begin{aligned}
\int_{\Omega} ([\mathbf{B}^e] [\Delta \mathbf{v}^e])^T A [\mathbf{B}^e] [\Delta \mathbf{u}^e] = & \int_{\Omega} ([\psi^e] [\Delta \mathbf{v}^e])^T \rho [\mathbf{f}^{n+1}] dV + \int_{\delta \Omega_2} ([\psi^e] [\Delta \mathbf{v}^e])^T [\mathbf{T}^{n+1}] dS \\
& + \int_{\Omega} ([\mathbf{B}^e] [\Delta \mathbf{v}^e])^T \Delta \varepsilon_{kl}^* A dV + \int_{\Omega} ([\mathbf{B}^e] [\Delta \mathbf{v}^e])^T B dV \\
& - \int_{\Omega} ([\mathbf{B}^e] [\Delta \mathbf{v}^e])^T [\sigma_{ji}^n] dV
\end{aligned} \tag{3.99}$$

Obtaining the final expression of the finite element notation was made possible with the relation that is shown in Eq. 3.100. It is noted that the constitutive equations might have a divergent character if a time step is chosen too large. This is displayed in Figure 3.9 for an arbitrary load case of uniaxial strain calculated with MATLAB.

$$\begin{aligned}
[\mathbf{D}] [\Delta \mathbf{u}] = [\mathbf{D}] [\Delta \mathbf{u}_h^e] &= [\mathbf{D}] [\psi^e] [\Delta \mathbf{u}^e] = [\mathbf{B}^e] [\Delta \mathbf{u}^e] \\
[\mathbf{D}] [\Delta \mathbf{v}] = [\mathbf{D}] [\Delta \mathbf{v}_h^e] &= [\mathbf{D}] [\psi^e] [\Delta \mathbf{v}^e] = [\mathbf{B}^e] [\Delta \mathbf{v}^e]
\end{aligned} \tag{3.100}$$

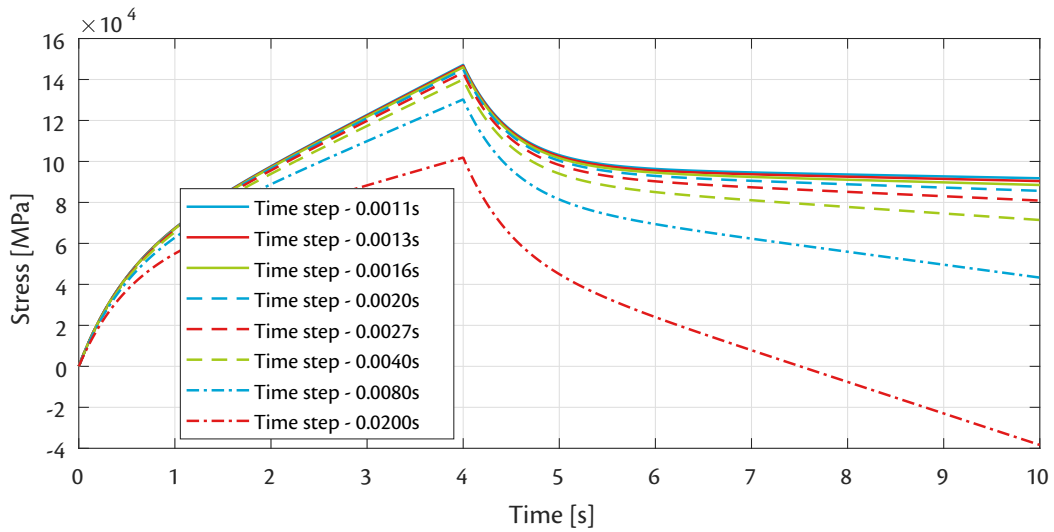


Figure 3.9 Influence of the time step size on the accuracy of the constitutive equations.





# 4

## Material characterisation

A material characterisation strategy can be set up after identification of the required material parameters for the numerical model. One of the major rules in working with finite element models is to keep in mind that the quality of the input will inherently influence the quality of the output. Hence, the consistency and validity of the experiments carried out for the material characterisation are significant for a successful simulation.

The first section of this chapter presents an overview of the experiments that have been carried out to characterise the viscoelastic hygrothermal deformation behaviour of the carbon-fibre reinforced thermoplastic. The subsequent sections describe one specific experiment in detail and provides the results as well as the conclusions that can be drawn from those results. The last section covers the micromechanical model that has been utilised to transform experimentally determined engineering parameters to laminate properties for the numerical model.

### 4.1 Overview of experimental characterisation

The viscoelastic deformation behaviour of the composite material subjected to the thermal loading inside the automotive drying ovens is driven by three mechanisms: thermal expansion, hygroscopic shrinkage, and polymer-chemical shrinkage. Please note that the changes in geometry due to diffusion is referred to as hygroscopic shrinkage, as opposed to -expansion, because the composite material is assumed to be moisture saturated at the beginning of the simulation and therefore moisture will diffuse out of the material. It is assumed that temperature and time are the only two independent variables that influence all involved mechanisms. The qualitative effects of temperature on these mechanisms are mentioned briefly in the next paragraph.

The influence of temperature on thermal expansion is obvious; the inter-molecular distance in the composite material increases due to rising temperature. Hygroscopic shrinkage is the result of temperature-driven diffusion of water molecules from the composite material into ambient air. A reduction of moisture content results in shrinkage of the material [15]. The effect of thermal expansion and hygroscopic shrinkage on internal stresses reduces at higher temperatures as the matrix material softens. The objective of the material characterisation is to quantitatively capture the influence of temperature and time on the mentioned mechanisms.

Thermal expansion of a material can be quantitatively described by means of a coefficient of thermal expansion, or CTE. The thermal expansion of an orthotropic composite material can be quantitatively described through three CTEs. Every CTE is defined as the increment in elongation along one of three principal axes of the composite material resulting from the increment in temperature. Experimental determination of CTEs is generally performed with a dilatometer. The definition of a CTE in longitudinal direction is shown in the first expression of Eq. 4.1. It is noted that the number of independent CTEs for the composite material in question reduces to two due to transverse isotropy.

Hygroscopic shrinkage can be described through a coefficient of moisture expansion, or CME, that is defined in an analogous manner to CTEs. Every CME of an orthotropic composite material is defined as the increment in elongation due to an increment in moisture concentration. It is necessary to know the time-dependent moisture concentration in a specimen to calculate a CME. As dilatometers are not capable of performing simultaneous weight- and length measurements, a more straightforward method of manually weighting and measuring length was chosen to determine the hygroscopic shrinkage behaviour.

$$\begin{aligned}\alpha_{T11} &= \frac{\partial \varepsilon_{11}}{\partial T} \\ \beta_{M11} &= \frac{\partial \varepsilon_{11}}{\partial M}\end{aligned}\tag{4.1}$$

The cost-saving benefit of running simulations over carrying out experiments is founded on the ability to simulate a broad range of different conditions and obtain accurate results without the necessity of performing experimental measurements specific to those conditions. It is therefore not desired to be required to measure the moisture concentration of a component for each set of conditions in order to ensure proper input for a simulation to calculate hygroscopic shrinkage. In other words, the material characterisation shall also capture how moisture concentration changes in the composite material over time at the range of temperatures of interest. This behaviour is known as mass diffusion and thermogravimetric analysis, or TGA, was chosen to determine mass diffusion coefficients.

The first objective of the material characterisation involves only thermal- and chemical experiments independent from mechanical properties. Simulation of introduced stresses resulting from thermal expansion and hygroscopic shrinkage do require mechanical properties. For a viscoelastic orthotropic material, the instantaneous mechanical response can be fully described by four engineering parameters. These constants are the longitudinal- and transverse relaxation modulus, the major Poisson's ratio, and the shear relaxation modulus, denoted with  $E_{11}$ ,  $E_{22}$ ,  $\nu_{12}$ , and  $G_{12}$ , respectively. It is noted that all engineering parameters must be considered time- and temperature-dependent to accurately describe viscoelastic behaviour.

Inspection of the recursive formulation of the constitutive equations that are shown at the end of Section 3.6 reveals that the relaxation behaviour of the composite material must be represented through a Prony series. The coefficients of this series represent the stiffness and relaxation times of the individual elements in the generalised Maxwell model. Moreover, the material characterisation shall yield the required William-Landel-Ferry coefficients to model the influence of temperature on the relaxation behaviour. The linearity of the viscoelasticity must also be validated to allow the use of time-temperature superposition without the need for introducing the concept of pseudo-strains. The concept of pseudo-strains was introduced in 1982 by Schapery [69] and was used by Nevière [70] as an extension to the time-temperature superposition for materials which display non-linear viscoelasticity.

Relaxation experiments were carried out to validate that the composite material shows linear viscoelasticity in the strain regime and temperature range of interest. However, it is noted that the most recent version of DIN EN ISO 6721-1 [71] on relaxation tests has been withdrawn. At the moment of carrying out this research, there was no standard available on relaxation tests. This led to concerns regarding the validity and consistency of relaxation tests. Consequently, the characterisation of the relaxation behaviour itself was performed through dynamic mechanical analysis, or DMA.

The region of linear viscoelasticity in addition to the relaxation behaviour can also be determined through DMA. The amplitude of the dynamic displacement of a specimen that is test by means of DMA is gradually increased and the measured modulus is assessed to determine the regime of linear viscoelasticity. It is noted that this experiment is carried out under isothermal conditions and that only one displacement frequency is applied. The modulus of the material' response shall display no variations if the increased amplitude of the dynamic displacement is still within the strain regime of linear viscoelasticity [61]. Instructions by TA Instruments [72] suggest that the linear viscoelastic strain regime extends to the strain at which the measured modulus is within 5% discrepancy in comparison to the modulus that is observed for the initially minimum applied strain.

The required force to carry out tensile mode DMA-measurements in longitudinal direction of the composite specimens was too large for the load measurement device to analyse. An alternative was to carry out DMA-measurements in longitudinal direction in three-point bending mode. However, the desired characterisation of relaxation behaviour is in tensile direction and thus obtained results would need to be transformed from flexural moduli to tensile moduli. Although this transformation is relatively accurate at room temperature, it is not recommended at elevated temperatures. The argumentation behind this statement is based on the different principles of how the tensile- and flexural stiffness are governed.

The tensile stiffness in longitudinal direction is driven by the fibres that are being pulled. The flexural stiffness is also provided by the fibres that must be bent, however, it is necessary for the matrix to stabilise the fibres from buckling on the compressive side of curvature. The longitudinal stiffness is less affected by the elevation of temperature as the matrix plays a minor role in this loading mode. The flexural modulus is, on the other hand, more affected as the compressively loaded fibres are more prone to deformation. For this reason it was decided to carry out tensile mode DMA-measurements in transverse direction to the fibres only.

DMA-measurements provide quantitative information on the stress that would be required to subject the material to a specific strain. Inversely, this information can also be used to calculate the stress that would be the result of a specific strain. However, there is no mode available for DMA-measurements to obtain any quantitative relationship between the strain in one direction and the consequential strain in transverse direction. The major Poisson's ratio describes this transverse deformation behaviour and quasi-static tensile tests have been carried out at various temperatures that span the temperature range of interest of the simulation to determine this parameter.

The quasi-static tensile tests displayed significant experimental scatter in the measured strains and the calculated Poisson's ratios showed unacceptable variation amongst tests of similar conditions. The strain measurement that was carried out with an extensometer was pinpointed as the source of error and digital image correlation was chosen as an alternative testing method. Nevertheless, the instantaneous tensile moduli that were obtained in the quasi-static tensile tests provide a measure of comparison for the constructed tensile moduli through the DMA results.

Table 4.1 provides an overview of the conducted experiments for the material characterisation. The table also includes the standards that have been followed for each experiment to maximise the reliability of the experimental data and to allow for repetition.

Table 4.1 *Overview of the conducted experiments for the material characterisation of the unidirectional composite material.*

Material parameter	Symbol	Type	Experimental determination
Fibre volume fraction	$v_f$	Mechanical	Taken from datasheet
Poisson's ratio	$\nu_{ij}$	Mechanical	Digital image correlation
Instantaneous moduli	$E_{ii}(t_0)$	Mechanical	Quasi-static tensile tests
Relaxation moduli	$E_{ii}(t, T)$	Mechanical	Dynamic mechanical analysis
Coefficient of thermal expansion	$\alpha_T(T)$	Thermal	Dilatometer
Thermal conductivity	$\lambda$	Thermal	Taken from datasheet
Specific heat	$C_p$	Thermal	Taken from datasheet
Coefficient of hygroscopic expansion	$\beta_C$	Chemical	Micrometer experiments
Diffusion coefficients	$D(T)$	Chemical	Thermogravimetric analysis

Not all material properties have been determined experimentally. Mass diffusion simulations in ABAQUS require both heat conductivity and -capacity to be known. Heat conductivity of composite materials is direction-dependent analogous to mechanical properties. In addition to the composite heat transfer parameters, mechanical properties concerning the carbon fibre constituent also are taken from references and serve as input for the micromechanical model. Based on the quasi-static tensile tests, the carbon fibre of the composite material was classified as a high tenacity fibre. Hence, mechanical properties of general high tenacity fibres have been taken from [73]. The same source also reports that the mechanical properties of the fibre remain constant up to a temperature of 400 °C. Lastly, the density of the composite material is also taken from the datasheet from the material supplier. All material properties that have not been determined through material characterisation experiments are shown in Table 4.2.

Table 4.2 *Material parameters that have been taken from the datasheet.*

Material parameter	Symbol	Value	Unit
Density	$\rho$	1,447	$kg/m^3$
Longitudinal heat conductivity	$\lambda_{11}$	5.52	$W/m \cdot K$
Longitudinal heat capacity	$C_{p11}$	1,280	$J/kg/K$
Longitudinal heat conductivity	$\lambda_{22}$	0.85	$W/m \cdot K$
Transverse heat capacity	$C_{p22}$	1,310	$J/kg/K$
Fibre volume fraction	$v_f$	0.48	—
Fibre longitudinal elastic modulus	$E_{11f}$	2.30	$GPa$
Fibre transverse elastic modulus	$E_{22f}$	0.28	$GPa$
Fibre shear modulus	$G_{12f}$	0.27	$GPa$
Fibre major in-plane Poisson's ratio	$\nu_{12f}$	0.256	—

## 4.2 Thermogravimetric analysis

The analysis of moisture transport through the composite material requires the mass diffusion coefficients to be known. These coefficients have been determined through TGA. The main objective of this research is to analyse the viscoelastic behaviour of the composite material at elevated temperatures. Hence, the most important analysis concerning moisture transport is the diffusion of moisture from the specimen to the ambient air. Therefore, specimens that had been fully saturated with moisture were examined.

The preparation of the specimens was done in accordance with standard DIN EN ISO 11358-1 [74]. The conditioning of the specimens is described in this standard to be carried out according to ISO 291. However, ISO 291 only governs standard atmospheres for plastics. The aim of conditioning the specimens is to reach a moisture content that is fully saturated. The conditioning of the specimens has been carried out according to DIN EN ISO 1110 to reduce the necessary time for conditioning that would otherwise be required to reach a saturated moisture content in a standardised atmosphere. In agreement to DIN EN ISO 1110, the specimens were conditioned in an environmental chamber at a temperature of 70 °C and a relative air humidity of 62%.

The TGA-measurements were carried out at temperatures of 80 °C, 120 °C, 150 °C, and 200 °C to ensure a proper spread of experimental values across the temperature range of interest. The duration of a TGA-measurement is dependent on the temperature at which the experiment is carried out. The reason is that a specimen must be measured at a constant elevated temperature until all moisture has diffused to be able to calculate a mass diffusion coefficient. Hence, the longest TGA-measurement took place at 80 °C and had a duration of 16 hours. The cutting edges of the specimens were sealed to minimise geometrical effects and to increase the validity of the assumption of one-dimensional diffusion.

To be able to calculate the mass diffusion coefficients, the weight loss over time must be calculated. The weight loss over time is defined to be equal to zero at the start of the measurement as the specimen is fully saturated. At the end of the measurement, the weight loss is defined to be equal to one as all moisture diffused from the specimen into the ambient air. A mathematical expression for the weight loss over time, denoted with  $W(t)$  is shown in Eq. 4.2. In this expression,  $W_0$  and  $W_\infty$  represent the weight values of the specimen at the beginning and end of the experiment, respectively.

$$G(t) = \frac{W(t) - W_0}{W_\infty - W_0} \quad 4.2$$

The one-dimensional mass diffusion coefficient can be used as a fitting parameter for Eq. 4.3. The terms  $l$  and  $N$  denote the length of diffusion possibility and the amount of terms included numerically for the summation, respectively. As the one-dimensional diffusion problem of the specimen is symmetric with respect to the thickness, the length of diffusion possibility is equal to half of the thickness of the specimen. The number of terms that have been numerically included in calculation of the diffusion coefficients is 11. With this method, a mass diffusion coefficient is obtained for each experiment.

$$G \approx 1 - \frac{8}{\pi^2} \sum_{k=0}^N \frac{1}{(2k+1)^2} \cdot e^{-(2k+1)^2 \pi^2 D \cdot t \cdot l^{-2}} \quad 4.3$$

A plot of the weight loss factors as a function of time for the experiments at different temperatures are shown in Figure 4.1. The respective mass diffusion coefficients that led to a least-squares optimised fit have also been included as well as the coefficient of determination for the obtained fit. The obtained mass diffusion coefficients are also shown in Table 4.3 for ease of reading. It must be stated that the obtained fits for the experiments of 120 °C, 150 °C, and 200 °C display a mass diffusion at a slightly higher rate than is actually measured.

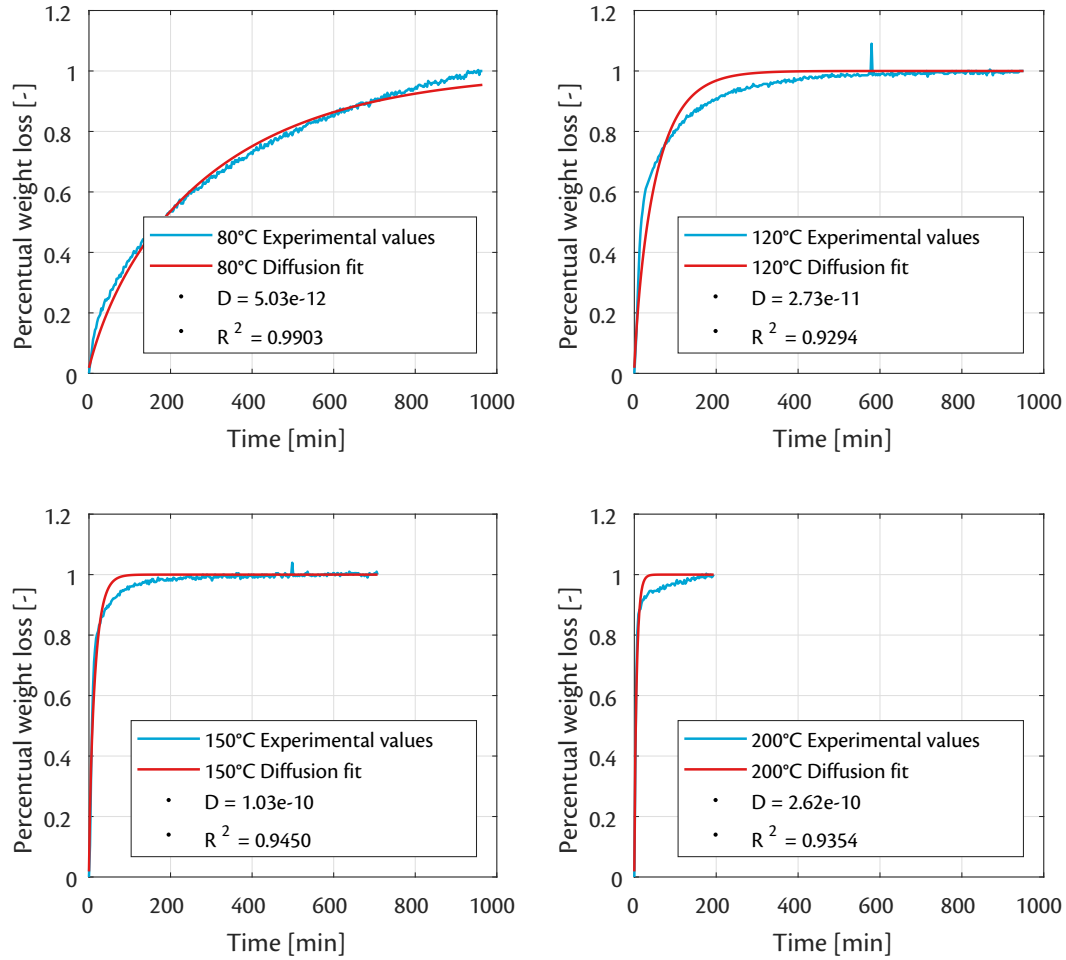


Figure 4.1 *Diffusion coefficients obtained for the composite material.*

It is required to have knowledge about the mass diffusion coefficient over the entire temperature range of interest as opposed to only four discrete points. The Arrhenius equation is used to this extent and the four obtained mass diffusion coefficients serve as points through which this equation shall be fitted. The Arrhenius equation is displayed in Eq. 4.4 and comprises two fitting parameters [75]. The fitting parameters are known as the frequency factor and the activation energy, indicated with  $D_0$  and  $E_A$  in Eq. 4.4, respectively. The resulting fit of the Arrhenius equation is shown in Figure 4.2 and the fitting parameters are shown in Table 4.4 for a clear overview throughout the thesis.

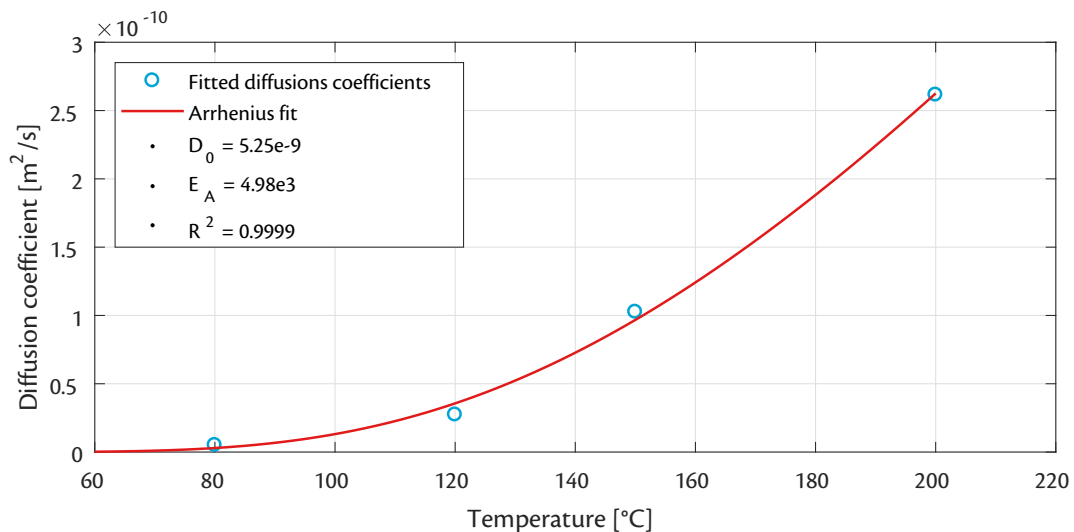
$$D = D_0 \cdot e^{\frac{E_A}{RT}} \quad 4.4$$

Table 4.3 *Diffusion coefficients at different temperatures.*

Temperature [ $^{\circ}\text{C}$ ]	Diffusion coefficient [ $\text{m}^2/\text{s}$ ]
80	$5.03e-12$
120	$2.73e-11$
150	$1.03e-10$
200	$2.62e-10$

Table 4.4 *Arrhenius fit parameters.*

Fit parameter	Symbol	Value	Unit
Frequency factor	$D_0$	$5.25e-9$	$\text{m}^2/\text{s}$
Activation energy	$E_A$	$4.98e3$	$\text{J/mol}$

Figure 4.2 *Arrhenius curve describing the development of the diffusion coefficient as a function of temperature.*

### 4.3 Dilatometer experiments

The thermal expansion of the composite material must be characterised to properly simulate the changes in size of the specimen when subjected to thermal loading. The Netzsch DIL 402 C dilatometer was used to measure the strain of unidirectional laminates in both longitudinal- and transverse fibre orientation. Measuring unidirectional laminates has the advantage of minimising interlaminar shear stresses from introducing errors in the strain measurement. Moreover, the numerical model is more versatile if it can accurately predict the thermal expansion of arbitrary lay-ups with only the input of thermal expansion of unidirectional layers. This also eliminates the need to perform lay-up specific experiments that would else be necessary to utilise the numerical model.

The thermal program of the dilatometer was chosen to represent the thermal envelope to which the components are subjected in the automotive painting ovens. However, the heating- and cooling rates were set to a fixed magnitude of  $2\text{ }^{\circ}\text{C}$  per minute to exclude any variations that might be influenced by different temperature rates. The Netzsch dilatometer detects elongations with a resolution of  $0.625\text{ nm}$  and the specimens had a size of  $100 \times 8 \times 2\text{ mm}^3$ . Two heat cycles were measured to evaluate the presence of eventual polymeric processes that introduce plastic strains.

The specimens were tested in both dry- and fully moisture saturated states. The conditioning of the specimens to a fully moisture saturated state was carried out with exactly the same method as was done for the TGA-measurement specimens. Drying the specimens was carried out by placing the specimens in an oven at  $80\text{ }^{\circ}\text{C}$ . The specimens are conditioned at a temperature that is  $13\text{ }^{\circ}$  higher than the glass transition temperature  $67\text{ }^{\circ}\text{C}$  and it is noted that recrystallisation is most likely present during the conditioning. However, the rate of recrystallisation is assumed to be of negligible influence because of the relatively small excess of the glass transition temperature. The specimens were considered to be fully dry in accordance with the weight measurement method described in DIN EN ISO 1110 [76]; the variation of weight must be smaller than 0.1% between three consecutive weight measurements, where each measurement must be separated in time by at least one full day.

The mentioned temperature profile and the strain results of the dry- and moisture saturated specimens that are cut transversely to the fibres are shown in Figure 4.3. Qualitatively it can be concluded from Figure 4.3 that moisture egress out of the composite material has shrinkage as a consequence. It can additionally be stated that polymeric reactions are visible in the strain development that presents itself during the temperature-hold period of both heat cycles. Additionally, post-shrinkage is evident as the strain value at the end of the first cooling phase differs with the initial strain. The post-shrinkage is accounted for by determining separate coefficients of thermal expansion for heating and cooling. Strain variation at the temperature-hold period are not implemented in the simulation.

A description of the polymeric effects is provided next. The degree of crystallinity of a semi-crystalline polymer has an influence on the polymer's density. The crystalline parts of a semi-crystalline polymer exist of oriented molecular chains and display a higher density than the amorphous parts. The density of polyamide 6 in a crystalline structure is reported in the book on polymer materials by Ehrenstein to be  $1,2400\text{ kg/m}^3$  [18]. The amorphous part of polyamide 6 is stated in the same book to have a density of  $1,080\text{ kg/m}^3$  and the semi-crystalline combination that has a usual degree of crystallinity in the range of 35% to 45% measures a density of  $1,140\text{ kg/m}^3$ .

The glass transition temperature of the composite material in completely dry state is  $67\text{ }^{\circ}\text{C}$  according to the DSC results. Thus, heating the specimens to a temperature of  $180\text{ }^{\circ}\text{C}$  in the dilatometer experiments increases the degree of crystallinity of the polyamide 6 matrix material as explained in Section 2.2. The density of the matrix constituent increases as a result and a reduction in matrix volume is observed. This is the explanation of the reduction in strain that is observed at the two temperature-hold periods visible in Figure 4.3. The negative strain at the end of the dilatometer experiment is a consequence of the increase in density because of the higher degree of crystallinity and is referred to as post-shrinkage [77]. The relatively slow cooling rate also contributes to the clearly noticeable post-shrinkage.



Additionally and specifically to polyamide 6, heating the polymer results in a transition of one crystalline form to another. It is reported that polyamide 6 has been identified to show at least two crystalline forms named the  $\alpha$ - and  $\gamma$ -form [78]. The density of the  $\alpha$ - and  $\gamma$ -form have been determined to be typically  $1,230\text{kg/m}^3$  and  $1,170\text{kg/m}^3$  [79], respectively. The  $\gamma$ -form was determined to be the preferred initial form for the crystalline structure of the investigated polyamide 6 fibres [78]. An annealing treatment was documented to display the conversion of crystals with an  $\gamma$ -form to an  $\alpha$ -form. This conversion is also expected to be present in the dilatometer experiments and confirms the decrease in strain during the temperature-hold periods and the negative strain at the end of the measurement.

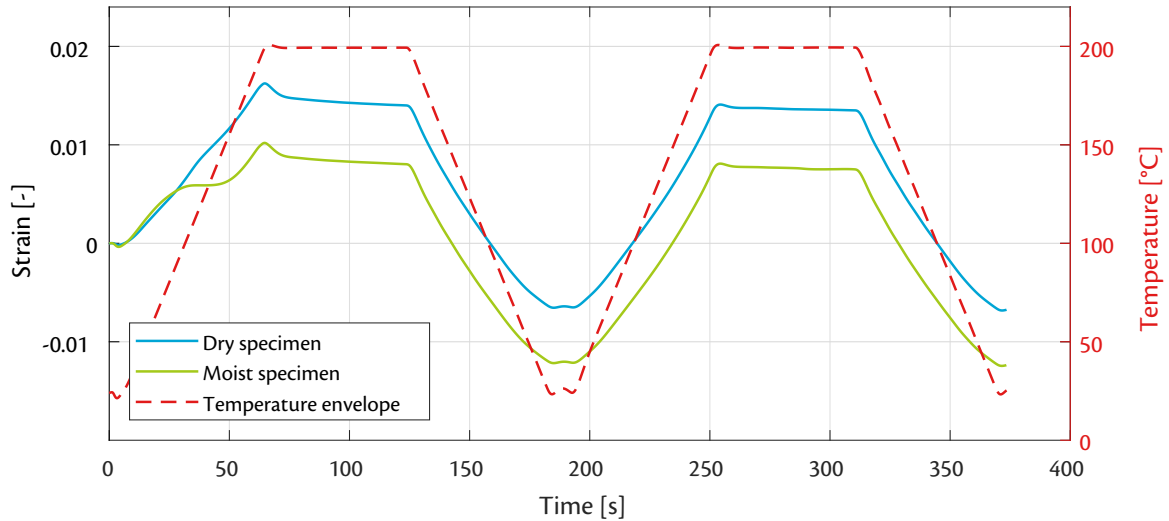


Figure 4.3 *Temperature profile and resulting strain values for the dry- and moist specimens in transverse direction in the dilatometer experiment.*

The coefficients of thermal expansion have been determined by using Eq. 4.5. It is noted that this procedure yields tangential coefficients of thermal expansion. The advantage of tangential coefficients is that they can be used regardless of reference- or initial temperature. However, ABAQUS requires the input of coefficients of thermal expansion to be in secant notation [68]. A possibility to use tangential coefficients would be through the use of a user subroutine, but this option was discarded because of the significant effort involved.

$$\alpha_{Tii} = \frac{d\varepsilon_{ii}}{dT} \quad 4.5$$

The calculation of secant coefficients of thermal expansion from the tangential coefficients has been performed with Eq. 4.6. The tangential coefficients of thermal expansion are first integrated from the initial temperature to the temperature at the moment of interest. The obtained strain is then divided by the difference between the temperature at the moment of interest and the reference temperature to obtain the secant coefficient of thermal expansion. The overline that is present in Eq. 4.6 is used to denote that the coefficient of thermal expansion is of secant type.

$$\bar{\alpha}_{Tii}(T) = \frac{\int_{T_{ref}}^T \alpha_{Tii} dT}{T - T_{ref}} \quad 4.6$$

The results of the calculation of the tangential coefficients of thermal expansion for the two heat cycles of the 90° dry specimen are shown in Figure 4.4. The polymeric changes are well visible by the different values that are present for the first heating and -cooling segments. It is noted that the difference between the first cooling, the second heating, and the second cooling is found to be negligible. Hence, only the tangential coefficients of thermal expansion for the first heating and -cooling have been taken into account for subsequent computations.

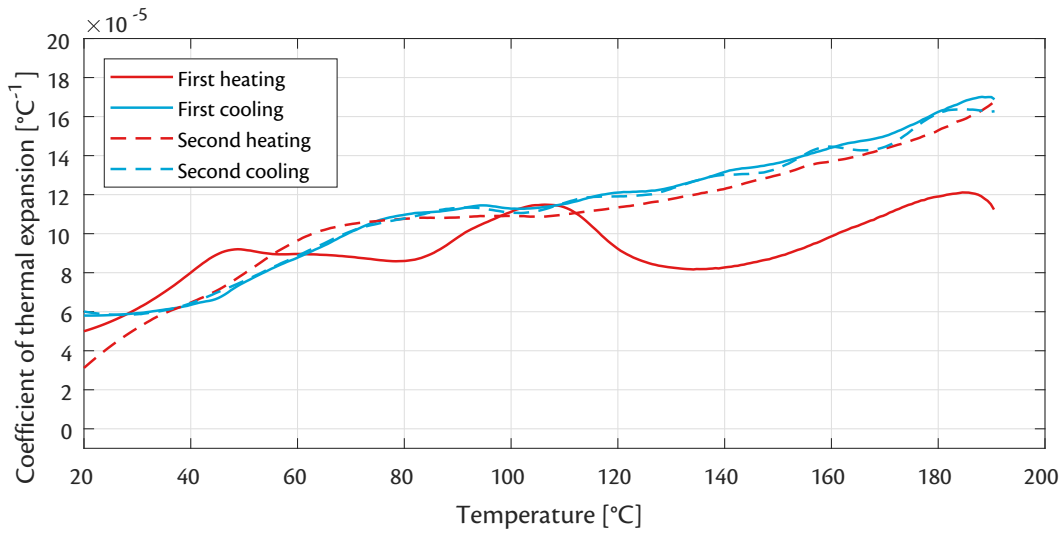


Figure 4.4 *Calculated tangential coefficients of thermal expansion of the dry composite material in transverse direction for two heat cycles.*

The initial strategy of the material characterisation was to utilise the difference between the coefficient of thermal expansion of the dry- and moisture saturated specimens to determine the coefficients of moisture expansion. The tangential coefficients of thermal expansion for the first heat cycle of the 90° dry- and moisture saturated specimens are shown in Figure 4.5. The determination of the coefficients of moisture expansion by utilising the difference in measured expansion of the dry- and moisture saturated specimens resulted in a quadratic relationship between moisture concentration and elongation. However, a linear relationship between moisture concentration and elongation is expected as an increment of moisture content can not have a different influence depending on the moisture content that is already present in the material.

In other words, an increase in moisture concentration must have the same resulting expansion regardless of the current moisture concentration. Hence, the obtained quadratic relationship between moisture concentration and elongation was discarded and micrometer- and weight measurements have been carried out to identify the coefficients of moisture expansion instead. The results and conclusions of these measurements are documented in Section 4.4. The failure of the initial strategy to determine the hygroscopic coefficients of expansion was concluded to be due to polymeric changes having different influences on the measurement of the dry- and moisture saturated specimens.

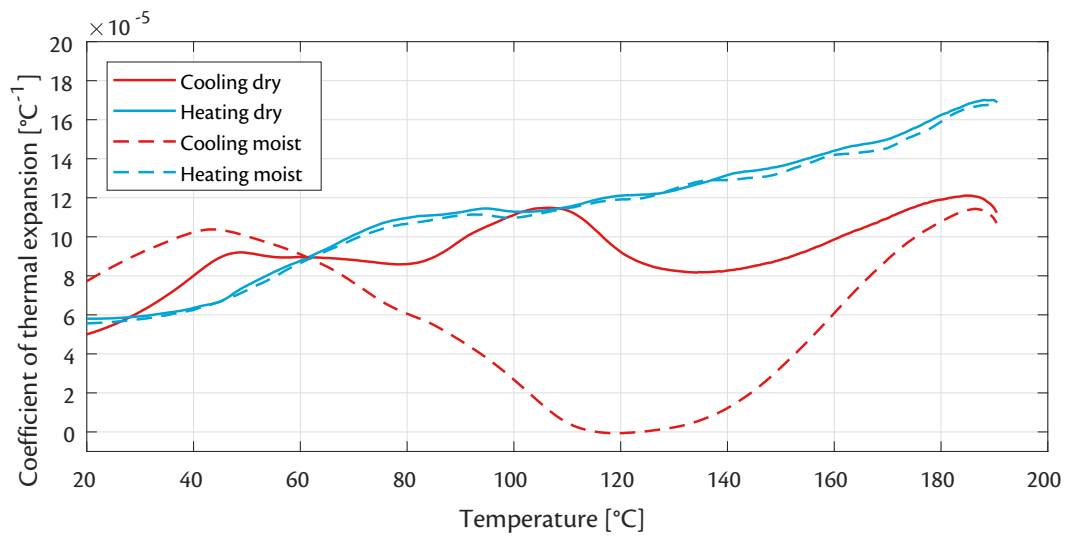


Figure 4.5 Comparison between the tangential coefficients of thermal expansion between the dry- and moisture saturated composite material in transverse direction for the first heat cycle.

The resulting strain of the specimens with the fibre orientation in longitudinal direction of the specimen in both dry- and moisture saturated state of conditioning is depicted in Figure 4.6. It is noted that the chosen temperature envelope for these measurements is equal to the temperature envelope that was used for the specimens with transverse fibre orientation shown in Figure 4.3. It can be concluded from Figure 4.6 that both the dry- and moisture saturated specimen initially show a positive coefficient of expansion.

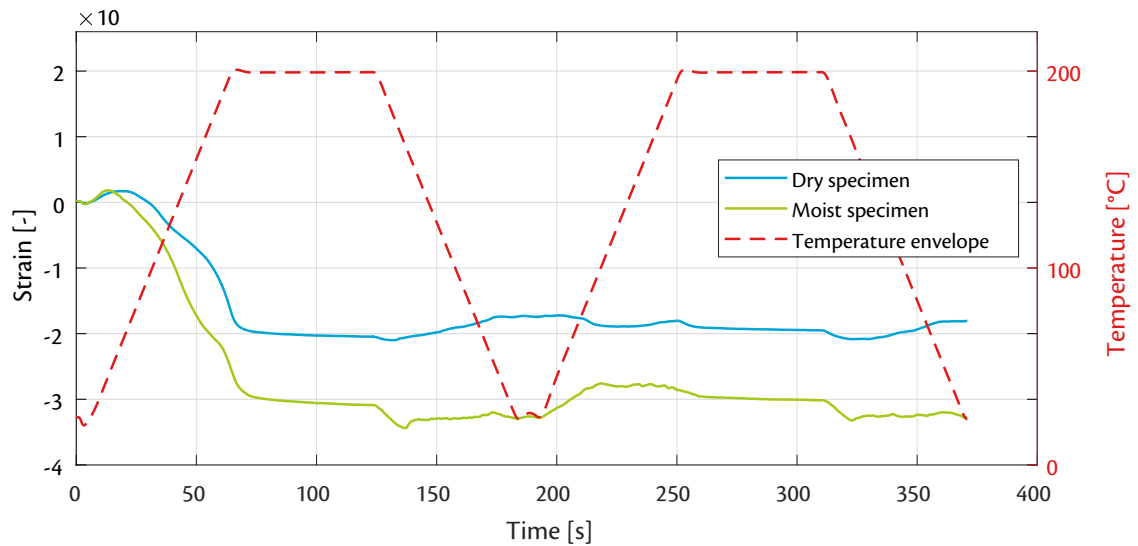


Figure 4.6 Temperature profile and resulting strain values for the dry- and moist specimens in longitudinal direction in the dilatometer experiment.

The specimens then continuously decrease in length from roughly 50 °C to the maximum temperature of the dilatometer test of 200 °C. It is striking that the polymer-chemical effects that are visible in Figure 4.3 are not present in longitudinal direction as the strain values remain approximately constant after reaching the maximum temperature of the first heating segment in Figure 4.6.

The conclusion that the thermal expansion of the unidirectional laminate in longitudinal direction remains approximately constant after the first heating segment is visible in the plots of the coefficients of thermal expansion shown in Figure 4.7 for a dry state of conditioning. It is assumed that the differences in thermal expansion coefficients for the first cooling, second heating, and second cooling can be neglected. The two sets of coefficients for the second heating- and -cooling segments are therefore discarded for the simulation. It is noted that this is analogous to the conclusions drawn from Figure 4.4 and implies that a total of four sets of coefficients of thermal expansion are used as input for the numerical model.

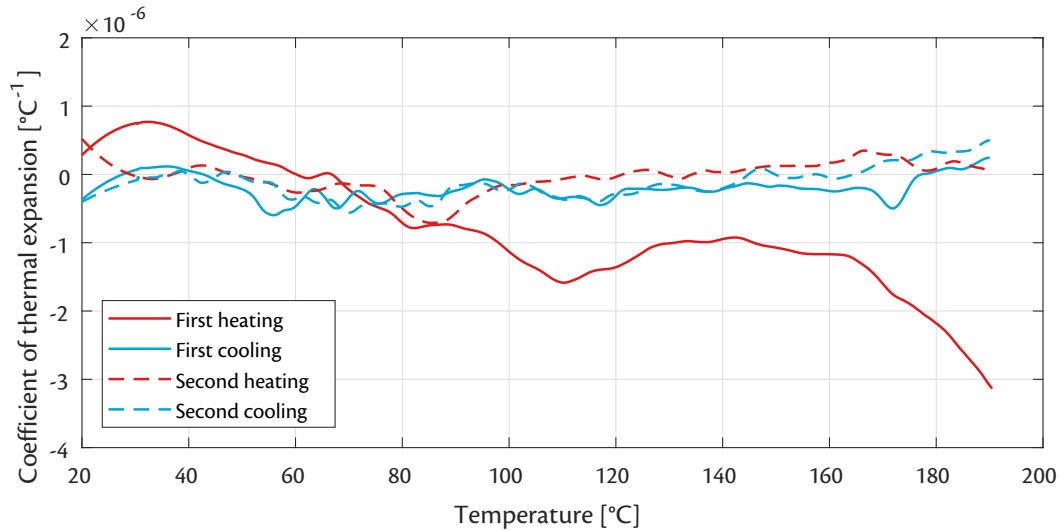


Figure 4.7 *Calculated tangential coefficients of thermal expansion of the dry composite material in longitudinal direction for two heat cycles.*

#### 4.4 Micrometer measurements

The approach of utilising the dilatometer experiment data of both the dry- and moisture saturated specimens to determine the coefficients of moisture expansion did not provide satisfactory results. The determined hygroscopic expansion as a function of moisture content was a parabola and was discarded as a straight line must be obtained based on the physical argumentation provided in Section 4.3. Micrometer measurements have been carried out in combination with consecutive weighing of mass to determine the coefficients of hygroscopic expansion. It is noted that three specimens have been measured in length that were cut both parallel- and perpendicular to the fibre orientation. The specimens with dimensions of  $100 \times 8 \times 2 \text{ mm}^3$  were first conditioned to a dry state in agreement with DIN EN ISO 1110 [76].

Control measurements were then carried out of the specimens to obtain a reference value for the length and weight. The specimens were then placed in an environmental chamber at  $70^\circ\text{C}$  with 62% relative air humidity to allow moisture uptake. The frequency between the weight- and length measurements was chosen to account for the declining rate of moisture uptake that was identified in the thermogravimetric measurements discussed in Section 4.2. This implied that two measurements were taken on the first day after which the interval was changed to once per day until moisture saturation inside the specimen was observed.

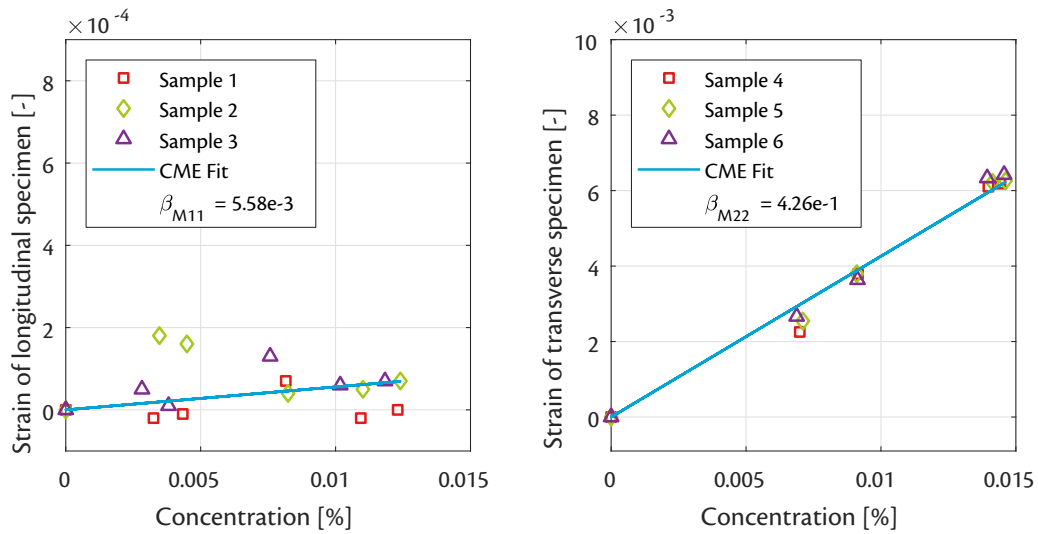


Figure 4.8 Micrometer measurements for the determination of the coefficients of moisture expansion.

The length measurements were carried out with an Atorn Keeptronic with a resolution of  $0.01 \text{ mm}$  and the weighing of the specimens was performed on a VWR LA Series with a resolution of  $0.1 \text{ mg}$ . The coefficient of moisture expansion can be determined from the length- and weight measurements with the expression shown in Eq. 4.7. The term  $C$  in Eq. 4.7 denotes the concentration of moisture in the specimen and represents the weight percentage of moisture as a fraction of the complete specimen. The expression on the right hand side of Eq. 4.7 displays the governing formula to calculate the concentration.

$$\beta_{Mii} = \frac{d\varepsilon_{ii}}{dM} \quad \text{with } M(t) = \frac{W(t) - W_0}{W(t)} \quad 4.7$$

The results of the micrometer experiments are shown in Figure 4.8. A linear relation between the concentration and the strain of the specimens that were oriented perpendicular to the fibres is clearly visible on the right hand side of Figure 4.8. It has therefore been decided to also fit the micrometer data with a first order polynomial that passes through the origin. The slope of the fit line represents the coefficient of moisture expansion and its values are also provided in Table 4.5 to provide a clear overview.

The data of the specimens that were cut parallel to the fibres shows significant experimental scatter. A linear line that passes through the origin has been fitted in an analogous manner. The relatively large amount of experimental scatter visible in the left hand side of Figure 4.8 provides an argument to question the accuracy of the coefficients of moisture expansion in longitudinal direction. This uncertainty was noted during the research and its influence on the accuracy of the numerical model is commented on in the experimental validation described in Section 7.2.

Table 4.5 Lamina coefficients of hygroscopic expansion.

Fibre orientation	$\beta_M[-]$
$0^\circ$	$5.58e-3$
$90^\circ$	$4.26e-1$

## 4.5 Quasi-static tensile tests

Obtaining the major Poisson's ratio of the unidirectional composite lamina was initially aimed to be performed with quasi-static tensile tests. The method that was applied to determine the major Poisson's ratio implied measuring both the longitudinal- and transverse strain of the specimen under unidirectional tensile loading. These tensile tests have been carried out on a Zwick/Roell Z250 universal testing machine with temperature chamber at a strain rate of  $2 \text{ mm/min}$  to eliminate dynamic effects. The specimens had been provided with strain gauges as optical measurements were not possible in combination with the temperature chamber.

The dimensions of the specimens with transverse fibre orientation were chosen in agreement with DIN EN ISO 527-4 [80] and the specimens were cut to a size of  $250 \times 25 \times 2 \text{ mm}^3$  by means of waterjet cutting to prevent any thermal influences to be present concerning the thermoplastic matrix material. The dimensions of the specimens with longitudinal fibre orientation were  $250 \times 15 \times 1 \text{ mm}^3$  in agreement with DIN EN ISO 527-5 [81]. The force introduction into the tensile test specimens was realised with the application of grip tabs to increase an even stress distribution in the test specimen. A total of 5 tests have been performed for both the low- and high temperature for testing the specimens in longitudinal- and transverse direction. It is noted that all specimens were dried according to DIN EN ISO 1110 [76] before testing.

The upper stress-strain curves shown in Figure 4.9 are the results of the unidirectional specimens with a longitudinal fibre orientation that were tested at room temperature. The average values of the instantaneous stiffness are displayed in Table 4.6 as well as the variance that was observed. The results for the quasi-static tests that were performed at elevated temperatures with the longitudinally oriented fibre direction are shown in the bottom part of Figure 4.9.

The results of the quasi-static tensile tests in transverse direction carried out at  $23^\circ\text{C}$  and  $180^\circ\text{C}$  are shown in Figure 4.10. The larger strain and smaller stresses visible in the lower part of Figure 4.10 in comparison to the upper part is to be expected due to softening of the matrix as a result of the increased temperature. It is concluded that the linear strain regimes in transverse direction of the unidirectional laminate extend up to strains of 0.004 and 0.008, respectively.

The magnitude of the ultimate strains that are visible in Figure 4.10 for the unidirectional specimens that were cut in transverse direction are lower than the ultimate strains for the specimens that have fibres in longitudinal direction of the testing direction as shown in Figure 4.9. It would be expected at first glance that a matrix-dominated tensile test yields higher ultimate strains because of the larger ultimate strain of the matrix constituent in comparison to the individual fibres. Nevertheless, the fibres running parallel to the direction of the tensile force provide a discontinuity in the matrix and decrease the effective area that is capable to be loaded. The ultimate stress of the transverse unidirectional laminate is lower in comparison to the pure matrix because of these imperfections [82].

The instantaneous moduli of the specimens with transverse fibre orientation that were found through the quasi-static tensile tests have been used as reference to check the plausibility of the transverse stiffness values that were found through the DMA measurements shown in Figure 4.21 in Section 4.8. Additionally, the measured longitudinal stiffness of the unidirectional laminate has been used to validate the application of the classical rules-of-mixtures for the calculation of the laminate longitudinal stiffness with the reference value of the fibre stiffness and the determined matrix stiffness by DMA.

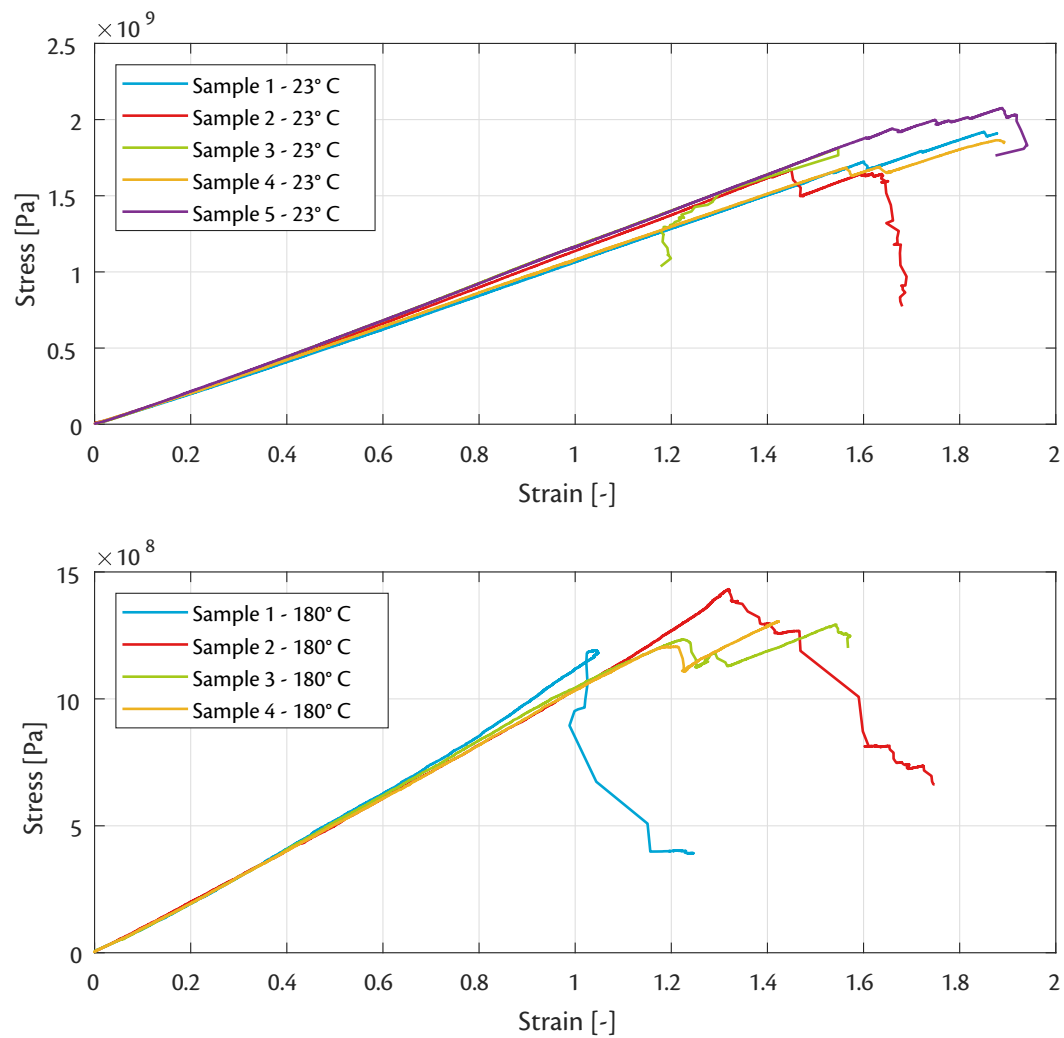


Figure 4.9 Stress-strain curves of the dry composite material in longitudinal direction at 23 °C and 180 °C, shown in the upper and lower part, respectively.

Table 4.6 Instantaneous moduli of CF60-PA6 at room temperature.

Fibre orientation	Temperature [°C]	Modulus [GPa]	Standard deviation [GPa]
0°	23	106.782	4.575
0°	180	98.489	1.163
90°	23	0.429	0.140
90°	180	0.082	0.034

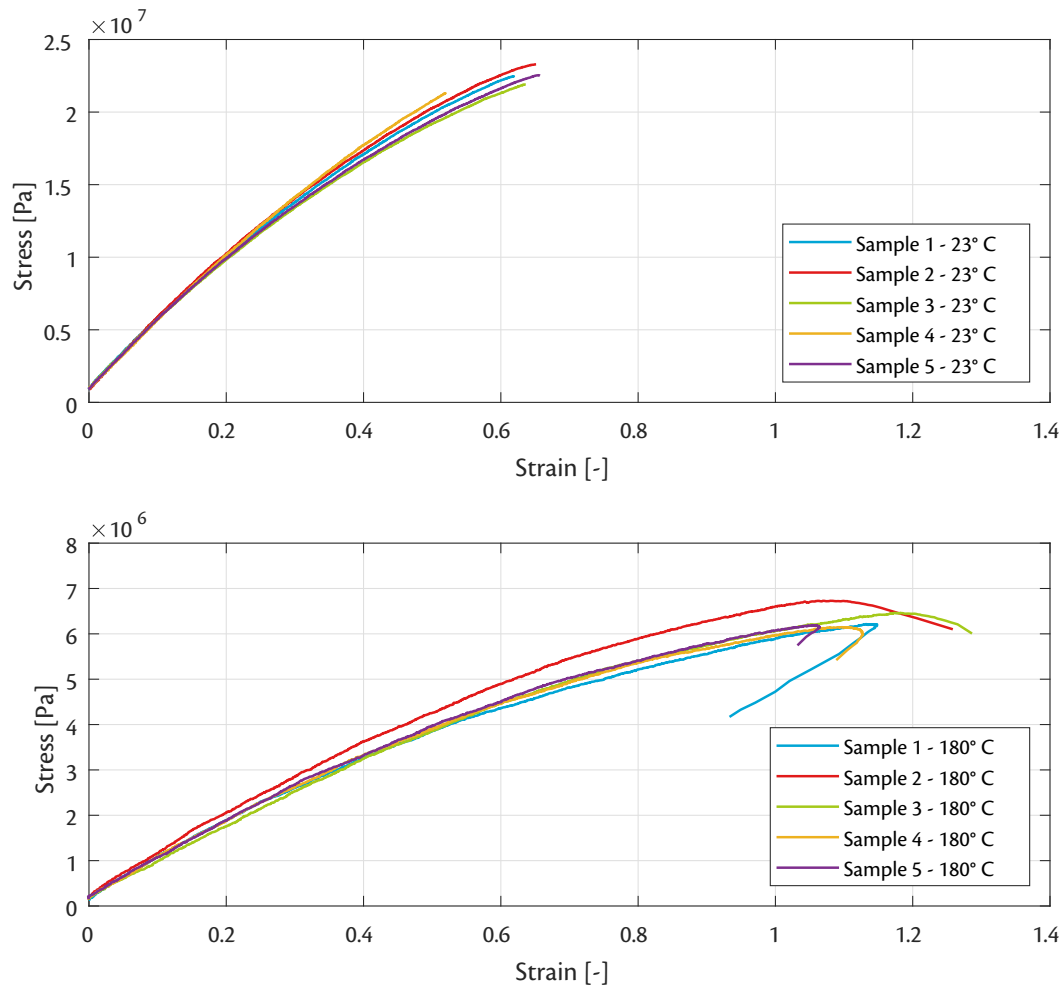


Figure 4.10 Stress-strain curves of the dry composite material in transverse direction at 23 °C and 180 °C, shown in the upper and lower part, respectively.

The major Poisson's values for the unidirectional laminate that had been calculated with the strain values measured from the strain gauges showed a scatter from a minimum of 0.23 to a maximum of 0.46. An average value that is found through this amount of scatter was evaluated to be unacceptable as material input for the numerical simulation. The digital image correlation experiments that are discussed in Section 4.6 have been carried out to obtain a more reliable value for the major Poisson's ratio.



## 4.6 Digital image correlation

The major Poisson's ratio measured during the quasi-static tensile tests showed unacceptable scatter as discussed in Section 4.5. Hence, DIC experiments have been carried out in an attempt to obtain values that have less variance. Specimens have only been tested in longitudinal direction as micromechanical rules-of-mixtures allow the minor Poisson's ratio to be determined when the longitudinal- and transverse stiffness values are known.

Like the major Poisson's ratio, the minor Poisson's ratio will be a function of temperature. A relationship between the temperature-dependent transverse stiffness and the major Poisson's ratio has been found in literature and is explained in further detail in Section 4.9. The temperature-dependent minor Poisson's ratio will be calculated with the temperature-dependent major Poisson's ratio and transverse stiffness, rendering experimental determination unusable.

The measurement of the Poisson's ratio has been performed at room temperature with the use of the ARAMIS measurement system developed by GOM. A speckled pattern had to be applied to the unidirectional specimen to enable the ARAMIS system to track parts of the specimen under deformation. A base layer of white spray paint is first applied to fully cover the specimen and allowed to dry for 30 minutes. Black speckles were applied afterwards by spraying black spray paint over the specimen as opposed to directly on the specimen.

The sensor that was used is the 'Deformation 2.3M' sensor with a measuring volume of  $140 \times 95 \times 90 \text{ mm}^3$  in length-, width-, and depth direction, respectively. The calibrated camera angle was  $25.492^\circ$  and the calibration was performed at a temperature of  $23.0^\circ\text{C}$ . Processing of the results was carried out with the ARAMIS Professional 2017 software. Two strain regimes were used to calculate the major Poisson's ratio of the unidirectional lamina.

Values of 0.004 and 0.005 were chosen as the reference strains for the computation of the major Poisson's ratio in agreement with DIN EN ISO 527-4 [80] that stipulates a strain value higher than 0.003. The calculation of the major Poisson's ratio was carried with the use of Eq. 4.8. The major Poisson's ratio calculated for each specimen at 0.004 and 0.005 strain have been averaged and these values were taken for each specimen. The value of the major Poisson's ratio at room temperature for an arbitrary lamina was then computed by averaging the values for all specimens and is displayed in Table 4.7.

$$\nu_{12} = -\frac{\varepsilon_{22}}{\varepsilon_{11}} \quad 4.8$$

Table 4.7 *Major Poisson's ratio at room temperature of unidirectional CF60-PA6.*

Poisson's ratio	Value [–]	Standard deviation[–]
$\nu_{12}$	0.400	0.024

It is noted that the major Poisson's ratio has only been determined at room temperature. The value of the major Poisson's ratio is expected to increase at elevated temperatures as the transverse stiffness is reduced. This effect has been taken into account in the micromechanical model that was used to calculate the engineering parameters of multi-directional laminates from the properties of the tested unidirectional laminates. See Eq. 4.16 for the expression that evaluates the major Poisson's ratio as a temperature dependent parameter.

## 4.7 Relaxation experiments

It is required for the composite material to be linearly viscoelastic to be able to apply the recursive formulation of the constitutive equations that are shown in Section 3.6. Relaxation experiments have been carried out on a Zwick/Roell Z250 at both extreme temperatures of the temperature range that is of interest for the simulation;  $23^{\circ}\text{C}$  and  $180^{\circ}\text{C}$ . The principle of a relaxation test is to apply a constant strain to the specimen and measure the required force to maintain this strain as a function of time. The internal stress of the specimen can then be calculated with the use of the cross-sectional dimensions of the specimen.

Testing of the specimens was carried out in agreement with DIN EN ISO 899-1 [83] for creep experiments as the latest version of the standard for relaxation tests had been withdrawn at the time of conducting the research. The specimen dimensions are stipulated in the standard to be equal to the tensile testing equivalent mentioned in DIN EN ISO 527-2 [84]. Hence, specimen dimensions were chosen to be  $250 \times 15 \times 1 \text{ mm}^3$  and  $250 \times 25 \times 2 \text{ mm}^3$  for the tests carried out in longitudinal- and transverse fibre direction, respectively.

It is common for thermoplastics to show linear viscoelasticity up to a certain strain magnitude, after which the viscoelasticity becomes non-linear [85], see the isochrones displayed in Figure 3.2 that have been taken from Campusplastics [50] as argument for this statement. A deviation from linearity of an isochrone indicates the beginning of the non-linear strain regime. Hence, the linearity of viscoelasticity must be validated for various strain magnitudes to identify an envelope of linear viscoelasticity. Moreover, linear viscoelasticity can only be expected in the linear stress-strain regime visible for the instantaneous response of the material. Hence, the strain magnitudes chosen for the relaxation experiments are in agreement with the results of the quasi-static tensile tests that are described in Section 4.5.

The specimen preparation was carried out with an analogous method to the quasi-static tensile testing; specimens were cut with water jet cutting, glass-fibre reinforced epoxy grip tabs were applied and the specimens were conditioned according to DIN EN ISO 1110 [76]. The load sensor indicated that forces were introduced into the specimens after instalment into the grips. It is unlikely that the force introduction originates from a difference in temperature between the testing clamps and the specimens as the specimens were put in the temperature chamber prior to instalment to attain the testing temperature. Hence, it is concluded that the force introduction is the result of a mismatch between heat conductivity and -capacity.

Validating the linearity of viscoelasticity was performed with two distinct methods. The first method is through normalisation of the relaxation curves. A test with a material that displays a linear viscoelastic character must yield equal normalised relaxation curves for different strain magnitudes. The second method is through testing whether the Boltzmann superposition principle holds. This was performed by reconstructing the stress response of a two-step strain input with the use of a single stress response to a one-step strain input.

The results of the normalisation method are shown in Figure 4.11 and Figure 4.12 for testing conditions of  $23^{\circ}\text{C}$  and  $180^{\circ}\text{C}$ , respectively. A maximum allowed discrepancy of 5% was chosen for the stress magnitude at the end of the test to still conclude that the material shows linear viscoelasticity. The results for the normalisation tests carried out at  $180^{\circ}\text{C}$  have been fitted to eliminate the disturbing effect of the oscillations that are present due to polymer-related hysteresis. It can be concluded that all stress responses are within 5% discrepancy and thus a linear viscoelastic character is considered to be validated within the region of investigated strain magnitudes.

These findings are in agreement with the results published in an article from Starkova [85] about the limits of linear viscoelastic behaviour of polymers. This work displays isochrones concerning one and three hours into the experiment of the creep compliance of polyamide-6 at room conditions. The viscoelastic behaviour can be considered to be linear up to a stress magnitude of 20 MPa, after which the isochrones clearly display non-linear viscoelasticity.

Ropers reported the observation of non-linear viscoelastic deformation behaviour of continuous glass-fibre reinforced polyamide-6 from rheometer measurements. On the other hand, only linear viscoelasticity was observed in the DMA measurements because of the limitation in strain imposed by the machine [86], indicating the existence of a linear viscoelastic regime. Soós reports on ensuring that the stress values of DMA measurements concerning injection moulded polyamide-6 reinforced with short glass fibres are inside the linear viscoelastic range [87], which also implies partial linear viscoelasticity.

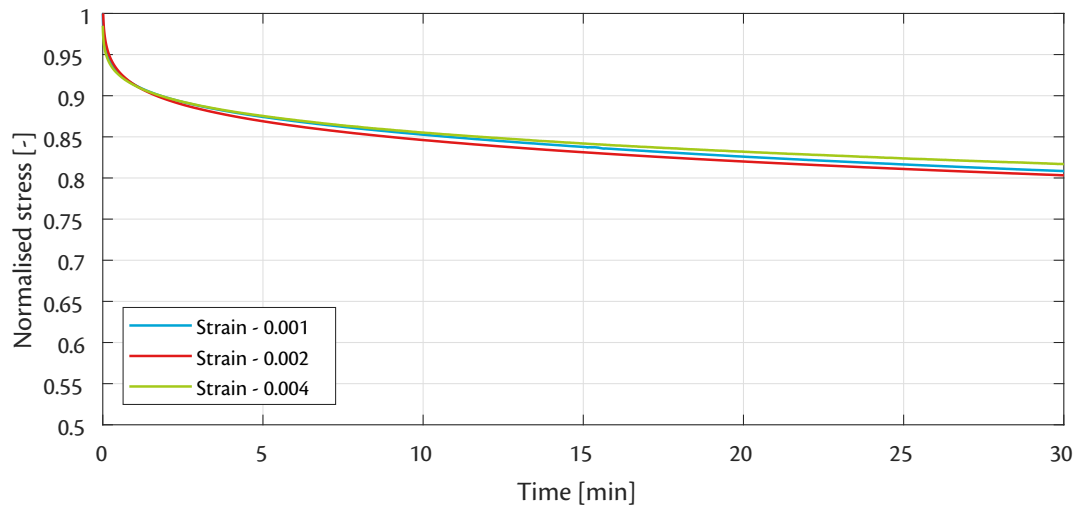


Figure 4.11 *Normalised relaxation curves of the dry composite material in transverse direction at 23 °C.*

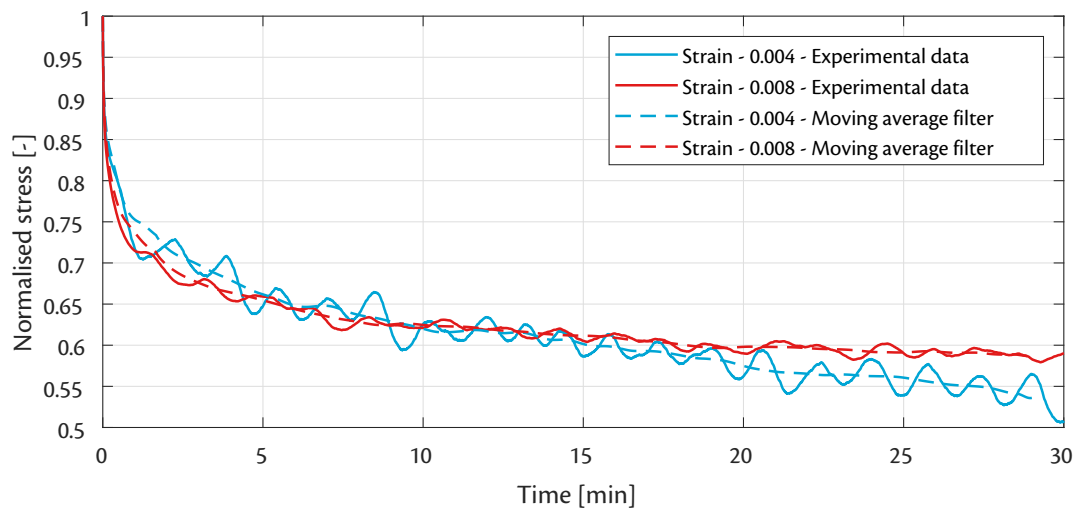


Figure 4.12 *Normalised relaxation curves of the dry composite material in transverse direction at 180 °C.*

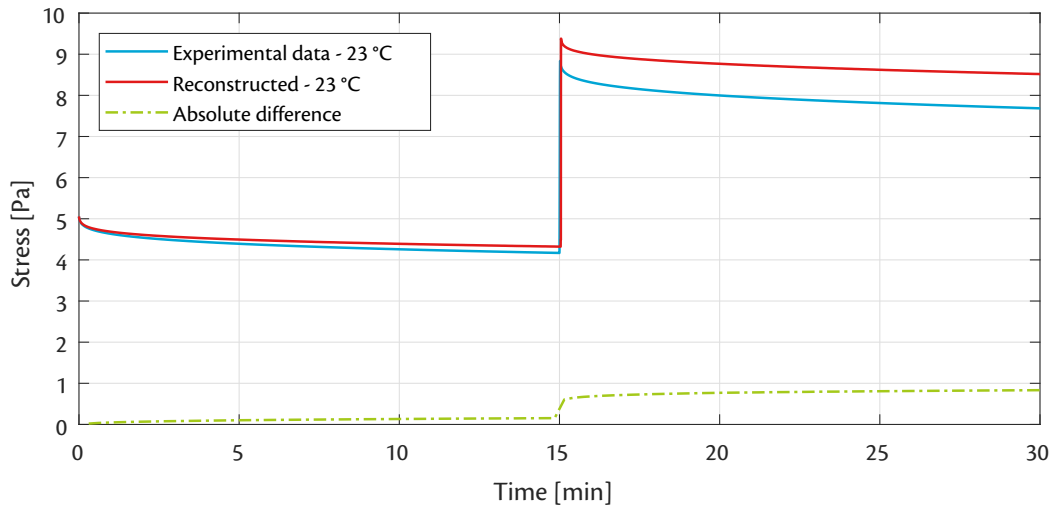


Figure 4.13 Reconstructed relaxation curve at 23 °C demonstrating the Boltzmann superposition principle of the dry composite material in transverse direction. The absolute difference between the two curves has been indicated with the dashed line.

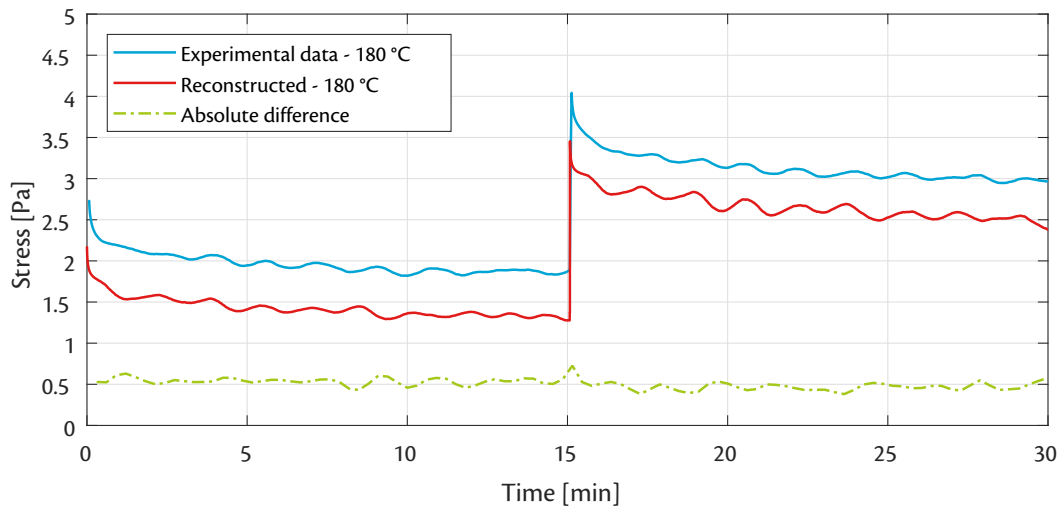


Figure 4.14 Reconstructed relaxation curve at 180 °C demonstrating the Boltzmann superposition principle of the dry composite material in transverse direction. The absolute difference between the two curves has been indicated with the dashed line.

## 4.8 Dynamic mechanical analysis

The relaxation behaviour of the composite material was determined through dynamic mechanical analysis, or DMA. A material is tested at various temperatures by cyclic strains of different frequencies with a relatively small magnitude. The required cyclic force to apply these strains is measured. The force response is transformed into a stress response in an analogous manner to the relaxation experiments. The stress response shows a delay in comparison with the strain input due to the viscous character of the polymer. The stiffness that can be derived from the magnitude of the stress and the delay in time therefore has a complex composition and is aptly named the complex modulus. The complex modulus is composed of a storage- and loss modulus according to Eq. 4.9.

$$E^*(\omega) = E'(\omega) + iE''(\omega) \quad 4.9$$

The aim of the DMA measurements carried out on a Netzsch EPLEXOR 500 N during the research was to determine the relaxation behaviour of the composite material over the entire temperature range of interest. This was achieved through carrying out frequency-sweep measurements at a finite range of temperatures. The selection of a suitable frequency range is depending on multiple factors. A broad frequency range is ideally desired to obtain results that show a clear overlap when shifting the curves for the construction of the mastercurve. Nonetheless, low frequencies inherently imply long testing times and high frequencies pose the threat of damaging the composite material which will introduce error for the measurements at a subsequent temperature level.

A frequency range of 0.3  $Hz$  to 30  $Hz$  was chosen with this trade-off in mind and in combination with advice documented in a DMA manual from TA Instruments. A total of 8 measurements was selected per frequency decade and a temperature range was chosen from 20  $^{\circ}C$  to 220  $^{\circ}C$  with increments of 10  $^{\circ}C$ . It is noted that the degree of crystallinity is increased during the DMA measurement as the temperature exceeds the glass transition temperature of 67  $^{\circ}C$  in dry state. As a result, measured mechanical properties will be higher [18] than encountered in the cathodic dip painting oven due to relatively long duration of the DMA measurement. The specimens that were measured had dimensions of 80 x 10 x 2  $mm^3$  in agreement with the tensile test fixture that was used. All specimens that were tested had been conditioned to a dry state according to DIN EN ISO 1110 [76]. The exclusion of specimens that have been conditioned to a state of full moisture saturation is based on the experimental challenge to contain the moisture during the measurements at elevated temperatures, especially up to 220  $^{\circ}C$ .

Constructing the mastercurve has been performed by the algorithm that is mentioned in Section 3.4. This procedure starts with fitting a polynomial of appropriate order through the curve that corresponds to the chosen reference temperature. The curve that corresponds to the adjacent temperature is then shifted along the time axis until the squared residual in comparison with the fit is minimised. A third order polynomial is then fitted through the extended curve that has been obtained by the shift. The curve to the subsequent adjacent temperature is then shifted with the same objective as before and this process is repeated until all curves have been shifted and a mastercurve is obtained. The mathematical expression shown in Eq. 4.10 represents the optimisation problem that is solved by shifting the curve to the fit.

$$\underset{a_T \in R^N}{\text{minimize}} \quad F(a_T) \equiv \sum_{i=1}^M \left( \frac{E'(\omega, a_T)}{E'(\omega)} - 1 \right)^2 \quad 4.10$$

The constructed mastercurve of the storage moduli that were obtained from the DMA measurements of the specimen in transverse fibre-direction is shown in Figure 4.15. A reference temperature of 20  $^{\circ}C$  has been chosen to ensure that time acceleration is required in the time-temperature superposition for all possible temperatures in the simulation as opposed to time deceleration. Additionally, choosing the reference temperature close to room temperature has the consequence that the reduced time at the beginning of the simulation is approximately real time. This allows an easier understanding of the size of the time step that is chosen in the numerical model at the beginning of the simulation. The final reason for choosing this reference temperature is that it allows calculation of the transverse at the same conditions of the measured Poisson's ratio, required for Eq. 4.16 in the micromechanical model.

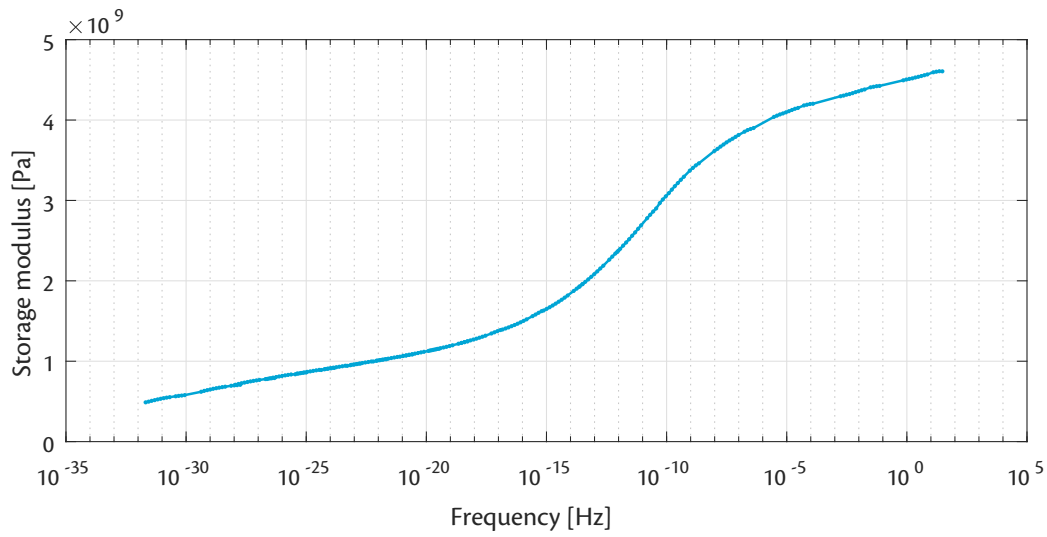


Figure 4.15 Mastercurve of the storage modulus in transverse direction of the composite material with  $20^\circ\text{C}$  taken as reference temperature.

One last reason for choosing  $20^\circ\text{C}$  as reference temperature is that the resulting relaxation curve is inherently valid for  $20^\circ\text{C}$  for which experimentally less complex validation experiments can be carried out. The reference temperature in literature is often chosen to be the glass transition temperature of the matrix constituent [47]. It is stated that the resulting determination of the relaxation behaviour will be equal independent of reference temperature, albeit that the time shift factors and coefficients of the Williams-Landel-Ferry equation will be different. The mastercurve constructed with  $20^\circ\text{C}$  as reference temperature is shifted along the time-axis to the mastercurve that was constructed with  $70^\circ\text{C}$  to demonstrate this statement. The result of this superposition is shown in Figure 4.16.

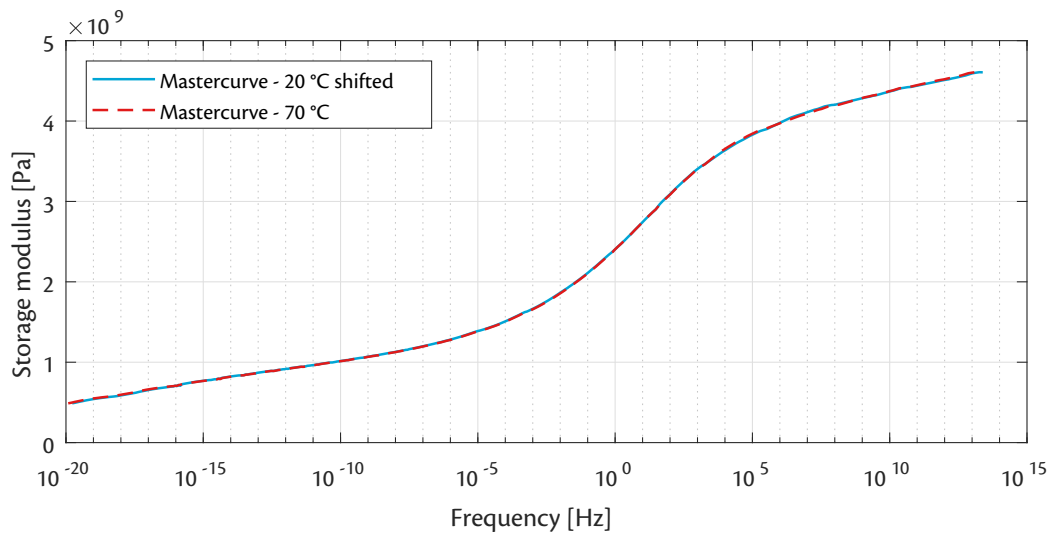


Figure 4.16 Mastercurve of the storage modulus in transverse direction of the composite material with  $20^\circ\text{C}$  taken as reference temperature superposed by means of one shift factor to the mastercurve constructed with  $70^\circ\text{C}$  as reference temperature.

Application of the shift factors that were obtained for the mastercurve of the storage modulus with a reference temperature of  $20\text{ }^{\circ}\text{C}$  to the measurements of the loss modulus revealed that a discontinuous mastercurve was obtained. This discontinuity implies that the composite material can not be classified as thermorheologically simple. Consequently, an attempt was made to apply both horizontal- and vertical shift factors to simultaneously obtain continuous curves for both the storage- and loss modulus. It was concluded that this is possible up to a temperature of  $130\text{ }^{\circ}\text{C}$ .

Discontinuous mastercurves provide evidence that the validity of time-temperature superposition is questionable for temperatures above  $130\text{ }^{\circ}\text{C}$ . The conclusion that a single continuous curve for both the storage- and loss modulus is not obtainable is reinforced by the Cole-Cole diagram that is shown in Figure 4.17. The Cole-Cole diagram does not show a continuous curve and time-temperature superposition above  $130\text{ }^{\circ}\text{C}$  is thus in principle not valid [61], see the theoretical background reported in Section 3.4 for a more detailed explanation. The DSC experiment that was carried out with the composite material did not display significant changes in heat flux around  $130\text{ }^{\circ}\text{C}$ .

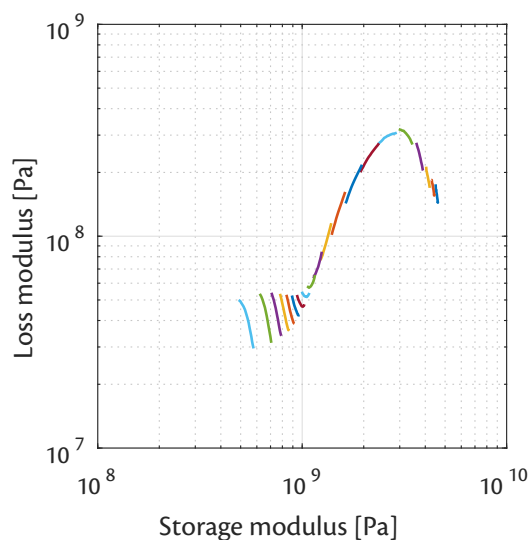


Figure 4.17 *Cole-cole diagram of the DMA measurements carried out in transverse direction to the fibre-orientation.*

Nevertheless, the constructed instantaneous moduli from the DMA measurement are in good agreement with the measured instantaneous moduli from the quasi-static tensile tests. A comparison between these values is shown in Figure 4.21 which has been placed at the end of this section to maintain the chronological order of research. Moreover, none of the obtained shift factors shows deviation from the expectation according to the Williams-Landel-Ferry equation [64]. These two results provide arguments to why the obtained relaxation moduli can still be accurately used to describe the relaxation behaviour of the composite material.

The method to obtain relaxation moduli from the constructed mastercurve of the storage moduli progresses by fitting the generalised Maxwell model to the mastercurve of the storage moduli. The mathematical expression of the generalised Maxwell model in the frequency domain is shown in Eq. 4.11. The frequency domain formulation is utilised as the storage moduli have been measured in the frequency domain. The terms  $E_{\infty}$  represents the fully relaxed stiffness value of the generalised Maxwell model and the terms  $E_i$  and  $\tau_i$  denote the individual stiffness values and relaxation times of the Maxwell elements in the generalised model. Lastly,  $\omega$  is used to represent the frequency and the number of elements in the model is indicated by  $N$ .

$$E'(\omega) = E_{\infty} + \sum_{i=1}^N \frac{E_i \omega^2 + \tau_i^2}{1 + \omega^2 \tau_i^2} \quad 4.11$$

A local optimiser IPOPT was initially used in an attempt to find optimal fitting parameters for the Maxwell model. The fitting was carried out based on an optimisation function that is shown in Eq. 4.12. The relaxation times were chosen to be fixed and had been selected to cover the entire frequency range of the mastercurve; ranging from  $10^2$  to  $10^{-32}$ . The resulting fit for low values of  $N$  appeared to be optimal and indicated proper implementation of the optimisation script. Nonetheless, values for  $N$  up to 12 yielded unacceptable fits as the error was still significant.

$$\underset{E, \tau \in R^N}{\text{minimize}} \quad F(E, \tau) \equiv \sum_{i=1}^M \left( \frac{E'(\omega_i)}{E'} - 1 \right)^2 \quad 4.12$$

Increasing the number of Maxwell elements led to the result that the local optimiser was not able to find a solution that appeared to be the global solution. This is in agreement with findings of Costa who reports an identical trend between the number of Maxwell elements and the satisfaction of the fit [88]. A genetic algorithm had been adopted to solve the fitting issue and satisfactory fits had been obtained for larger numbers of Maxwell elements. It must be noted, however, that the involved computational time is relatively large as the evolution of the fitting parameters must be kept low to ensure that the solution utilises all stiffness terms and does not evolve too quickly. Conclusions from this experience have had a result on the adopted modelling strategy that is outlined in Chapter 5.

A convergence study has been carried out to assess the influence of the number of Maxwell elements in the generalised Maxwell model on the accuracy of representing the mastercurve. The number of elements chosen for the convergence study ranges from 4 to 64 and doubles with every next computation. Table 4.8 shows the sum of the squared residuals for the calculated number of Maxwell elements. It is interesting to see that the genetic algorithm was not able to find a better fit for 64 Maxwell elements in comparison to 32 Maxwell elements. The finite number of experimental points are expected to be the cause for this behaviour. It was concluded to continue the material characterisation with 32 Maxwell elements based on the convergence study.

Table 4.8 *Convergence table for number of Prony terms for fit of storage modulus mastercurve.*

No. of Prony terms	RSS
4	11.833
8	1.640
16	0.373
32	0.075
64	0.099

The resulting fit of the generalised Maxwell model to the storage modulus mastercurve is depicted in Figure 4.18. The average residual found for the fit is equal to 1.09% and the fit is thus regarded as satisfactory. Nevertheless, it must be stated that from inspection of Figure 4.18 it is concluded to be possible to obtain a better fit by fine-tuning the parameters of the genetic algorithm.



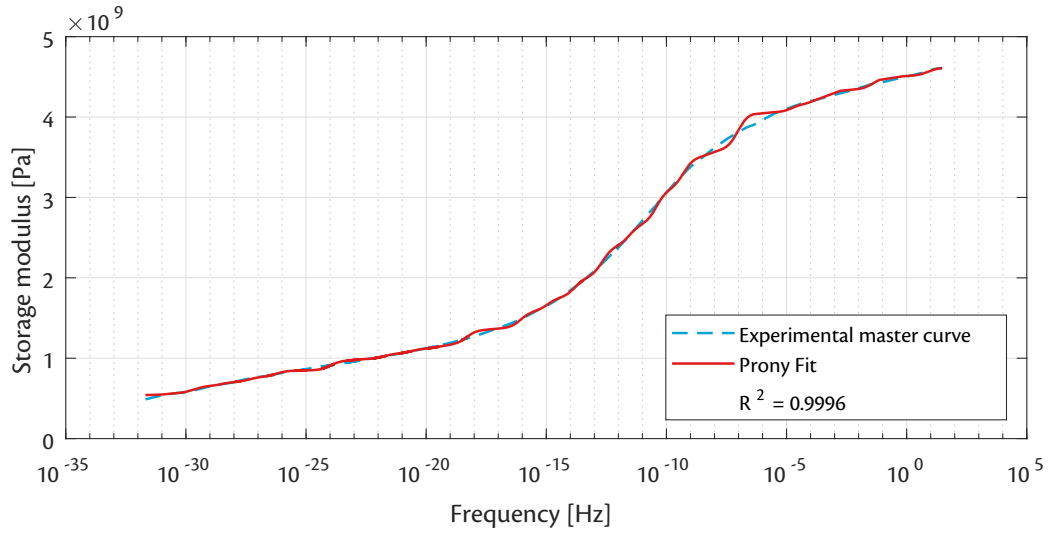


Figure 4.18 *Fitted Prony series with 32 terms for the mastercurve of the storage modulus of the dry composite material in transverse direction.*

The relaxation behaviour of the composite material in transverse direction to the fibres can be constructed by applying the obtained Maxwell elements for the frequency domain in the time domain. The mathematical expression for the generalised Maxwell model is displayed in Eq. 3.42 and is provided in Eq. 4.13 for ease of reading. The resulting relaxation curve from the parameters of the generalised Maxwell models is shown in Figure 4.19.

$$E(t) = E_{\infty} + \sum_{i=1}^N E_i \cdot e^{-\frac{t}{\tau_i}} \quad 4.13$$

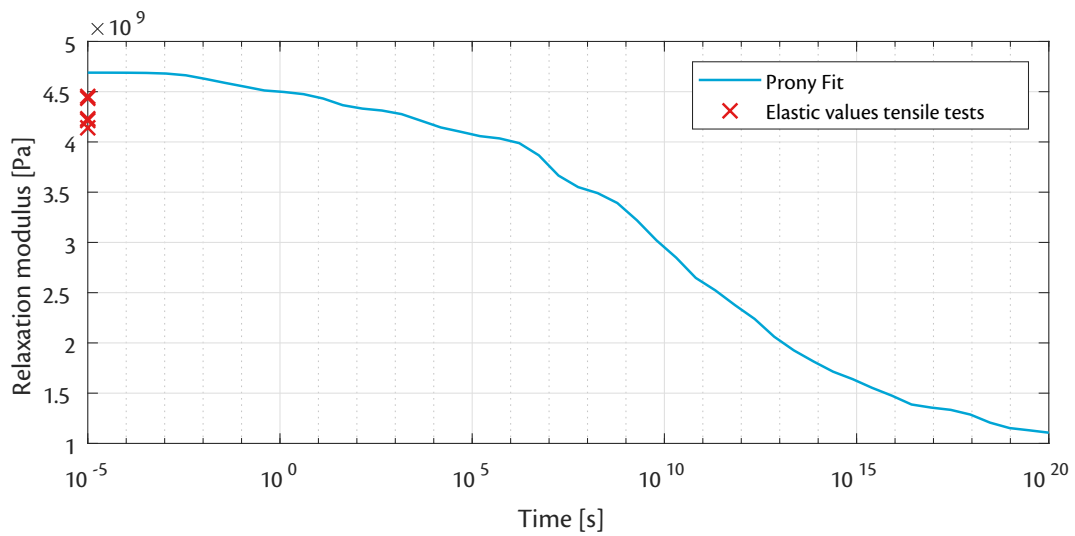


Figure 4.19 *Relaxation modulus of the dry composite material in transverse direction obtained through the fitted Prony series of the storage modulus.*

The influence of temperature on the relaxation behaviour can also be determined through the DMA measurement. The coefficients  $C_1$  and  $C_2$  of the Williams-Landel-Ferry equation can be obtained by utilising them as fitting parameters to fit the logarithmic shift factors as a function of time. The result of fitting the Williams-Landel-Ferry function is displayed in Figure 4.20 and is concluded to have yielded satisfactory results.

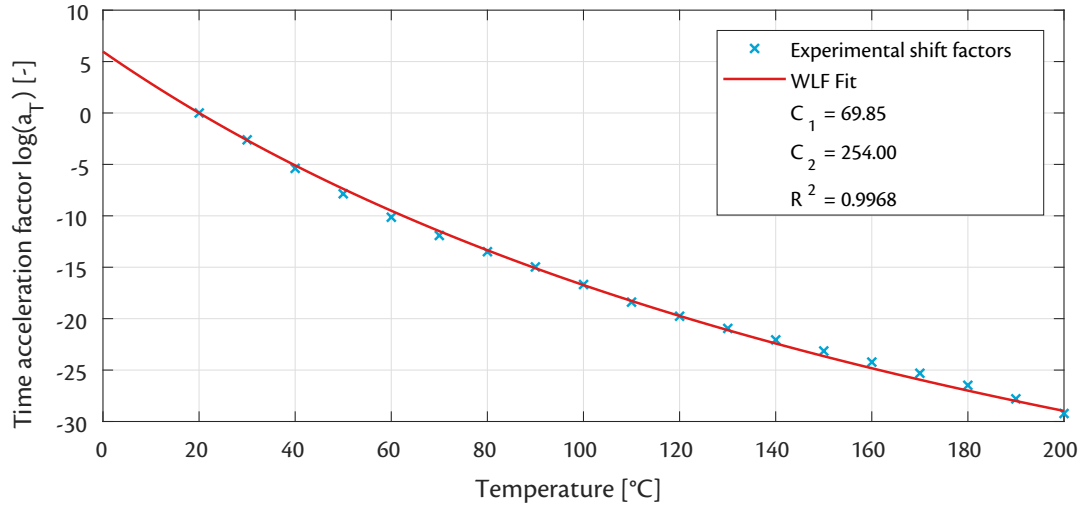


Figure 4.20 Fit of the Williams-Landel-Ferry equation of the experimentally determined shift factors.

Finally, a comparison between the moduli of the composite material in transverse direction to the fibres calculated through the DMA measurement and the instantaneous moduli obtained from the quasi-static tensile tests is shown in Figure 4.21. It must be noted that inherently variation exists in how the instantaneous stiffness value is calculated from the DMA results. An instantaneous stiffness value would normally be calculated at time equal to zero with the Prony series. However, choosing the time at which the instantaneous stiffness is evaluated to be zero does not allow the influence of temperature to be accounted for.

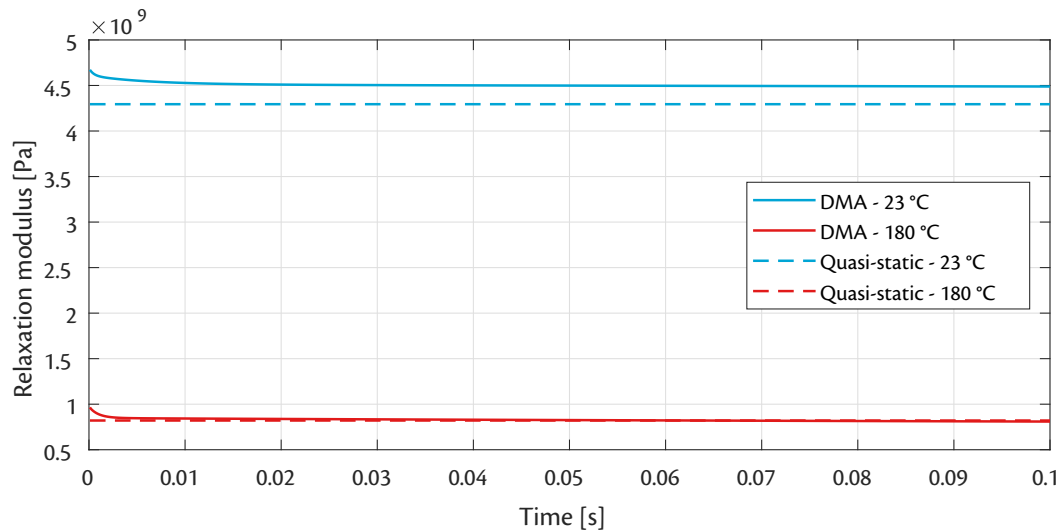


Figure 4.21 Instantaneous transverse stiffness moduli obtained by DMA and comparable values from quasi-static tensile tests.

The reason for this is because the reduced time that would be calculated with the time-temperature superposition principle to account for the effect of temperature is also zero. It then holds that all instantaneous stiffness magnitudes for different temperature conditions would be equal to the instantaneous stiffness at the reference temperature. The curves shown in Figure 4.21 were generated for a time period of 1E-4s to 1E-1s. This observation is important for the improvement of the numerical model that is described in Section 7.1.

## 4.9 Micromechanical model

The material characterisation yielded information on the thermal expansion, hygroscopic shrinkage, and mechanical properties of a unidirectional laminate of the composite material. As can be observed from the constitutive equations that are displayed in Section 3.6, the input for the numerical model must be formulated as a Prony series for each stiffness component. The total amount of stiffness components is reduced to nine because of the orthotropic nature of the unidirectional laminate [67]. This section presents the micromechanical model that is used to calculate these stiffness components from the mechanical properties that have been identified in the material characterisation. It is noted that the coefficients for thermal expansion and hygroscopic shrinkage do not need any further processing. The applied micromechanical model makes use of rules-of-mixtures for which the assumptions stated in the list below apply. The calculations that are carried out in the micromechanical model are depicted schematically in Figure 4.23 after the textual discussion and equations for a clear overview.

- The matrix is linearly viscoelastic isotropic
- The matrix does not contain any voids
- The fibres are linearly elastic orthotropic
- The fibres are distributed uniformly throughout the matrix
- The matrix and fibre are perfectly bonded to each other
- The lamina is initially in a stress-free state

The required engineering parameters to fully describe the mechanical behaviour of an orthotropic unidirectional lamina are the stiffness in longitudinal direction, the shear modulus, the stiffness in transverse direction, and the major Poisson's ratio. Only the latter two were experimentally determined. The two remaining engineering parameters were calculated by means of micromechanical equations prior to calculating the orthotropic stiffness coefficients on lamina level. All laminate-related properties have been indicated with a bar notation in the following equations of this section.

The first engineering parameter that is calculated is the longitudinal relaxation modulus. It is assumed that the viscoelastic behaviour of the composite material is fully attributed to the matrix constituent. The calculation of the longitudinal modulus requires the fibre' longitudinal elastic modulus and matrix' relaxation modulus to be known. Hence, the relaxation modulus of the matrix constituent, denoted with  $E_m$ , is calculated with Eq. 4.14 [89].

$$E_m = v_m \left( \frac{1}{\bar{E}_{22}} - \frac{v_f}{E_{22f}} \right)^{-1} \quad 4.14$$

The terms  $v_f$  and  $v_m$  in Eq. 4.14 represent the fibre- and matrix volume content, respectively. Moreover, the fibre' transverse elastic modulus and the transverse unidirectional laminate' relaxation modulus are represented by  $E_{22f}$  and  $\bar{E}_{22}$ , respectively. The longitudinal relaxation modulus of the unidirectional laminate can be calculated with the expression shown in Eq. 4.15.

$$\bar{E}_{11} = v_f \cdot E_{11f} + v_m \cdot E_m \quad 4.15$$

The last engineering parameter that must be calculated is the shear modulus, represented with the symbol  $\bar{G}_{12}$ . The calculation of the shear modulus is also carried out in a micromechanical manner and requires the shear moduli of the fibre- and matrix constituents to be known. The value for the shear modulus of the fibre constituent is taken from literature [73] as shown in Section 4.1 and the shear modulus of the matrix is calculated through the isotropic relationship [89] between shear- and Young's modulus and major Poisson's ratio. Hence, the matrix' major Poisson's ratio is derived from the unidirectional laminate' major Poisson's ratio.

Prior to presenting this calculation it must be noted that the major Poisson's ratio of the unidirectional laminate was only experimentally determined at room temperature. It is reported that both the major and minor Poisson's ratios were often assumed to be independent of temperature throughout literature [90]. However, Pandini [91] reports that this often leads to significant variation between simulations and experiments. Hence, the major Poisson's ratio is regarded as temperature-dependent in the micromechanical model.

For this temperature-dependency, it has been assumed that the longitudinal modulus of the laminate remains constants independent of the temperature. It then follows that the change in Poisson's ratio is fully governed by the variation in transverse stiffness that is the result of an increased temperature. Furthermore, the volumetric change for a material without any transverse stiffness must be equal to 0.5 per definition. An empirical relation shown in Eq. 4.16 was defined by Giencke [92] to describe the temperature-dependent Poisson's ratio whilst complying to the upper limit that is bound by the previous physical argumentation on volumetric change.

$$\nu_{12} = 0.5 - (0.5 - \tilde{\nu}_{12}) \frac{\bar{E}_{22}}{\tilde{E}_{22}} \quad 4.16$$

The symbols  $\tilde{\nu}_{12}$  and  $\tilde{E}_{22}$  represent the experimentally determined major Poisson's ratio at room temperature and the corresponding transverse instantaneous stiffness of the laminate. The major Poisson's ratio of the matrix is inherently also temperature-dependent and can be calculated with the classical rule-of-mixtures that is shown in Eq. 4.17.

$$\nu_{12m} = \frac{1}{v_m} (\bar{\nu}_{12} - v_f \cdot \nu_{21f}) \quad 4.17$$

The shear modulus of the matrix constituent can then be calculated with the knowledge about the relaxation modulus and the major Poisson's ratio with the use of the isotropic relation shown in Eq. 4.18.

$$G_{12m} = \frac{E_m}{2(1 + \nu_{12m})} \quad 4.18$$

The shear modulus of the laminate can be determined as a last step to obtain all required engineering parameters by means of the classical rule-of-mixtures that is displayed in Eq. 4.19.

$$\bar{G}_{12} = \frac{G_{12m} \cdot G_{12f}}{v_m \cdot G_{12f} + v_f \cdot G_{12m}} \quad 4.19$$

The transverse out-of-plane Poisson's ratios are calculated through the Halpin-Tsai equations [93]. The polymer bulk modulus and a auxiliary parameter, denoted with  $K_m$  and  $\Xi$ , respectively, must first be calculated by utilising the two expression that are presented in Eq. 4.20.

$$\begin{aligned} K_m &= \frac{E_m}{3 - 6 \cdot \nu_{12m}} \\ \Xi &= \frac{\frac{K_m}{G_{12m}}}{\frac{K_m}{G_{12m}} + 2} \end{aligned} \quad 4.20$$

The two transverse out-of-plane Poisson's ratios are equal to each other due to the orthotropic character of the unidirectional laminate. Calculation of these Poisson's ratios is carried out with the relation shown in Eq. 4.21 that is part of the Halpin-Tsai micromechanical model.

$$\bar{\nu}_{23} = \bar{\nu}_{32} = \frac{\Xi (3 - 4 \cdot \bar{\nu}_{12}^2) - 1}{\Xi + 1} \quad 4.21$$

The out-of-plane shear modulus can then be calculated with the use of the transverse out-of-plane Poisson's ratios with Eq. 4.22 that originates from classical isotropic rules-of-mixtures [89].

$$\bar{G}_{23} = \frac{\bar{E}_{22}}{2(1 + \bar{\nu}_{23})} \quad 4.22$$

The only two laminate unknowns that remain are the longitudinal out-of-plane Poisson's ratios. These Poisson's ratios are equal to the transverse out-of-plane Poisson's ratios due to the transverse isotropy. The mathematical expressions are shown in Eq. 4.23 for completeness.

$$\begin{aligned} \bar{\nu}_{13} &= \bar{\nu}_{12} \\ \bar{\nu}_{31} &= \bar{\nu}_{21} \end{aligned} \quad 4.23$$

The last step that is performed in the micromechanical model is to calculate the nine stiffness coefficients of the unidirectional laminate. There are only six unique stiffness components due to transverse isotropy and the expressions that have been used for the calculation are shown in Eq. 4.24. The relations that are displayed in Eq. 4.24 have been obtained from the elastic relationships [94] by means of the viscoelastic correspondence principle that is explained in Section 3.5. Please note that the bar notation is dropped in Eq. 4.24 as all present symbols are laminate properties.

$$\begin{aligned}
\lambda &= 1 - \nu_{12}\nu_{21} - \nu_{23}\nu_{32} - \nu_{13}\nu_{31} - 2\nu_{21}\nu_{32}\nu_{13} \\
C_{11} &= E_{11} \cdot \lambda^{-1} (1 - \nu_{23}\nu_{32}) \\
C_{12} &= E_{11} \cdot \lambda^{-1} (\nu_{21} - \nu_{31}\nu_{23}) \\
C_{13} &= E_{11} \cdot \lambda^{-1} (\nu_{31} - \nu_{21}\nu_{32}) \\
C_{22} &= E_{22} \cdot \lambda^{-1} (1 - \nu_{31}\nu_{13}) \\
C_{23} &= E_{22} \cdot \lambda^{-1} (\nu_{32} - \nu_{12}\nu_{31}) \\
C_{33} &= E_{22} \cdot \lambda^{-1} (1 - \nu_{12}\nu_{21}) \\
C_{44} &= G_{12} \\
C_{55} &= G_{23} \\
C_{66} &= G_{23}
\end{aligned} \tag{4.24}$$

The computed stiffness coefficients can then be assembled in agreement to the Voigt notation that is applied in ABAQUS as shown in Eq. 4.25 [68]. The nine independent stiffness coefficients shown in Eq. 4.25 are in agreement with the stiffness matrix that is derived in the book on mechanics of anisotropic materials by Skrzypek [67].

$$C_{ij} = \begin{bmatrix} C_{11} & C_{12} & C_{13} & 0 & 0 & 0 \\ C_{12} & C_{22} & C_{23} & 0 & 0 & 0 \\ C_{13} & C_{23} & C_{33} & 0 & 0 & 0 \\ 0 & 0 & 0 & C_{44} & 0 & 0 \\ 0 & 0 & 0 & 0 & C_{55} & 0 \\ 0 & 0 & 0 & 0 & 0 & C_{66} \end{bmatrix} \tag{4.25}$$

It is noted that all laminate stiffness coefficients are time-dependent and that this dependency is accounted for in the preprocessing steps for the numerical model. The resulting stiffness coefficients of the composite material are shown in Figure 4.22. A total of six independent Prony series have been determined for the mechanical properties of the unidirectional lamina. The relaxation times for every Prony series is kept equal for simplicity and to prevent possible errors in input. The resulting Prony terms for the independent stiffness coefficients are displayed in Table 4.9.

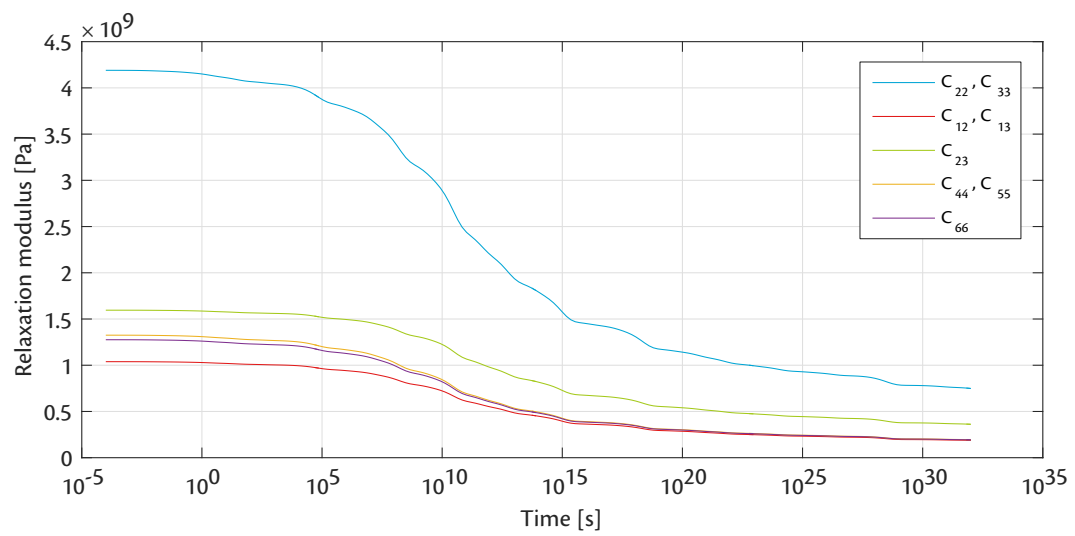


Figure 4.22 Orthotropic stiffness coefficients of the unidirectional laminate as a function of time.

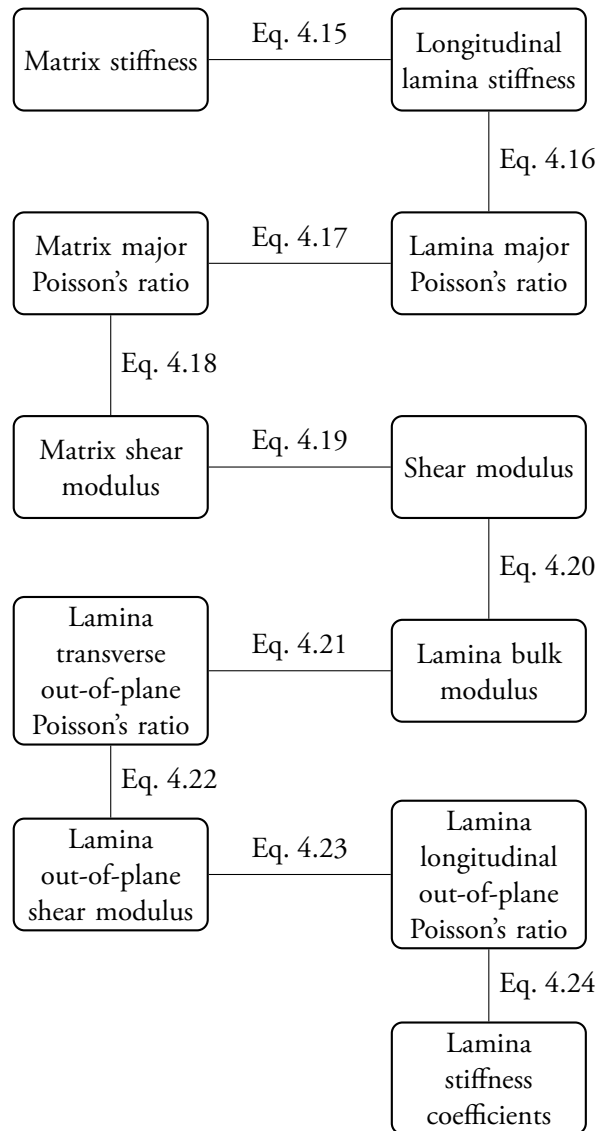


Figure 4.23 A schematic overview of the order of calculations carried out in the micromechanical model.



Table 4.9 *Values of the relaxation times and determined Prony coefficients for the independent stiffness components of a unidirectional layer of CF60-PA6.*

$i$	$\tau_i$	$C_{11i}$	$C_{12i}$	$C_{22i}$	$C_{23i}$	$C_{44i}$	$C_{66i}$
1	1.00E-02	3.04E+08	1.18E+07	6.42E+07	2.55E+07	4.09E+07	2.83E+07
2	1.35E-01	1.00E+00	5.75E+07	1.04E+08	6.84E+06	1.49E+07	2.41E+07
3	1.81E+00	1.26E+00	9.52E+06	6.41E+07	4.20E+07	5.33E+07	4.81E+07
4	2.44E+01	1.53E+08	1.00E+00	1.95E+07	5.72E-01	1.70E+07	2.40E+07
5	3.28E+02	9.62E-01	7.45E+07	1.95E+08	5.26E+07	1.13E+07	7.75E+06
6	4.42E+03	1.00E+00	2.54E+07	8.47E+07	1.29E+06	1.26E+08	8.08E+07
7	5.95E+04	2.22E+07	1.09E+07	6.83E+07	7.20E+06	1.24E+07	1.47E+07
8	8.00E+05	1.35E-01	6.68E+07	3.64E+07	9.68E+07	4.49E+07	7.98E+06
9	1.08E+07	1.00E+00	4.66E+06	4.60E+08	7.25E+06	5.14E+06	2.11E+08
10	1.45E+08	1.00E+00	2.05E+08	1.98E+08	1.66E+08	2.93E+08	1.14E+07
11	1.95E+09	1.67E+00	3.52E+06	1.52E+08	1.00E+00	3.01E+07	1.82E+08
12	2.63E+10	1.79E+00	3.62E+08	7.18E+08	3.33E+08	1.50E+08	2.00E+07
13	3.53E+11	8.59E-01	1.11E+07	4.69E+07	3.71E+07	1.74E+08	2.97E+08
14	4.76E+12	6.72E-01	3.71E+07	5.56E+08	1.88E+08	5.97E+07	1.91E+07
15	6.40E+13	2.16E+09	3.05E+08	1.87E+08	1.36E+08	1.76E+08	1.09E+08
16	8.62E+14	1.00E+00	6.81E+06	1.63E+08	1.91E+07	3.20E+07	9.60E+07
17	1.16E+16	1.38E+00	4.22E+07	1.90E+08	2.10E+08	4.73E+07	3.05E+06
18	1.56E+17	1.09E+00	6.60E+07	9.82E+07	4.78E-01	7.24E+07	9.24E+07
19	2.10E+18	1.00E+00	7.17E+07	1.23E+08	4.15E+07	1.16E+06	8.97E+06
20	2.83E+19	1.47E+00	2.77E+07	8.21E+07	8.22E+07	4.77E+07	1.69E+07
21	3.81E+20	1.00E+00	4.62E+06	4.90E+06	1.45E+07	2.06E+07	3.78E+07
22	5.12E+21	4.78E-01	1.06E+06	1.30E+08	1.06E+07	2.40E+07	1.96E+07
23	6.90E+22	7.60E+08	9.98E+07	2.64E+07	6.84E+07	1.21E+07	2.71E-01
24	9.28E+23	1.36E+00	9.77E+06	6.63E+07	2.18E+07	1.85E+07	5.06E+07
25	1.25E+25	9.03E-01	1.21E+07	2.91E+07	1.45E-02	4.50E+05	1.12E+07
26	1.68E+26	7.78E-01	1.47E+07	9.29E+07	1.09E+08	6.60E+07	8.19E+06
27	2.26E+27	1.00E+00	1.00E+00	1.69E-01	6.95E+05	1.98E+06	0.00E+00
28	3.05E+28	2.24E-01	1.03E+08	1.55E+08	1.43E+07	1.42E+07	6.72E+07
29	4.10E+29	1.19E+00	6.28E+06	6.30E+06	6.98E+07	1.70E+07	2.20E+06
30	5.52E+30	1.00E+00	5.07E+05	5.31E+07	1.25E+06	2.43E+07	6.61E+06
31	7.43E+31	1.00E+00	6.56E+05	4.30E+06	1.38E+07	2.83E-02	1.91E+06
32	1.00E+33	1.00E+00	8.94E+06	1.00E+00	5.29E-01	0.00E+00	4.48E+06



# 5

## Finite element modelling

Modelling the viscoelastic deformation behaviour of complex components requires the application of finite element models to account for the geometrical non-linearity that is expected. This expectation is founded on the degree of matrix softening that was observed in the DMA measurements described in Section 4.8. This chapter provides a detailed overview of how the finite element simulation is carried out and discusses the arguments that have driven specific modelling decisions. Moreover, the development of a material user subroutine to implement anisotropic viscoelastic material behaviour is documented as well as the verification of this material user subroutine. A mesh convergence study and an analysis of the sensitivity of the simulation to the input parameters and modelling choices are provided as the concluding section.

### 5.1 Model framework

The sequence of the simulation is derived from how the actual cathodic dip painting process introduces stresses into the thermoplastic components. From Section 2.1 it can be concluded that the BIW is subjected only to thermal loads in the cathodic dip painting ovens. It is therefore assumed that temperature and time are the only independent variables in the simulation. The thermal loading to which the objective component is subjected to governs thermal expansion, hygroscopic shrinkage, and material property changes of the matrix constituent.

There is a direct interaction between the thermal loading and the thermal expansion of the material. The ambient air temperature is entered as input for the entire duration of the simulation to allow the numerical model to be used as an assessment tool to analyse the influence of changing the temperature profile in the cathodic dip painting ovens. However, the thermal expansion of the material must be calculated through the temperature of the component as opposed to the ambient air temperature. A heat transfer analysis is required for this purpose and this forms the first step in the model framework. It is assumed that the only mechanism of heat transfer is convection, for which the governing expression is shown in Eq. 5.1.

$$q_{conv} = hA_s (T_{air} - T_{sur}) \quad 5.1$$

The temperature profile is entered based on the maximum air temperature that was measured during the experiment. A predefined field is applied as boundary conditions with a tabular amplitude that is computed with MATLAB to specify the temperature at a given moment in time. The initial temperature of the specimen is retrieved from the temperature measurement of the specimen's surface during the experiment. The heat convection is implemented in ABAQUS by means of a film condition interaction for which a convection coefficient has been determined by measuring the air temperature and the surface temperature of the specimen.

The mesh of the heat transfer model exhibits more nodes to the outside of the specimen as large temperature gradients are to be expected in that region. The mesh that was chosen for the heat transfer model is discussed in Section 5.4. The output of the heat transfer simulation contains the nodal temperature of the mesh and will be used as input for the mass diffusion simulation that is ran afterwards. Hence, the mesh of the heat transfer- and mass diffusion simulation are equal. It was decided to carry out a one-dimensional heat transfer simulation in through-thickness direction only. The argumentation for this decision is discussed in Section 5.4.

The rising temperature inside the component drives the diffusion of water molecules out of the component into the ambient air. The egress of water molecules leads to hygroscopic shrinkage and has a significant effect on the deformation behaviour according to the coefficients of hygroscopic expansion that have been determined in Section 4.4. Hence, a mass diffusion simulation is carried out after obtaining the temperature distribution throughout the specimen with the preceding heat transfer analysis.

The mass diffusion simulation is carried out governed by the diffusion coefficients that are entered as tabular values obtained by evaluating the fitted Arrhenius equation that was established during the material characterisation. The coefficients of the fitted Arrhenius equation can be found in Table 4.4. Analogous to the heat transfer simulation, the mass diffusion simulation is carried out as a one-dimensional through-thickness simulation which is argued in Section 5.4.

The solubility of the composite material was determined during the micrometer experiments that were carried out to determine the coefficients of moisture expansion. The concentration boundary conditions that must be entered for the top and bottom of the specimen are based on two empirical values. It is assumed that the relative humidity of the air at room temperature is high enough for the specimen to reach moisture saturation and the boundary condition is set to the solubility value. The concentration boundary condition at a temperature of 100 °C is set to zero as moisture will only be present in gaseous form. Intermediate values for temperature in between 23 °C and 100 °C are linearly interpolated.

The heat transfer- and mass diffusion simulation are treated as sequential simulations and the two processes are assumed to be uncoupled. This means that the changes in moisture concentration of the specimen are assumed to have no influence on the heat transfer physics. Coupling between the heat transfer- and mass diffusion processes would occur if phase changes or chemical decomposition would be present for the medium that governs the heat transfer. This is because the mentioned mass diffusion processes require latent heat that will affect the heat transfer and hence cause coupling. The saturation moisture concentration is only 1.62% and the heat transfer through the composite can thus be assumed to be governed by the composite material only. The melting temperature of the matrix constituent has been determined by DSC to be 222.3 °C and a phase transition of the heat transfer medium does not occur, allowing uncoupling between the heat transfer and mass diffusion.

A stress simulation can be carried out after identifying the temperature- and moisture distribution inside the specimen. The thermal expansion and hygroscopic shrinkage are implemented through specifying total coefficients of expansion that are pre-calculated in MATLAB with the information from the preceding simulations. These coefficients of expansion are entered to be dependent on a field variable that is set equal to the independent variable time. The change in material properties due to the thermal loading is accounted for by the constitutive equations that are outlined in Section 3.6 through a user subroutine. The development of the user subroutine is extensively discussed in the next section.

The simulation allows the analysis of multi-directional laminates through the choice of utilising solid elements with a composite lay-up in ABAQUS. The composite lay-up method also allows a deviating number of plies to be analysed that does not comply with the element thickness. This is especially valuable concerning the validation lay-ups that have been chosen due to manufacturing reasons. For the correct implementation of layer orientation it is required to define a reference orientation to each element.

The reference orientation is chosen to correspond with the fibre-direction that a lamina of  $0^\circ$  orientation would have. A discrete material orientation method has been adopted because of the curved geometry of the component. This curved geometry prohibits a global material orientation from working correctly. Hence, each element is provided its own local material orientation with one global  $0^\circ$  direction and its own specific element normal. It is noted that the mesh stacking direction must be defined in ABAQUS to ensure a proper axis of rotation for the ply orientation that is entered in the composite lay-up settings.

The solid mesh of the component has been generated with HyperMesh that was developed by Altair. The applied meshing strategy involved so called solid mapping. Surfaces that are connected by sweep lines for the solid mesh are meshed as a surface first. These meshed surfaces are then extruded along the sweep lines and the extrusion is further divided into solid elements of dimensions that approach unity. Redundant construction lines in the CAD model for manufacturing purposes of the component have been suppressed to ensure clearly defined cross-sections and guiding lines for the generation of the mesh.

The boundary conditions of the coupon- and component stress simulations are shown in Figure 5.1 and Figure 5.2, respectively. It is noted that the applied temperature field has been hidden for both boundary condition images to increase the clarity of the illustrations. The orange arrows on the left hand side of Figure 5.1 represent the initial displacement that is implemented in the simulation to create an imperfection. No out-of-plane deformation would be simulated without the addition of the vertical displacement. The magnitude of the imperfection has been minimised to limit the disturbing effect on the displacement solution. This minimisation is documented in Section 5.4.

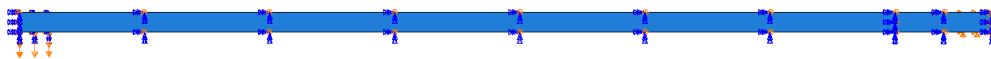


Figure 5.1 *The boundary conditions for the stress simulation of the validation coupon.*

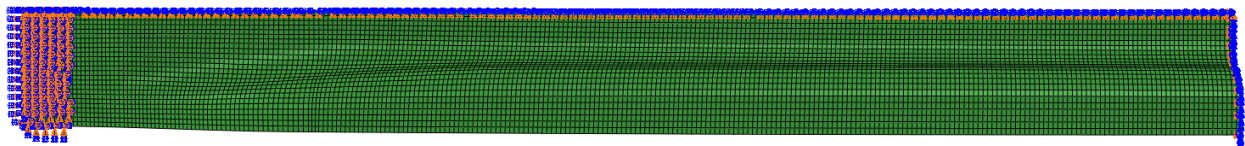


Figure 5.2 *The boundary conditions for the stress simulation of the validation component.*

A list of all the assumptions that were made for the three simulations is presented next. These assumptions have been made partly based on the material characterisation and partly based on the sensitivity studies that are discussed in Section 5.4. The key simulation parameters that have been applied for every individual simulation are shown in Table 5.1. The complete model framework is visualised schematically in Figure 5.3 and it is noted that the preprocessing- and carrying out of the mass diffusion simulation is not necessary for the simulation of dry composite material.

- The only mechanism of heat transfer is convection.
- The relaxation behaviour of the matrix is unaffected by moisture content.
- All properties of the fibre constituent remain unchanged during the CDP process.
- Three-dimensional geometrical effects can be neglected for the heat transfer- and mass diffusion.

Table 5.1 *Simulation parameters in ABAQUS.*

Simulation	Parameter	Setting
Heat transfer	Element type	Heat transfer element
	Material input	$C_p, \lambda, \rho$
	Maximum temperature increment	1 °C
	Maximum time increment	30s
	Temperature input	Predefined field with amplitude
Mass diffusion	Element type	Mass diffusion element
	Material input	$D(t), K, \rho$
	Maximum time increment	30s
	Maximum concentration increment	0.001
	Temperature input	Nodal temperatures
Stress	Element type	Solid fully integrated linear 3D stress
	Through-thickness representation	Single element with composite lay-up
	Integration points per layer	1
	Material input	$C_{ii\infty}, C_{ij}, \tau_i, C_1, C_2$
	Maximum time increment	0.25s
	Geometrical non-linearity	On

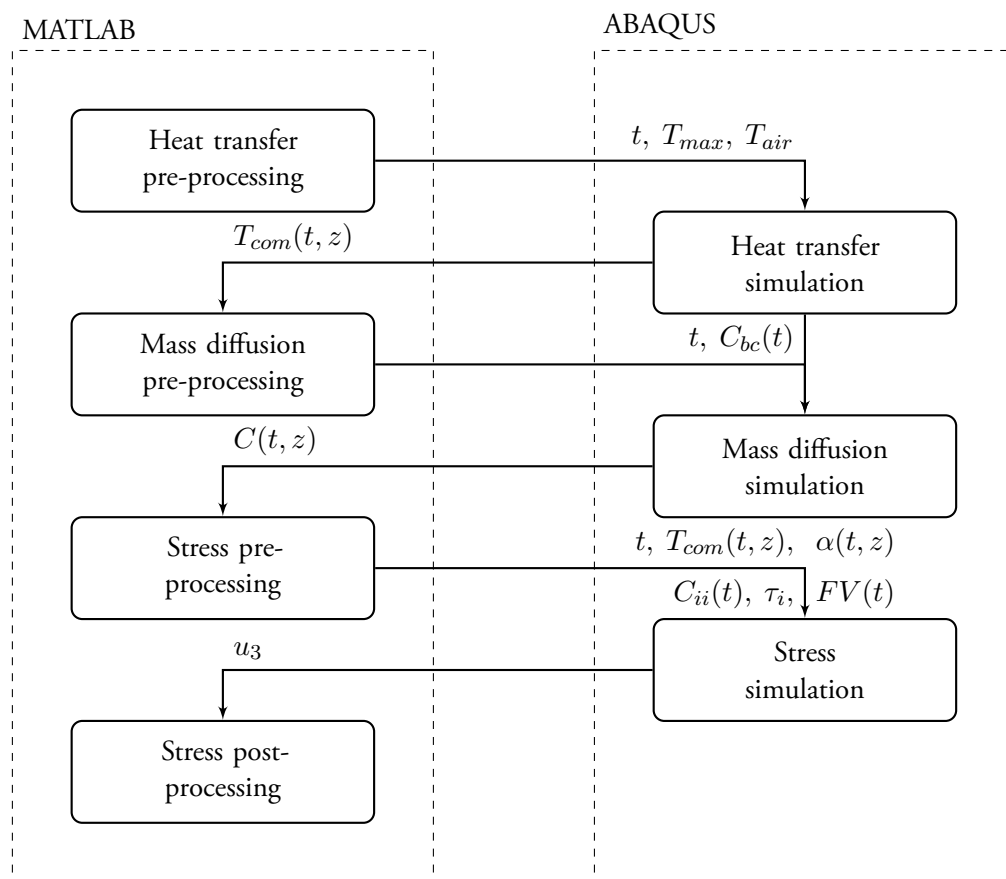


Figure 5.3 Flowchart of the numerical modelling workflow for a moisture saturated specimen.

## 5.2 User subroutine development

The application of the constitutive equations that were derived in Section 3.6 is not implemented in ABAQUS by standard subroutines. Hence, a user subroutine had to be written that defines the material behaviour, effectively linking stresses to strains. The user subroutine format that governs the constitutive material behaviour in ABAQUS is called UMAT. This section describes the development of the user subroutine to implement the anisotropic viscoelastic material behaviour necessary for the numerical model.

The two essential activities that must be carried out by a UMAT is the definition of the Jacobian and providing the updated stresses based on the incremental strain that ABAQUS proposes [68]. The Jacobian is a 6 x 6 matrix considering the fact that solid elements have been chosen in the model framework in Section 5.1. The stress tensor that must be updated consists of 3 normal- and 3 shear stress components.

Material properties for a UMAT can only be passed as a single-column table in ABAQUS. This implied that passing the material properties in a logical order allowed to apply efficient programming to allocate the properties into matrices. The number of solution dependent variables, or SDVs, must also be stated in the material definition that is created for the UMAT. Entering an incorrect number for the amount of SDVs that should be created during the analysis carries the risk of incorrect assignment of data.

The recursive formulation of the constitutive equations stipulates that every Prony term requires its own SDV to store the recursive part and update it during every time increment. The strain derivative that is characteristic for the applied constitutive equations gets calculated for every time increment, but it is not necessary to store it for future calculations. Hence, the recursive stress contributions are the only parameters that require storage in SDVs. The number of Prony terms for each stiffness component was determined in Section 4.8 to be 32. Hence, a total of 192 SDVs are created in the UMAT to account for all recursive stress contributions of each Maxwell element for all 6 stress components.

The time-temperature superposition is implemented in the user subroutine by transforming the time increment in real time to an accelerated time increment through the time shift factor that is calculated at the beginning of the subroutine. It holds that the two coefficients of the Williams-Landel-Ferry equation and the reference temperature of the mastercurve for the Prony terms must also be entered in the material properties. The list of material properties includes a total of 233 values. These values are comprised of 6 relaxed stiffness components, 32 relaxation times, 192 stiffness values of the Maxwell elements for every independent stiffness component, and the 3 mentioned values necessary for the time-temperature superposition.

The following part describes the steps taken by the user subroutine in chronological order and provides the pieces of code that correspond to these calculation steps. It is noted that the complete user subroutine is provided in Appendix A to allow inspection of the code in one continuous read. The header of the user subroutine follows the default format that is defined for a UMAT.

```

SUBROUTINE UMAT (STRESS, STATEV, DDSDE, SSE, SPD, SCD,
1 RPL, DDSDDT, DRPLDE, DRPLDT,
2 STRAN, DSTRAN, TIME, DTIME, TEMP, DTEMP, PREDEF, DPRED, CMNAME,
3 NDI, NSHR, NTENS, NSTATV, PROPS, NPROPS, COORDS, DROT, PNEWDT,
4 CELENT, DFGRD0, DFGRD1, NOEL, NPT, LAYER, KSPT, JSTEP, KINC)
C
  INCLUDE 'ABA_PARAM.INC'
C
  CHARACTER*8 CMNAME
  DIMENSION STRESS(NTENS), STATEV(NSTATV),
1 DDSDE(NTENS, NTENS),
2 DDSDDT(NTENS), DRPLDE(NTENS),
3 STRAN(NTENS), DSTRAN(NTENS), TIME(2), PREDEF(1), DPRED(1),
4 PROPS(NPROPS), COORDS(3), DROT(3,3), DFGRD0(3,3), DFGRD1(3,3),
5 JSTEP(4)

```



The first two steps performed in the user subroutine are the definition of the natural logarithm of 10 and the declaration of all the variables that will be used in the user subroutine. The natural logarithm of 10 is defined to enable the usage of the EXP function in Fortran.

```

PARAMETER(DLNTEN=2.30258509299d0)
C
REAL*8 C(7,33),DDSN(3,3),DDSS(3,3),DSTRES(6),EXPP(32),DTIMEI,DTIMEA,STIFFA,STIFFB

```

The time increment is converted to a reduced time increment based on the application of the Williams-Landel-Ferry equation as shown in Eq. 3.44. The terms  $C_1$ ,  $C_2$ , and  $T_{ref}$  have been placed at the end of the material property list to avoid confusing values for the indices concerning the Prony terms and relaxation times.

```
DTIMEA = DTIME*EXP(DLNTEN*PROPS(231)*(TEMP-PROPS(233))/(PROPS(232)+TEMP-PROPS(233)))
```

The strain derivative that is required for the constitutive equations is calculated with the reduced time increment by means of the following three lines of code. It is noted that NTENS represents the total amount of entries in the stress tensor and is equal to 6 for a solid element.

```

DO I=1,NTENS
  STATEV(I) = DSTRAN(I)/DTIMEA
END DO

```

The Prony terms and relaxation times that have to be entered through a list are reordered in a matrix to allow the usage of loops for the subsequent computations. It is noted that the relaxation terms are entered on the first row. The six individual series of Prony terms that are shown in Table 4.9 are allocated to rows 2 to 7.

```

C(1,1) = 0.
DO I=1,6
  C(I+1,1) = PROPS(I)
END DO
DO I=1,32
  C(1,I+1) = PROPS(I+6)
  C(2,I+1) = PROPS(I+38)
  C(3,I+1) = PROPS(I+70)
  C(4,I+1) = PROPS(I+102)
  C(5,I+1) = PROPS(I+134)
  C(6,I+1) = PROPS(I+166)
  C(7,I+1) = PROPS(I+198)
END DO

```

The formatted Prony terms and relaxation times are then used to update the recursive notation that is necessary to calculate the stress contribution of the recursive part.

```

DO I=1,32
  EXPP(I) = EXP(-DTIMEA/C(1,I+1))
  STATEV(I+6) = EXPP(I)*STATEV(I+6) + STATEV(1)*C(2,I+1)*C(1,I+1)*(1-EXPP(I))
  STATEV(I+38) = EXPP(I)*STATEV(I+38) + STATEV(2)*C(4,I+1)*C(1,I+1)*(1-EXPP(I))
  STATEV(I+70) = EXPP(I)*STATEV(I+70) + STATEV(3)*C(4,I+1)*C(1,I+1)*(1-EXPP(I))
  STATEV(I+102) = EXPP(I)*STATEV(I+102) + STATEV(4)*C(6,I+1)*C(1,I+1)*(1-EXPP(I))
  STATEV(I+134) = EXPP(I)*STATEV(I+134) + STATEV(5)*C(6,I+1)*C(1,I+1)*(1-EXPP(I))
  STATEV(I+166) = EXPP(I)*STATEV(I+166) + STATEV(6)*C(7,I+1)*C(1,I+1)*(1-EXPP(I))
END DO

```

The next step in the user subroutine is to calculate the normal stress stiffness values that are required to determine the resulting stress from the incremental strain of the currently calculated time step. It is noted that the part of the Jacobian that governs normal stress is symmetric. Hence, computations are only performed for the independent components and the dependent components are simply copied for computational efficiency.

```

DTIMEI = 1./DTIMEA
DDSN(1,1) = C(2,1)

```

```

DDSN(1,2) = C(3,1)
DDSN(2,2) = C(4,1)
DDSN(2,3) = C(5,1)
DO I=2,33
    DDSN(1,1) = DDSN(1,1) + DTIMEI*C(2,I)*C(1,I)*(1-EXP(-DTIMEA/C(1,I)))
    DDSN(1,2) = DDSN(1,2) + DTIMEI*C(3,I)*C(1,I)*(1-EXP(-DTIMEA/C(1,I)))
    DDSN(2,2) = DDSN(2,2) + DTIMEI*C(4,I)*C(1,I)*(1-EXP(-DTIMEA/C(1,I)))
    DDSN(2,3) = DDSN(2,3) + DTIMEI*C(5,I)*C(1,I)*(1-EXP(-DTIMEA/C(1,I)))
END DO
DDSN(1,3) = DDSN(1,2)
DDSN(2,1) = DDSN(1,2)
DDSN(3,1) = DDSN(1,2)
DDSN(3,2) = DDSN(2,3)
DDSN(3,3) = DDSN(2,2)

```

The components that enter the part of the Jacobian governing the shear stress are calculated afterwards. The split in normal- and shear stress part of the Jacobian has been chosen for ease of pinpointing potential errors in the user subroutine.

```

DDSS(1,1) = C(6,1)
DDSS(3,3) = C(7,1)
DO I =2,33
    DDSS(1,1) = DDSS(1,1) + DTIMEI*C(6,I)*C(1,I)*(1-EXP(-DTIMEA/C(1,I)))
    DDSS(3,3) = DDSS(3,3) + DTIMEI*C(7,I)*C(1,I)*(1-EXP(-DTIMEA/C(1,I)))
END DO
DDSS(2,2) = DDSS(1,1)

```

The Jacobian is assembled with the following loops after the individual entries have been calculated. The terms NDI and NSHR indicating the lengths of the two loops are defined in ABAQUS as the amount of normal- and shear stress entries in the stress tensor for the finite element, respectively.

```

DO I=1,NDI
    DO J=1,NDI
        DDSDE(I,J) = DDSN(I,J)
    END DO
END DO
DO I=1,NSHR
    DDSDE(NDI+I,NDI+I) = DDSS(I,I)
END DO

```

The instantaneous stresses that are a direct result of the incremental strains are then calculated by means of the assembled Jacobian in the first loop of the following code. Additionally, the stress contributions of the recursive part are accounted for in the second loop. This is the final step in the user subroutine as both the task of defining the Jacobian and providing ABAQUS with the updated stresses have been fulfilled.

```

DO I=1,NTENS
    DSTRES(I) = 0.
    DO J=1,NTENS
        DSTRES(I) = DSTRES(I) + DSTRAN(J)*DDSDE(I,J)
    END DO
    DO J=1,32
        DSTRES(I) = DSTRES(I) - (1-EXPP(J))*STATEV(6+32*(I-1)+J)
    END DO
    STRESS(I) = STRESS(I) + DSTRES(I)
END DO

```

### 5.3 Verification of user subroutine

An essential part that was carried out prior to generating the simulations for the validation experiments was the verification of the UMAT. Several verification tests were performed to ensure that the calculations in the UMAT were in perfect agreement to the intended computations. Verification of the subroutine is of crucial importance to be able to rule out any flaws in the software when assessing the validation results.

The verification tests were designed to increase in complexity to allow straightforward debugging if the verification results were not in agreement with the analytical- or reference value. A total of five verification tests have been conducted and an overview is given in the list below. Verification tests 1, 2, 4, and 5 have been carried out with an element that has dimensions of  $1 \times 1 \times 1$ . The relevance of the element dimensions has also been investigated of which the result is shown in Section 5.4.

1. Isothermal uniaxial step strain input
2. Isothermal bi-axial step strain input
3. Verification according to an example in Zocher's paper [44]
4. Non-isothermal uniaxial step strain input
5. Non-isothermal uniaxial single square-wave pulse strain input

The relevant material parameters that have been used as input for the verification tests are shown in Table 5.2. The fourth and fifth verification tests include thermal boundary conditions. Hence, a start- and end temperature are displayed in Table 5.2 and it is noted that the temperature is increasing in a linear manner for both verification tests that include time-temperature superposition. The mechanical boundary conditions for every verification test have been chosen to be the bare minimum that is required for the analysis to eliminate any disturbing effects. All boundary conditions are shown in Figure 5.4 for the verification tests in logical order from left to right.

Table 5.2 *Material parameters that have been used for the user subroutine verification.*

Parameter	Unit	Test 1	Test 2	Test 3	Test 4	Test 5
$E_{11\infty}$	Pa	2.0E6	2.0E6	1.0E5	2.0E6	2.0E6
$E_{111}$	Pa	5.5E6	5.5E6	4.0E5	5.5E6	5.5E6
$\tau_{11}$	s	0.25	0.25	1.00	1E11	1E7
$E_{12\infty}$	Pa	n.a.	5.0E5	n.a.	n.a.	n.a.
$E_{121}$	Pa	n.a.	5.0E5	n.a.	n.a.	n.a.
$\tau_{121}$	s	n.a.	1.00	n.a.	n.a.	n.a.
$C_1$	—	n.a.	n.a.	n.a.	69.85	69.85
$C_2$	—	n.a.	n.a.	n.a.	254.00	254.00
$T_{ref}$	°C	n.a.	n.a.	n.a.	20	20
$T_{start}$	°C	n.a.	n.a.	n.a.	40	40
$T_{end}$	°C	n.a.	n.a.	n.a.	85	45

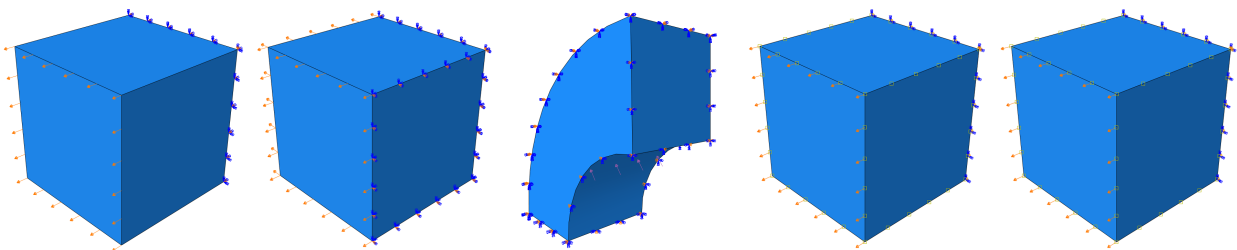


Figure 5.4 *Applied boundary conditions for the verification tests in order from 1 to 5 from left to right.*

The first verification test comprises the calculation of the stress response to a uniaxial step strain input. A single Maxwell model connected in parallel is chosen for simplicity for this verification test. Hence, only the terms  $E_{11\infty}$ ,  $E_{111}$ , and  $\tau_{11}$  are of importance for the relaxation behaviour of the material. The magnitude of the strain is decided to be 0.01 as this allows easy comparison between the expected- and simulated value of the stress. The only boundary conditions for this verification test are zero displacement in longitudinal direction of the longitudinal plane of the element and zero displacement in all directions for one node that corresponds to the nodes of the previous boundary condition to prevent numerical problems.

The total duration of the verification test is 1 second and a time increment of 0.01 second has been chosen for the analysis. The instantaneous stress response is expected to be  $7.5e4 \text{ Pa}$  based on the stiffness values and relaxation time shown in Table 5.2. The results of the simulation are shown in Figure 5.5 and agree perfectly with the analytical solution for which the expression is provided in Eq. 5.2. The analytical solution is obtained from the expression of the generalised Maxwell model displayed in Eq. 4.13 evaluated for one Maxwell element and multiplied by the applied strain.

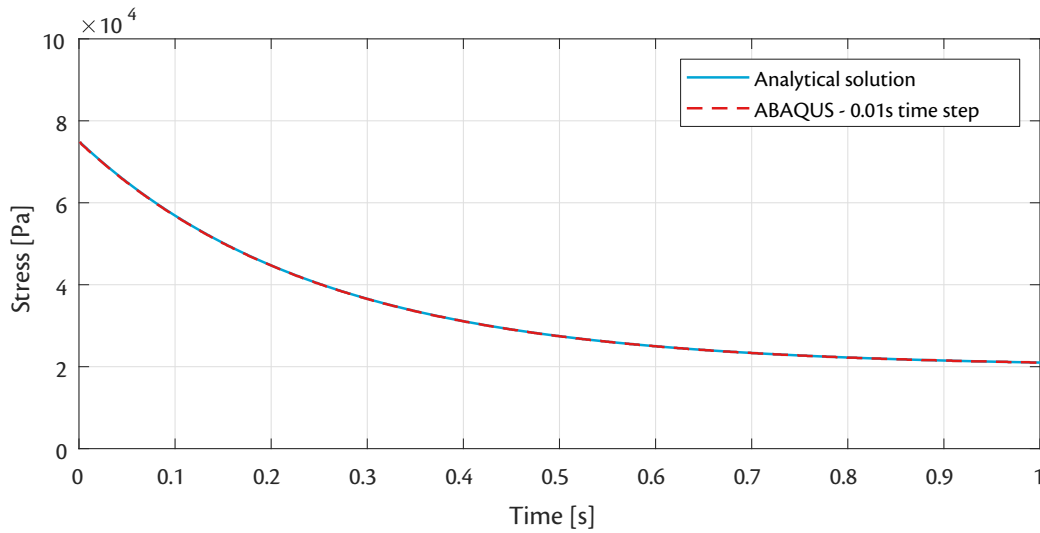


Figure 5.5 *Verification results of the uniaxial isothermal step strain input.*

$$\sigma(t) = \left( E_{11\infty} + E_{111} \cdot e^{-\frac{t}{\tau_{11}}} \right) \cdot \varepsilon_0 \quad 5.2$$

The second verification test follows up the first verification test by adding a strain component in transverse direction to the already applied strain. Zero displacement boundary conditions have been added in transverse direction of the nodes on one transverse plane to ensure the modelling of a bi-axial load case. The intended purpose of this verification test is to validate the correct calculation of the transverse stress coupling through the Poisson's ratio. This effect is tested by means of a single element generalised Maxwell element to describe an arbitrary relaxation behaviour of  $E_{12}$ , skipping any calculations involving a Poisson's ratio.

An analytical solution to this problem is not available without significant mathematical effort and it has been decided to implement the recursive formulation in MATLAB to obtain a reference solution for verification. The implementation in MATLAB is possible due to the geometrical simplicity of the problem that does not require a finite element approach and the evaluated expression is shown in Eq. 5.3. The results of both the MATLAB reference solution and the ABAQUS solution of the user subroutine are shown in Figure 5.6. The time step in MATLAB was chosen relatively small to minimise discretisation errors. It can be concluded by comparison of the two plots that the user subroutine carries out the calculations as intended.

$$\sigma(t + \Delta t) = \sigma(t) + \Delta \varepsilon \left( C_{11\infty} + \frac{1}{\Delta t} \left[ C_{111}\rho_{111} \left( 1 - e^{-\Delta t/\rho_{111}} \right) + C_{121}\rho_{121} \left( 1 - e^{-\Delta t/\rho_{121}} \right) \right] \right) - \left( 1 - e^{-\Delta t/\rho_{111}} \right) \left[ e^{-\Delta t/\rho_{111}} \cdot R(t - \Delta t) + G_{\varepsilon}^{-} \cdot \rho_{111} \left( 1 - e^{-\Delta t/\rho_{111}} \right) \right] \quad 5.3$$

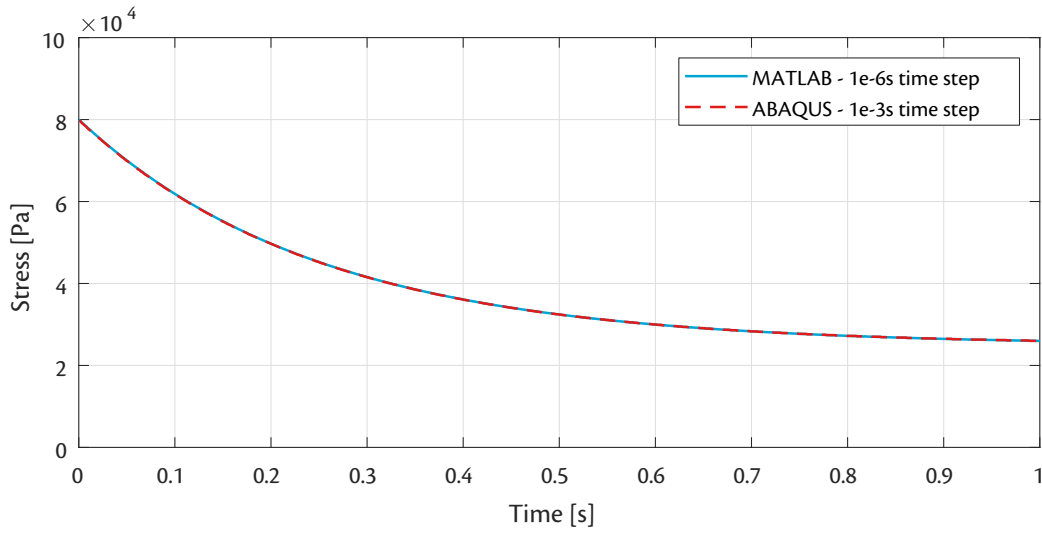


Figure 5.6 Verification results of the bi-axial isothermal step strain input.

The third verification example is taken from the original paper of Zocher [44] that discusses the constitutive equations of the numerical model that has been developed during the thesis. The verification problem treats a long thick-walled viscoelastic cylinder that is enclosed by a rigid casing from the outside and subjected to an internal pressure from the inside. The mesh of the viscoelastic cylinder has been chosen to be exactly similar to the mesh that was used in the original paper.

The internal pressure, denoted with  $p_0$ , is assumed to be constant throughout the simulation and has a magnitude of  $100 \text{ Pa}$ . An analytical solution for the displacement in radial direction of the viscoelastic cylinder can be obtained by the viscoelastic correspondence principle of which the mathematical expression is shown in Eq. 5.4. The terms  $r$ ,  $a$ ,  $b$ , and  $\nu$  represent the radius of interest, the inner- and outer radius, and the Poisson's ratio of the material, respectively.

$$u_r = \frac{p_0 a^2 b (1 + \nu) (1 - 2\nu)}{a^2 + (1 - 2\nu) b^2} \left( \frac{b}{r} - \frac{r}{b} \right) D(t) \quad 5.4$$

The term  $D(t)$  in Eq. 5.4 denotes the compliance of the cylinder and can be calculated with the formula in Eq. 5.5. The expression on the left hand side of Eq. 5.5 requires the terms  $D_0$ ,  $E_0$ ,  $D_1$ , and  $\lambda_1$  for which the definitions are displayed on the right hand side of Eq. 5.5.

$$D(t) = D_0 + D_1 \left(1 - e^{-\frac{t}{\lambda_1}}\right) \quad \text{where} \quad \begin{aligned} D_0 &\equiv \frac{1}{E_0} \\ E_0 &\equiv E_\infty + E_1 \\ D_1 &\equiv \left(\frac{1}{E_\infty} - \frac{1}{E_0}\right) \\ \lambda_1 &\equiv \frac{E_0 \cdot \rho_1}{E_\infty} \end{aligned} \quad 5.5$$

The results of the third verification test can be seen in Figure 5.7. It is noted that there is a growing discrepancy between the analytical solution and the values that have been obtained through the numerical model utilising the user subroutine. The original paper does not mention whether the problem must be treated as a plain strain or not. Nevertheless, the ABAQUS analysis of this verification test has been modelled as a plain strain problem because the mesh in the original paper is shown in two dimensions only and because of the description of a long thick-walled cylinder. The previous may explain the discrepancy between the analytical solution from Figure 5.7 and the numerical results. Nevertheless, an identical relaxation behaviour is observed and it was concluded that the user subroutine performs as intended.

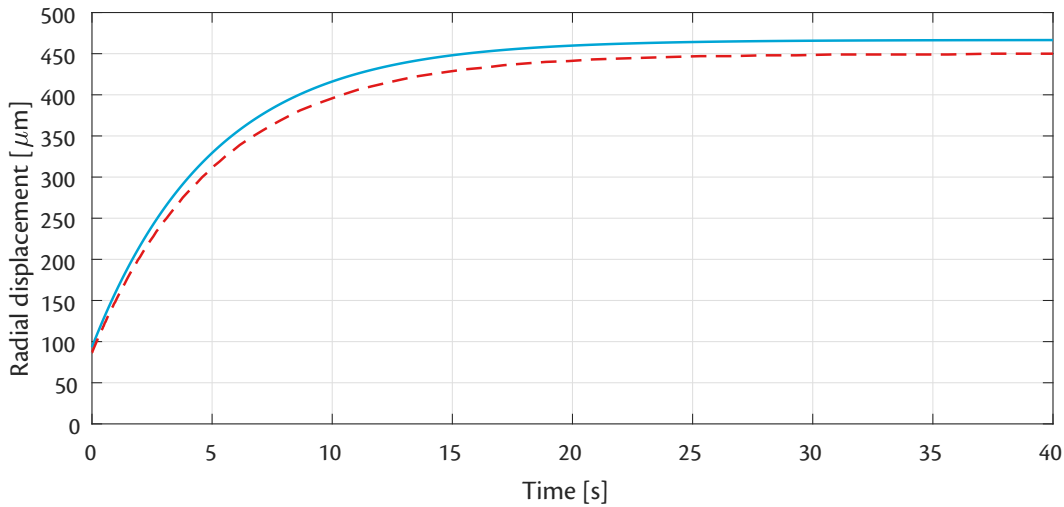


Figure 5.7 *Verification results of pressurised linear viscoelastic rocket fuel under isothermal conditions.*

The fourth- and fifth verification tests have been chosen to assess the implementation of the time-temperature superposition in the user subroutine. Both verification tests concern uniaxial strain input only as the coupling was already verified through verification test 2. Hence, the boundary conditions for these verifications tests are identical to the boundary conditions used in verification test 1. The difference in the last two verification tests is the shape of the strain input. The fourth verification test has a step strain input analogous to the first two verification tests. The fifth verification test, on the other hand, analyses the stress response to a single square-wave pulse strain input. The thermal boundary conditions have been applied to all nodes and its magnitude and the associated reduced times are shown in the lower plot of Figure 5.8.

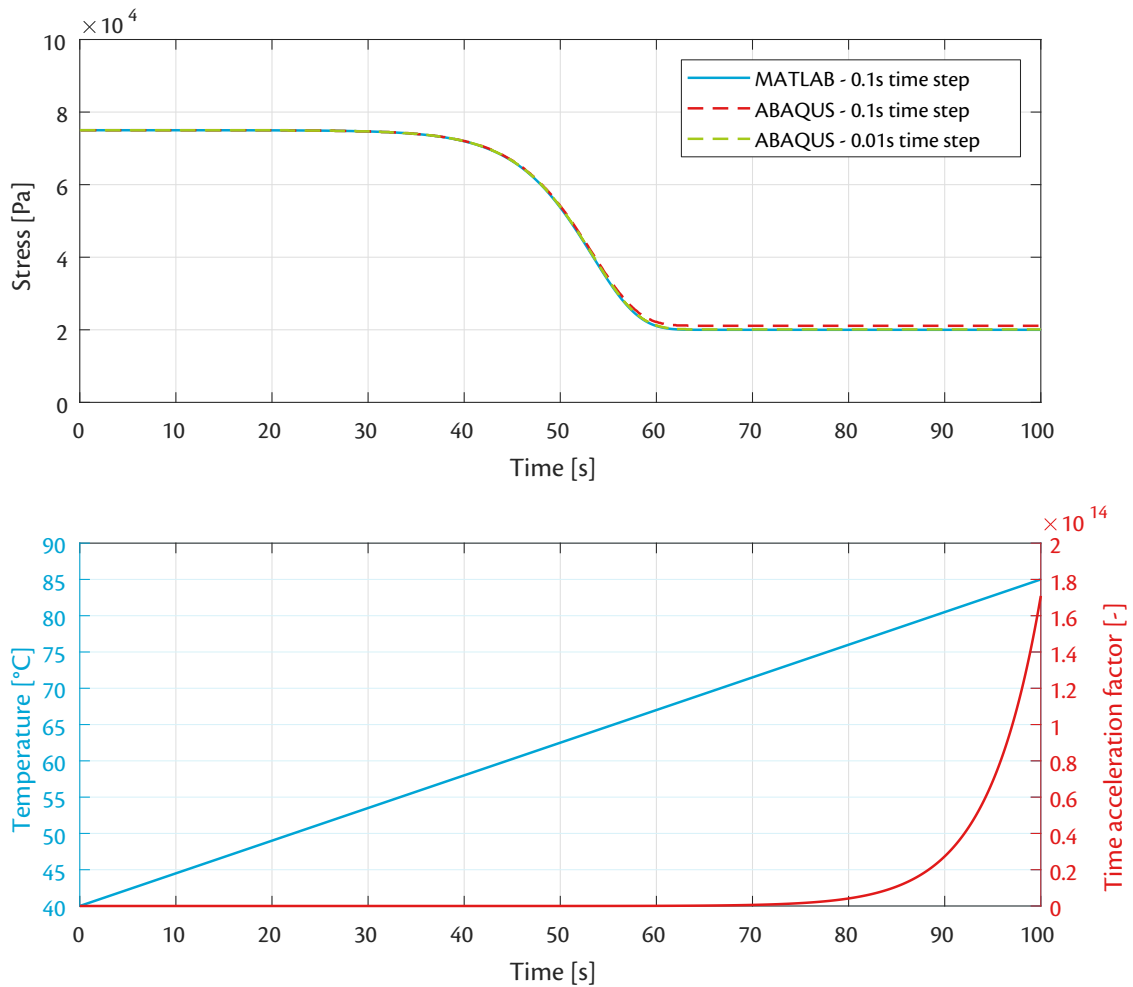


Figure 5.8 Verification results and thermal boundary conditions of the non-isothermal uniaxial step strain input.

The numerical results in both Figure 5.8 and Figure 5.9 are in excellent agreement with the reference results that have been generated in MATLAB and indicate that the time-temperature superposition principle is also correctly implemented. It is noted that the generated results for MATLAB have been generated by scaling the complete real time scale to the reduced time scale as described by the shift factors obtained through time-temperature superposition. The solution is then obtained by progressing in the reduced time scale with one constant time step. This approach is different from the method that is implemented in the subroutine as the subroutine takes real time steps and converts those to reduced time steps and progresses the solution in real time. This strategy was adopted to identify possible misinterpretation of the necessary transformation from real time step to reduced time step. If any errors would have been present in the user subroutine concerning the reduction in time step size, this verification would have identified it.

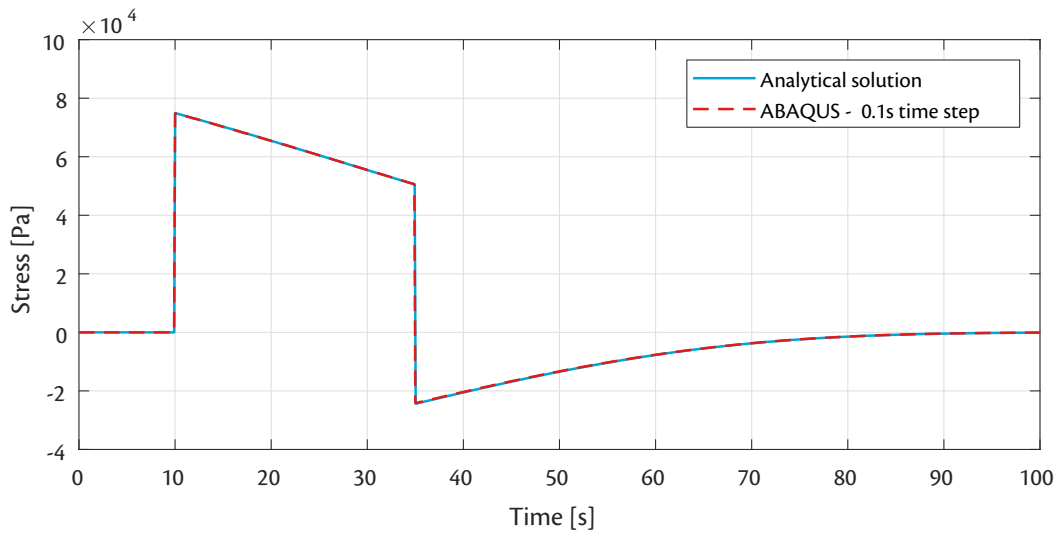


Figure 5.9 Verification results of the non-isothermal uniaxial single square-wave pulse strain input.

#### 5.4 Convergence- and simplification verification studies

The heat transfer- and mass diffusion simulations are carried out in a one-dimensional manner as described in Section 5.1. This section presents the sensitivity studies that have been carried out to justify the choice of one-dimensional simulations for computational reasons and straightforward processing of the numerical results. Additionally, mesh convergence studies are provided regarding the element size and magnitude of the time step of the stress simulation.

Three dimensional heat transfer- and mass diffusion simulations have been carried out to evaluate the distribution of temperature and moisture content in the three-dimensional case. These simulations have been carried out for a specimen with two finite edges to ensure the largest influence of the edge effects are analysed. The temperature- and moisture content distributions are assessed at the mid-plane of the specimen. The results of the three-dimensional heat transfer simulation that utilises the boundary conditions of the control validation experiment are shown in Figure 5.10.

The left hand side of Figure 5.10 shows the temperature distribution at 1150 seconds into the simulation, which is still during the heating phase. The numerical results show a lower temperature at areas that are further away from the edges, as expected. It is also noted that the temperature distribution is not similar in longitudinal- and transverse direction due to the orientation dependency of the heat conductivity of the fibre-reinforced thermoplastic material.

The simulation result on the right hand side of Figure 5.10 shows the temperature distribution of the mid-plane of the specimen during the cooling phase at 2200 seconds, where the largest temperature difference in the specimen was observed. It is noted that the variation in temperature distribution is larger in comparison to the heating phase of the simulation. Nevertheless, the maximum difference that is observed is only  $3.5^{\circ}\text{C}$  and it was concluded that limiting the heat transfer simulation to one dimension has no significant effect on the simulation of the deformation behaviour. Moreover, the through-thickness distribution of the temperature was found to be negligible as well. Hence, the temperature at every node in the stress simulation is set equal to the value that was calculated from the convection simulation.



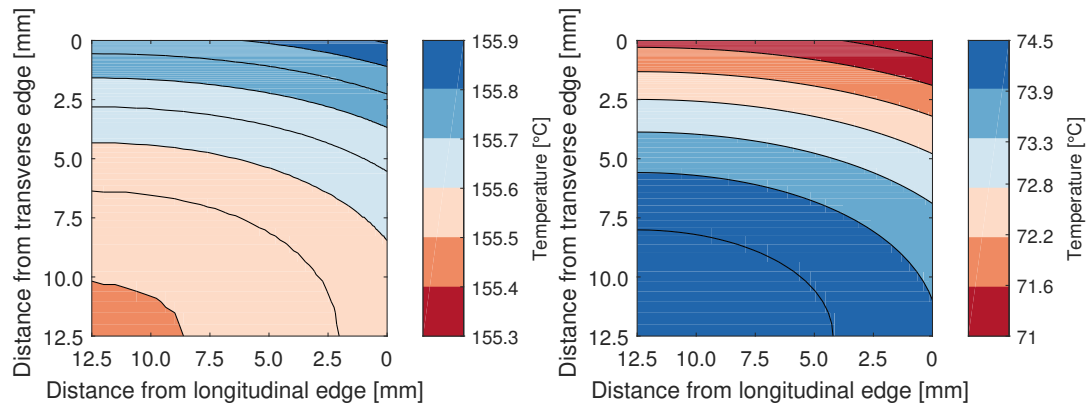


Figure 5.10 *Sensitivity analysis to limiting the heat transfer simulation to one dimension.*

The simulation results for the three-dimensional mass transfer simulation are shown in Figure 5.11 for equal moments in time as provided for the temperature distributions that are shown in Figure 5.10. A significant variation in moisture content due to the finite edges is visible during both the heating and cooling phase. It is concluded that the finite edge effects are confined to a distance of 2.5 mm from the edges of the specimen. Although the three-dimensional effects may be argued to have an effect on the strain in transverse direction of the specimen, this is of little importance for the bending deformation.

The finite edge effects on the moisture content distribution in longitudinal direction can be concluded to be of importance for 2% of the entire length of the coupon. Therefore, it was concluded that the finite edges effects can be neglected in determining the moisture content through the thickness of the coupon. Moreover, the affected area over the complete width at the two ends of the coupon are located inside the clamps and hence do not influence the bending deformation behaviour.

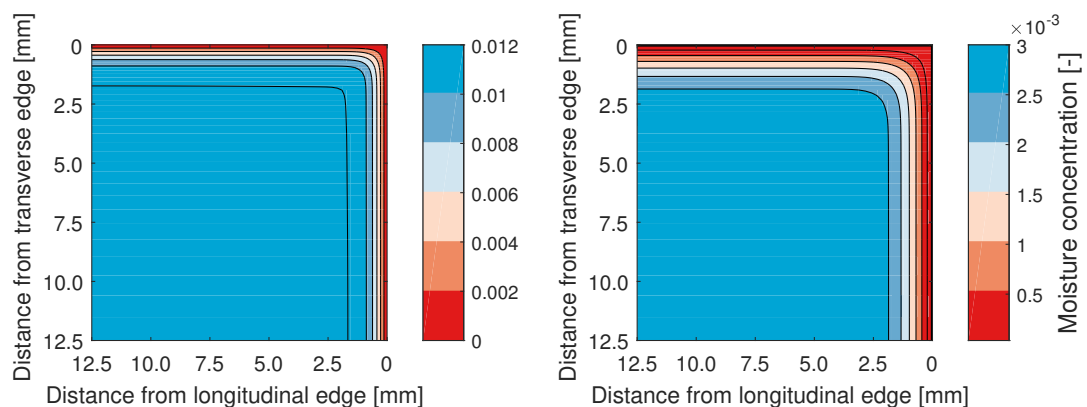


Figure 5.11 *Sensitivity analysis to limiting the mass diffusion simulation to one dimension.*

The results of the mesh convergence study for the moisture saturated component simulation with a lay-up of  $[90_{16}]$  are shown in Figure 5.12. The mesh generation was carried out in HyperMesh with element sizes ranging from 1 mm to 6 mm. It is noted that the amount of elements in through-thickness direction was kept to 1 for all meshes. The deformation behaviour shown in Figure 5.12 allows a clear conclusion. It is noted that the bending deformation is hugely underestimated for the meshes with a target element size of 4 mm and 6 mm. Moreover, reducing the element size from 2 mm to 1 mm was concluded to be of negligible difference and a mesh with a target element size of 1 mm has been utilised for all the consecutive stress simulations.

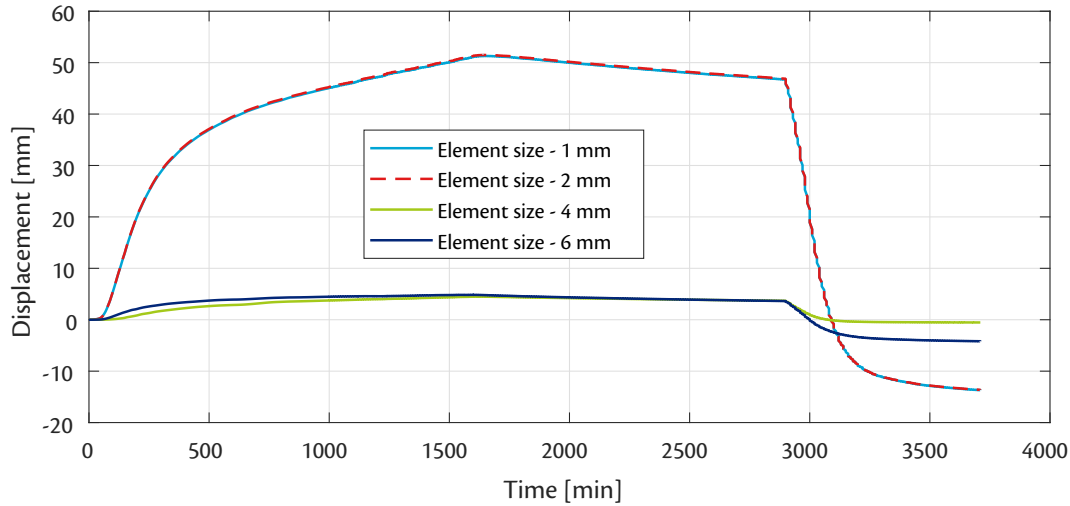


Figure 5.12 Results of the mesh convergence study of the stress simulation for the component validation experiment.

The qualitative influence of the time step size is displayed in Figure 3.9 and the effect on the deformation behaviour in the stress simulation for the moisture saturated component with a  $[90_{16}]$  lay-up is presented in Figure 5.13. It was concluded that the stress simulation results did not converge for the smallest time step of 0.05s. Although the deformation results have not converged yet, a time step of 0.25s was chosen for the consecutive simulations to keep the computational expenses to a comprehensible size.

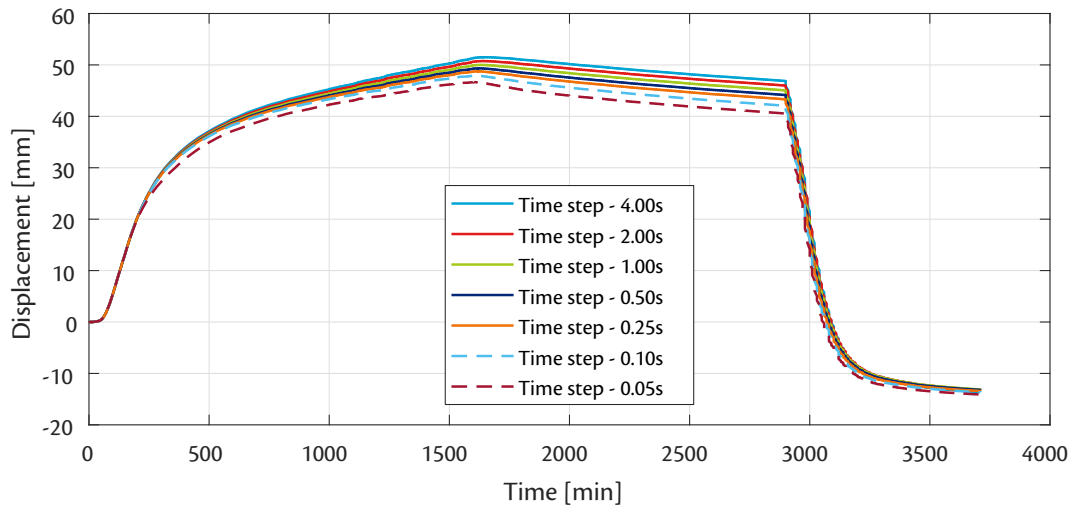


Figure 5.13 Results of the time step size convergence study of the stress simulation for the component validation experiment.





# 6

## Experimental validation

The strength and usability of a numerical model is mainly defined by its accuracy. The main purpose of the developed simulation is to assess the deformation behaviour of fibre reinforced thermoplastics during the automotive painting process. A validated simulation could for instance be used to assess the influence of changing the fibre orientation in a component to counteract undesired deformation during the thermal- and hygroscopic loading which may lead to lasting deformations when the matrix system cools down.

It is therefore important that the developed simulation is validated against experimental results. This chapter discusses the validation strategies that have been adopted and how the validation has been split into different levels of complexity. The subsequent sections each focus on one of the validation levels. Every section presents the chosen experimental setup, the results, and the conclusions that have been drawn from the comparison between the simulation and the experimental data.

### 6.1 Validation strategies

The main focus during the definition of the validation strategies was on making sure that potential errors or discrepancies could be effectively traced to either input parameters or modelling choices. Hence, the validation strategies have been chosen to grow in complexity level and to eliminate specific mechanisms to allow pinpointing of mechanisms that were not simulated correctly. The validation strategies have been carried out in the logical order of simple experiments to more advanced. This meant that potential discrepancies could either be corrected for or at the very least that these flaws were known before carrying out more complex experiments.

The experimental validation was divided into three separate levels. The first experimental validation was carried out with a dilatometer and implied that the specimen was free to expand under the thermal- and hygroscopic loads it was subjected to. The idea behind this method of validation is that it eliminates the dependence on stiffness. This only holds for unidirectional laminates as interlaminar stresses develop if there is a variation in fibre direction. The aim of the dilatometer validation method is to analyse if the thermal expansion, hygroscopic shrinkage, and polymer-chemical shrinkage are predicted correctly.

The stress relaxation behaviour could then be experimentally validated by restraining the expansion of the material that was previously unrestricted. The second validation method is based on measuring the out-of-plane deformation of a clamped tensile test specimen that is subjected to a specific temperature profile. The temperature profile has been chosen to resemble the thermal loads that the cathodic dip painting oven subjects the BIW to during the actual manufacturing process of a series model. The obvious reason is to rule out any differences that may exist on the polymer-chemical effects between an arbitrary temperature profile and the actual one which may influence the validity of the experiments regarding its intended usage.

The last set of validation experiments were carried out in an analogous method. However, these experiments were carried out with carbon fibre reinforced thermoplastic components that have the geometry of thermoset components currently in series production. The difference with the second validation level is the introduced geometric complexity. It is to be expected that the constitutive equations provide equal accuracy regardless of geometry. Nevertheless, the usability of the numerical model can only be properly tested with components as opposed to flat specimens. The chosen lay-ups for the components have been chosen to grow in complexity as well. The errors that have been identified by analysing the simulations and the corresponding experimental validation results have been used to improve the simulation prior to carrying out the simulations for the next validation level.

## 6.2 Dilatometer validation

The prediction of geometric changes of the thermoplastic composite material is validated through dilatometer experiments. The dilatometer experiments have been carried out with five different lay-ups for both dry and moisture saturated specimens. The selection of these lay-ups and the two conditioning states is congruent with the concept of increasing complexity. Any hygroscopic shrinkage or -expansion is eliminated when testing specimens that are dry. Applying this elimination technique allows to validate if the coefficients of thermal expansion have been derived correctly.

A control validation test has been carried out with a unidirectional specimen in transverse direction. This validation test is exactly similar to the transverse dilatometer experiment that was performed during the material characterisation that is described in Chapter 4. The result of the simulation is expected to be in close agreement with the validation experiment as there are no significant sources for error other than material scatter. Table 6.1 shows the lay-ups that have been tested and provides the reasons for choosing the specific laminates.

Table 6.1 *Lay-up selection for dilatometer validation experiments.*

Lay-up	Reason for selection
$[90_{16}^{\circ}]$	Calculation method for coefficient of thermal expansion
$[+30_4^{\circ} / -30_4^{\circ}]_s$	Correct prediction for interlaminar interaction in fibre-dominated direction
$[+60_4^{\circ} / -60_4^{\circ}]_s$	Correct prediction for interlaminar interaction in matrix-dominated direction
$[0_4^{\circ} / 90_4^{\circ}]_s$	Correct prediction of interlaminar interaction for largest stiffness variation
$[+45^{\circ} / -45^{\circ} / 0_5]_s$	Correct prediction for objective lay-up of series production component

The simulation of hygroscopic shrinkage can be validated with the moisture saturated specimens when the thermal expansion has been validated with the dry specimens. Hence, all presented lay-ups were tested for specimens in both dry and moisture saturated conditions. The conditioning of the specimens was carried out according to DIN EN ISO 1110 [76] in analogous manner to the conditioning of the specimens for the material characterisation, see Section 4.7. The specimen dimensions were also chosen similar to the material characterisation experiments and were prepared by waterjet cutting to be  $100 \times 8 \times 2 \text{ mm}^3$ .

The simulations of the dilatometer experiments require a temperature envelope as input. For these simulations it was assumed that the temperature distribution throughout the specimen is equal to the ambient temperature. This assumption had to be made due to inability to measure the surface temperature of the specimen inside the dilatometer. The ambient atmosphere inside the dilatometer consists of helium. The thermal conductivity of Helium at  $167\text{ }^{\circ}\text{C}$  is  $202.5\text{ mW}/(\text{m K})$  [95] and roughly 5.5 times as high in comparison to the thermal conductivity of air at that temperature. The excellent thermal conductivity of helium provides an argument for the validity of the mentioned assumption. The temperature envelope of the dilatometer validation experiments is shown in Figure 6.1.

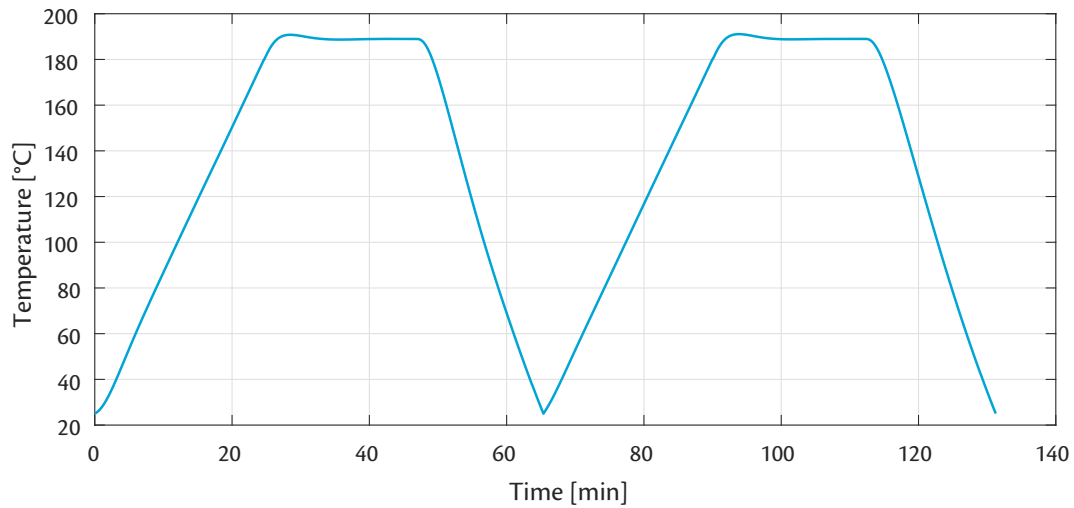


Figure 6.1 *The temperature envelope used for the validation dilatometer experiments.*

The experimental results of the dilatometer experiments are shown in chronological order of testing. The simulation results are also depicted in the figures for comparison and to draw conclusions on the accuracy of the prediction. The drawn conclusions are stated in between the figures for a convenient reading style. As mentioned, the first dilatometer validation experiment that was carried out concerned the dry unidirectional laminate measured in transverse direction. The results of this experiment are shown in Figure 6.2.

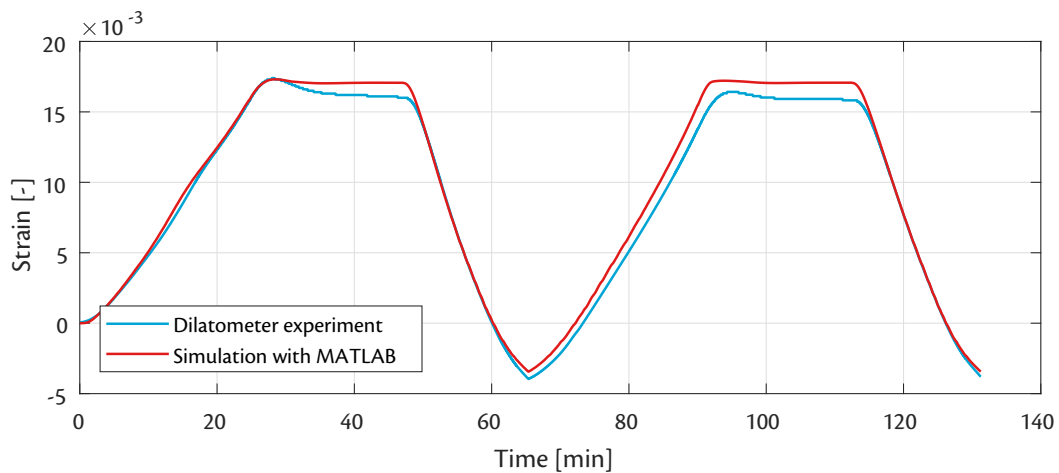


Figure 6.2 *Experimental data and simulation of validation dilatometer experiment with a dry specimen with a  $[90_{16}^{\circ}]$  lay-up.*

From comparison of the experimental data and the simulation of the dry specimen with the  $[90_{16}]$  lay-up that is shown in Figure 6.2 it can be concluded that the derivation of the coefficients of thermal expansion was carried out correctly. The maximum error found between the simulation and the experimental data is situated at the end of the hold period after the second heating. The constant discrepancy during the second heating indicates that the coefficients of thermal expansion are accurate. The offset between the two lines can be attributed to the inability to capture the shrinkage during the first hold period. This shrinkage occurs due to the change from  $\gamma$ -form into  $\alpha$ -form of the crystals which has not been accounted for. The results of the dilatometer experiment that was carried out with the specimen that had a lay-up of  $[+30_4 / -30_4]_s$  are shown in Figure 6.3 together with the predicted according to the simulation.

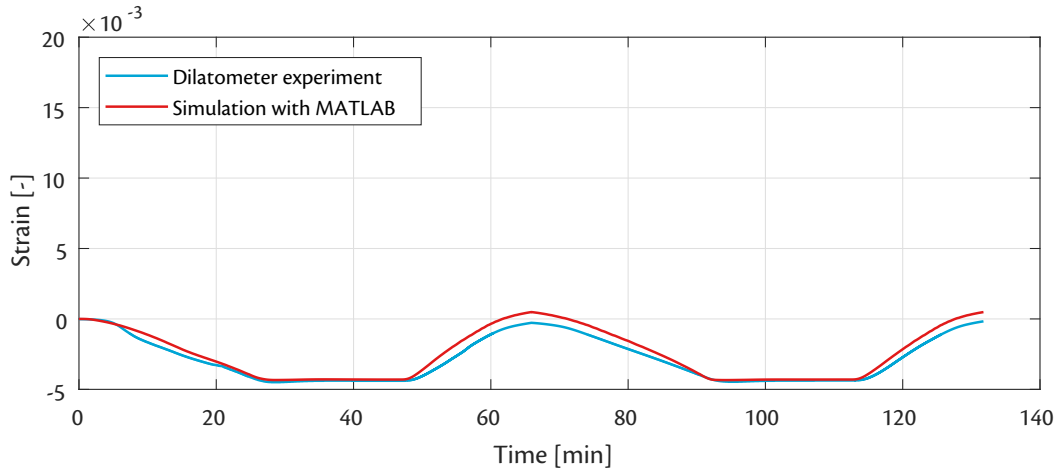


Figure 6.3 *Experimental data and simulation of validation dilatometer experiment with a dry specimen with a  $[+30_4 / -30_4]_s$  lay-up.*

By comparing the two plots in Figure 6.3 it can be stated that both the qualitative and quantitative prediction is in proper agreement with the experimental results. The maximum error is found at the lowest temperature after the first heating cycle, contrary to the location of maximum error for the  $[90_{16}]$  lay-up. The predicted value at the maximum temperature shows marginal discrepancies from which it can be concluded that possible sources of error are the coefficients of thermal expansion for the cooling segment in longitudinal direction.

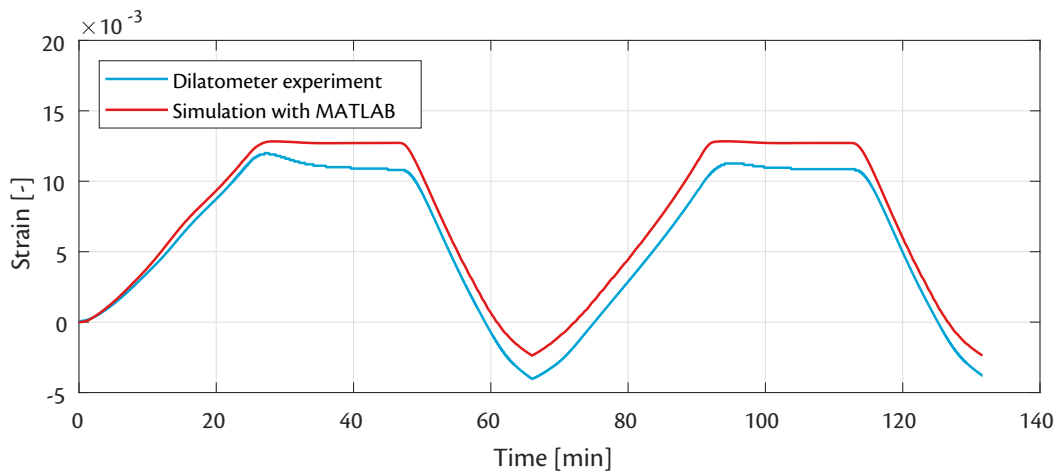


Figure 6.4 *Experimental data and simulation of validation dilatometer experiment with a dry specimen with a  $[+60_4 / -60_4]_s$  lay-up.*



The simulation of the  $[+60_4^\circ / -60_4^\circ]_s$  lay-up was intended to analyse how well the expansion of a multi-directional laminate in matrix-dominated direction could be predicted. The two plots in Figure 6.4 show excellent qualitative agreement. However, the quantitative differences are larger in comparison to the results that are shown in Figure 6.2 for the unidirectional laminate in transverse direction. Interlaminar stresses that are formed because of stiffness jumps between the two sets of laminae are concluded to be the reason for this observation. The suspicion of possible sources of error in the cooling coefficients of the lamina in longitudinal direction is reinforced by the results for the  $[0_4^\circ / 90_4^\circ]_s$  lay-up, shown in Figure 6.5. Please note that the scale of the strain has been adjusted in comparison to the previous figures to allow proper inspection.

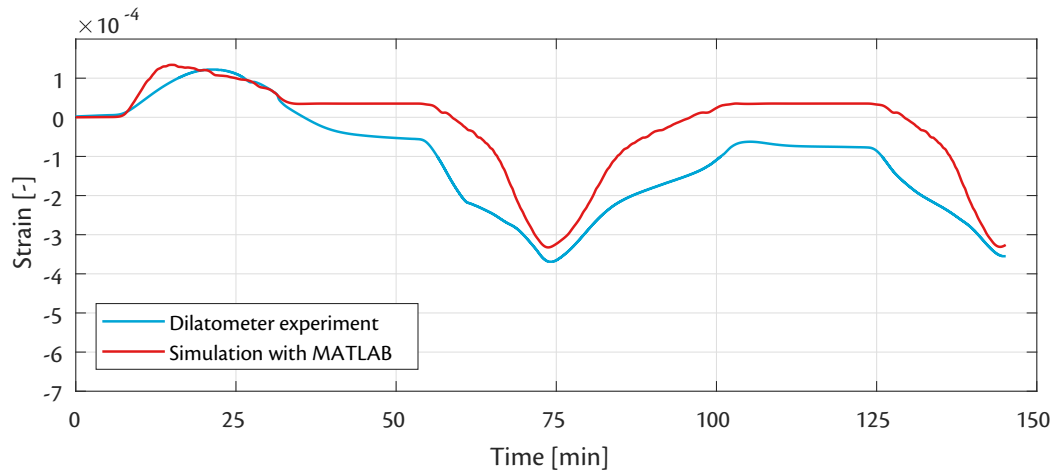


Figure 6.5 *Experimental data and simulation of validation dilatometer experiment with a dry specimen with a  $[0_4^\circ / 90_4^\circ]_s$  lay-up.*

It can be concluded that the predicted strain values shown in Figure 6.5 are too small in comparison to the measured values. The proper agreement between the simulation and the experimental values for the  $[90_{16}^\circ]$  lay-up in Figure 6.2 rules out that this behaviour can be attributed to the coefficients of thermal expansion in transverse direction. Hence, it is concluded that the poor agreement shown in Figure 6.5 could be attributed to three individual mechanisms.

The first possibility is that the predicted shrinkage of the laminae with a  $0^\circ$  orientation is too small. The other two possibilities are that the shrinkage of the layers with a  $0^\circ$  orientation is contributing too little to the overall deformation or that the expansion of the  $90^\circ$  orientation laminae are contributing too much. It is expected that the predicted shrinkage of the layers with a  $0^\circ$  orientation is too small as this was also concluded from the results shown in Figure 6.3. Another reason for this expectation is the extreme stiffness difference in longitudinal direction between the  $0^\circ$  and  $90^\circ$  layers. A miscalculation in matrix stiffness does not cause large discrepancies in laminate strain as the difference in longitudinal stiffness of the two distinct layers is already factor 10.

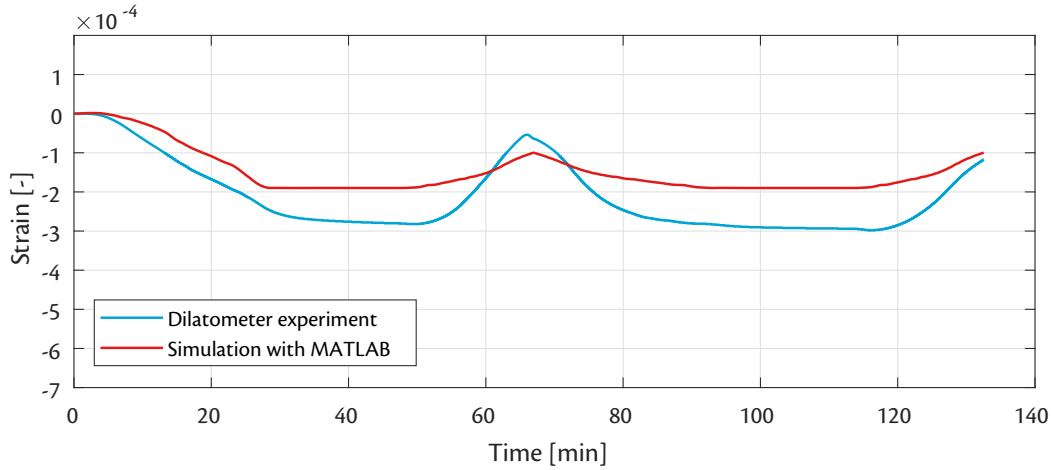


Figure 6.6 *Experimental data and simulation of validation dilatometer experiment with a dry specimen with a  $[+45^\circ / -45^\circ / 0_5]_s$  lay-up.*

The results for the laminate with the lay-up  $[+45^\circ / -45^\circ / 0_5]_s$  are shown in Figure 6.6 and show a similar behaviour in terms of discrepancy in comparison to Figure 6.5 that displays the experimental data and simulation of the  $[0_4 / 90_4]_s$  lay-up. The simulated strain is in general lower than the experimentally measured strain. This specific lay-up has only four layers in total that are not aligned in longitudinal direction of the laminate. This reinforces the argumentation for why it is believed that the coefficients of thermal expansion in longitudinal direction of the laminae are not fully correct. However, it must be stated that the strain scale in Figures 6.5 and 6.6 are almost a complete order of magnitude lower and that the qualitative prediction is in proper agreement.

The experimentally measured strain and the corresponding predicted values for the specimens that had been conditioned to saturation moisture content are shown in the same order as the dry specimens throughout Figures 6.7 to 6.11. The results of these dilatometer experiments will be discussed concerning the accuracy of the coefficients of hygroscopic expansion derived in Section 4.4 and the diffusion coefficients that have been determined in Section 4.2. The findings for the coefficients of thermal expansion based on Figures 6.2 to 6.6 will be accounted for in the evaluation of the data. Figure 6.7 provides the results for the moisture saturated laminate with a  $[90_{16}]$  lay-up.

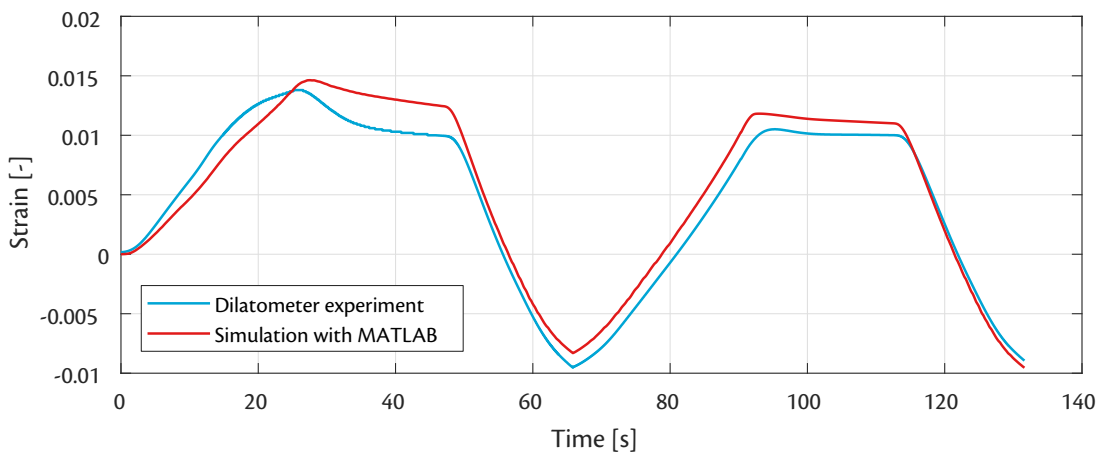


Figure 6.7 *Experimental data and simulation of validation dilatometer experiment with a specimen conditioned to full moisture saturation with a  $[90_{16}]$  lay-up.*

It was concluded that any discrepancies visible in Figure 6.7 can be fully attributed to the coefficients of hygroscopic expansion and the diffusion coefficients due to the excellent agreement of the predicted maximum strain with the measured value after the first heating for the dry specimen with similar lay-up. Moisture that is leaving the specimen has hygroscopic shrinkage of the matrix constituent as a consequence. The overshoot that is visible in Figure 6.7 after reaching the maximum temperature can thus be explained by either too low diffusion coefficients or too low coefficients of hygroscopic expansion in transverse direction.

However, the excellent agreement during the second cooling segment confirms the correct values of hygroscopic expansion in transverse direction. Higher simulated strain values are to be expected at every moment in time if the diffusion coefficients are too low in general. Yet, the simulated strain values are lower than the measurement for the first heating. It is therefore concluded that the moisture egress at the relatively low temperatures is simulated to be too fast. It then holds that the diffusion behaviour at elevated temperatures is predicted to be too slow, resulting in the overshoot.

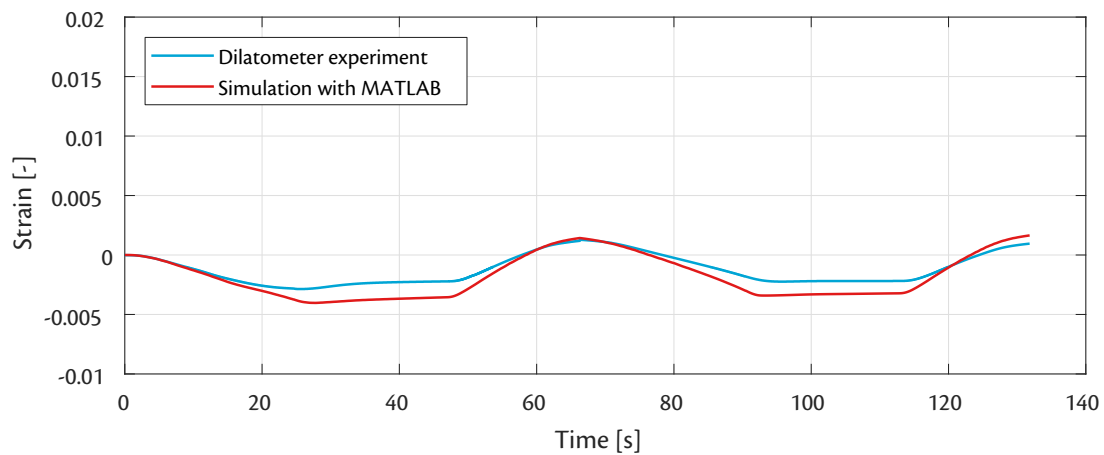


Figure 6.8 *Experimental data and simulation of validation dilatometer experiment with a specimen conditioned to full moisture saturation with a  $[+30_4^\circ / -30_4^\circ]_s$  lay-up.*

Figures 6.3 and 6.8 display the simulations and the measured strain values for the  $[+30_4^\circ / -30_4^\circ]_s$  in dry and moisture saturated condition, respectively. The high level of agreement between the predicted values and the measurements at the hold period that is visible for the dry specimen is not found for the specimen conditioned to saturation moisture content. Shrinkage of the lamina in transverse direction leads to a decrease in strain in longitudinal direction for the  $[+30_4^\circ / -30_4^\circ]_s$  lay-up.

It must be concluded by inspection of Figure 6.8 that the moisture content is simulated to be too low in comparison to the actual moisture content. This conclusion is based on the proper agreement that is found in Figure 6.3 and the assumption that the coefficients of hygrothermal expansion are correct based on the excellent agreement at the end of the dilatometer experiment with the moisture saturated specimen with the  $[90_{16}]$  lay-up. It is noted that this conclusion is in conflict with the reasoning provided for the unidirectional moisture saturated lay-up shown in Figure 6.7.

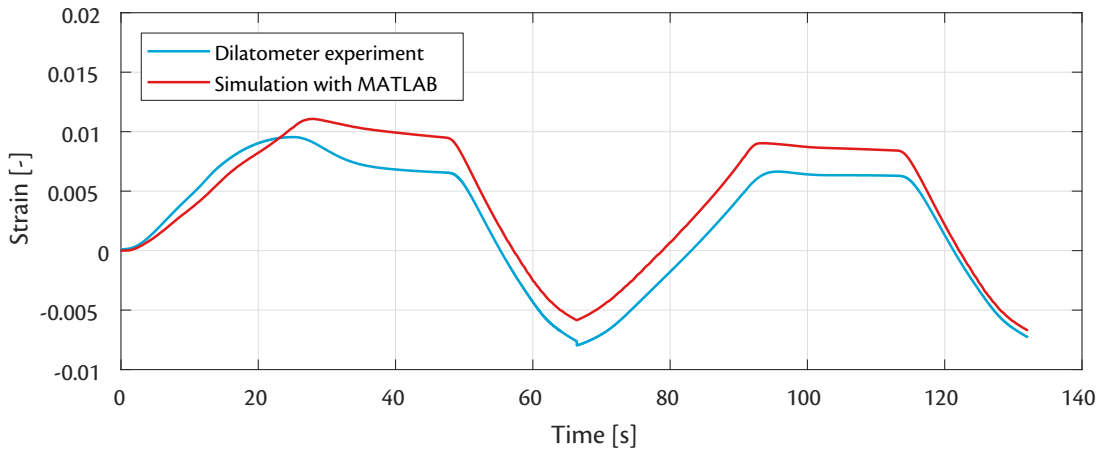


Figure 6.9 *Experimental data and simulation of validation dilatometer experiment with a specimen conditioned to full moisture saturation with a  $[+60_4^\circ / -60_4^\circ]_s$  lay-up.*

The discrepancy between the simulated strain values and the experimental data from the dilatometer experiments of the moisture saturated laminate with a lay-up of  $[+60_4^\circ / -60_4^\circ]_s$  depicted in Figure 6.9 show an identical trend to that of the comparable specimen with the  $[90_{16}^\circ]$  lay-up. It is therefore stated that the calculation of the effective coefficient of expansion, necessary due to the different orientation of the plies, is carried out correctly.

The qualitative agreement between the simulated strain and the experimentally measured strain for the laminate that was chosen for the largest jump in stiffness between the plies is of satisfactory level. The quantitative values shown in Figure 6.10 are only in good agreement for the low temperature range after the first- and second cooling periods. The discrepancy that is visible at elevated temperatures is expected to be due to the moisture diffusion being simulated to be too quick. This reasoning was also mentioned for the results of the laminate with the  $[+30_4^\circ / -30_4^\circ]_s$  lay-up of which the results are shown in Figure 6.8.

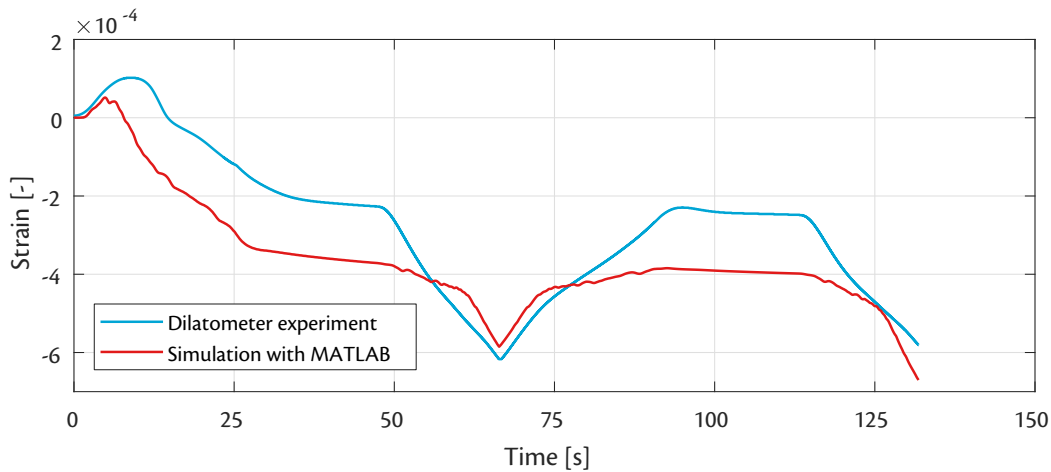


Figure 6.10 *Experimental data and simulation of validation dilatometer experiment with a specimen conditioned to full moisture saturation with a  $[0_4^\circ / 90_4^\circ]_s$  lay-up.*

The results for the laminate with the  $[+45^\circ / -45^\circ / 0_5]_s$  lay-up are shown in Figure 6.11. It can be stated that the discrepancies are larger for the moisture saturated specimen in comparison with the results of the corresponding dry laminate that is shown in Figure 6.6. As the magnitude of the coefficients of hygroscopic expansion have been validated by the comparison for the  $[+60_4^\circ / -60_4^\circ]_s$  lay-up in Figure 6.9, this mismatch between simulation and measurement has been attributed to the exaggerated rate of moisture egress.

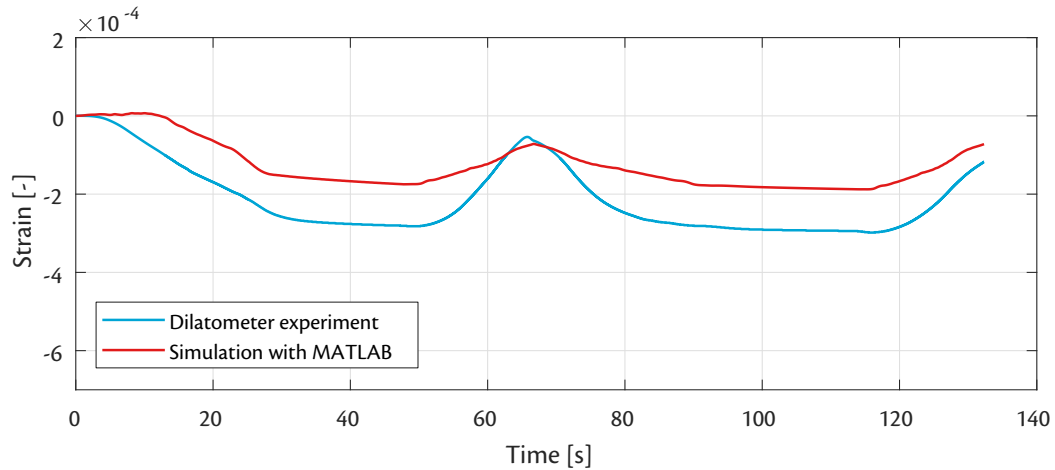


Figure 6.11 *Experimental data and simulation of validation dilatometer experiment with a specimen conditioned to full moisture saturation with a  $[+45^\circ / -45^\circ / 0_5]_s$  lay-up.*

It is noted in conclusion of this section that the magnitudes of both the coefficients of thermal- and -hygroscopic expansion have been successfully determined during the material characterisation tests. However, comparisons between the simulations and the measured values for the moisture saturated strains have yielded conflicting trends for the rate at which moisture diffuses out of the matrix material. These remarks have been taken into account during the assessment of both the coupon- and component level of validation. The discrepancies of all simulations and the experimental dilatometer data at the moment of reaching the maximum temperature and at the end of the experiment are displayed in Table 6.2. Please note that the error at the end of the simulation is calculated as the difference in strain at the end of the measurement divided by the measured value at maximum temperature. This allows comparison between the quality of the prediction for both moments in time.

Table 6.2 *Discrepancies between simulation and experimental data for the dilatometer validation experiments.*

Laminate	Conditioning	Error at max T	Error at max t	Graph
$[90_{16}^\circ]$	Dry	-0.6%	2.1%	Figure 6.2
$[+30_4^\circ / -30_4^\circ]_s$	Dry	-3.4%	-15.1%	Figure 6.3
$[+60_4^\circ / -60_4^\circ]_s$	Dry	6.6%	11.2%	Figure 6.4
$[0_4^\circ / 90_4^\circ]_s$	Dry	9.9%	21.6%	Figure 6.5
$[+45^\circ / -45^\circ / 0_5]_s$	Dry	-22.8%	-9.3%	Figure 6.6
$[90_{16}^\circ]$	Moist	7.5%	-4.1%	Figure 6.7
$[+30_4^\circ / -30_4^\circ]_s$	Moist	40.1%	-17.3%	Figure 6.8
$[+60_4^\circ / -60_4^\circ]_s$	Moist	21.2%	5.2%	Figure 6.9
$[0_4^\circ / 90_4^\circ]_s$	Moist	127.3%	27.8%	Figure 6.10
$[+45^\circ / -45^\circ / 0_5]_s$	Moist	-39.4%	-30.9%	Figure 6.11

### 6.3 Coupon level validation

The level of accuracy of the relaxation behaviour of the composite material was aimed to be validated by conducting the coupon level validation experiments. These experiments were carried out after the dilatometer validation experiments to already have knowledge about the validity of the thermal expansion, hygroscopic shrinkage, polymer-chemical shrinkage, and diffusion behaviour of the carbon fibre-reinforced thermoplastic. This section describes how the coupon level validation experiment was defined and displays the results of both the experimental measurements and the predicted values that were generated through simulations. The conclusions that were to be carried over to the component level validation are mentioned as concluding part to this section.

The necessity to measure a stiffness related parameter was derived inherently from the goal of this validation level. The ultimate goal of the numerical model that was developed is to predict the deformation behaviour of a clamped series component subjected to the thermal envelope equivalent to a drying oven after the cathodic dip painting process. Hence, it was decided to measure the out-of-plane bending deformation of a tensile test specimen as this parameter is also of interest for the overall objective of the numerical model.

In determining the experimental setup of the coupon level validation experiments it had to be taken into account that measuring the bending deformation of the tensile test specimen had to be performed through a glass panel of the test oven. The usage of a distance measuring device relying on a laser was discarded because of this. There are proximity sensors that operate through glass, but the detection naturally only works for one particular spot only. Utilising optical measurement systems allow measurements to be made through glass as well and they provide the opportunity to measure more than one location on the specimen.

The measurements of the out-of-plane deformation during the coupon level validation experiments were carried out with the PONTOS tracking system by GOM. The method of tracking the deformation was chosen to be point tracking and reflective markers to infrared light had to be placed on the tensile test specimen. The diameter of the markers was larger than the thickness of the test specimen and for this reason reinforcing strips of aluminium have been applied to create a larger contact area for the markers. The aluminium has only been applied on the side area of the tensile test specimen to limit the increase in bending stiffness of the test specimen by the metal.

Additional measurements have been carried out with an ARAMIS system by GOM to obtain a strain field at the center of the test specimen. This measurement was performed to validate the prediction of the strain field at the center of the test specimen during the out-of-plane displacement. The application of the speckled pattern required for the ARAMIS system has been carried out in an analogous method to the ARAMIS measurements that were used for the determination of the major Poisson's ratio, as described in Section 4.6.

A fixture has been designed to clamp the test specimen during the validation experiments. A list of requirements for this fixture was defined to come up with design concepts after which the final design was realised. This list of requirements is shown below.

- The thermal expansion of the experimental setup must be minimised.
- The material of the experimental setup must be resistant to the temperature profile.
- The experimental setup must facilitate clamped boundary conditions as close as possible.
- The specimen must be visible from the side to allow proper measuring of midplane deformation.
- The experimental setup is subjected to a feasible cost budget.

The fixture has been designed to compensate thermal expansion of the material that is utilised. Geometrical compensation for the thermal expansion is only possible when parts of the fixture are manufactured from at least two materials that have a variation in coefficient of thermal expansion. The principle of geometrical compensation has been applied to the conceptual geometry shown in Figure 6.12. The conceptual geometry that is displayed in Figure 6.12 has been chosen to keep the calculations and manufacturing of the fixture as simple as possible. The symbolic definitions of the different lengths and the only independent angle of the geometry are also indicated in Figure 6.12.

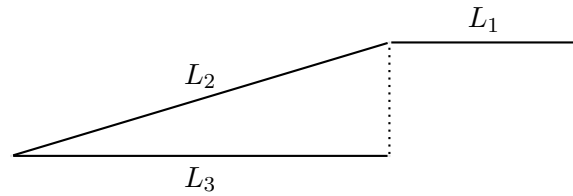


Figure 6.12 *Geometrical concept to incorporate geometric compensation for the thermal expansion of the fixture.*

The distance between the boundary conditions of the test specimen is 200 mm. The objective in defining the lengths that are shown in Figure 6.12 is to maintain a constant length between the boundary conditions irrespective of temperature. This is achieved when the displacement of the variable  $x$ , as defined in Figure 6.12, remains equal to zero. The mathematical expression for this variable is shown in Eq. 6.1. It is noted that the end of segment  $L_1$  must be chosen to be exactly above the end of length segment  $L_3$  for Eq. 6.1 to be valid. The angle  $\beta$  can be chosen arbitrarily, but does influence the size of the fixture.

$$x(T) = L_1\alpha_1\Delta T + L_2\alpha_2\Delta T \cdot \cos \beta - L_3\alpha_3\Delta T \quad 6.1$$

The term  $\Delta T$  is used in Eq. 6.1 to indicate the change in temperature that the fixture is subjected to. Furthermore, the relation shown in Eq. 6.1 contains three individual lengths of which  $L_2$  can be fully expressed by means of  $L_3$  and  $\beta$ . The expression shown in Eq. 6.2 allows substitution back into Eq. 6.1 to eliminate the occurrence of  $L_2$ .

$$L_2 = \frac{L_3}{\cos \beta} \quad 6.2$$

The result of the mentioned substitution is shown in Eq. 6.3 after factoring out the change in temperature. It is mentioned that the part inside the parentheses must be equal to zero to obtain a non-trivial solution to the displacement of point  $x$ .

$$x(T) = \Delta T (L_1\alpha_1 + L_3\alpha_2 - L_3\alpha_3) \quad 6.3$$

It is then decided that the material of segments 1 and 2 are identical. The material of segment 3 must have a larger coefficient of expansion than segments 1 and 2 in order for a geometric compensation to be possible. A constant of proportionality between the coefficients of thermal expansion is defined with the symbol  $k$ . The mathematical implications of the previous are shown in Eq. 6.4.

$$\begin{aligned}\alpha_3 &= k \cdot \alpha_1 \\ \alpha_2 &= \alpha_1\end{aligned}\tag{6.4}$$

Substitution of the relations shown in Eq. 6.4 into the expression of Eq. 6.3 results in a governing formula that only consists of one coefficient of expansion and the constant of proportionality, as shown in Eq. 6.5.

$$x(T) = \Delta T (L_1 \alpha_1 + L_3 \alpha_1 - L_3 k \cdot \alpha_1)\tag{6.5}$$

The required proportions between segments 1 and 3 that ensure zero movement of the location of the boundary conditions can be expressed as displayed in Eq. 6.6.

$$x(T) = 0 \quad \Rightarrow \quad L_3 = \frac{L_1}{k - 1} \quad (\text{or } \Delta T = 0)\tag{6.6}$$

The material of the fixture for the coupon level validation experiments was chosen to be graphite due to its low coefficient of thermal expansion. Two types of graphite material had been selected and the manufacturing of the fixture was ordered at SGL Group. Measurements of the coefficients of thermal expansion have been performed on the blocks that were used for the manufacturing of the fixture in order to adjust the dimensions of the fixture specifically to the material prior to manufacturing. The results of these measurements are shown in Figure 6.13.

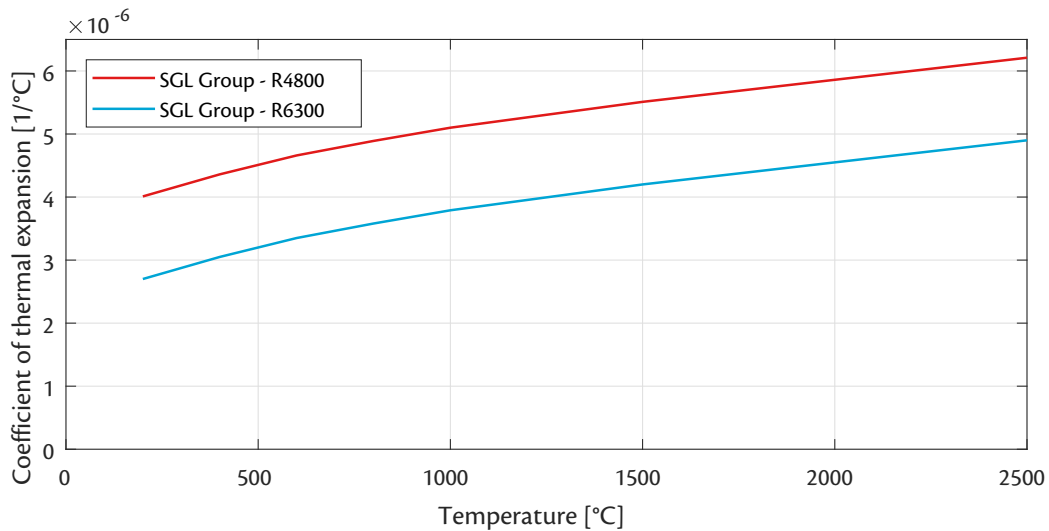


Figure 6.13 Coefficients of thermal expansion of the two types of graphite material that were used for the fixture of the coupon level validation experiments.



The length of segment  $L_3$  was calculated to be 206.11 mm, based on the values of the coefficients of thermal expansion that were provided by SGL Group. The finalised fixture for the coupon level validation is shown in Figure 6.14 and the corresponding technical drawings are shown in Appendix B in Figure B.1 and Figure B.2. The manufacturing tolerances were set lower for the surfaces of the parts that were in contact with each other. This has been decided to increase the precision of the fit of the test specimen between the two clamping arms. A precise fit is necessary to realise clamped boundary conditions throughout the entire validation experiment.



Figure 6.14 *The fixture for clamping the tensile test specimen during the coupon level validation experiments.*

A control experiment without test specimen in the fixture has been performed to measure the deformation of the fixture to see if the geometric compensation yielded the intended result. Additionally, both the air temperature inside the oven and the surface temperature of a suspended specimen were measured to allow the determination of a convection coefficient. The convection coefficient is specific to different ovens as it depends on the volume inside the oven and the circulation of air [96]. It is noted that the same oven was used for all coupon- and component level validation experiments.

The heating- and cooling rate of the oven were determined to be roughly  $4\text{ }^{\circ}\text{C}/\text{min}$  and  $50\text{ }^{\circ}\text{C}/\text{min}$ , respectively. The maximum temperature of the ambient air and of the surface are not equal due to the reduction in circulation as the ambient air reaches a constant temperature. This has been included in the heat transfer simulation for the coupon- and component level models. The convection coefficient was determined to be  $25\text{ W}/(\text{m}^2\text{ K})$  and a comparison between the simulated- and measured surface temperature of the specimen is given in Figure 6.15.

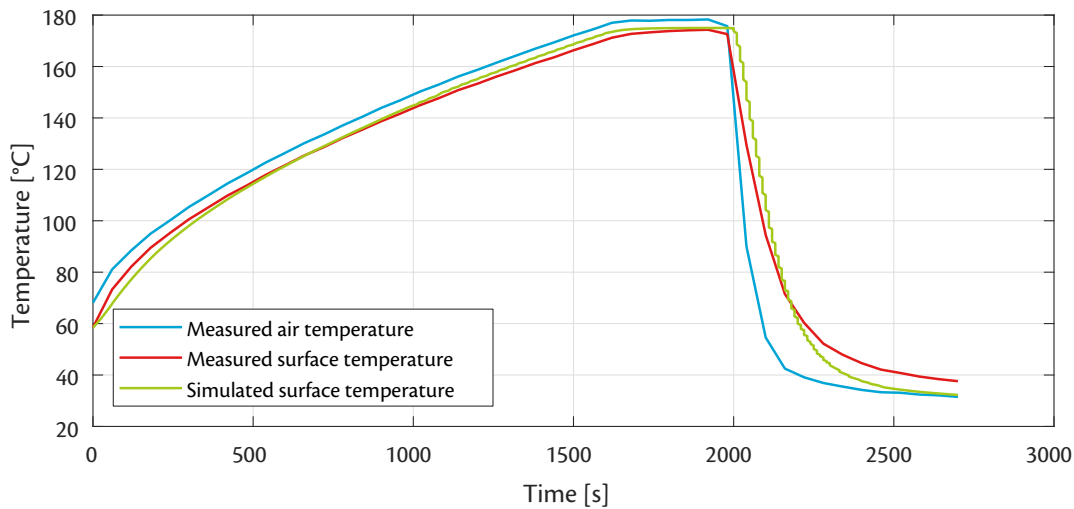


Figure 6.15 *Simulated surface temperature by means of convection in comparison to the measured air- and measured surface temperature of the suspended specimen.*

The predicted values of the center out-of-plane deformation for the dry- and moisture saturated that were obtained by means of simulation are shown in comparison with the obtained values from the optical measurements in Figure 6.17. An image of the experimental setup during the measurement is shown in Figure 6.16. The upper part of Figure 6.17 shows the comparison for the dry coupon with a unidirectional lay-up of  $[90_{16}^{\circ}]$  and it is concluded that the agreement between simulation and experiment are satisfactory. The maximum deflection is captured at both the right moment and with the right magnitude. Furthermore, the prediction that the component does not show zero deflection at the end of the experiment is also correct. It is noted that the deformation during the heating segment is overestimated.

It is concluded by inspection of the lower part of Figure 6.17 that the magnitude of deflection for the moisture saturated component with a lay-up of  $[90_{16}^{\circ}]$  has also been correctly predicted. However, the moment in time of maximum deflection is significantly later for the simulation in comparison with the measurement. The deflection during the heating segment is underestimated contrary to the simulation for the dry component. Nevertheless, the agreement between simulation and experiment is concluded to be satisfactory as the discrepancies at maximum deflection are equal to 0.9% and 1.5% for the dry- and moisture saturated coupons, respectively.



Figure 6.16 *The utilised experimental setup to measure the deflection of the coupons and components.*

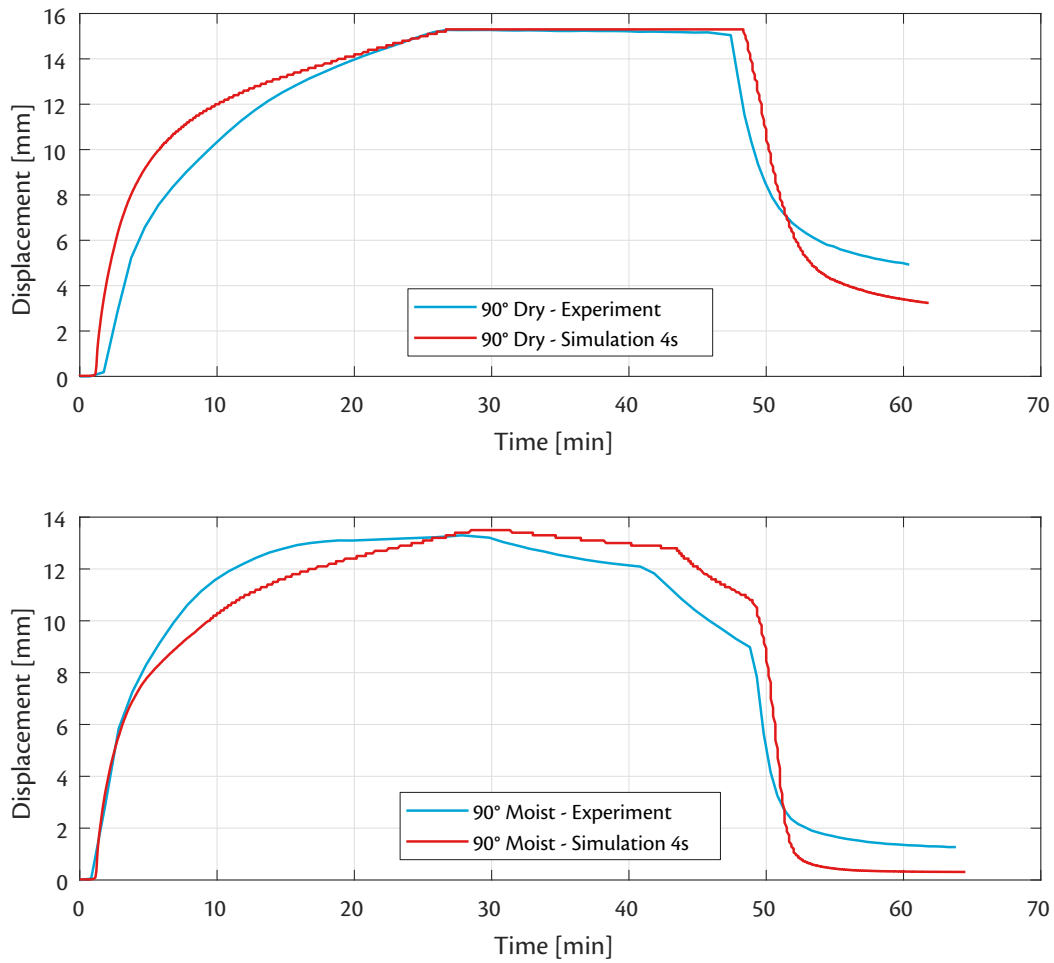


Figure 6.17 *Experimental data and simulation of the center out-of-plane deformation of a dry- and moisture saturated tensile test specimen with  $[90_{16}^{\circ}]$  lay-up subjected to the cathodic dip painting temperature profile.*

It is noted that the fixture displayed bending deformation in the two oblique arms due to the force that is introduced by the thermal expansion of the coupon. The variation in clamping length of the specimen has a significant effect on the out-of-plane deformation during the experiment. It is therefore suggested as a recommendation for further research to include the variation in clamping length in the numerical model to analyse the effect of this disturbance. A varying clamping length of the roof bow is also found in the actual manufacturing process because of the thermal expansion of the metal roof supports it is clamped to. Hence, validating the numerical model to include varying boundary conditions will improve its usefulness for design purposes.

## 6.4 Component level validation

A similar approach as described in Section 6.3 was taken for the component level validation. The components were clamped on both ends by means of clamping pressure and bolts that pass through the component. Again, a temperature profile was selected for the experiment similar to the one utilised in the cathodic dip painting oven found in the industrial process. However, the geometric compensation of thermal expansion of the fixture that was adopted for the coupon level validation experiments could not be implemented for the fixture of the component due to size constraints imposed by the oven used during the measurements. The fixture that was used for the component level validation experiments is shown in Figure 6.18. The technical drawings of the fixture used for the component level validation can be found in Appendix B.



Figure 6.18 *The fixture for clamping the component during the component level validation experiments.*

The results of the validation experiment for the roof bow that was manufactured with a lay-up of  $[90_{16}^{\circ}]$  are shown in Figure 6.19. The optical measurement of the dry component with the  $[90_{16}^{\circ}]$  lay-up was not usable for comparison due to loss of the tracking points during the early stage of the measurement. It is noted that the sharp variation in the measured out-of-plane deflection at the center of the component visible in Figure 6.19 is due to failure of the laminate close to one of the clamped sides. This occurred at roughly 57 minutes and an annotation has been added in the plot for clarity.

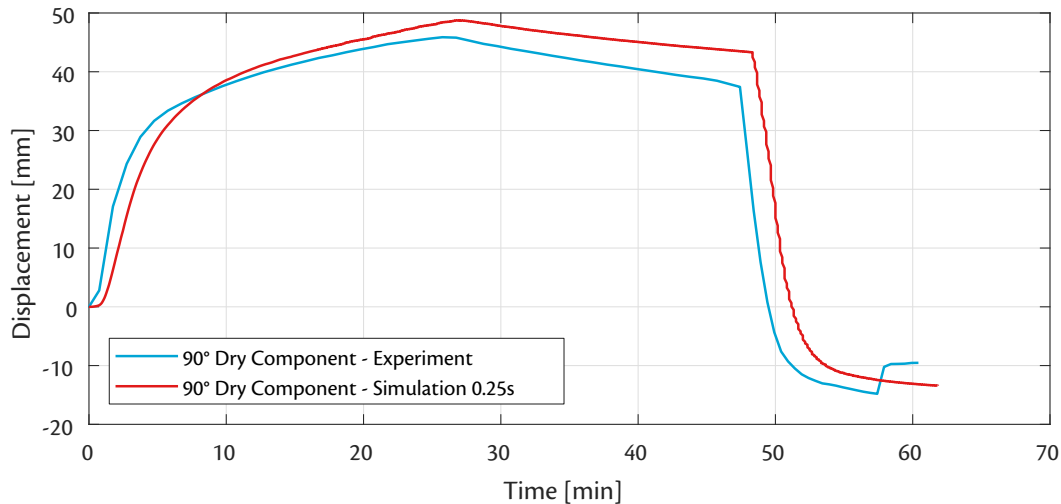


Figure 6.19 *Experimental data and results of the initial simulation approach of the center out-of-plane deformation of a dry reference component with  $[90_{16}^{\circ}]$  lay-up subjected to the cathodic dip painting temperature profile.*

The level of agreement between the simulation and the measured deflection is slightly lower than found for the  $[90_{16}]$  coupon, shown in Figure 6.17. The discrepancy of the maximum deflection between the measurement and the predicted value by the numerical model is roughly 6.2%. The prediction that the maximum deflection decreases during the temperature-hold period because of moisture diffusing out of the composite material is correctly simulated. The moment in time at which the maximum deflection occurs is precisely simulated and also the simulated negative deflection at the end of the experiment is correct.

The rate of decrease in the deflection of the component with the  $[90_{16}]$  lay-up is underestimated which may indicate that the moisture egress is simulated to be too slow. Conflicting conclusions were drawn about the rate of mass diffusion for the dilatometer validation experiments and this result provides an argument in favour of the conclusion that the mass diffusion is simulated too slowly. Nevertheless, the maximum positive deflection is conservatively simulated and could be used for initial design purposes. It must be stated, however, that a lay-up of  $[90_{16}]$  is not realistic for series production.

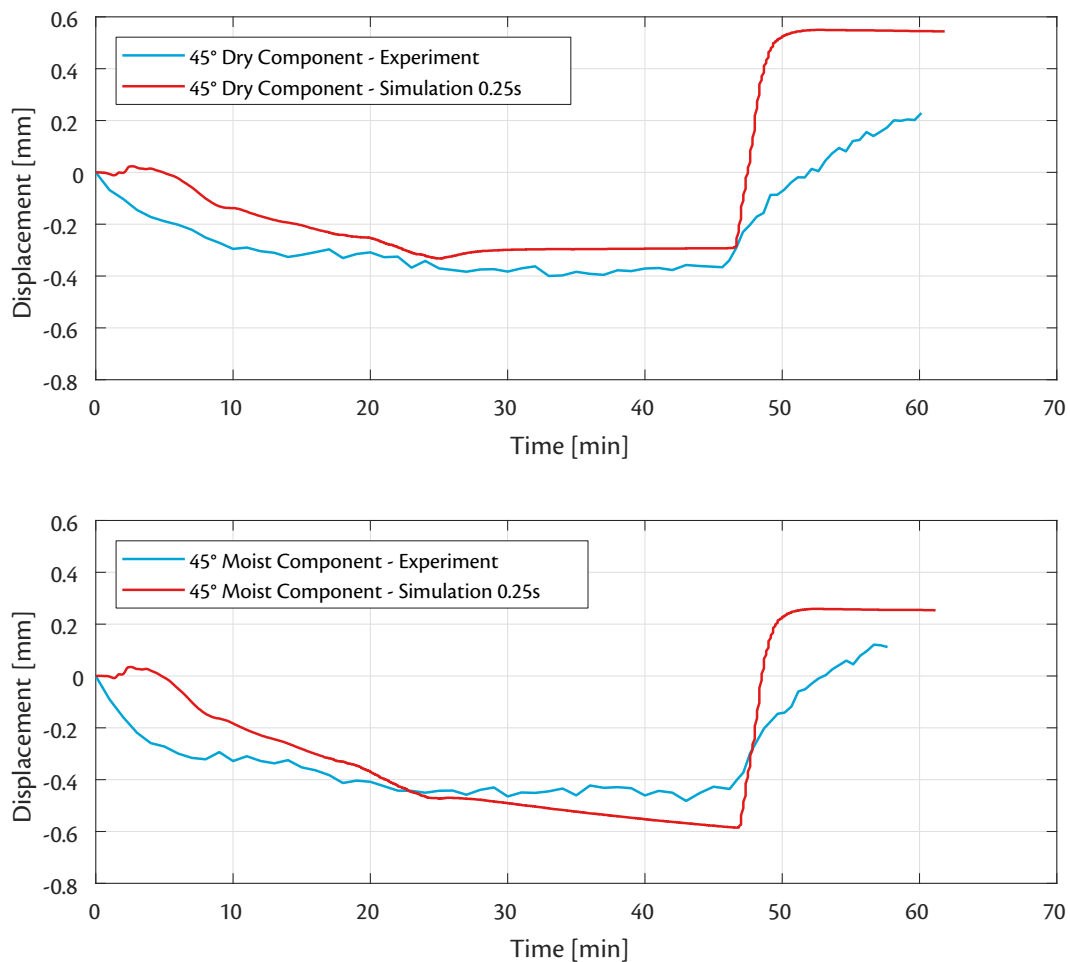


Figure 6.20 *Experimental data and results of the initial simulation approach of the center out-of-plane deformation of a dry reference component with  $[0/+45^\circ/-45^\circ/0_4]_s$  lay-up subjected to the cathodic dip painting temperature profile.*

The objective lay-up for the roof bow of the 7 Series is equal to  $[0/+45^\circ/-45^\circ/0_4]_s$  and both measurements and simulations were carried out with this lay-up to assess the accuracy of the simulation for a realistic composite lay-up plausible for industrial application. The results of both the experiment and the simulation are shown in Figure 6.20. The upper part of Figure 6.20 applies to the dry component, whereas the lower part displays the results of the moisture saturated component. By inspection of Figure 6.20 it can be concluded that the general deformation behaviour of the component is simulated correctly. The out-of-plane deformation behaviour during the heating phase of the measurement is downwards because of the many plies in the lay-up with fibres parallel to the longitudinal direction of the component.

From the results of the dilatometer experiments carried out with unidirectional laminates in longitudinal direction, shown in Figure 4.6, it is known that a contraction of the laminate is observed under thermal loading. A contraction of the  $[0/+45^\circ/-45^\circ/0_4]_s$  lay-up is also to be expected and implies that the center of the component must move downwards for the component to become shorter. The simulation results indicate that the initial out-of-plane deformation of the center of the component is upwards. This is not in agreement with the experimental measurements and thus questions the validity of the simulation. Moreover, the decline in simulated deflection that is shown at approximately 25 minutes in the upper part of Figure 6.20 is not to be expected because the component is dry and the expansion behaviour of  $0^\circ$  plies shown in Figure 4.6 provide no indication for this decline.

A component in both dry- and moisture saturated conditions with a lay-up of  $[(+60^\circ/-60^\circ)_3/0^\circ]_s$  was both measured and simulated in addition to the two previous lay-ups to include a component with a multi-directional laminate with a large fraction of matrix-dominant plies. The results of the experiment and simulation for this lay-up are shown in Figure 6.21 and have revealed erroneous calculations in the simulation approach as presented in Chapter 5.

It is noted that the experimental measurement shown in the lower part of Figure 6.21 is believed to be incorrect. The maximum measured deflection is already reached at 5 minutes into the experiment which is clearly in error compared to all other experimental measurements. This error was attributed to improper clamping which prevents the component by deforming in out-of-plane direction as the movement in longitudinal direction is not fully constrained.

Nevertheless, the level of agreement between the simulation and the experimental measurement of the dry component with a lay-up of  $[(+60^\circ/-60^\circ)_3/0^\circ]_s$  are highly unsatisfactory. The initial upward deflection is simulated correctly. However, the magnitude of the simulated deflection decreases again after approximately 2 minutes. This behaviour represents the expectation for a component with a unidirectional laminate with fibres parallel to longitudinal direction, based on the thermal expansion shown in the dilatometer results, as depicted in Figure 4.6.

It was concluded that the geometric changes of the laminate as a whole, regardless due to either thermal- or hygroscopic loading, was not simulated correctly. Incorrect simulation of expansion and shrinkage of the composite laminate is the only reason that could be found for the erroneous results. It was suspected that the incorrect calculation of changes in dimensions of the laminate resulted from an incompatibility of the material user subroutine with the normal subroutine in ABAQUS that is used to determine thermal strains in combination with the composite lay-up option in ABAQUS. The initial simulation approach, including the composite lay-up property, has shown to yield satisfactory results for a unidirectional laminate, as shown in Figure 6.19.

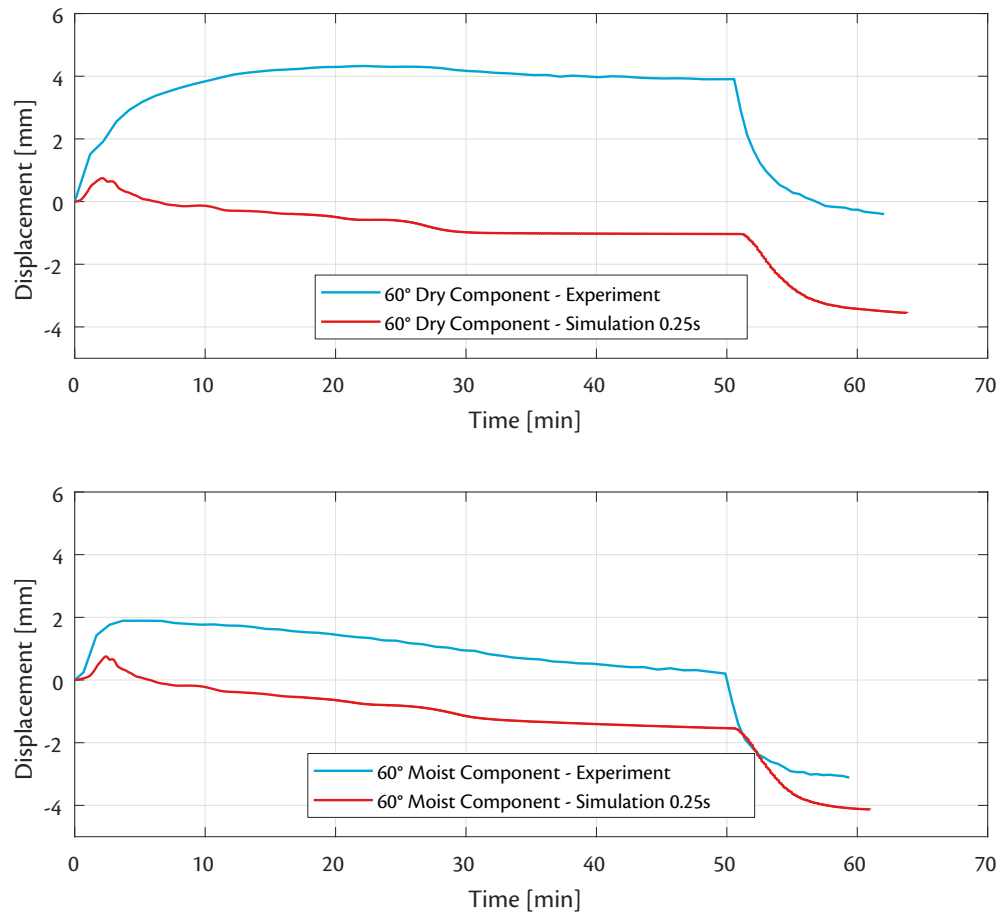


Figure 6.21 *Experimental data and results of the initial simulation approach of the center out-of-plane deformation of a dry reference component with  $[(+60^\circ / -60^\circ)_3 / 0^\circ]_s$  lay-up subjected to the cathodic dip painting temperature profile.*

However, introducing different orientations introduces unacceptable error. Solving this problem was believed to be possible by two approaches. The first approach was to implement hygrothermal expansion directly into the material user subroutine. However, the time- and temperature-dependent coefficients of thermal expansion as a result of polymer-chemical effects implied the need to include table look-ups into the material user subroutine which was not favourable due to its numerical complexity. The second approach was to carry out the hygrothermal expansion in an analytical manner by means of classical laminate theory and then input the results into ABAQUS for a solid element. The second approach was opted for and the implementation as well as the corresponding results are documented in Chapter 7.





## Improvement of the simulation

The unsatisfactory numerical results that were obtained through the initial simulation approach were identified to be caused by improper calculation of geometric changes due to hygrothermal loading especially for multi-directional laminates. Hence, an analytical approach was adopted to carry out this calculation outside of ABAQUS and eliminate the possible incompatibility of the user material subroutine with the composite lay-up method performed as a standard subroutine in ABAQUS. The analytical approach is based on classical laminate theory and assesses the hygrothermal response of all individual plies to the laminate as a whole.

Section 7.1 discusses the analytical procedure that was adopted to calculate the expansion and shrinkage of multi-directional laminates whilst taking into account the influence of temperature. The results of the adapted simulation approach are presented in comparison to the initial simulation approach and the experimental measurements in Section 7.2. Finally, the sensitivity of the adopted simulation approach to physical effects such as time-temperature superposition, hygroscopic shrinkage, and polymer-chemical effects are analysed in Section 7.3. Additionally, the influence of fibre orientation on the simulation results are assessed in this section.

### 7.1 Analytical hygrothermal expansion of multi-directional laminates

Classical laminate theory was applied to calculate the hygrothermal expansion of the multi-directional laminates by assessing the influence of the individual plies. It is assumed that every ply is initially in a stress-free condition and has zero strain. Furthermore, it is assumed that the laminate is in plane stress conditions. This assumption is justified by the relatively small thickness of the laminate of approximately  $1.75 \text{ mm}$ . It is noted that the effect of interlaminar stresses is not accounted for by means of classical laminate theory and that the viscoelastic stress relaxation in between plies is therefore not included. The following iterative procedure was followed to determine the free expansion and -shrinkage of the laminate subjected to hygrothermal loading.

- Incremental temperature and concentration are obtained from heat transfer- and mass diffusion.
- Hygrothermal strains of all plies are determined with the increments in temperature and moisture content.
- Hygrothermal resultants are calculated with temperature-dependent stiffness values of the plies.
- Global hygrothermal resultant is calculated to determine the load on the laminate.
- Resulting global strain is calculated with the temperature-dependent stiffness values of the laminate.
- The current global strain is updated with the incremental global strain.

The calculation of the hygrothermal strains of the individual plies is straightforward as the coefficients of thermal- and -hygroscopic expansion are known. The hygrothermal resultants that are a consequence of the individual plies being connected to each other requires the reduced stiffness matrix for every ply to be known. This calculation starts with the stiffness matrix that is equal for every ply as it is defined in the ply' local coordinate system. The ply' stiffness matrix is denoted with  $\mathbf{Q}$  and the corresponding expression is shown in Eq. 7.1 [97]. It is noted that the stiffness matrix shown in Eq. 7.1 is valid for an orthotropic lamina only.

$$\mathbf{Q} = \begin{bmatrix} Q_{11} & Q_{12} & 0 \\ Q_{12} & Q_{22} & 0 \\ 0 & 0 & Q_{66} \end{bmatrix} \quad \text{where} \quad \begin{aligned} Q_{11} &= \frac{E_{11}}{1 - \nu_{12}\nu_{21}} \\ Q_{12} &= \frac{\nu_{12}E_{22}}{1 - \nu_{12}\nu_{21}} \\ Q_{22} &= \frac{E_{22}}{1 - \nu_{12}\nu_{21}} \\ Q_{66} &= G_{12} \end{aligned} \quad 7.1$$

It is important to note that the ply' stiffness matrix is calculated to be dependent on temperature. This is achieved by means of the micromechanical model that is described in Section 4.9. The instantaneous modulus in transverse direction, denoted with  $E_{22}$ , is calculated with the Prony series shown in Figure 4.19 at a time equal to 1e-2s. The effect of temperature on the softening of the matrix and its consequential reduction of transverse stiffness is accounted for by applying the time-temperature superposition to the evaluation time of 1e-2s. The Williams-Landel-Ferry equation is used for the time-temperature superposition and the corresponding coefficients determined in Figure 4.20.

The calculation of the other mechanical properties shown on the right hand side of Eq. 7.1 follows as outlined in the micromechanical model and thus all include temperature dependency as they are calculated through the temperature-dependent  $E_{22}$ . The ply' stiffness matrix must be rotated in order to assess the thermal resultant of the ply in the global coordinate system. The two rotation matrices that are required for this transformation are displayed in Eq. 7.2 [97]. It is noted that every ply has its own transformation matrix and will have its own reduced stiffness matrix based on the orientation with respect to the global coordinate system,  $\theta_i$ . The subscript  $i$  has been used to indicate the relevance to the  $i^{\text{th}}$  ply.

$$\begin{aligned} \mathbf{T}_1(\theta_i) &= \begin{bmatrix} c^2 & s^2 & 2cs \\ s^2 & c^2 & -2cs \\ -cs & cs & c^2 - s^2 \end{bmatrix} \\ \mathbf{T}_2(\theta_i) &= \begin{bmatrix} c^2 & s^2 & cs \\ s^2 & c^2 & -cs \\ -2cs & 2cs & c^2 - s^2 \end{bmatrix} \end{aligned} \quad \text{where} \quad \begin{aligned} c &= \cos \theta_i \\ s &= \sin \theta_i \end{aligned} \quad 7.2$$

The reduced lamina stiffness matrix can then be calculated for the  $i^{\text{th}}$  ply with Eq. 7.3. Please note that the bar notation applied to the symbol on the left hand side of Eq. 7.3 has been used to indicate the transformation of the stiffness matrix to the global coordinate system of the laminate.

$$\bar{\mathbf{Q}}_i = \mathbf{T}_1^{-1}(\theta_i) \cdot \mathbf{Q} \cdot \mathbf{T}_2(\theta_i) \quad 7.3$$

The incremental thermal- and hygroscopic resultants can then be calculated for every ply with Eq. 7.4. It is noted that the coefficient of thermal expansion, denoted with  $\alpha_T(t, T)$ , has been indicated with both a time- and temperature-dependency as the polymer-chemical effects are accounted for by using different coefficients of thermal expansion during the heating- and cooling phase of the simulation. The incremental thermal- and hygroscopic resultants of the individual plies are indicated with  $\Delta N_{Ti}$  and  $\Delta N_{Mi}$ , respectively.

$$\begin{aligned}\Delta N_{Ti} &= [z(i+1) - z(i)] \Delta T \cdot \bar{\mathbf{Q}}_i \cdot \alpha_T(t, T) \\ \Delta N_{Mi} &= [z(i+1) - z(i)] \Delta M \cdot \bar{\mathbf{Q}}_i \cdot \beta_M\end{aligned}\tag{7.4}$$

The letter  $z$  has been applied to indicate the through-thickness coordinates at the edges of each ply. The calculation shown in Eq. 7.4 is effectively a multiplication by the thickness of the respective ply. The total incremental hygrothermal resultant that acts on the laminate as a whole can be determined through the summation of the thermal- and hygroscopic resultants of the individual plies. This calculation step is shown mathematically in Eq. 7.5. Please note that the symbol  $I$  is used to represent the total number of plies in the laminate.

$$\Delta N = \sum_{i=1}^I \Delta N_{Ti} + \sum_{i=1}^I \Delta N_{Mi}\tag{7.5}$$

It is necessary to determine the in-plane compliance matrix of the laminate to calculate the increment in global strain that is the result of the incremental total hygrothermal resultant. The in-plane compliance matrix is the inverse of the in-plane stiffness matrix, denoted with  $\mathbf{A}$ , as all laminates are both symmetric and balanced. The in-plane stiffness matrix is calculated with the expression shown in Eq. 7.6 [97].

$$\mathbf{A} = \sum_{i=1}^I \bar{\mathbf{Q}}_i \cdot [z(i+1) - z(i)]\tag{7.6}$$

The increment in global strain is calculated by multiplication of the in-plane compliance matrix by the incremental total hygrothermal resultant. Keeping in mind that the in-plane compliance matrix is the inverse of the in-plane stiffness matrix due to special orthotropy, the expression shown in Eq. 7.7 can be used to determine the increment in global strain.

$$\Delta \varepsilon(\Delta t) = \mathbf{A}^{-1} \cdot \Delta N\tag{7.7}$$

The total global strain of the laminate is determined by adding the incremental global strain to the previous known condition. For completeness, this final step is shown in Eq. 7.8.

$$\varepsilon(t + \Delta T) = \varepsilon(t) + \Delta \varepsilon(\Delta t)\tag{7.8}$$

It is stated that the outlined incremental procedure takes into account the effect of temperature on the stiffness values of the individual plies as the ply' laminate stiffness matrix is calculated for each increment in time through the temperature-dependent mechanical properties obtained from the micromechanical model as described in Section 4.9. The finite element implication for the semi-numerical approach does not utilise a composite lay-up anymore as this was suspected to be the source of the unacceptable discrepancies in combination with the material user subroutine. The use of solid elements has a consequence on the input of the mechanical properties in the simulation.

Whereas the fully numerical approach allowed one set of Prony coefficients to be used for arbitrary lay-ups, the semi-numerical approach requires a set of Prony coefficients to be determined for every specific lay-up that is simulated. Hence, sets of Prony coefficients were determined for the specific lay-ups that have been simulated. The stiffness coefficients of a specific global laminate have been taken from the in-plane stiffness matrix as calculated with Eq. 7.6 for the reference temperature of  $20^\circ\text{C}$ . The time-temperature superposition and mechanical stress relaxation is still carried out by the material user subroutine that has remained unchanged.

$$\mathbf{a} = \mathbf{A}^{-1} = \begin{bmatrix} a_{11} & a_{12} & 0 \\ a_{12} & a_{22} & 0 \\ 0 & 0 & a_{66} \end{bmatrix} \quad \text{where} \quad \begin{aligned} C_{11} &= a_{11} \\ C_{12} &= a_{12} \\ C_{22} &= a_{22} \\ C_{44} &= a_{66} \end{aligned} \quad 7.9$$

The expressions in Eq. 7.9 show which coefficients have been used for the material user subroutine. The terms  $a_{16}$  and  $a_{26}$  are equal to zero as there is no extension-shear coupling for a symmetric and balanced laminate. It is noted that the values taken for the out-of-plane stiffness coefficients  $C_{13}$  and  $C_{33}$  are equal to  $C_{12}$  and  $C_{22}$ , respectively, as the material user subroutine was developed with a transversely orthotropic laminate in mind, based on the initial simulation approach. The stiffness coefficients for  $C_{23}$ ,  $C_{55}$ , and  $C_{66}$  are taken from the unidirectional laminate shown in Table 4.9 as these can not be determined by means of classical laminate theory. Nevertheless, the disturbing effect of these coefficients will be marginal due to the finite element representation of only one element in thickness direction.

## 7.2 Results of improved simulation

This section presents the results of the semi-numerical simulation approach for the component level validation. The results are displayed in the same order as adopted in Section 6.4. An overview of the magnitudes of the discrepancies between experimentally measured- and simulated maximum deflection values are shown in Table 7.1 at the end of this section to provide a quantitative indication of the accuracy of the semi-numerical approach. The numerical result for the moisture saturated component with a  $[90_{16}^\circ]$  lay-up is shown in Figure 7.1. Please note that the first approach has also been included for comparison. Furthermore, all simulations have been carried out with equal meshes and maximum time step sizes.

In comparison to the fully numerical approach, the simulated maximum deflection of the component has improved slightly. A difference is found at the end of the simulation as the fully numerical simulation underestimates the negative deflection and the semi-numerical approach displays a negative deflection that is larger than was measured. It is noted that overestimating the negative deflection at the end of the simulation will most likely yield a conservative lay-up choice if the final deflection is chosen to be a design driver. The discrepancy between the maximum deflection of the semi-numerical simulation and the experimental measurement is 4.0%.

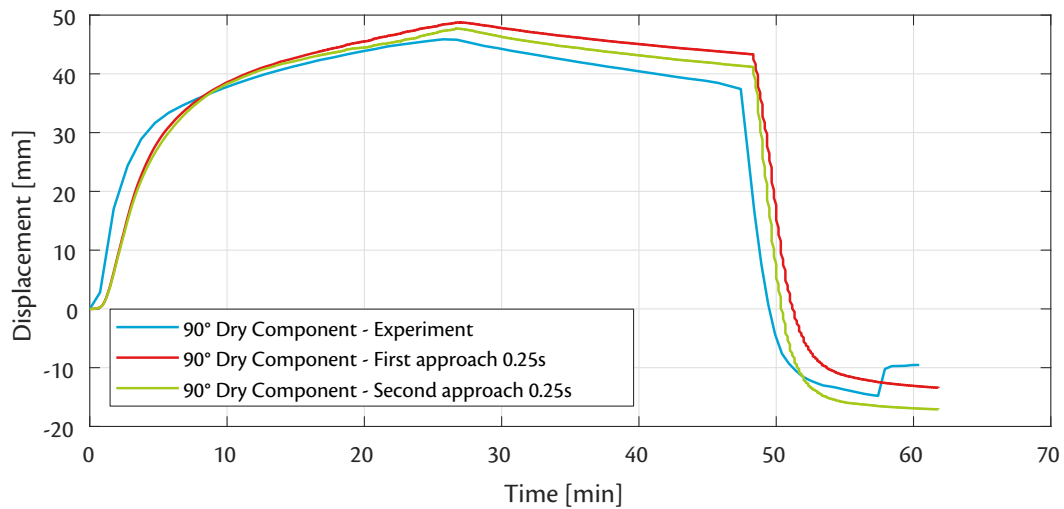


Figure 7.1 Numerical results of the improved simulation approach of the center out-of-plane deformation of a dry reference component with  $[90_{16}^{\circ}]$  lay-up subjected to the cathodic dip painting temperature profile.

A comparable level of agreement is found for the simulations that were carried out for the dry component with a lay-up of  $[0/+45^{\circ}/-45^{\circ}/0_4]_s$ . The comparison between the experimental measurements and the predicted values by the semi-numerical analysis is shown in Figure 7.2. The maximum negative deflection of the dry specimen is captured with high accuracy and also the rate of deflection is simulated in proper agreement with the measurements. Contrarily, the upward rate of deflection during the cooling phase of the experiment is simulated to be significantly too quick and too much. However, it must be stated that the simulation results of the semi-numerical approach are in better agreement with the experimental measurement than the simulations results of the fully numerical approach. The effect of recrystallisation and  $\gamma$ - to  $\alpha$ -form transition of the crystals is simulated to be more significant than was measured. This is concluded from the overestimation of the remaining deflection after the cooling phase.

The simulation of the moisture saturated component with a  $[0/+45^{\circ}/-45^{\circ}/0_4]_s$  lay-up is qualitatively in good agreement with the experimental measurement. The initial simulated rate of downward deformation displays a slight delay in comparison with the measurement of the component. The measurement shows a constant magnitude of deflection for the temperature-hold period that roughly starts at 25 minutes. However, both the semi- and fully numerical simulations predict that moisture still egresses from the composite material and an overestimation of the maximum negative deflection is observed. The discrepancies between the maximum negative deflections of the semi-numerical and experimental measurement for both the dry- and moisture saturated components are -4.2% and 31%, respectively.

The experimental measurement of the moisture saturated component with the  $[90_{16}^{\circ}]$  lay-up, however, clearly shows that moisture must still be diffusing out of the composite material during the temperature-hold period. The constant deflection that is visible in the measurement is not in line with the expectation. Nevertheless, the large material scatter found in the micrometer experiments carried out with unidirectional laminates in longitudinal direction explains the high likelihood of discrepancies between both numerical simulations and the optical measurements. This is because the large amount of plies with a  $0^{\circ}$  orientation has the logical consequence that this simulation is highly sensitive to the coefficient of hygroscopic expansion in longitudinal direction.

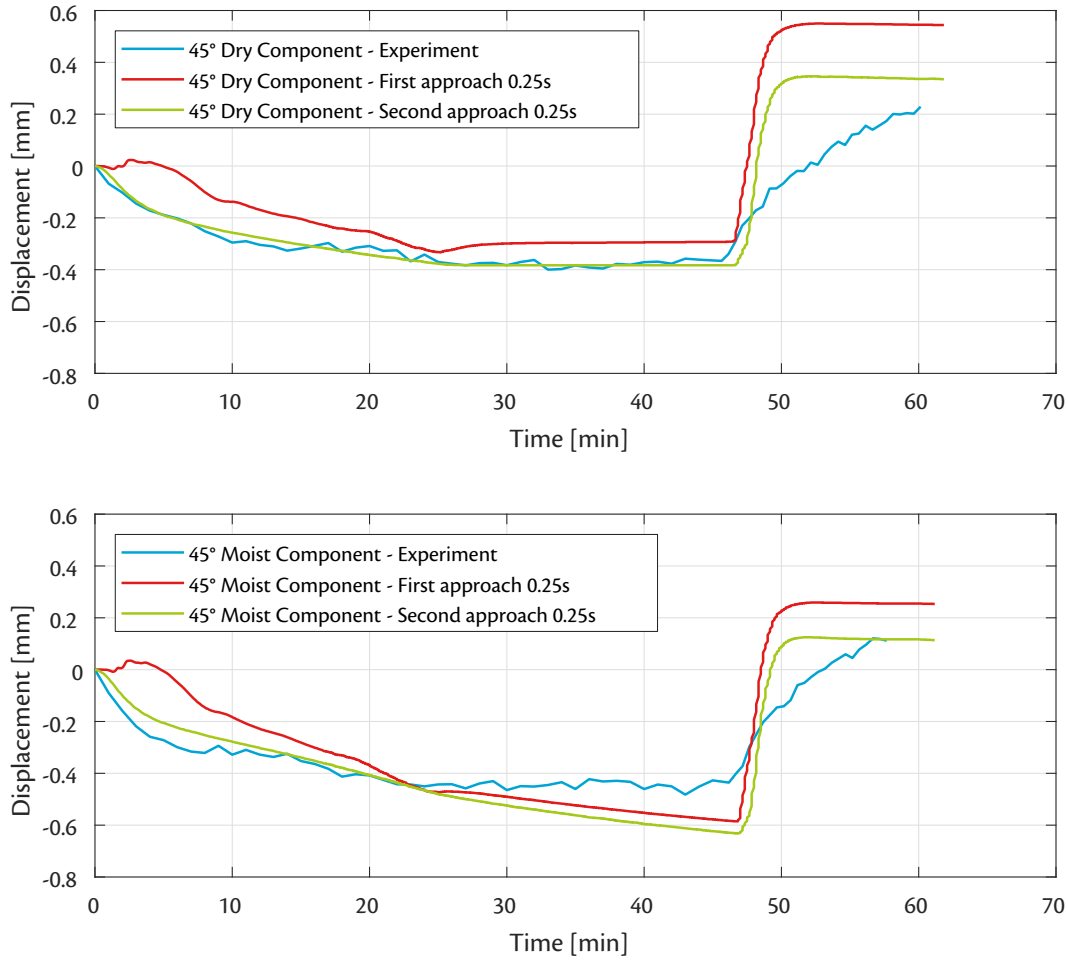


Figure 7.2 Numerical results of the improved simulation approach of the center out-of-plane deformation of a dry reference component with  $[0/+45^\circ/-45^\circ/0_4]_s$  lay-up subjected to the cathodic dip painting temperature profile.

Similar comparisons between experimental measurements and simulations are provided in Figure 7.3 for both dry- and moisture saturated components manufactured with a  $[(+60^\circ/-60^\circ)_3/0^\circ]_s$  lay-up. There is a good qualitative agreement between the semi-numerical model and the experimental results that are shown in the upper part of Figure 7.3. The rate of deformation during the heating phase of the experiment carried out with the dry component is simulated to an excellent degree. However, a growing discrepancy is visible from approximately 20 minutes until the end of the temperature-hold period. The discrepancy at the end of the temperature-hold period between the semi-numerical simulation and the measured deflection is 18.8%. The maximum deflection is simulated with a better agreement as the discrepancy has a value of 7.3%.

No valuable conclusions can be drawn from the lower part of Figure 7.3 as the experimental measurement was found to be highly unreliable. The hygroscopic shrinkage of the composite material during heating is evident in the semi-numerical simulation in comparison to the upper part of Figure 7.3 as the predicted maximum deflection was observed to be lower. The negative deformation at the end of the simulation is also significantly larger for the simulation of the moisture saturated component in comparison to the dry component.

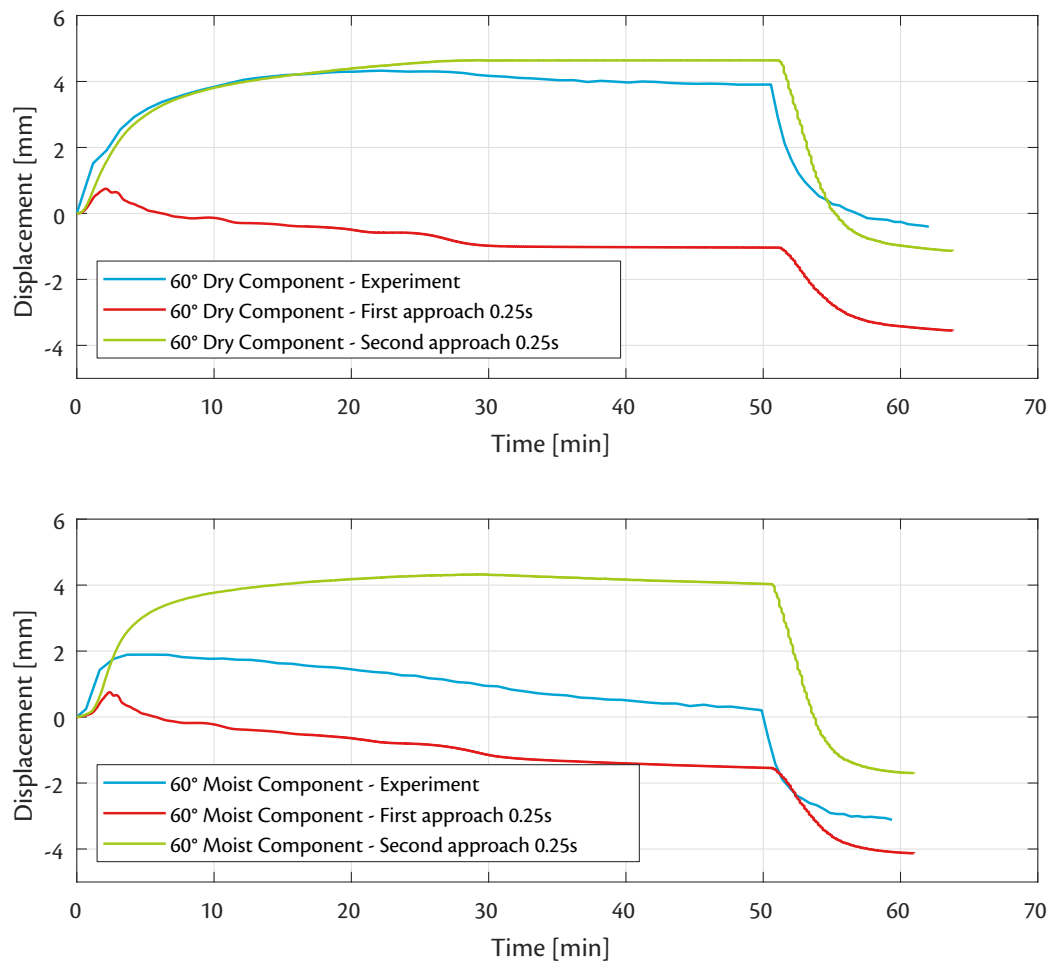


Figure 7.3 Numerical results of the improved simulation approach of the center out-of-plane deformation of a dry reference component with  $[(+60^\circ / -60^\circ)_3 / 0^\circ]_s$  lay-up subjected to the cathodic dip painting temperature profile.

All simulation results that could be compared to experimental measurements are found to be in satisfactory agreement and the discrepancies between the maximum deflection as predicted in comparison to the measurements are shown in Table 7.1.

Table 7.1 Discrepancy between improved simulation result and experimental measurement at maximum deflection.

Lay-up	Moisture content	Discrepancy
$[90^\circ_{16}]$	Moist	4.0%
$[0 / +45^\circ / -45^\circ / 0_4]_s$	Dry	-4.2%
$[0 / +45^\circ / -45^\circ / 0_4]_s$	Moist	31.0%
$[(+60^\circ / -60^\circ)_3 / 0^\circ]_s$	Dry	7.3%
$[(+60^\circ / -60^\circ)_3 / 0^\circ]_s$	Moist	<i>n.a.</i>

### 7.3 Sensitivity to physical effects and fibre orientation

The sensitivity of the semi-numerical simulation approach to various input parameters is assessed in this section. The scenarios that have been assessed can be divided into either accounting for physical effects or describing an influence that is concerned with the fibre orientation of the component. The effect of excluding specific physical effects are presented first. The simulations for all lay-ups used in the validation experiments have been assessed for the excluding time-temperature superposition and neglecting the effect of recrystallisation. Additionally, the simulations for the components that were moisture saturated have also been assessed whilst neglecting hygroscopic shrinkage to assess the effect of moisture on the predicted deflection.

The influence of the mentioned physical effects on the deformation behaviour of the moisture saturated component with a lay-up of  $[90^\circ_{16}]$  are shown in Figure 7.4. It is concluded that hygroscopic shrinkage has the most significant effect on both the maximum deflection and the remaining deflection. It can also be concluded that the effect of hygroscopic shrinkage can be neglected for approximately the first 10 minutes of the cathodic dip drying process. This provides an argument to discard the validation measurement that was carried out for the moisture saturated component with a  $[(+60^\circ / -60^\circ)_3 / 0^\circ]_s$  lay-up shown in Figure 7.3.

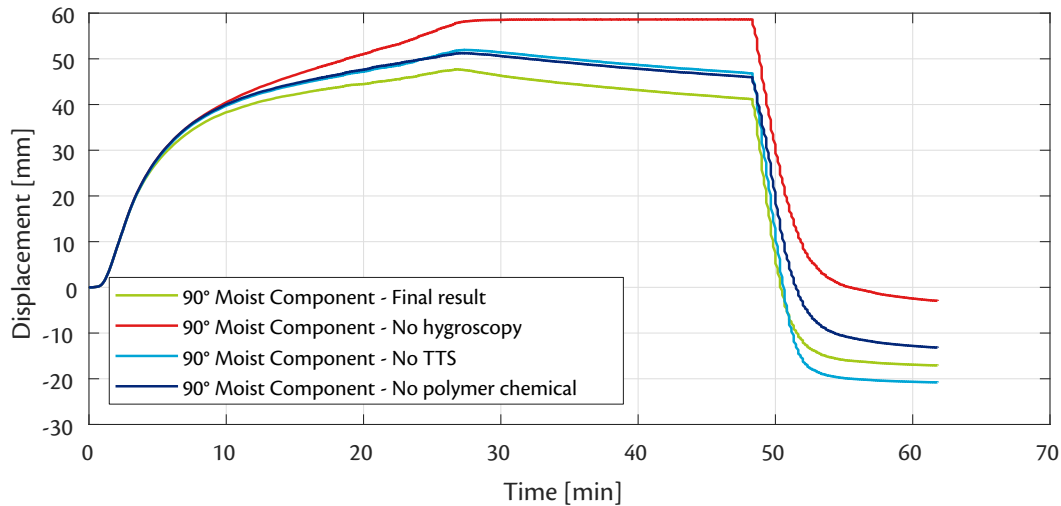


Figure 7.4 Results of the sensitivity study for the component with a  $[90^\circ_{16}]$  lay-up to the influence of time-temperature superposition, hygroscopic shrinkage, and polymer-chemical effects.

Inspection of Figure 7.4 reveals that the effect of excluding time-temperature-superposition and the effect of excluding polymer-chemical effects on the maximum deflection of the moisture saturated component with the  $[90^\circ_{16}]$  lay-up are roughly similar. However, neglecting time-temperature superposition yields a larger negative remaining deflection in comparison to the default simulation and not taking into account polymer-chemical effects results in a smaller negative remaining deflection in comparison to the default simulation. It is noted that neglecting time-temperature superposition also means that the analytical calculation of the global strain does not take into account matrix softening. Lastly, it is important to note that all physical effects have a significant contribution to the deformation behaviour of the unidirectional component.



A similar analysis has been made for the dry- and moisture saturated components that were manufactured with a lay-up that is equal to  $[0/+45^\circ/-45^\circ/0_4]_s$ . The results of this analysis are shown in Figure 7.5 for the dry- and moisture saturated component in the lower and upper part, respectively. From inspection of Figure 7.5 it is concluded that excluding time-temperature superposition increases the magnitude of the predicted negative deflection of the component. The difference in remaining deflection at the end of the simulation is, however, negligibly affected.

Not taking into account the polymer-chemical effects has the most significant effect on the outcome of the semi-numerical simulation. The predicted and measured positive remaining deflection at the end of the cathodic dip drying process is not correctly simulated when polymer-chemical effects are not implemented in the simulation. Even more so, the simulation without polymer-chemical effects provides the wrong prediction that a negative deflection remains at the end of the process. Lastly, disregarding the hygroscopic shrinkage of the moisture saturated composite material lowers the maximum negative deflection and increases the remaining positive deflection, diverging more from the experimentally measured value. In agreement with the simulation of the component with the  $[90_{16}]$  lay-up, it must be noted that all physical effects significantly contribute to the deformation behaviour and can not be neglected.

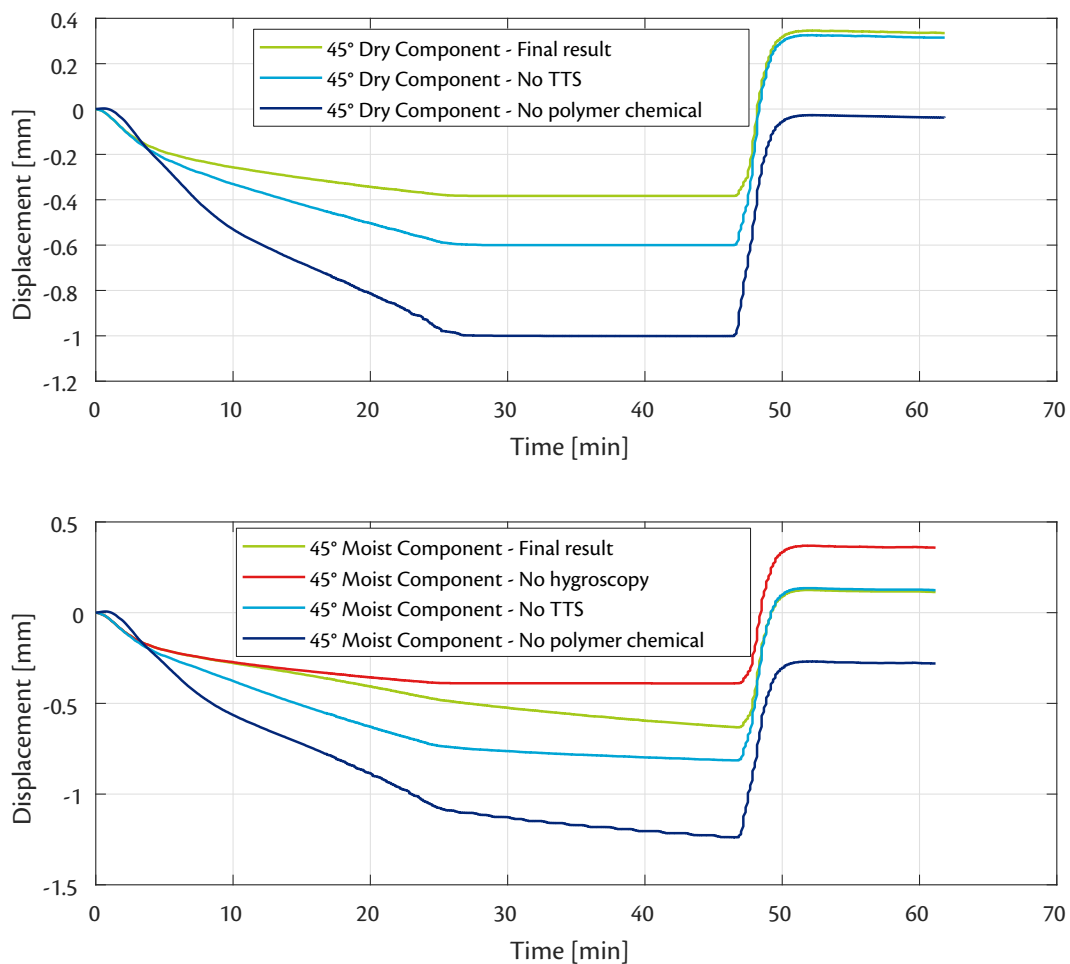


Figure 7.5 Results of the sensitivity study for the component with a  $[0/+45^\circ/-45^\circ/0_4]_s$  lay-up to the influence of time-temperature superposition, hygroscopic shrinkage, and polymer-chemical effects.

By inspection of Figure 7.6 it can be argued that neglecting the polymer-chemical effects for the component with a lay-up of  $[(+60^\circ / -60^\circ)_3 / 0^\circ]_s$  does not significantly affect the maximum deflection. Nevertheless, the differences in coefficients of thermal expansion during cooling in both longitudinal and transverse direction of the individual plies have a significant effect on the remaining deflection that is observed after the cooling phase. Excluding time-temperature superposition from the simulation has the most significant influence on both the maximum deflection during the temperature-hold period and the permanent deflection after cooling the component down.

Neglecting hygroscopic shrinkage in the simulation of the moisture saturated component with a  $[(+60^\circ / -60^\circ)_3 / 0^\circ]_s$  lay-up also has a significant effect on both assessed values at the temperature-hold period and after cooling. However, it is stated that the effect of neglecting the hygroscopic content is significantly less harmful for the  $[(+60^\circ / -60^\circ)_3 / 0^\circ]_s$  lay-up in comparison to the  $[90^\circ_{16}]_s$ - and  $[0^\circ / +45^\circ / -45^\circ / 0^\circ_4]_s$  lay-ups. Also, if the maximum deflection is driving the choice of lay-up and determines if a lay-up is fit for manufacturing, excluding the hygroscopic content yields conservative lay-up choices.

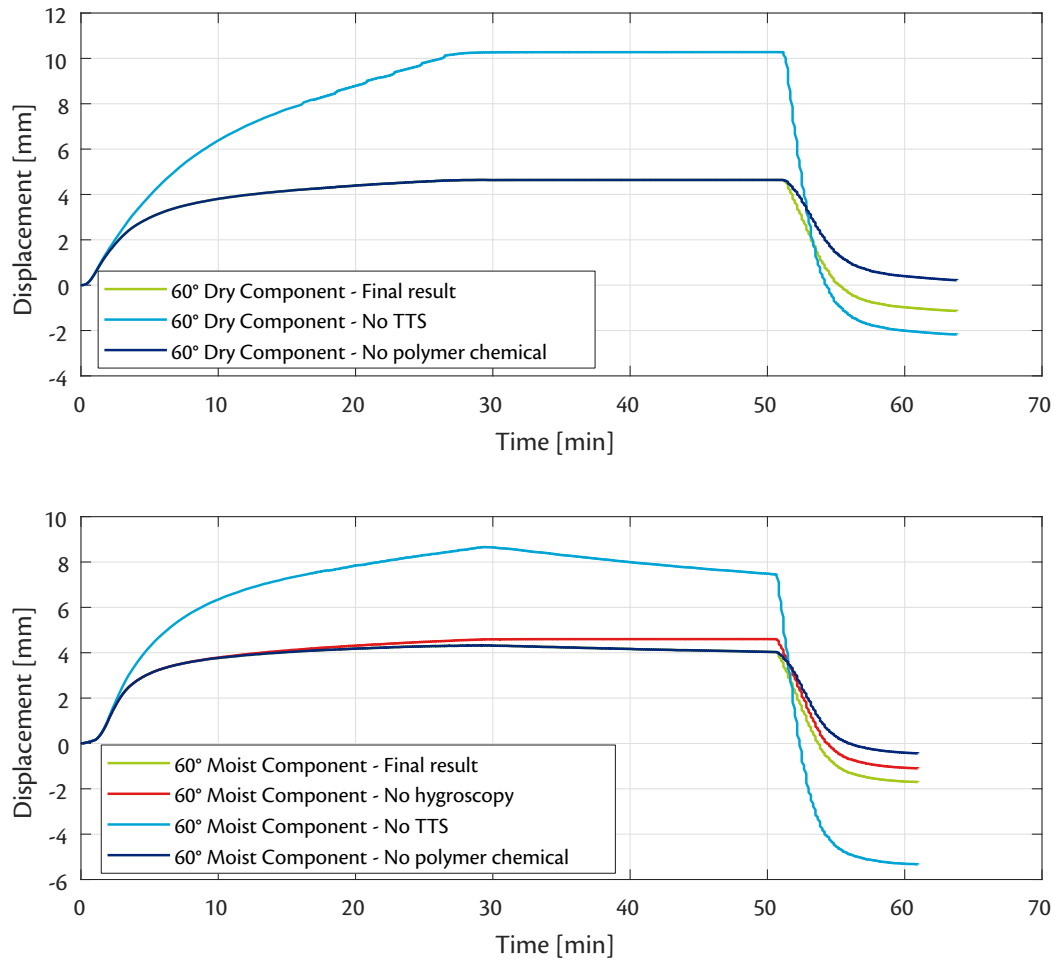


Figure 7.6 Results of the sensitivity study for the component with a  $[(+60^\circ / -60^\circ)_3 / 0^\circ]_s$  lay-up to the influence of time-temperature superposition, hygroscopic shrinkage, and polymer-chemical effects.

The influence of fibre orientation has been evaluated by means of simulations carried out for three possible scenarios. The components that were measured during the validation experiments had been manufactured by manually inserting the lay-ups in a wet compression moulding machine that was used to effectively thermoform the thermoplastic composite material. Hence, the first scenario assumes that the composite lay-up was inserted with an erroneous rotation of  $5^\circ$  with respect to the correct orientation. The two other scenarios assess the influence of a  $5^\circ$  shear rotation of the fibres during the thermoforming process, both when subjected to tension and compression during the process. The  $0^\circ$  plies in the simulated lay-ups are assumed to be unaffected by the shear rotation. Table 7.2 shows the lay-ups that have been simulated for each scenario.

The effect of fibre orientation on the predicted deformation behaviour of the dry- and moisture saturated components with a target lay-up of  $[0/ + 45^\circ / - 45^\circ / 0_4]_s$  are shown in Figure 7.7. It is striking that rotating the lay-up with  $5^\circ$  has a less significant effect than the effect of the change in orientation of the fibres due to shearing either through tensile or compressive forces. It is noted that a  $5^\circ$  angle already has a significant influence on the maximum deformation. It is also observed that the remaining deflection at the end of the simulation is much less affected by a change in fibre orientation, albeit that the moisture saturated component displays a larger variation at the end of the cathodic dip drying process.

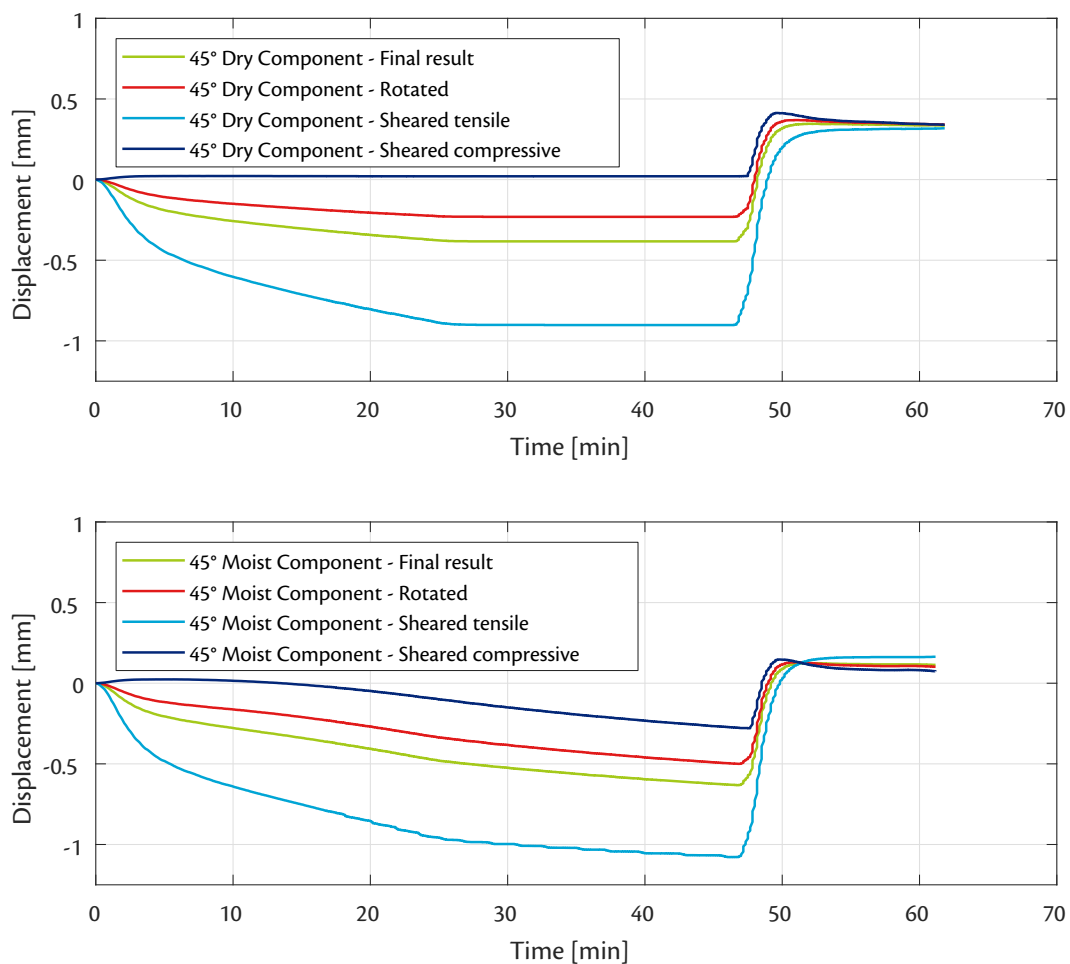


Figure 7.7 Results of the sensitivity study for the component with a  $[0/ + 45^\circ / - 45^\circ / 0_4]_s$  lay-up to the influence of imperfections in fibre orientation.

Table 7.2 *Simulated lay-ups to assess the influence of fibre orientation on the out-of-plane deformation behaviour.*

Ideal lay-up	Rotated	Tensile sheared	Compressive sheared
$[0/+45^\circ/-45^\circ/0_4]_s$	$[5/+50^\circ/-40^\circ/5_4]_s$	$[0/+40^\circ/-40^\circ/0_4]_s$	$[0/+50^\circ/-50^\circ/0_4]_s$
$[(+60^\circ/-60^\circ)_3/0^\circ]_s$	$[(+65^\circ/-55^\circ)_3/5^\circ]_s$	$[(+55^\circ/-55^\circ)_3/0^\circ]_s$	$[(+65^\circ/-65^\circ)_3/0^\circ]_s$

Subjecting a laminate to longitudinal tensile forces during the thermoforming will lead to a reduction of the observed angle between the fibres of the angled plies and the longitudinal axis of the component. Hence, tensile shearing results in a laminate that is more fibre-dominant in longitudinal direction as compared to the ideal laminate that does not undergo shearing. A more fibre-dominant lay-up will display a more negative deflection. In case of the tensile shearing for the  $[(+60^\circ/-60^\circ)_3/0^\circ]_s$  laminate, this translates to a less positive deflection, as shown in Figure 7.8.

Analogous to the  $[0/+45^\circ/-45^\circ/0_4]_s$  lay-up, shearing the laminate with either tensile- or compressive forces during the thermoforming has a more significant impact on the deformation behaviour than rotating it. The reason for this is logical as in the case of rotation the turning away from the longitudinal of one ply is partly counteracted by the turning towards the longitudinal by its neighbouring angled ply. This counteracting effect of balancing a more fibre-dominant ply with a more matrix-dominant ply is not present when the laminate is sheared. In this situation, both the plies with positive- and negative orientation either turn towards or -away from the longitudinal.

An interesting observation is made when the deflections of the rotated, tensile sheared, and compressive sheared moisture saturated laminates are compared, shown in the bottom part of Figure 7.8. The deflection of the rotated laminate is roughly equal to the deflection of the compressive sheared at the end of the temperature-hold period. Remarkably, the deflection of the rotated laminate then appears to transition to the deflection of the tensile sheared laminate which it closely approaches at the end of the simulation. Contrarily to the  $[0/+45^\circ/-45^\circ/0_4]_s$  lay-up, rotating or shearing the  $[(+60^\circ/-60^\circ)_3/0^\circ]_s$  laminate has a significant effect on the remaining deflection if the laminate is moisture saturated.

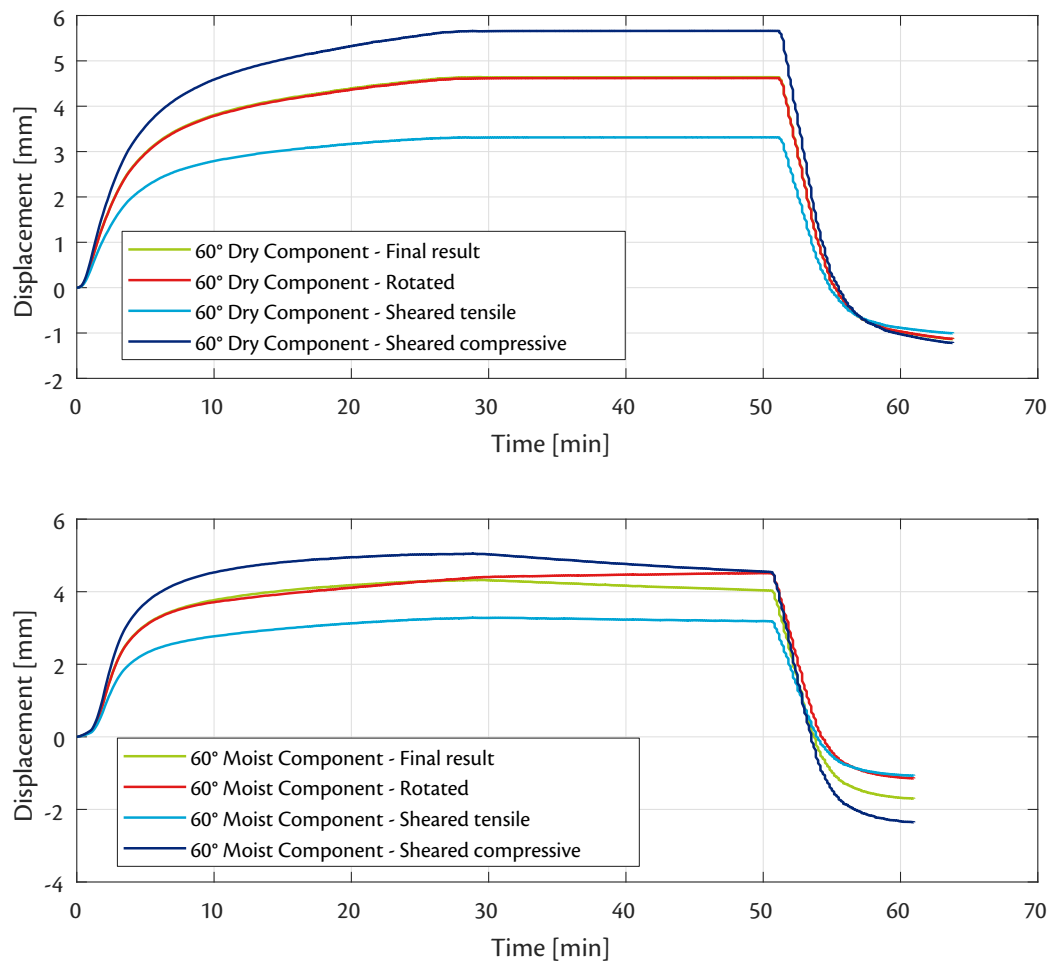


Figure 7.8 Results of the sensitivity study for the component with a  $[(+60^\circ / -60^\circ)_3 / 0^\circ]_s$  lay-up to the influence of imperfections in fibre orientation.



# 8

## Conclusion

The conducted thesis research had the objective to provide the possibility to predict the structural performance of thermoplastic composite parts that are subjected to hygrothermal loading when passing through the automotive painting process. This objective was achieved by developing a numerical simulation of the viscoelastic deformation behaviour of fibre-reinforced thermoplastics that are subjected to transient hygrothermal loading.

The effects of hygrothermal loading to the deformation behaviour of thermoplastics have been identified during a literature review in the early stages of the research. Thermal loading leads to a softening of the matrix and will accelerate the stress relaxation behaviour as a result. Heating a unidirectional carbon-fibre reinforced thermoplastic laminate causes shrinkage in longitudinal direction and expansion in transverse direction because of the negative- and positive coefficients of thermal expansion of the fibre and matrix, respectively.

The linear viscoelastic material behaviour that was observed for the fibre-reinforced thermoplastic material with the trading name Celstran CF60-PA6 was accounted for in the numerical simulation. The implementation of a recursive formulation of the integral constitutive equations for linear viscoelastic material behaviour led to a numerical model that does not require the entire strain history to be stored. This proved to be beneficial in terms of memory usage as the duration of the drying phase in the cathodic dip painting process is over 45 minutes.

All tests that have been carried out during the material characterisation of the thesis research were derived from the material input stipulated by the constitutive equations and the framework of the numerical model. Successful identification of the expansion behaviour of unidirectional laminates under the influence of hygrothermal loading was performed with dilatometer- and micrometer experiments. Polymer-chemical effects in the form of recrystallisation and transition of the crystal form were discovered and have been included in the simulation. The linearity of the viscoelastic material behaviour was confirmed with relaxation tests as deviation from this would invalidate the choice of constitutive model.

Furthermore, the rate of mass diffusion was measured by thermogravimetric analysis and dynamic mechanical analysis was used to quantify the viscoelastic mechanical behaviour. DIC was applied to determine the interaction between the in-plane strains in the two principal directions of the unidirectional laminate. The computation of relaxation moduli through the results of the dynamic mechanical analysis was validated by comparison with the instantaneous stiffness values obtained by quasi-static testing at the two extreme temperatures of interest. A micromechanical model was defined to calculate the remaining temperature-dependent mechanical properties of a unidirectional layer that had not been experimentally determined.

The finite element software ABAQUS was utilised to accommodate the simulation workflow that was comprised of three sequential analyses. One-dimensional heat transfer- and mass diffusion simulations were carried out to determine the temperature- and moisture content distribution through the thickness of the composite material. A third simulation was carried out to compute the stresses and strains in the clamped component as it was subjected to the temperature envelope that represents the cathodic dip painting oven. Taking advantage of symmetry in the simulation reduced the computational expenses.

Multi-directional lay-ups were simulated with the use of the composite lay-ups possibility in ABAQUS and the thickness direction of the component was represented by single solid elements. A material user subroutine was written and verified against multiple load cases to achieve orthotropic viscoelastic material behaviour with the application of time-temperature superposition in the finite element software. Convergence studies have been carried out for the element size utilised for the mesh generation and for the magnitude of the time step in the stress simulation. Although a mesh convergence was observed at an element size of 2 mm, the deformation of the mid-plane did not yet converge at a time step of 0.05s and a time step of 0.25s was taken because of the significant reduction in runtime that is beneficial to iterative design usage.

The sensitivity studies that were conducted to assess the influence of limiting the heat transfer- and mass diffusion simulation to a single through-thickness dimension provided proof that the temperature- and moisture content distribution are not significantly affected. The temperature distribution throughout the specimen in all directions was concluded to show negligible differences. As such, the stress simulation was carried out with equal temperature values for all elements. The moisture content distribution displayed significant variation due to finite edge effects. However, the affected area is limited up to only 2.5 mm away from the edges and the significance on the deformation behaviour as predicted by the simulation was assumed to be negligible.

Validation of the numerical model was carried out in three levels that grew in complexity. The correct prediction of moisture diffusion and hygrothermal expansion was validated by conducting dilatometer experiments with specimens of various multi-directional lay-ups. The quantified coefficients of thermal- and -moisture expansion were proven to be correctly determined. However, conflicting conclusions were drawn about the rate of moisture diffusion. Comparisons between measurement and simulation of two different lay-ups indicated the simulation of too slow moisture diffusion, whereas the comparison for a third different lay-up provided arguments for the simulation of too quick moisture diffusion.

The second level of validation was carried out with tensile test specimens clamped on the two longitudinal ends that were subjected to a temperature envelope chosen to be similar to the actual cathodic dip painting oven. The clamping fixture was designed to display minimum thermal expansion by selecting graphite as material and implementing geometrical compensation by utilising two types of graphite. Clamping the specimens meant that an out-of-plane bending deformation was present as thermal buckling occurred. Measuring the displacement of the center of the specimens allowed to compare the experimental values with the predicted displacement from the simulations. The maximum deflections that were simulated for both dry- and moisture saturated specimens are in good agreement with the experimental data. Also the moment in time of maximum deflection is captured accurately and the remaining displacement after cooling was simulated correctly.



The last validation experiments were carried out with components manufactured with the geometry of the roof header currently in series production of the 7 Series and with unidirectional as well as multi-directional laminates. The simulation of the moisture saturated component with a unidirectional lay-up in transverse direction showed agreement of 6.2% discrepancy for the maximum deflection. Also the permanent out-of-plane deformation and the moments in time of the displacement were accurately captured. It was concluded that the moisture egress was simulated to be too slowly. The simulations that were carried out for the lay-ups  $[0/ + 45^\circ / - 45^\circ / 0_4]_s$  and  $[(+60^\circ / - 60^\circ)_3 / 0^\circ]_s$  produced unacceptable discrepancies with the experiments and also the qualitative behaviour was incorrect.

The change from a unidirectional laminate to a multi-directional lay-up was believed to be the source of the error and there was evidence to suspect that the calculation of the expansion of the laminate was not carried out as intended. Hence, an analytical approach was adopted to compute the strains of the laminate based on the strains and temperature-dependent stiffness values of the individual plies. This analytical method was based on classical laminate theory and was implemented in an incremental method that progresses through time and determines the global strain of the laminate. The semi-numerical simulation approach yielded a higher accuracy for the unidirectional component and the measurements and simulations of the  $[0/ + 45^\circ / - 45^\circ / 0_4]_s$  and  $[(+60^\circ / - 60^\circ)_3 / 0^\circ]_s$  laminates were mostly within 8% discrepancy; which is generally considered to be accurate for continuous fibre-reinforced composites.

From sensitivity studies carried out with the semi-numerical simulations it can be concluded that all physical effects that are taken into account are significant towards the predictions of the deformation behaviour of the component. Excluding the mentioned polymer chemical effects has the largest influence for the component with a  $[0/ + 45^\circ / - 45^\circ / 0_4]_s$  lay-up, whereas neglecting the effect of temperature on the softening of the matrix affects the deformation behaviour of the  $[(+60^\circ / - 60^\circ)_3 / 0^\circ]_s$  the most. Additionally, an alteration of  $5^\circ$  in fibre orientation was discovered to already have a significant effect for both mentioned lay-ups on both the maximum deflection and the remaining deflection after cooling. Rotating the entire lay-up was concluded to have less influence than a change in fibre orientation potentially caused by shearing the fibres due to the thermoforming manufacturing.

The semi-numerical approach requires that the through-thickness representation of the geometry in ABAQUS is carried out with single solid elements. Therefore, Prony series must be constructed for the stiffness coefficients of every unique laminate that shall be simulated. This can be considered to be a disadvantage and limit the usability of the simulation approach. On the other hand, the analytical calculation of the hygrothermal expansion behaviour of the multi-directional laminate occurs relatively quick and provides a thorough insight in how the component will deform during the drying process. Ideally, the semi-numerical approach is used with coarse stiffness coefficients to obtain a first indication of how the component will deform. The fully numerical simulation approach can then be used to compute the deformation behaviour of the laminate after it has been altered based on the first indication. It is noted, however, that the fully numerical simulation can not be used in its current state.

Reflecting on the gained experience and findings, it can be stated that relatively little effort is required in determining the viscoelastic material behaviour to carry out simulations because of the micromechanical model that was set up in combination with dynamic mechanical analysis. Theoretically speaking, all mechanical characterisation with the exception of the Poisson's ratio can be performed with dynamic mechanical analysis. Although the principle of time-temperature superposition was strictly speaking not valid for the entire temperature range of interest, the results of the semi-numerical simulations are in proper agreement with the validation experiments. It is finally concluded that the recursive formulation of the integral linear viscoelastic constitutive equations effectively eliminates the necessity of storing much data, especially for long simulations as was the case in the thesis research.



# 9

## Recommendations

The conducted material characterisation and the developed semi-numerical simulation are concluded yield satisfactory results. Nevertheless, specific parts have been identified that require either further investigation or could have been carried out in a manner that is expected to produce better results. Recommendations are presented below that are believed to contribute to an improvement of the thesis research.

The effective coefficient of expansion for a multi-directional lay-up was identified to be sensitive for the shear modulus of the unidirectional lamina it is comprised of. The shear modulus of the matrix is currently calculated by means of an isotropic rule-of-mixtures. The matrix' shear modulus is then used to compute the shear modulus of the composite unidirectional ply. It is recommended that the calculation of the shear modulus is analysed for its correctness and that the predicted temperature-dependence holds. This validation can be carried out by dynamic mechanical analysis of a laminate with a symmetric and balanced  $\pm 45^\circ$  orientation.

An improved design of the fixture for the small coupon validation experiment would have reduced the bending of the fixture' arms due to the thermal expansion of the specimen. A reduction in bending deformation of the fixture leads to a more accurate implementation of the stationary boundary conditions. More reliable validation data is obtained if the movement of the boundary conditions can be reduced. An improved design would be to have the connecting structure on both sides of the specimen and this can be achieved with a fully symmetric structure. However, this would impose the requirement to be able to measure the center deflection from the top side of the coupon. This was unfortunately not possible with the used experimental setup. On the other hand, the implementation of moving boundary conditions and the validation thereof increases the usefulness of the simulation in the sense that the tool can be used to more realistically simulate industrial processes.

Only one measurement with dynamic mechanical analysis is performed in the current thesis work. Carrying out the material characterisation to identify the relaxation behaviour multiple times will provide information on the material scatter shown by the investigated material. This knowledge allows to draw conclusions with more confidence about the deformation of thermoplastic components when they pass through the cathodic dip painting oven. After conducting the material characterisation tests it is believed that the entire identification of material parameters with the exception of the major Poisson's ratio can be carried out with a machine suitable for dynamic mechanical analysis that supports thermogravimetric analysis. This is considered to be worth investigating as it significantly reduces the required experimental setups for material characterisation.



# References

- [1] European Parliament. 'Regulation (EC) No 443/2009 of the European Parliament and of the Council of 23 April 2009 setting emission performance standards for new passenger cars as part of the Community's integrated approach to reduce CO<sub>2</sub> emissions from light-duty vehicles'. In: *Regulations* (2009).
- [2] P. Mock, U. Tietge, J. German and A. Bandivadekar. 'Road Transport in the EU Emissions Trading System: An Engineering Perspective'. In: (2014).
- [3] European Parliament. 'Directive 2000/53/EC of the European Parliament and of the Council of 18 September 2000 on end-of-life vehicles'. In: *Regulations* (2000).
- [4] H.-J. Streitberger and K.-F. Dossel. *Automotive paints and coatings*. 2nd ed. John Wiley & Sons, 2008. ISBN: 978-3-527-30971-9.
- [5] M. Biron. *Material selection for thermoplastic parts: Practical and advanced information for plastics engineers*. Amsterdam: Elsevier, 2016. ISBN: 978-0-7020-6284-1. URL: <http://www.sciencedirect.com/science/book/9780702062841>.
- [6] N. Akafuah, S. Poozesh, A. Salaimah, G. Patrick, K. Lawler and K. Saito. 'Evolution of the Automotive Body Coating Process - A Review'. In: 6 (2 2016), p. 24. DOI: 10.3390/coatings6020024.
- [7] *Emission Control - High-Volume Car Body Painting Plants*. Standard VDI 3455. VDI Commission on Air Pollution, 2013.
- [8] T. Yilmaz and T. Sinmazcelik. 'Effects of Hydrothermal Aging on Glass-Fiber/Polyetherimide (PEI) Composites'. In: *Journal of Materials Science* 45.2 (2010), pp. 399–404. ISSN: 0022-2461. DOI: 10.1007/s10853-009-3954-1.
- [9] N. Boualem and Z. Sereir. 'Accelerated Aging of Unidirectional Hybrid Composites under the Long-Term Elevated Temperature and Moisture Concentration'. In: *Theoretical and Applied Fracture Mechanics* 55.1 (2011), pp. 68–75. ISSN: 01678442. DOI: 10.1016/j.tafmec.2011.01.007.
- [10] B. Yu and J. Yang. 'Hygrothermal Effects in Composites'. In: *Reference Module in Materials Science and Materials Engineering*. Elsevier, 2017, pp. 502–519. ISBN: 9780081005347. DOI: 10.1016/B978-0-12-803581-8.09887-8.
- [11] A. Fick. 'On Liquid Diffusion'. In: *Philosophical Magazine*. 4th ser. 10 (63 1855), pp. 30–39.
- [12] O. de La Osa, V. Alvarez and A. Avazquez. 'Effect of Hygrothermal History on Water and Mechanical Properties of Glass/Vinylester Composites'. In: *Journal of Composite Materials* 40.22 (2006), pp. 2009–2023. ISSN: 0021-9983. DOI: 10.1177/0021998306061319.
- [13] A. Hassan, N. A. Rahman and R. Yahya. 'Moisture Absorption Effect on Thermal, Dynamic Mechanical and Mechanical Properties of Injection-Molded Short Glass-Fiber/Polyamide 6,6 Composites'. In: *Fibers and Polymers* 13.7 (2012), pp. 899–906. ISSN: 1229-9197. DOI: 10.1007/s12221-012-0899-9.
- [14] N. L. Batista, K. Iha and E. C. Botelho. 'Evaluation of Weather Influence on Mechanical and Viscoelastic Properties of Polyetherimide/Carbon Fiber Composites'. In: *Journal of Reinforced Plastics and Composites* 32.12 (2013), pp. 863–874. ISSN: 0731-6844. DOI: 10.1177/0731684413482994.
- [15] A. A. Arici. 'Effect of Hygrothermal Aging on Polyetherimide Composites'. In: *Journal of Reinforced Plastics and Composites* 26.18 (2007), pp. 1937–1942. DOI: 10.1177/0731684407082630.
- [16] G. C. Papanicolaou, A. G. Xepapadaki and G. D. Tagaris. 'Effect of Thermal Shock Cycling on the Creep Behavior of Glass-Epoxy Composites'. In: *Composite Structures* 88.3 (2009), pp. 436–442. ISSN: 02638223. DOI: 10.1016/j.compstruct.2008.05.003.

- [17] M. Eftekhari and A. Fatemi. 'Tensile Behavior of Thermoplastic Composites Including Temperature, Moisture, and Hygrothermal Effects'. In: *Polymer Testing* 51 (2016), pp. 151–164. ISSN: 01429418. DOI: 10.1016/j.polymertesting.2016.03.011.
- [18] G. Ehrenstein. *Polymer Werkstoffe*. 3rd ed. Hanser, 2011. ISBN: 978-3-446-42283-4.
- [19] D. van Krevelen. *Properties of Polymers*. 3rd ed. Elsevier, 1997. ISBN: 978-0-08-054819-7.
- [20] N. Dencheva, Z. Denchev, M. Oliveira and S. Funari. 'Relationship Between Crystalline Structure and Mechanical Behavior in Isotropic and Oriented Polyamide 6'. In: *Journal of Applied Polymer Science* 103 (2006), pp. 2242–2252. DOI: 10.1002/app.25250.
- [21] S. Marques and G. Creus. *Computational Viscoelasticity*. Springer, 2012. ISBN: 978-3-642-25310-2. DOI: 10.1007/978-3-642-25311-9.
- [22] I. Hopkins and R. Hamming. 'On Creep and Relaxation'. In: *Journal of Applied Physics* 28.8 (1957), pp. 906–909.
- [23] E. H. Lee and T. G. Rogers. 'Solution of Viscoelastic Stress Analysis Problems Using Measured Creep or Relaxation Functions'. In: *Journal of Applied Mechanics* 30.1 (1963), p. 127. ISSN: 00218936. DOI: 10.1115/1.3630057.
- [24] B. Gross. *Mathematical Structure of the Theories of Viscoelasticity*. Paris: Hermann & Cie, 1953.
- [25] A. Zak. 'Structural Analysis of Realistic Solid Propellant Materials'. In: *Journal of Spacecraft and Rockets* 5.3 (1968), pp. 270–275. ISSN: 0022-4650. DOI: 10.2514/3.29237.
- [26] I. King. 'On the Finite Element Analysis of Two-Dimensional Problems with Time Dependent Properties'. PhD thesis. University of California, Berkeley, CA, 1965.
- [27] R. L. Taylor and T. Y. Chang. 'An Approximate Method for Thermoviscoelastic Stress Analysis'. In: *Nuclear Engineering and Design* 4.1 (1966), pp. 21–28. ISSN: 00295493. DOI: 10.1016/0029-5493(66)90023-9.
- [28] R. L. Taylor, K. S. Pister and G. L. Goudreau. 'Thermomechanical Analysis of Viscoelastic Solids'. In: *International Journal for Numerical Methods in Engineering* 2.1 (1970), pp. 45–59. ISSN: 0029-5981. DOI: 10.1002/nme.1620020106.
- [29] O. Zienkiewicz and M. Watson. 'Some Creep Effects in Stress Analysis with Particular Reference to Concrete Pressure Vessels'. In: *Nuclear Engineering and Design* 4 (1966), pp. 406–412.
- [30] F. de S. Lynch. 'A Finite Element Method of Viscoelastic Stress Analysis with Application to Rolling Contact Problems'. In: *International Journal for Numerical Methods in Engineering* 1.4 (1969), pp. 379–394. ISSN: 0029-5981. DOI: 10.1002/nme.1620010405.
- [31] J. White. *Finite Elements in Linear Viscoelasticity*. Tech. rep. The Boeing Company, 1968.
- [32] Y. R. Rashid and W. Rockenhauser. 'Pressure Vessel Analysis by Finite Element Techniques'. In: *Prestressed Concrete Pressure Vessels*. 1967, pp. 375–383. DOI: 10.1680/pcpv.44760.0043.
- [33] O. C. Zienkiewicz, M. Watson and I. P. King. 'A Numerical Method of Visco-Elastic Stress Analysis'. In: *International Journal of Mechanical Sciences* 10.10 (1968), pp. 807–827. ISSN: 00207403. DOI: 10.1016/0020-7403(68)90022-2.
- [34] G. Greenbaum and M. Rubinstein. 'Creep Analysis of Axisymmetric Bodies Using Finite Elements'. In: *Nuclear Engineering and Design* (1968), pp. 379–397.
- [35] J. P. H. Webber. 'Stress Analysis in Viscoelastic Bodies Using Finite Elements and a Correspondence Rule with Elasticity'. In: *Journal of Strain Analysis* 4.3 (1969), pp. 236–243. ISSN: 0022-4758. DOI: 10.1243/03093247V043236.
- [36] Z. P. Bažant. 'Matrix Differential Equation and Higher-Order Numerical Methods for Problems of Non-Linear Creep, Viscoelasticity and Elasto-Plasticity'. In: *International Journal for Numerical Methods in Engineering* 4.1 (1972), pp. 11–15. ISSN: 0029-5981. DOI: 10.1002/nme.1620040104.
- [37] W. C. Carpenter. 'Viscoelastic Stress Analysis'. In: *International Journal for Numerical Methods in Engineering* 4.3 (1972), pp. 357–366. ISSN: 0029-5981. DOI: 10.1002/nme.1620040306.

- [38] R. A. Schapery. 'Nonlinear Viscoelastic and Viscoplastic Constitutive Equations Based on Thermodynamics'. In: *Mechanics of Time-Dependent Materials* 1.2 (1997), pp. 209–240. ISSN: 13852000. DOI: 10.1023/A:1009767812821.
- [39] K. Lin and I. Hwang. 'Thermo-Viscoelastic Analysis of Composite Materials'. In: *Journal of Composite Materials* 23.6 (1989), pp. 554–569. DOI: 10.1177/002199838902300602.
- [40] H. Hilton and S. Yi. 'Anisotropic Viscoelastic Finite Element Analysis of Mechanically and Hygrothermally Loaded Composites'. In: *Composites Engineering* 3.2 (1993), pp. 123–135. ISSN: 0961-9526. DOI: 10.1016/0961-9526(93)90037-K.
- [41] S. Yi. 'Thermoviscoelastic Analysis of Delamination Onset and Free Edge Response in Laminated Composites'. In: 31.12 (1993), pp. 2320–2328. DOI: 10.1177/002199838902300602.
- [42] T. Kennedy and M. Wang. 'Three-Dimensional, Non-Linear Viscoelastic Analysis of Laminated Composites'. In: *Journal of Composite Materials* 28 (1994), pp. 902–925. DOI: 10.1177/002199839402801002.
- [43] R. Schapery and Y. Lou. 'Viscoelastic Characterization of a Non-Linear Fiber Reinforced Plastic'. In: *Journal of Composite Materials* 5 (1971), pp. 208–234. DOI: 10.1177/002199837100500206.
- [44] M. A. Zocher, S. E. Groves and D. H. Allen. 'A Three Dimensional Finite Element Formulation for Thermoviscoelastic Orthotropic Media'. In: *International Journal for Numerical Methods in Engineering* 40.12 (1997), pp. 2267–2288. ISSN: 0029-5981. DOI: 10.1002/(SICI)1097-0207(19970630)40:12<2267::AID-NME156>3.0.CO;2-P.
- [45] A. Ding, S. Li, J. Sun, J. Wang and L. Zu. " In: *Composite Structures* 136.Supplement C (2016), pp. 34–43. ISSN: 0263-8223. DOI: 10.1016/j.compstruct.2015.09.014.
- [46] M. Abouhamzeh, J. Sinke, K. Jansen and R. Benedictus. 'A New Procedure for Thermo-Viscoelastic Modelling of Composites with General Orthotropy and Geometry'. In: *Composite Structures* 133 (2015), pp. 871–877. DOI: 10.1016/j.compstruct.2015.08.050.
- [47] M. Abouhamzeh, J. Sinke, K. Jansen and R. Benedictus. 'Thermo-Viscoelastic Analysis of GLARE'. In: *Composites Part B: Engineering* 99 (2016), pp. 1–8. DOI: 10.1016/j.compositesb.2016.05.060.
- [48] T. A. Osswald and G. Menges. *Material science of polymers for engineers*. 3rd ed. Munich and Cincinnati Ohio: Hanser, 2012. ISBN: 978-1-56990-514-2.
- [49] D. Gutierrez-Lemini. *Engineering Viscoelasticity*. Boston, MA: Springer US, 2014. ISBN: 978-1-4614-8138-6. DOI: 10.1007/978-1-4614-8139-3.
- [50] DSM Engineering Plastics. *Datasheet of Akulon Ultraflow K-FHG0*. 2017. URL: <http://www.campusplastics.com/campus/en/datasheet/Akulon%5C%C2%5C%AE+Ultraflow+K-FHG0/DSM+Engineering+Plastics/50/69dc210e>.
- [51] E. Klompen and L. Govaert. 'Nonlinear Viscoelastic Behaviour of Thermorheologically Complex Materials'. In: *Mechanics of Time-Dependent Materials* 3 (1999), pp. 49–69. DOI: 10.1023/A:1009853024441.
- [52] R. Colby. 'Breakdown of Time-Temperature Superposition in Miscible Polymer Blends'. In: *Polymer* 30.7 (1989), pp. 1275–1278. ISSN: 00323861. DOI: 10.1016/0032-3861(89)90048-7.
- [53] C. Dae Han and J. K. Kim. 'On the Use of Time-Temperature Superposition in Multicomponent/Multiphase Polymer Systems'. In: *Polymer* 34.12 (1993), pp. 2533–2539. ISSN: 00323861. DOI: 10.1016/0032-3861(93)90585-X.
- [54] K. S. Cho. *Viscoelasticity of Polymers*. Vol. 241. Dordrecht: Springer Netherlands, 2016. ISBN: 978-94-017-7562-5. DOI: 10.1007/978-94-017-7564-9.
- [55] J. Ferry. *Viscoelastic Properties of Polymers*. 3rd ed. John Wiley & Sons, 1980. ISBN: 978-0-471-04894-7.
- [56] D. Fesko and N. Tschoegl. 'Time-Temperature Superposition in Thermorheologically Complex Materials'. In: *Journal of Polymer Science Part C: Polymer Letters* (1971), pp. 51–69. DOI: 10.1002/polc.5070350106.
- [57] A. Oseli, A. Aulova, M. Gergesova and I. Emri. 'Time-Temperature Superposition in Linear and Non-Linear Domain'. In: *Materials Today: Proceedings* 3 (2016), pp. 1118–1123. DOI: 10.1016/j.matpr.2016.03.059.

- [58] A. Tobolsky and J. McLoughlin. 'Elastoviscous Properties of Polyisobutylene. V. The Transition Region'. In: *Journal of Polymer Science* 8.5 (1952), pp. 543–553.
- [59] J. D. Ferry. 'Mechanical Properties of Substances of High Molecular Weight. VI. Dispersion in Concentrated Polymer Solutions and its Dependence on Temperature and Concentration'. In: *Journal of the American Chemical Society* 72.8 (1950), pp. 3746–3752. ISSN: 0002-7863. DOI: 10.1021/ja01164a117.
- [60] H. Leaderman, R. G. Smith and R. W. Jones. 'Rheology of Polyisobutylene. II. Low Molecular Weight Polymers'. In: *Journal of Polymer Science* 14.73 (1954), pp. 47–80. ISSN: 00223832. DOI: 10.1002/pol.1954.120147306.
- [61] L. Rouleau, R. Pirk, B. Pluymers and W. Desmet. 'Characterization and Modeling of the Viscoelastic Behaviour of a Self-Adhesive Rubber Using Dynamic Mechanical Analysis Tests'. In: *Journal of Aerospace Technology and Management* 7.2 (2015), pp. 200–208. DOI: 10.5028/jatm.v7i2.474.
- [62] A. Maiti. 'A Geometry-Based Approach to Determining Time-Temperature Superposition Shifts in Aging Experiments'. In: *Rheologica Acta* 55 (2016), pp. 83–90. DOI: 10.1007/s00397-015-0898-z.
- [63] A. K. Doolittle. 'Studies in Newtonian Flow. II. The Dependence of the Viscosity of Liquids on Free-Space'. In: *Journal of Applied Physics* 22.12 (1951), pp. 1471–1475. ISSN: 0021-8979. DOI: 10.1063/1.1699894.
- [64] M. L. Williams, R. F. Landel and J. D. Ferry. 'The Temperature Dependence of Relaxation Mechanisms in Amorphous Polymers and Other Glass-forming Liquids'. In: *Journal of the American Chemical Society* 77.14 (1955), pp. 3701–3707. ISSN: 0002-7863. DOI: 10.1021/ja01619a008.
- [65] R. Maksimov, E. Sokolov and V. Mochalov. 'Effect of Temperature and Moisture on the Creep of Polymeric Materials 1. One-Dimensional Extension under Stationary Temperature-Moisture Conditions'. In: (1975), pp. 393–399.
- [66] K. Patankar, D. Dillard, S. Case, M. Ellis, Y.-H. Lai and C. Gittleman. 'Linear Hygrothermal Viscoelastic Characterization of Nafion NRE 211 Proton Exchange Membrane'. In: *Fuel Cells* 12 (2012). DOI: 10.1002/fuce.201100134.
- [67] J. Skrzypek and A. Ganczarski, eds. *Mechanics of Anisotropic Materials*. Springer International Publishing, 2015. ISBN: 978-3-319-17160-9. DOI: 10.1007/978-3-319-17160-9.
- [68] Dassault Systèmes. *Abaqus 6.14 Online Documentation*. <http://abaqusdoc.muc/v6.14/index.html>. 2014.
- [69] R. Schapery. 'Models for Damage Growth and Fracture in Nonlinear Viscoelastic Particulate Composites'. In: *Proceedings of the Ninth U.S. National Congress of Applied Mechanics*. 1982, pp. 237–245.
- [70] R. Nevière. 'An Extension of the Time-Temperature Superposition Principle to Non-Linear Viscoelastic Solids'. In: *International Journal of Solids and Structures* 43.17 (2006), pp. 5295–5306. ISSN: 00207683. DOI: 10.1016/j.ijsolstr.2005.09.009.
- [71] *Plastics – Determination of dynamic mechanical properties – Part 1: General principles*. Standard ISO 6721-1:2011. rue de Stassart 36, Brussels: European Committee for Standardization, 2011.
- [72] TA Instruments. *Thermal Solutions - Determination of the Linear Viscoelastic Region of a Polymer Using a Strain Sweep on the DMA 2980*.
- [73] H. Schürmann. *Konstruieren mit Faser-Kunststoff-Verbunden*. Berlin, Heidelberg: Springer Berlin Heidelberg, 2007. ISBN: 978-3-540-72189-5. DOI: 10.1007/978-3-540-72190-1.
- [74] *Plastics – Thermogravimetry (TG) of polymers – Part 1: General principles*. Standard ISO 11358-1:2014. rue de Stassart 36, Brussels: European Committee for Standardization, 2014.
- [75] S. Arrhenius. 'On the Reaction Velocity of the Inversion of Cane Sugar by Acids'. In: *Zeitschrift für Physikalische Chemie* 4 (1889), p. 226.
- [76] *Polyamides – Accelerated conditioning of test specimens*. Standard ISO 1110:1995. rue de Stassart 36, Brussels: European Committee for Standardization, 1998.
- [77] G. Menges, E. Haberstroh, W. Michaeli and E. Schmachtenberg. *Menges Werkstoffkunde Kunststoffe*. 6th ed. Hanser, 2011. ISBN: 978-3-446-42762-4.



- [78] N. Murthy, S. Aharoni and A. Szollosi. 'Stability of the  $\gamma$  Form and the Development of the  $\alpha$  Form in Nylon 6'. In: *Journal of Polymer Science: Polymer Physics Edition* 23 (1985), pp. 2549–2565. doi: 10.1002/pol.1985.180231212.
- [79] R. Stepaniak, A. Garton, D. Carlsson and D. Wiles. 'The Characterization of Nylon Filaments by X-Ray Diffraction'. In: *Journal of Polymer Science: Polymer Physics Edition* 23 (6 1979), pp. 1747–1757. doi: 10.1002/app.1979.070230615.
- [80] *Plastics – Determination of tensile properties – Part 4: Test conditions for isotropic and orthotropic fibre-reinforced plastic composites*. Standard ISO 527-4:1997. rue de Stassart 36, Brussels: European Committee for Standardization, 1997.
- [81] *Plastics – Determination of tensile properties – Part 5: Test conditions for unidirectional fibre-reinforced plastic composites*. Standard ISO 527-5:2009. rue de Stassart 36, Brussels: European Committee for Standardization, 2009.
- [82] G. Ehrenstein. *Faserverbund-Kunststoffe*. 2nd ed. Hanser, 2006. ISBN: 978-3-446-22716-3.
- [83] *Plastics – Determination of creep behaviour – Part 1: Tensile creep*. Standard ISO 899-1:2003. rue de Stassart 36, Brussels: European Committee for Standardization, 2003.
- [84] *Plastics – Determination of tensile properties – Part 1: General principles*. Standard ISO 527-1:2012. rue de Stassart 36, Brussels: European Committee for Standardization, 2012.
- [85] O. Starkova and A. Aniskevich. 'Limits of Linear Viscoelastic Behaviour of Polymers'. In: *Mechanics of Time-Dependent Materials* 11 (2007), pp. 111–126. doi: 10.1007/s11043-007-9036-3.
- [86] S. Ropers. 'Bending Behavior of Thermoplastic Composite Sheets'. Friedrich-Alexander University Erlangen Nuremberg, 2016. ISBN: 978-3-658-17593-1. doi: 10.1007/978-3-658-17594-8.
- [87] E. Soós and T. Goda. 'Mechanical Behavior of Glass Fiber-Reinforced Bosses: Experiments and FE Simulations'. In: *Periodica Polytechnica Mechanical Engineering* 55.1 (2011), pp. 3–14. doi: 10.3311/pp.me.2011-1.01.
- [88] M. Costa and C. Ribeiro. 'Parameter Estimation of Viscoelastic Materials: A Test Case with Different Strategies'. In: *Conf. Proc. ICNAAM 2011* (2011), pp. 771–774. doi: 10.1063/1.3636846.
- [89] J. Whitney. 'Elastic Moduli of Unidirectional Composites with Anisotropic Filaments'. In: *Journal of Composite Materials* 1 (1967), pp. 188–193. doi: 10.1177/002199836700100208.
- [90] D.-L. Chen, T.-C. Chiu, T.-C. Chen, M.-H. Chung, P.-F. Yang and Y.-S. Lai. 'Using DMA to Simultaneously Acquire Young's Relaxation Modulus and Time-Dependent Poisson's Ratio of a Viscoelastic Material'. In: *Procedia Engineering* 79 (2014), pp. 153–159. doi: 10.1016/j.proeng.2014.06.324.
- [91] S. Pandini and A. Pegoretti. 'Time and Temperature Effects on Poisson's Ratio of Poly(butylene terephthalate)'. In: *Express Polymer Letters* 5 (8 2011), pp. 685–697. doi: 10.3144/expresspolymlett.2011.67.
- [92] E. Giencke and G. Meder. 'Calculation of the Creep Function for Two Dimensional Loaded Resins and GP-UP From the Experimental Values for Uniaxial Resins'. In: *Materialpruefung* 23.3 (1981), pp. 69–74.
- [93] J. Halpin and J. Kardos. 'The Halpin-Tsai Equations: A Review'. In: *Polymer Engineering and Science* 16.5 (1976), pp. 344–352. doi: 10.1002/pen.760160512.
- [94] T. Kroupa, H. Srbová and R. Zemčík. 'Micromechanical Model of the Substituents of a Unidirectional Fiber-Reinforced Composite and Its Response to the Tensile Cyclic Loading'. In: *Materials and Technologies* 49 (2015), pp. 99–102.
- [95] E. Bich, J. Millat and E. Vogel. 'The Viscosity and Thermal Conductivity of Pure Monoatomic Gases from Their Boiling Point Up to 5000K in the Limit of Zero Density and At 0.101325 MPa'. In: *Journal of Physical and Chemical Reference Data* 19 (1990), pp. 1289–1305.
- [96] P. F. Monaghan, M. T. Brogan and P. H. Oosthuizen. 'Heat Transfer in an Autoclave for Processing Thermoplastic Composites'. In: *Composites Manufacturing* 2.3-4 (1991), pp. 233–242. ISSN: 09567143. doi: 10.1016/0956-7143(91)90145-7.
- [97] C. Kassapoglou. *Design and Analysis of Composite Structures*. 2nd ed. John Wiley & Sons, 2013. ISBN: 978-1-118-53694-0.



# Appendix A: UMAT user subroutine

```
SUBROUTINE UMAT(STRESS,STATEV,DDSDDE,SSE,SPD,SCD,  
1 RPL,DDSDDT,DRPLDE,DRPLDT,  
2 STRAN,DSTRAN,TIME,DTIME,TEMP,DTEMP,PREDEF,DPRED,CMNAME,  
3 NDI,NSHR,NTENS,NSTATV,PROPS,NPROPS,COORDS,DROT,PNEWDT,  
4 CELENT,DFGRD0,DFGRD1,NOEL,NPT,LAYER,KSPT,JSTEP,KINC)  
  
C  
C   INCLUDE 'ABA_PARAM.INC'  
  
C  
C   CHARACTER*8 CMNAME  
C   DIMENSION STRESS(NTENS),STATEV(NSTATV),  
1 DDSDDE(NTENS,NTENS),  
2 DDSDDT(NTENS),DRPLDE(NTENS),  
3 STRAN(NTENS),DSTRAN(NTENS),TIME(2),PREDEF(1),DPRED(1),  
4 PROPS(NPROPS),COORDS(3),DROT(3,3),DFGRD0(3,3),DFGRD1(3,3),  
5 JSTEP(4)  
  
C  
C   PARAMETER(DLNTEN=2.30258509299d0)  
  
C  
C   REAL*8 C(7,33),DDSN(3,3),DDSS(3,3),DSTRES(6),EXPP(32),DTIMEI,DTIMEA,STIFFA,STIFFB  
  
C  
C   DTIMEA = DTIME*EXP(DLNTEN*PROPS(231)*(TEMP-PROPS(233))/(PROPS(232)+TEMP-PROPS(233)))  
  
C  
C   DO I=1,NTENS  
C     STATEV(I) = DSTRAN(I)/DTIMEA  
C   END DO  
  
C  
C(1,1) = 0.  
C   DO I=1,6  
C     C(I+1,1) = PROPS(I)  
C   END DO  
C   DO I=1,32  
C     C(1,I+1) = PROPS(I+6)  
C     C(2,I+1) = PROPS(I+38)  
C     C(3,I+1) = PROPS(I+70)  
C     C(4,I+1) = PROPS(I+102)  
C     C(5,I+1) = PROPS(I+134)  
C     C(6,I+1) = PROPS(I+166)  
C     C(7,I+1) = PROPS(I+198)  
C   END DO  
  
C  
C   DO I=1,32  
C     EXPP(I) = EXP(-DTIMEA/C(1,I+1))  
C     STATEV(I+6) = EXPP(I)*STATEV(I+6) + STATEV(1)*C(2,I+1)*C(1,I+1)*(1-EXPP(I))  
C     STATEV(I+38) = EXPP(I)*STATEV(I+38) + STATEV(2)*C(4,I+1)*C(1,I+1)*(1-EXPP(I))  
C     STATEV(I+70) = EXPP(I)*STATEV(I+70) + STATEV(3)*C(4,I+1)*C(1,I+1)*(1-EXPP(I))  
C     STATEV(I+102) = EXPP(I)*STATEV(I+102) + STATEV(4)*C(6,I+1)*C(1,I+1)*(1-EXPP(I))  
C     STATEV(I+134) = EXPP(I)*STATEV(I+134) + STATEV(5)*C(6,I+1)*C(1,I+1)*(1-EXPP(I))  
C     STATEV(I+166) = EXPP(I)*STATEV(I+166) + STATEV(6)*C(7,I+1)*C(1,I+1)*(1-EXPP(I))  
C   END DO  
  
C  
C   DTIMEI = 1./DTIMEA  
C   DDSN(1,1) = C(2,1)  
C   DDSN(1,2) = C(3,1)  
C   DDSN(2,2) = C(4,1)  
C   DDSN(2,3) = C(5,1)  
  
C  
C   DO I=2,33  
C     DDSN(1,1) = DDSN(1,1) + DTIMEI*C(2,I)*C(1,I)*(1-EXP(-DTIMEA/C(1,I)))  
C     DDSN(1,2) = DDSN(1,2) + DTIMEI*C(3,I)*C(1,I)*(1-EXP(-DTIMEA/C(1,I)))  
C     DDSN(2,2) = DDSN(2,2) + DTIMEI*C(4,I)*C(1,I)*(1-EXP(-DTIMEA/C(1,I)))
```

```

      DDSN(2,3) = DDSN(2,3) + DTIMEI*C(5,I)*C(1,I)*(1-EXP(-DTIMEA/C(1,I)))
END DO
      DDSN(1,3) = DDSN(1,2)
      DDSN(2,1) = DDSN(1,2)
      DDSN(3,1) = DDSN(1,2)
      DDSN(3,2) = DDSN(2,3)
      DDSN(3,3) = DDSN(2,2)
C
      DDSS(1,1) = C(6,1)
      DDSS(3,3) = C(7,1)
      DO I = 2,33
        DDSS(1,1) = DDSS(1,1) + DTIMEI*C(6,I)*C(1,I)*(1-EXP(-DTIMEA/C(1,I)))
        DDSS(3,3) = DDSS(3,3) + DTIMEI*C(7,I)*C(1,I)*(1-EXP(-DTIMEA/C(1,I)))
      END DO
      DDSS(2,2) = DDSS(1,1)
C
      DO I=1,NDI
        DO J=1,NDI
          DDSDE(I,J) = DDSN(I,J)
        END DO
      END DO
      DO I=1,NSHR
        DDSDE(NDI+I,NDI+I) = DDSS(I,I)
      END DO
C
      DO I=1,NTENS
        DSTRES(I) = 0.
        DO J=1,NTENS
          DSTRES(I) = DSTRES(I) + DSTRAN(J)*DDSDE(I,J)
        END DO
        DO J=1,32
          DSTRES(I) = DSTRES(I) - (1-EXP(J))*STATEV(6+32*(I-1)+J)
        END DO
        STRESS(I) = STRESS(I) + DSTRES(I)
      END DO

```

## Appendix B: Technical drawings

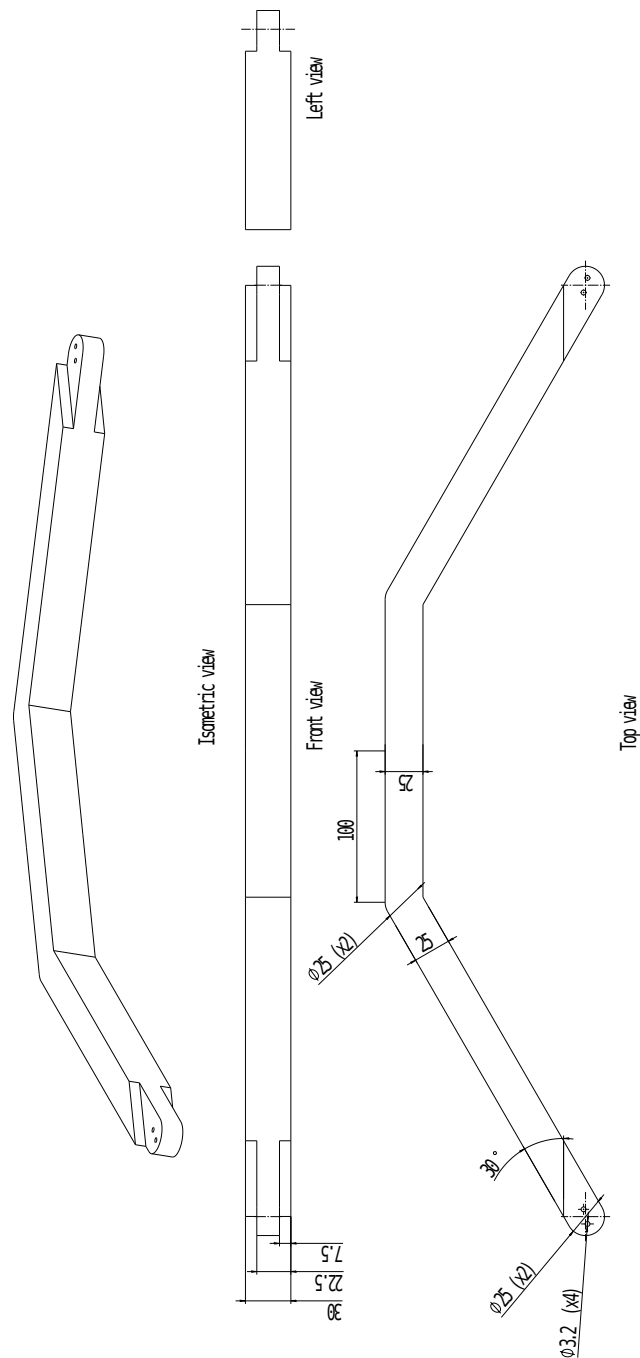


Figure B.1 *Technical drawing of the main part of the fixture for the coupon level validation experiments.*

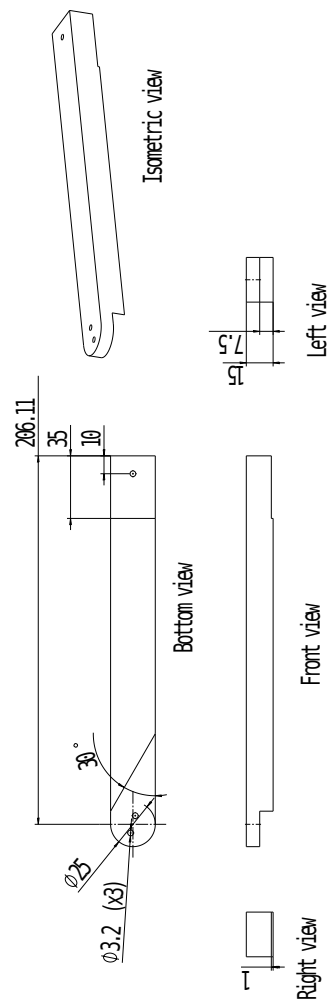


Figure B.2 *Technical drawing of the parts used for clamping the coupon in the fixture for the coupon level validation experiments.*

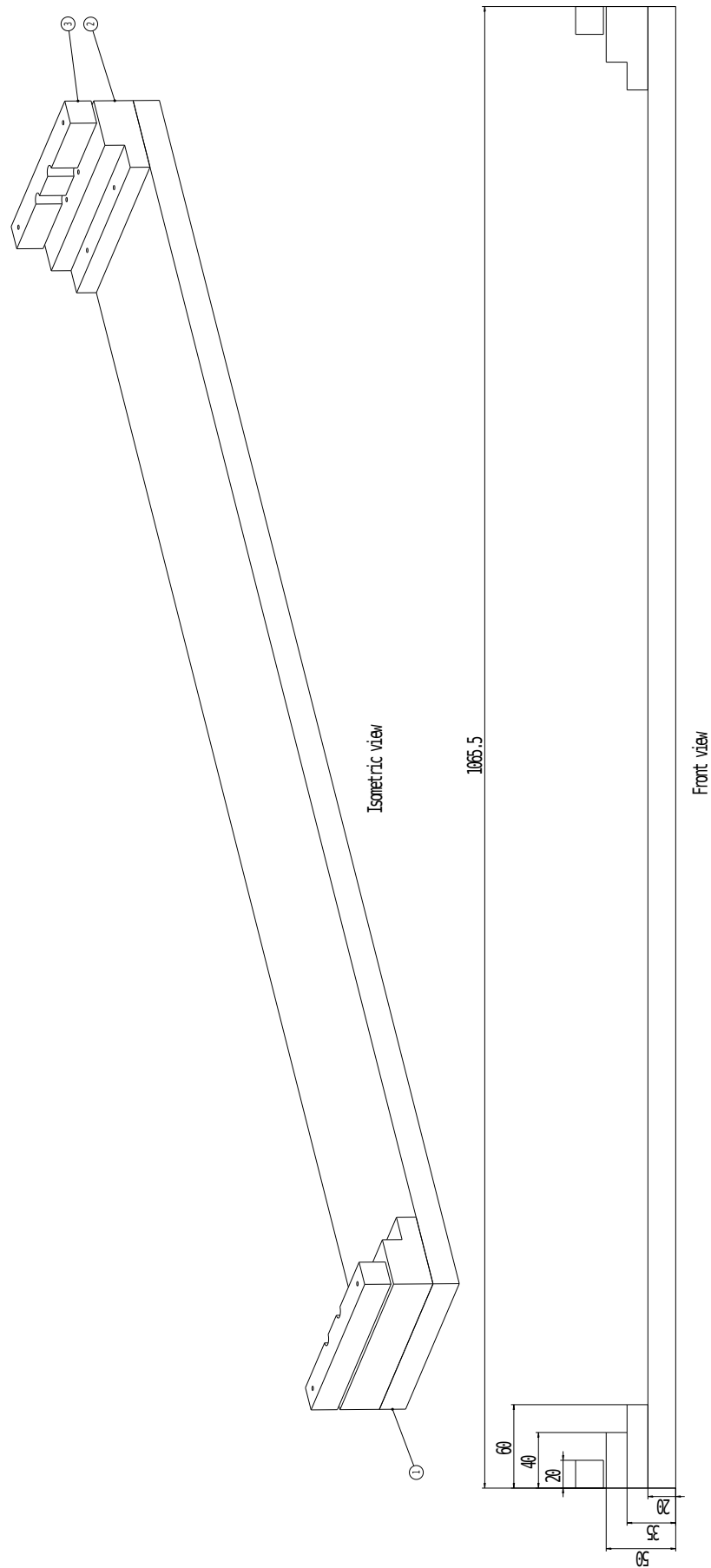


Figure B.3 *Technical drawings of the fixture for the component level validation experiments.*



